FACULTY OF ENGINEERING AND ARCHITECTURE

Wavelength Division Multiplexing Filters in Silicon Photonics

Ahmed Bayoumi

Doctoral dissertation submitted to obtain the academic degree of
Doctor of Photonics Engineering

Supervisors

Prof. Wim Bogaerts, PhD* - Qingzhong Deng, PhD**

* Department of Information Technology
Faculty of Engineering and Architecture, Ghent University

** imec

October 2025

GHENT UNIVERSITY

ISBN 978-94-93464-51-3
NUR 959, 924
Wettelijk depot: D/2025/10.500/111

Members of the Examination Board

Chair

Prof. Luc Dupré, PhD, Ghent University

Other members entitled to vote

Nagarjun Katta Pradeep Kumar, PhD, Ghent University
Prof. Xaveer J. M. Leijtens, PhD, Technische Universiteit Eindhoven, the Netherlands
Pieter Neutens, PhD, imec
Prof. Xin Yin, PhD, Ghent University

Supervisors

Prof. Wim Bogaerts, PhD, Ghent University
Qingzhong Deng, PhD, imec

Acknowledgements

"And whatever you have of favor - it is from Allah." - Surah An-Nahl (16:53)

I would like to start this acknowledgement by praising God, the Almighty, for giving me all what was needed to complete this PhD journey: good health, a sound mind, a suitable environment, and most importantly great supervisors, family, and friends. I am truly lucky and blessed for having had those blessings in my life. These should not be taken for granted, in particular taking into account the current state of the world.

My deepest gratitude and appreciation go to my supervisors Dr. Qingzhong (Quincy) Deng and Prof. Wim Bogaerts for their continuous support, guidance, and encouragement throughout my PhD. Having had the chance to work with them has been a great honor and privilege. Thank you so much for all your efforts, and I would like to say I feel really lucky to have had you as my supervisors.

Thank you so much Quincy, as my daily supervisor, I was truly lucky to have you as my mentor throughout this journey and learn from you on a daily basis. Having already transitioned to industry, I now realize you have guided me to learn skills that are highly useful and appreciated. From photonics, to software development, project management skills, and the list goes on. You always had a clear vision and were able to always think multiple steps ahead, which really helped me to stay on track and focus on what is important. I learned a lot from you, thank you for all the time you gave me and all the support. I would like to thank you for letting me graduate despite not being able to speak Chinese fluently (joke), but maybe now, given the circumstances, is the time.

Thank you so much Wim. The first time I saw Wim was during my M.Sc. course on Photonic Integrated Circuits. I had to travel from Brussels, where I lived at the time, to Gent, which was not always a convenient journey. Living in Brussels, I rarely had to travel or commute for study, as my university room was literally a few minutes walk from the lecture halls. Despite the tiring travels, I was always looking forward to attending your lectures and having discussions with you. I really have great memories about this course, and it convinced me further to pursue a PhD in

this field. And here we are four and a half years later. Thank you so much for all your support and guidance throughout this journey.

I would like to thank my thesis jury members, Prof. Luc Dupré, Prof. Xaveer Leijtens, Prof. Xin Yin, Dr. Pieter Neutens, and Dr. Nagarjun K. P. Kumar. I am really grateful for your time and effort in reviewing my thesis and for your valuable comments and suggestions. I really enjoyed our discussions during the private defense. I highly appreciate all your comments, and I believe they have improved the thesis significantly. Thank you.

Thank you to all my colleagues at IMEC's Optical IO team and at the Photonics Research Group at UGent for the great working atmosphere and the friendships I made. I really enjoyed working with you all, and I enjoyed our early lunches and our discussions. Performing my PhD at IMEC and UGent has been a great experience and privilege, where I was working with some of the best researchers in the field with access to top-notch facilities. IMEC is such an incredible place to work and do research, I really liked its inclusivity and open-minded culture. Those traits should not be taken for granted. I would like to particularly thank my managers: Maumita Chakrabarti, Dimitrios Velenis, Joris Van Campenhout, Peter De Heyn, Sebastien Lardenois, Philippe Absil, Filippo Ferraro, and Yoojin Ban. Thank you to everyone who contributed to making this experience so special and unforgettable. I would like to thank my colleagues: Ahmed Kandeel, Ahmed Khalil, Amir Shahin, Alaa Elshazly, Mehmet Oktay, Zuhaddin Ahmad, Hakim Kobbi, Jef Van Asch, Husseyin Sar, Aimen Zelaci, Eslam Bakry, Sarah Masaad, Menna Kandil, Mohammed Aftab, Minkyu Kim, Abubakr Nada, Sumi Radhakrishnan, Emmanuel Le Boulbar, Simei Mao, Lirong Cheng, Nicolas Pantano, Javad Rahimi, Bilal Naffaa, Aliaksandra Ivinskaya, Dieter Bode, and Swetanshu Bipul.

A PhD acknowledgement would not be complete without reminiscing about late-night measurements, it felt a bit weird (sometimes scary) to be (probably?) alone in such a big building in the middle of the night. Special thanks to my colleagues in the test team for their help and support in the lab, especially Hakim Kobbi. Hakim was always the right person to ask for help when things went wrong during measurements. You always helped (everyone), even after work hours, thank you Hakim.

Now, I can not hide that I feel the urge to thank Belgium; what does thanking a country even mean? I do not know, but I have to acknowledge Belgium, for giving me a good environment to do my PhD. Starting from my masters at the VUB and Ghent University, to my internship at IMEC, to my PhD, I have always felt I was offered the capabilities needed to succeed. Alhamdullah.

Thank you Mama Amani, Baba Hesham (may Allah bless your soul), and my sister, Yomna. My dad passed away sooner that we expected, and we as a family (and specially me) did not have the time to thank him enough for all what he has offered us. As often in life, we realize some important things sometimes too late. Thank you Baba for everything. We will reunite soon in shaa Allah. Mama, Baba, Yomna:

you are all the reason I am where I am today. I am so blessed to have you in my life. Now that I am old (30 years!), I realize not everyone gets lucky enough to have a loving family. A thank you will never be enough to express my gratitude towards you. I love you. Thank you so much for 3mo Mahmoud, you were always there for me. Thanks Mohammad, Tant Amal and Tant Eman.

Now I realize that reaching this far in the acknowledgement without thanking my wife puts my marriage in grave danger. And here is another reason to thank Belgium: My wife. Thank you, Oumaimae, for supporting me effortlessly throughout this journey. You are the piece that completes me and I am so thankful for you. Alhamdullah. I realize a lot of times I was not able to be there as much as I ideally wanted while being busy working on my PhD, and you were so patient and supportive throughout. Now that the PhD is coming to an end, I will not (probably) have to work on a tapeout or paper writing during our vacations again. I am really grateful for having you in my life and our little ones, Nour and Aisha. I love you all so much. Special thanks go to my daughters, albeit they still can not talk (one of them is fluent in gibberish), they have taught me a valuable life lesson: Time is precious. Thank you for making me appreciate the rare moments of silence. You brought so much happiness to my life. I can not wait to watch you grow in shaa Allah. Special thanks to Lalla Samira, Yassine, Mimon, 3mi Mohamed, Ali, Zakaria, Chaimae, and Manal. I am so lucky to have a second family in Belgium. Thank you so much Lalla Samira, your help and support throughout these years have been invaluable. Thank you so much for taking care of Nour when Aisha was hospitalized a few days before my PhD private defense. You made my life so much easier.

I would like to thank all my friends who supported me throughout this journey. I consider myself a lucky person. I have had the privilege to be accompanied by great friends who have made my life so much better. Thank you to all the Ahmeds (Ahmed Khalil, Ahmed Kandeel, Ahmed Hassaneen, Ahmed Khaled, Ahmed Taher, Ahmed Essam, Ahmed Reweeny, Ahmed Hegazi, Ahmed Sami, Ahmed Elsharabasy), Alaa Elshazly, Amir Shahin, Mohamed Adel, Bader, Omar Shaikhani, Adam ElMrabet, Dries Ver Elst, Abdou Reweeny, Youssef Badawy, Anas Megahed, Haleem, Yousry, Marawan, Mohamed Gamal, Albreem, Mohamed Abdelgawad, Mohamed Saad, Khaled Khalaf, .. Now that I have moved to Gent, I appreciate your friendship and companionship even more. I will always remember the (extra) early coffee meetups we had. Au Flan Breton Leuven Vesalius: you have a special place in my heart.

I would like to particularly acknowledge my dear friends Ahmed Kandeel and Ahmed Khalil. You were not only my friends, but also my brothers. Ahmed Kandeel, you have been my friend and companion for the past 6 years, throughout the masters and the PhD. We had almost identical paths so far, and I could not be happier to have had you by my side, and I hope the ride goes on. I always felt supported by you and always appreciated taking your advice and asking for your opinion. Ahmed Khalil, you are always there whenever needed. I really appreciate not only your support, but offering the support deep from your heart

without expecting anything in return. Your enthusiasm about whatever you are interested in is contagious. I really appreciate your friendship and I am really lucky to have you as my friend. May Allah reward you guys.

I can not in my right mind end this acknowledgement without talking about the guilt I have felt during the concluding part of my PhD and during thesis writing. Seeing photos and video of children getting killed, burnt alive, and suffering on almost a daily basis for the last two years have been too much to handle. This is not normal. I write these words with a heavy heart. My heart, my thoughts, and my prayers (I know this is too little to offer..) are with Gaza. During my PhD, I have made a few Palestinian friends, and during this two-year massacre (still ongoing to this very moment), I received many sad news that many of their relatives have 'passed away'.. I am sorry, and I wish you and all the opressed people in this world find all the courage and strength needed. We, the people with a sound heart, are all sorry.

"My success is not but through Allah. Upon Him I have relied, and to Him I return." - Surah Hud (11:88)

A PhD is not only about what one learns, but the flexibility to be able to learn new things, and to think independently.

"And say, My Lord, increase me in knowledge." - Surah Ta-Ha (20:114)

Gent, Belgium, October 2025
Ahmed Bayoumi

Contents

Contents **i**

List of Figures **iii**

List of Tables **v**

List of Acronyms **vii**

Nederlandse Samenvatting **xiii**

1 Inleiding xiii

2 Breedband Gebogen Directionele Koppelaars xvii

3 Breedband Adiabatische Koppelaars xix

4 Dense Wavelength Division Multiplexing Systemen xxii

5 Coarse Wavelength Division Multiplexing Systemen xxvi

6 Conclusies xxx

Referenties xxxiii

English Summary **xxxix**

1 Introduction xxxix

2 Broadband Bent Directional Couplers xlii

3 Broadband Adiabatic Couplers xlv

4 Dense Wavelength Division Multiplexing Systems xlviii

5 Coarse Wavelength Division Multiplexing Systems li

6 Conclusions lv

References lvii

1 Introduction **1**

1.1 Silicon Photonics 2

Silicon Photonics Fabrication 3

Silicon Photonics Applications 5

Essential Building Blocks 7

1.2 Simulation methods 13

Finite-Difference Time-Domain Method (FDTD) 14

Finite Element Method (FEM) 15

Beam Propagation Method (BPM) 16

Eigenmode Expansion Method (EME) 16

Transfer Matrix Method (TMM) 17

1.3 Thesis Objectives 19

Optical Links and Wavelength Division Multiplexing 19

Challenges in Current WDM Architectures 20

Thesis Contributions and Outline 21

1.4 Publications 26

Journal Papers 26

International Conferences 27

References 28

2 Wavelength Filters Fundamentals **35**

2.1 Introduction 36

2.2 Optical Filters in Communication Systems 37

2.3 WDM Key Performance Metrics 41

2.4 WDM Filter Architectures in Silicon Photonics 44

Finite impulse response (FIR) filters 44

Microring Resonators (MRRs) 49

Arrayed Waveguide Gratings (AWGs) 52
Echelle Diffraction Gratings (EDGs) 54
2.5 Challenges in WDM Filters and Research Directions 56
Fabrication Variability and Tolerance 56
Thermal Sensitivity and Power Consumption 56
Spectral Density and Scalability 57
2.6 Conclusion 57
References 59

3 Broadband Bent Directional Couplers 65
3.1 Introduction 66
Operational principle of directional couplers 66
Performance metrics for 2×2 splitters 68
State of the art 68
Bent directional coupler 71
3.2 Proposed design and analysis 72
Coupled mode theory analysis 72
Optical characterization methodology 77
3.3 3-dB coupler results and wafer mapping 81
3.4 Model for arbitrary broadband coupling ratios 86
3.5 Compatibility with 200 mm and 300 mm platforms 89
3.6 Conclusion 90
References 93

4 Broadband Adiabatic Couplers 99
4.1 State of the art 100
4.2 Design and optimization scheme for the 3 dB splitter 102
4.3 Broadband coupling and arbitrary coupling ratios 108
4.4 Impact of the waveguide width and coupling gap 110

4.5 Conclusions 112
References 115

5 Dense Wavelength Division Multiplexing Systems 119
5.1 State of the art 120
5.2 DWDM-2 ×100 GHz 122
Design and Results 122
Wafer mapping 127
Comparison with the state of the art 128
5.3 DWDM-4 ×100 GHz 130
5.4 DWDM-16 Systems 131
DWDM-16 ×800 GHz 132
DWDM-16 ×200 GHz 132
5.5 Conclusions 139
References 140

6 Coarse Wavelength Division Multiplexing Systems 145
6.1 State of the art 146
6.2 Scaling WDM filters with CWDM architectures 148
FSR tolerance bounds for CWDM-2 149
6.3 CWDM-2 systems 152
CWDM-2 × 3.2 THz 152
CWDM-2 × 6.4 THz 157
Phase error improvement in CWDM-2 systems 161
6.4 CWDM-4 × 3.2 THz 166
6.5 Conclusions 169
References 171

7 Conclusions 175

7.1 Summary of Key Contributions 175
7.2 Perspectives 177

A Appendix **179**

A.1 Coupled Mode Theory 179
Unperturbed Waveguide Modes 180
Perturbation and Mode Coupling 181
Single Waveguide Coupling 182
Multiple Waveguide Coupling 185
Two-Mode Coupling 188
Co-directional Coupling 190
Supermode Formulation 193
Phase Retardation in DCs 195
A.2 Mach-Zehnder Interferometer Analysis 198
Transfer Matrix Analysis of Mach-Zehnder Interferometer 198
Power Transmission at Output Ports 199
Extinction Ratio 200
Working Wavelength and Free Spectral Range (FSR) 202
Thermal Tuning of MZI Filters 205
A.3 Uncertainty Analysis for Directional Coupler Coupling Ratio Extraction 209
Direct Method 209
Ring Based Method 210
Cutback Method 212
Comparison and Conclusions 214
References 217

List of Figures

1 Schematisch van een optische verbinding met de belangrijkste componenten: multi-golflengte laserbron, demultiplexerfilter voor kanaalscheiding, een modulator voor het coderen van data op het optische signaal, een multiplexer voor het combineren van meerdere golflengte kanalen, en een ontvanger met fotodetector voor signaalconversie. De WDM-filters maken parallelle transmissie van meerdere datastromen mogelijk, wat de primaire focus is van dit proefschrift. xiii

2 Schematische weergave van het voorgestelde DWDM-128×100 GHz-systeem. De architectuur integreert een 4-kanaals MZI-stadium, microringresonatoren (MRRs), en CWDM-4-filters. Het MZI-stadium verdeelt de input in vier groepen, elk geleid naar een bus-golfgeleider met 8 verschoven MRRs (32 in totaal). Elke MRR drop-poort is in cascade geschakeld met een CWDM-4-filter, wat demultiplexing naar 128 kanalen met 100 GHz-afstand mogelijk maakt. De metalen routering en de uitgangstroosters worden hier niet getoond. De inzet toont een uitvergroot beeld van een van de ring-CWDM-eenheden. xvi

3 Schematische weergave van de rechte DC (a), breedbandige gebogen DC (b), en SEM-afbeeldingen van de gefabriceerde gebogen DC (c, d), gefabriceerd met behulp van IMEC's iSiPP300-platform. xvii

4 Vergelijking van koppelingsverhoudingen tussen rechte DC's (a) en gebogen DC's (b) over een golflengtebereik van 80 nm, waarbij de aanzienlijk verbeterde golflengte-ongevoeligheid van het gebogen DC-ontwerp wordt aangetoond. xix

5 Gemiddelde kruiskoppelingsafwijking ten opzichte van de centrale die (a) en kruiskoppelingsvariatie (b) over een golflengtebandbreedte van 80 nm voor de voorgestelde 0.5:0.5 gebogen DC-splitter over de 300 mm wafer, waarbij alle 63 dies worden gedekt. xx

6 Schematische weergave van de voorgestelde adiabatische koppelaar met de ontwerpparameters. Het ontwerp is niet op schaal en is uitsluitend bedoeld ter illustratie. xxi

7 H_y-veldplot van de voorgestelde 3-dB splitter bij λ=1.31 μm (a). TE even (b) en oneven (c) modusvermogensuitbreidingen in het midden van de koppelaar tonen aan dat het grootste deel van het vermogen (98.3% bij λ=1.31 μm) aanwezig is in de TE even modus, wat de adiabatische aard van de splitter bewijst. xxii

8 Maximale kruiskoppelingsafwijking van 0.5 over een $120\,\mathrm{nm}$ golflengtebereik als functie van de overgangslengte (L) en het initiële golfgeleiderbreedteverschil (ΔW). xxiii

9 3-dB splitter optische transmissie met behulp van de voorgestelde adiabatische koppelaar (a) in vergelijking met de traditionele rechte koppelaar (b) over een golflengtebereik van 120 nm dat de O-band omvat. Een significante reductie van 16.6$\times$ in de koppelingsvariatie wordt bereikt met het voorgestelde ontwerp in vergelijking met de rechte DC-tegenhanger. xxiv

10 Schematische weergave van de interleaver die wordt gebruikt in het WDM-128 $\times$ 100 GHz-systeem op basis van breedband gebogen DC's. De eerste MZI-fase interleaveert 128 kanalen in twee uitgangen van 64 kanalen. De tweede fase, met het dubbele van de FSR, interleaveert deze verder in vier golfgeleiders, elk met 32 kanalen. xxiv

11 Het voorgestelde DWDM-2 $\times$100 GHz interleaver-spectrum gebaseerd op gebogen DC's (a), en het traditionele DWDM-2-spectrum gebaseerd op rechte DC's (b). Minimale en maximale ER-waarden zijn gemarkeerd. Een verbetering van minstens 2.7$\times$ in het ER-golflengtewerkingsbereik voor de voorgestelde interleaver wordt getoond. . xxv

12 DWDM-16 $\times$800 GHz-systeemspectra berekend met de transfermatrixmethode gebaseerd op (a) gebogen DC's en (b) rechte DC's. Het systeem gebaseerd op gebogen DC's toont aanzienlijke verbeteringen in kanaalisolatie en invoegverlies. xxvi

13 Schematische weergave van de cascaded ring-CWDM-architectuur die DWDM-128 $\times$ 100 GHz mogelijk maakt. De drop-poort van een ringresonator met $\mathrm{FSR} = 3.2\,\mathrm{THz}$ is verbonden met een CWDM-2 en vervolgens een CWDM-4, wat een viervoudige toename in het aantal kanalen mogelijk maakt. xxvii

14 Gemeten spectra van de CWDM-2 $\times$ 3.2 THz voor breedbandige gebogen directionele koppelaars (DC's) (a) en rechte gebogen DC's (b). xxviii

15 De optische vermogenstransmissie in kruiskoppeling voor 8 identieke traditionele MZI's naast elkaar op de reticle, die de impact van fasefouten op de golflengterespons laat zien. xxix

16 Optisch spectrum voor het CWDM-4 $\times$ 3.2 THz-systeem gebaseerd op breedband gebogen DC's over 54 dies, waarbij elke kleur een ander kanaal vertegenwoordigt. De metingen tonen de robuustheid van het ontwerp voor gebruik in massaproductie. xxx

1 Schematic of an optical link showing the key components: multi-wavelength laser source, demultiplexing filter for channel separation, a modulator for encoding data onto the optical signal, a multiplexer for combining multiple wavelength channels, and receiver with photodetector for signal conversion. The WDM filters enable parallel transmission of multiple data streams, which is the primary focus of this thesis. xxxix

2 Schematic of the proposed DWDM-128$\times$100 GHz system. The architecture integrates a 4-channel MZI stage, microring resonators (MRRs), and CWDM-4 filters. The MZI stage divides the input into four groups, each routed to a bus waveguide with 8 staggered MRRs (32 in total). Each MRR drop port is cascaded with a CWDM-4 filter, enabling demultiplexing into 128 channels with 100 GHz spacing. The metal routing and the output gratings are not shown here. The inset shows a zoomed-in image for one of the ring-CWDM units. xli

3 Schematic of the straight DC (a), broadband bent DC (b), and SEM images of the fabricated bent DC (c, d), fabricated using IMEC's iSiPP300 platform. xliii

4 Coupling ratio comparison between straight DCs (a) and bent DCs (b) across 80 nm wavelength range, demonstrating the significantly improved wavelength insensitivity of the bent DC design. xliv

5 Average cross coupling deviation with respect to the central die (a) and cross coupling variation (b) over 80 nm bandwidth for the proposed 0.5:0.5 bent DC splitter over the 300 mm wafer, covering all 63 dies. xlv

6 Schematic of the proposed adiabatic coupler showing the design parameters. The design is not to scale and is for illustration purposes.xlvi

7 H_y field plot of the proposed 3-dB splitter at λ=1.31 μm (a). TE even (b) and odd (c) mode power expansions at the middle of the coupler showing most of the power (98.3% at λ=1.31 μm) existing in the TE even mode, proving the adiabatic nature of the splitter. . xlvii

8 Maximum cross-coupling deviation from 0.5 over a $120\,\mathrm{nm}$ wavelength range as a function of the taper length (L) and the initial waveguide width difference (ΔW), based on 3D finite-difference time-domain simulations. xlviii

9 3-dB splitter optical transmission using the proposed adiabatic coupler (a) as compared to the traditional straight coupler (b) over 120 nm wavelength range covering the O-band. Significant reduction of 16.6× in the coupling variation is achieved using the proposed design compared to the straight DC counterpart. xlix

10 Schematic of the interleaver used in WDM-128 × 100 GHz system based on broadband bent DCs. The first MZI stage interleaves 128 channels into two outputs of 64 channels. The second stage, with double the FSR, further interleaves these into four waveguides, each with 32 channels. xlix

11 The proposed DWDM-2 ×100 GHz interleaver spectrum based on bent DCs (a), and the traditional DWDM-2 spectrum based on straight DCs (b). Minimum and maximum ER values are marked. At least 2.7× improvement in the ER wavelength operational range for the proposed interleaver is shown. l

12 DWDM-16 ×800 GHz system spectra simulated using the transfer matrix method based on (a) bent DCs and (b) straight DCs. The bent DC-based system shows significant improvements in channel isolation and insertion loss. li

13 Schematic of the cascaded ring-CWDM architecture enabling DWDM-128 × 100 GHz. The drop port of a ring resonator with $\mathrm{FSR} = 3.2\,\mathrm{THz}$ is connected to a CWDM-2 and subsequently a CWDM-4, enabling a fourfold increase in channel count. lii

14 Measured spectra of the the CWDM-2 × 3.2 THz for broadband bent directional couplers (DCs) (a) and straight bent DCs (b). . . . liii

15 The cross power transmission for 8 identical traditional MZI next to each other on the reticle, showing the impact of phase errors on wavelength response. liv

16 Optical spectrum for the CWDM-4 × 3.2 THz system based on broadband bent DCs over 54 dies, where each color represents a different channel. The measurements show the robustness of the design to be used in mass manufacturing. lv

1.1 Fabrication flow for SOI nanophotonic waveguides, where BARC refers to Bottom Anti Reflective Coating [18, 19]. 3

1.2 Schematic cross-section of IMEC's silicon photonics platform, showing fundamental passive and active building blocks and devices [17, 19]. 4

1.3 Silicon photonics market growth projections from 2022 to 2028, highlighting the compound annual growth rate (CAGR) of 44% driven by increasing demand for high-data-rate modules in data centers and machine learning servers [20]. 6

1.4 3D schematic of a silicon waveguide with SiO_2 cladding (a) 2D cross section of the typical geometry and dimensions for a single mode silicon-on-insulator strip waveguide with silicon oxide cladding. W is for the width which is often 380 nm or 450 nm for O and C band based waveguides, respectively. 7

1.5 Schematic of the TOPIC bend design in comparison to the circular bend: (a) The baseline of the TOPIC and circular bends, (b) Schematic of a TOPIC bend with a fixed waveguide width, (c) Optical field evolutions ($|E|$) in circular and TOPIC bends, (d) Different TOPIC shapes based on manipulating parameter θ_p, and (e) TOPIC bend with varying waveguide width resulting in a whispering gallery mode (WGM) [29]. 9

1.6 Measured insertion losses for different 180° waveguide bends. (a) Measured losses of constant-width TOPIC bends with varying θ_p. (b, c, e, f) Schematics (b, c) and corresponding measured losses (e, f) for waveguide bends with constant width (b, e) and varying width (c, f). (d, g) Comparison of curvature (d) and curvature derivative (g) between constant-width Euler and TOPIC bends. The waveguides consist of a silicon nitride (SiN) core clad in silicon oxide, operating at a wavelength of 638 nm. The SiN layer thickness is 150 nm, and the waveguide width, except in regions with varying width, is 500 nm. The bend radius is $R = 15$ μm. The parameter $W_{\max}$ represents the maximum waveguide width along a varying-width bend. In traditional varying-width designs, the outer boundary follows a circular arc, while the inner boundary is oval, adjusted via its semi-minor axis to achieve the target $W_{\max}$. For varying-width TOPIC bends, the outer boundary angle $\theta_{p,o}$ is fixed at 30°, and the inner boundary angle $\theta_{p,i}$ is tuned to obtain the desired $W_{\max}$. Loss measurements were performed using the cut-back method, with multiple identical bends cascaded to enable linear regression analysis of transmission data. The plotted loss values represent the mean and standard deviation across measurements from all dies on a 200 mm wafer fabricated using the imec pix4life platform. [29]. 10

1.7 Several silicon photonic devices are based on coupling and/or interference mechanisms, including (a) directional coupler, (b) ring resonator, and (c) 1×2 splitter, (d) MZI. 12

1.8 Schematic of a typical optical interconnect architecture. The system consists of a multi-wavelength CW laser source, a MUX, a DEMUX, and a TIA. The MUX and DEMUX enable simultaneous signals to be transmitted over a single optical fiber. 20

1.9 Schematic of the taped-out DWDM-128 × 100 GHz system. The architecture integrates a 4-channel MZI interleaver, microring resonators (MRRs), and CWDM-4 filters. The interleaver divides the input into four groups, each routed to a bus waveguide with 8 staggered MRRs (32 in total). Each MRR drop port is cascaded with a CWDM-4 filter, enabling demultiplexing into 128 channels with 100 GHz spacing. In the initial design run, the CWDM-4 filters are thermally tuned to compensate for fabrication variations; future iterations aim for heater-free operation. SI_COR represents fully etched silicon, PE_TRE partially etched silicon, N1 an N-type implant, NBODY an N-type body implant, and NPLUS an N-type contact implant. 22

1.10 Zoomed in view of the interleaver used in the DWDM-128×100 GHz system in Fig. 1.9 23

1.11 Zoomed in view of one of the ring racks used in the DWDM-128×100 GHz system in Fig. 1.9 23

1.12 Zoomed in view of one of the CWDM-4 used in the DWDM-128×100 GHz system in Fig. 1.9 24

2.1 Different types of optical filters. (a) Filtering of a specific wavelength. (b) Multiplexer combining multiple wavelengths into a single output; the reverse operation is called demultiplexing. (c) Interleaver used to interleave or separate wavelength channels. (d) Optical add-drop multiplexer (OADM) where channel λ_k is added and channel λ_1 is dropped from the WDM spectrum. 37

2.2 Comparison of low pass (a), band pass (b), and high pass (c) filter responses. The low-pass filter transmits longer wavelengths (lower frequencies) while blocking shorter ones. The bandpass filter allows transmission of light within a specific wavelength range while attenuating light outside this range. The high-pass filter transmits shorter wavelengths while blocking longer ones. The ideal filter response is shown in dashed grey, while the non-ideal filter response is shown in blue. 38

2.3 Key performance metrics for WDM filters including insertion loss (IL), free spectral range (FSR), full width at half maximum (FWHM), Intra-band and out-of-band ripple, crosstalk, and roll-off rate. The green dotted curves are ideal filters, while the red lines indicate typical actual performance of practical designs [21]. . . . 42

2.4 Schematic illustrating the signal band and the guard band in a WDM system. The signal band is the central spectral region where the modulated optical signal carries information, while the guard band is the spectral region between adjacent channels that prevents inter-channel interference. 43

2.5 Schematic of an optical filter with M delay lines. The filter consists of an input port, M delay lines with different lengths, and an output port. The output signal is a superposition of the delayed signals from each delay line, resulting in a wavelength-dependent interference pattern. The transfer function of the filter can be expressed as a finite impulse response (FIR) filter in the time domain. 45

2.6 Schematic of an MZI filter. The MZI consists of an optical splitter, two waveguide arms with a length difference, allowing for wavelength-selective interference, and an optical combiner. The output is determined by the relative phase difference between the two arms, which can be tuned using thermal or electro-optic methods. 45

2.7 Schematic of cascaded MZI systems and their effect on passband flatness. The figure shows one-stage, two-stage, and three-stage MZI filters. The one-stage MZI uses two $0.5 : 0.5$ couplers. The two-stage MZI uses three couplers with cross coupling ratios of 0.5, 0.29, and 0.08. The three-stage MZI uses four couplers with cross coupling ratios of 0.5, 0.2, 0.2, and 0.04. The MZI spectra are simulated with transfer matrix method. The MZI diagrams are adapted from [23]. 46

2.8 Schematics of microring resonator (MRR) filters. The MRR consists of a circular waveguide that is coupled to a bus waveguide. Light is coupled into the ring and can be dropped or added at specific wavelengths based on the resonance condition. Resonance wavelength condition is satisfied (a). Resonance wavelength condition is not satisfied (b). Example of MRR-based WDM filter based on cascaded ring resonators on a shared bus waveguide (c). 50

2.9 Schematics of different MRR-based filter architectures including Coupled-Resonator Optical Waveguides (CROWs) (a), Side-Coupled Integrated Spaced Sequence of Optical Resonators (SCISSOR) (b), and Vernier filters (c). 51

2.10 Schematic of an Arrayed Waveguide Grating (AWG) filter [32]. The AWG consists of an input free-propagation region (FPR), a waveguide array with linearly incremented path lengths, and an output FPR. Light entering the input FPR is diffracted into the waveguide array, where it accumulates wavelength-dependent phase delays. The phase-shifted signals interfere constructively at specific positions in the output FPR, enabling spatial demultiplexing of individual wavelength channels 53

2.11 Echelle diffraction grating (EDG) filter [39]. The EDG consists of a concave slab waveguide with a blazed grating structure. Light entering the slab is diffracted by the grating, and different wavelengths are focused onto discrete output ports based on their diffraction angles. The concave geometry provides natural focusing, enabling compact designs for coarse wavelength-division multiplexing (CWDM) applications. 55

3.1 Schematic of the traditional straight directional coupler (DC) with L representing the coupling length. The DC consists of three sections: the input, coupling region, and output. Optical power remaining in the same waveguide as the input is often termed as 'through', while power transferred to the adjacent waveguide is often termed as 'cross'. 66

3.2 Evolution of supermodes in a symmetric directional coupler. Dashed curves indicate the even and odd supermodes, while solid curves show the total fields. As the supermodes propagate in the coupler, the power is coupled from waveguide 'a' to waveguide 'b'. Figure is adapted from [1]. 66

3.3 Coupling behavior of a straight symmetric silicon directional coupler with variation more than 0.45 for $0.5 : 0.5$ splitting. The figure is from [6]. 67

3.4 Various examples on demonstrations of broadband 2×2 splitters based on manipulating the directional coupler (DC), including DC with phase compensation section (a) [15], rib-waveguide based DC (b) [16], and MZI-based 2×2 splitter (c) [17]. It is worth noting that the DC with phase compensation section has the same working principle as the MZI-based 2×2 splitter. 69

3.5 Schematic (a) and scanning electron microscope (SEM) image (b) of the proposed bent DC with R as the coupling radius, and θ as the coupling angle. All bent DC curves are designed with low-loss bends [23], while the straight DC input and output ports have traditional circular bends with a bending radius of $5\ \mu\mathrm{m}$. SEM image of the cross section of the proposed bent DC in the coupling region (c). The waveguide material stacks are SOI with silicon oxide as top cladding, using IMEC iSiPP300 platform. All DCs are based on strip waveguides with nominal silicon thickness of 220 nm, and waveguide width of 380 nm. The coupling gap is nominally 100 nm. 70

3.6 Wavelength dependence analysis for the straight and bent DC with lines showing broadband criteria. Contour plot of Δn_g as a function of the gap and the waveguide width for the straight symmetric DC (a). Contour plots of Δn_g (b) and $d\Delta n_{eff}/d\lambda$ (c) for the bent DC as a function of gap and radius, where the waveguide widths are fixed as $0.38\ \mu\mathrm{m}$, along with lines showing where $\Delta n_g = 0$ (blue) and $d\Delta n_{eff}/d\lambda = 0$ (black). The results are based on finite element method simulations using COMSOL Multiphysics in cylindrical coordinates for bent waveguides. 74

3.7 Microscope image of the cascaded identical bent DCs used for robust measurements. The power is input at the port (in) and measured at all the cascaded output stages. The labels determine whether the cascaded through (Th) or cascaded cross (Cr) coupled power is extracted, and the number indicates the number of times the measured value (through or cross) was repeated for that measurement. The proposed 0.5:0.5 broadband bent DC has a bending radius of $25\ \mu\mathrm{m}$, a gap of $0.1\ \mu\mathrm{m}$, and a coupling angle of $8.5\ \mathrm{degrees}$. . . 75

3.8 Data processing for coupling ratio extraction of the proposed 0.5:0.5 bent DC. The device has a bending radius of $25\ \mu\mathrm{m}$, a gap of $0.1\ \mu\mathrm{m}$, and a coupling angle of $8.5\ \mathrm{degrees}$. (a) Power at the through ports as a function of wavelength, where Savitzky-Golay filter is utilized to get rid of the noise (shown in black lines). (b) Linear regression between the power and the number of cascaded devices. (c) Correlation of the linear regression as a function of wavelength. (d) Extracted power from the slope of the linear regression as a function of wavelength. (e-h) Corresponding analysis for the cross ports. 76

3.9 Sinusoidal fitting of the cross coupling (κ^2) and through coupling (r^2) with the coupling length for the straight DC (a) and with the coupling angle for the bent DC (b) at $\lambda = 1.31$ μm for the proposed devices. Both designs have a gap of 0.1 μm. The bent DC has a bending radius of 25 μm. Dots represent measured values, and lines depict the fitting. 79

3.10 Extracted model parameters wavelength response with linear fitting based on experimental data. A_t, A_c, m, β_c, and ϕ for the 0.5:0.5 straight DC (a-d) and for the proposed 0.5:0.5 bent DC (e-h). The mean and standard deviation values for A_t and A_c for the straight (a) and bent DC (e) show the reduction of the loss by the introduction of the low-loss bends in the bent DC as compared to the traditional circular bends in the straight DC. The model parameters show expected wavelength dependence of the parameters. The symmetric straight DC has a matching coefficient, $\mathrm{m} \approx 1$, as expected (b), while the bent DC has a wavelength dependent matching coefficient with $m = 0.704$ at $\lambda = 1.31$. The straight DC has a coupling length of 5.23 μm and a gap of 0.1 μm. The bent DC has a bending radius of 25 μm, a gap of 0.1 μm, and a coupling angle of 8.5 degrees. . 80

3.11 Cross coupling wavelength derivative ($d\kappa^2/d\lambda$, Eq. 3.2) of the bent DC, along with its constituent terms, demonstrating that broadband coupling (i.e. $d\kappa^2/d\lambda = 0$) can take place at the intersection of the positive and negative parts (marked by stars) of the sinusoid terms at a specific design regime. The black stars indicate points where the terms cancel each other. The proposed 0.5:0.5 bent DC has a bending radius of 25 μm and a gap of 0.1 μm. 81

3.12 The cross coupling (κ^2) and the cross coupling derivative ($d\kappa^2/d\lambda$) as a function of the coupling length for the straight DC (a) and as a function of the coupling angle for the bent DC (b). The introduced asymmetry presented in the bent DC shifted the broadband cross coupling point ($\kappa^2|_{d\kappa^2/d\lambda=0}$) from $\kappa^2|_{d\kappa^2/d\lambda=0} = 1$ to $\kappa^2|_{d\kappa^2/d\lambda=0} \sim 0.5$, this idea makes it possible to have broadband coupling at distinct coupling ratios based on the bending radius value. Points A and B represent the coupling derivative at 0.5 coupling. All the designs have a gap of 0.1 μm. The bent DC has a bending radius of 25 μm and a gap of 0.1 μm. 82

3.13 The measured coupling ratios of the traditional straight DC (a) and the proposed bent DC (b) at $0.5 : 0.5$ coupling. The straight DC has a coupling length of 5.23 μm and a gap of 0.1 μm. The bent DC has a bending radius of 25 μm, a gap of 0.1 μm, and a coupling angle of 8.5 degrees. The bent DC shows broadband coupling with a minimal variation of 0.051 achieving 7.67 times reduction in coupling variation as compared to the straight DC. Non transparent lines show the model fitting, while the transparent lines show the measured experimental data. 83

3.14 Fabrication tolerance analysis based on 3D FDTD simulations of the traditional straight DC (a) and the proposed $0.5 : 0.5$ bent DC (b). Coupling spectrum simulation results of the nominal design ($\delta w = 0$) along with waveguide width deviations of -20, -10, 10, 20 nm. Through couplings are shown in solid lines and the cross couplings are shown in dashed lines. The inset figure depicts the waveguide width (W) deviation and the corresponding gap deviation for the SOI-based DCs. The nominal straight DC design has a coupling length of 5.23 μm and a gap (g) of 0.1 μm. The nominal bent DC design has a bending radius (R) of 25 μm, a g of 0.1 μm, and a coupling angle of 8.5 degrees. 84

3.15 Average cross coupling deviation with respect to the central die (a) and cross coupling variation (b) over 80 nm bandwidth for the proposed 0.5:0.5 bent DC splitter over the 300 mm wafer, covering all 63 dies. Low variation is shown over all dies except a relatively higher variation at the edges of the wafer, as expected due to process variation. The bent DC has a bending radius of 25 μm, a gap of 0.1 μm, and a coupling angle of 8.5 degrees. 85

3.16 Contour plot for the cross coupling wavelength derivative (a) and the cross coupling (b) as a function of the design parameters (bending radius and coupling angle). A few cross coupling values are plotted along the zero derivative contour in (b). The coupling gap and waveguides widths are fixed as 0.1 μm and 0.38 μm, respectively. 87

3.17 The proposed model for extracting broadband bent DCs with arbitrary coupling ratios. Broadband cross coupling values as a function of the bending radius (a). The corresponding coupling angle as a function of bending radius (b). The experimental data is shown in dots while the fitting model is depicted as a solid line. The coupling gap and waveguides widths are fixed as 0.1 μm and 0.38 μm, respectively. 88

3.18 Examples of broadband bent DCs with arbitrary coupling ratios in accordance with the proposed model, where the through and cross coupling are shown as a function of wavelength. Devices with broadband 0.4 (a), 0.5 (b), 0.6 (c), and 0.7 (d) cross coupling values are presented. The bending radii and the coupling angles of the devices are: 23 μm and 12 degrees (a), 25 μm and 8.5 degrees (b), 29 μm and 6 degrees (c), and 34 μm and 4 degrees (d). All the designs have a gap of 0.1 μm. 89

3.19 The coupling spectrum of the proposed 3-dB bent DC with a gap of 150 nm, designed for compatibility with 200 mm platforms. The device features a bending radius of 47 μm and a coupling angle of 8.8 degrees. Transparent lines represent the measured data, while solid lines depict the smoothed data. 91

3.20 Schematic illustrating the FIB cross section taken from the fabricated bent DC with an 80 nm gap (a). Multiple FIB cross sections were analyzed around the region highlighted in red. The resulting FIB image at the indicated cross section (b) reveals minor unevenness in the gap filling observed in certain cross sections. The cross section shows a typical sloped sidewall of the waveguides with a base gap of $\approx$ 83 nm, and a top gap of $\approx$ 104 nm. 92

3.21 The coupling spectrum of a bent DC device with an 80 nm gap, demonstrating normal optical behavior without any resonances indicative of significant scattering. Transparent lines represent the measured data, while solid lines depict the smoothed data. 92

4.1 Examples of existing adiabatic couplers in the literature. (a) Adiabatic coupler with a total length of 165 μm [14]. (b) Adiabatic coupler with a total length of 240 μm [15]. 101

4.2 Schematic of the proposed adiabatic coupler (a), where the top waveguide width increases in the propagation direction, while the bottom waveguide width decreases. The schematic of the traditional straight directional coupler (b) with fixed waveguide width of W which is used as a benchmark for comparison. Both designs have a fixed gap of g. The schematic is for illustration purposes and is not intended to be in scale. 103

4.3 Maximum cross-coupling deviation from 0.5 over a $120\,\mathrm{nm}$ wavelength range as a function of the taper length (L) and the initial waveguide width difference (ΔW), based on 3D FDTD simulations. The fixed design parameters are $W_1 = 0.26\,\mu\mathrm{m}$, $g = 0.08\,\mu\mathrm{m}$, and t_p = 0.5. Each line represents the coupling deviation at a certain ΔW. The coupling deviation is minimized at $\Delta W = 0.06\,\mu\mathrm{m}$ with a compact $L = 1.44\,\mu\mathrm{m}$. 104

4.4 3 dB splitter optical transmission using the proposed adiabatic coupler (a) as compared to the traditional straight coupler (b) over 120 nm wavelength range covering the O-band, based on 3D FDTD simulations. Significant reduction of 16.6x in the coupling variation is achieved using the proposed design compared to the straight DC counterpart. 105

4.5 H_y field plot of the proposed 3 dB splitter at λ=1.31 μm (a). TE even (b) and odd (c) mode power expansions at the middle of the coupler showing most of the power (98.3% at λ=1.31 μm) existing in the TE even mode, proving the adiabatic nature of the splitter. . 106

4.6 Demonstration of broadband coupling using the proposed tapered DC for cross-coupling values of 0.2, 0.3, 0.4, 0.5, and 0.55 over a $120\,\mathrm{nm}$ wavelength range (a). Taper length (L) as a function of the taper percentage (t_p) (b). t_p is chosen to have the same value as the required cross-coupling value. Dots represent the data while the line is a quadratic fitting. All the presented devices have the same parameters except for t_p and L. The results are based on 3D FDTD simulations. 109

4.7 Coupling spectrum of the proposed adiabatic coupler with a larger waveguide width of $0.34\,\mu\mathrm{m}$ and a larger gap of $0.1\,\mu\mathrm{m}$ based on 3D FDTD simulations. The coupling deviation is 0.037 over the 120 nm wavelength range. 112

4.8 Layout of the cascaded adiabatic coupler, which has been taped out and is currently under fabrication. 113

4.9 Layout of the MZI based on adiabatic couplers, which has been taped out and is currently under fabrication. 114

5.1 Schematic of a Mach–Zehnder interferometer (MZI) (a). Schematic of a 4 channel MZI interleaver (b). 120

5.2 Microscope image for DWDM-2 $\times$100 GHz interleaver based on $0.5 : 0.5$ bent DCs (d) and based on $0.5 : 0.5$ straight DCs (e). The bent DC has an $R = 16\,\mu\mathrm{m}$ and $\theta = 9.2°$. The straight DC has an $L = 2\,\mu\mathrm{m}$. Waveguide material stacks are SOI with silicon oxide as top cladding, using imec iSiPP300 platform. All DCs are based on strip waveguides with nominal silicon thickness of 220 nm, waveguide width of 450 nm, and coupling gap of 100 nm. 121

5.3 The proposed DWDM-2 $\times$100 GHz interleaver spectrum based on bent DCs (a), and the traditional DWDM-2 spectrum based on straight DCs (b). Minimum and maximum ER values are marked. At least $2.7\times$ improvement in the ER wavelength operational range for the proposed interleaver is shown. The channel spacing for both DWDMs is designed to be 100 GHz. 122

5.4 The normalized optical spectrum for the DWDM-2 $\times$100 GHz interleaver based on bent DCs with the 'standard' measurement setting (a) and the adjusted measurement setting (b). The 'standard' measurement setting shows a lot of nonuniformity in the dips, which is removed with the proposed measurement method. The laser wavelength spacing should be minimized to achieve accurate ER measurements with such a narrow channel spacing. The spectrum had to be measured in two subsequent steps (to ensure fine spacing and an extended wavelength range) with a low measurement power range setting (to ensure that even very small power values can be measured accurately), ultimately leading to more accurate dip values. 123

5.5 The normalized optical spectrum for the DWDM-2 $\times$100 GHz interleaver based on straight DCs with the 'standard' measurement setting (a) and the adjusted measurement setting (b). 124

5.6 The reference waveguide transmission measurements over the wafer. Each color represents one die measurement. The line in bold black represents the average measurement over the whole wafer (63 dies) 125

5.7 Wafer mapping of the reference waveguide transmission measurement over the wafer at λ = 1.59 μm. 126

5.8 The measured coupling ratios of the bent DC (a) and straight DC (b) along with the cross coupling spectra for bent DC over 63 measured dies in a 300 mm wafer (c), where each color represents one die. 3.7 $\times$ less coupling variation is observed in the bent DC as compared to the straight DC. Robust performance of the bent DC is observed over the wafer. 127

5.9 ER values wafer mapping for the DWDM-2 ×100 GHz interleaver based on bent DCs (a) and the interleaver based on straight DCs (b) over the 300 mm wafer. Robust high ER values across the wafer is present in the interleaver based on bent DCs, showing the reliability of the design for mass production. The interleaver based on straight DCs shows significantly lower ER values across the wafer. 129

5.10 The schematic of DWDM-4 ×100 GHz filter based on cascaded MZIs, used in the transfer matrix method calculations. The MZI blocks are as illustrated in Fig. 5.2(a, b). 130

5.11 Transfer matrix method (TMM) simulation for DWDM-4× 100 GHz interleaver based on cascaded MZIs spectrum, with a channel spacing of 100 GHz, based on the measured bent DC (a) and straight DC (b). Significant improvement is observed in channels isolation and insertion loss for the WDM system based on bent DCs. 131

5.12 The schematic of 16 −channel WDM filter based on cascaded MZIs, used in the transfer matrix method calculations. The MZI blocks are as illustrated in Fig. 5.2(a, b). 132

5.13 16 −channel cascaded MZI WDM spectrum, with a channel spacing of 800 GHz, based on the measured bent DC (a) and straight DC (b) simulated using the transfer matrix method. Significant improvement is observed in channels isolation and insertion loss for the WDM system based on bent DCs. 133

5.14 Microscope image of the fabricated DWDM-16 ×200 GHz system based on bent DCs. The system uses cascaded MZIs with integrated heaters for wavelength tuning. The layout also enables subsystem measurements of the WDM-8×400 GHz configuration. 134

5.15 Zoomed-in image of the first MZI stage (MZ1) in the DWDM-16 ×200 GHz system, showing the implementation of three bent DCs with cross coupling ratios of 0.5, 0.29, and 0.08 to achieve flat-top passbands. 134

5.16 Measured coupling spectra from the selected die showing bent DCs with design goals of (a) 0.5:0.5, (b) 0.29:0.71, and (c) 0.08:0.92 coupling ratios. 135

5.17 Output spectrum of the DWDM-16×200 GHz system without any phase tuning, showing significant signal distortions that require optimization. 135

5.18 Normalized sum of eight output channels during the MZ1 tuning process, showing limited extinction ratio despite optimization efforts. 136

5.19 Untuned output spectrum of the WDM-8×400 GHz subsystem, showing better performance overall compared to the full WDM-16 system. 136

5.20 Summed, normalized measurements for two output waveguides during tuning of MZ 3.1 in the WDM-8×400 GHz subsystem. . . 137

5.21 Normalized measurements for one output waveguide during tuning of MZ 4.1 in the WDM-8×400 GHz subsystem. 138

5.22 Normalized measurements for one output waveguide of both MZ 4.1 and of MZ 4.2 in the WDM-8×400 GHz subsystem. The channels centers locations are annotated in the figure. 138

6.1 Simplified block diagram of DWDM-CWDM architecture where a drop port of a ring resonator is connected to a CWDM-2 and subsequently a CWDM-4 to eventually demultiplex 4 channels. . . 147

6.2 Schematic of the cascaded DWDM–CWDM architecture enabling DWDM-128 × 100 GHz. The drop port of a ring resonator with $\mathrm{FSR} = 3.2\,\mathrm{THz}$ is connected to a CWDM-2 and subsequently a CWDM-4, enabling a fourfold increase in channel count. The CWDM filters are designed to scale the channel count by leveraging differences in arm lengths, while maintaining passive operation without thermal tuning. 148

6.3 The layout of the CWDM-2 × 3.2 THz system using bent DCs. The design incorporates minimized common arm lengths to reduce phase errors. 152

6.4 The layout of the CWDM-2 × 3.2 THz system using straight DCs. This structure serves as a reference to evaluate the performance improvements enabled by bent DCs. 152

6.5 Measured spectra of the CWDM-2 × 3.2 THz for bent DCs (a) and straight DCs (b). A significant improvement in the lowest extinction ratio (ER) is observed with the use of broadband bent DCs. The bent DC design achieves a higher worst-case ER of 18.1 dB, compared to 12.8 dB for the straight DC configuration. The corresponding designs are shown in Fig. 6.3 and Fig. 6.4 for the bent and straight DCs, respectively. 153

6.6 Wafer mapping of the extinction ratio (ER) for CWDM-2 × 3.2 THz for a few dies, showing the improvement in ER with the use of bent DCs compared to straight DCs. The CWDM-2 × 3.2 THz based on the bent DC demonstrates ER values ranging from 16.5 to 18.8 dB, while the straight DC shows ER values from 10.9 to 11.7 dB. 154

6.7 Linear fitting between the designed extra arm length difference and the inverse of the free spectral range ($1/\text{FSR}$) for the CWDM-2 structure where the arm length difference is utilizing half the ring. Extra arm length difference is added to half of the ring to fine tune the FSR. This relationship is used to determine the arm length required to achieve an FSR of $6.4\,\text{THz}$. The extra arm length differences are chosen for the given range only to make sure an FSR of $6.4\,\text{THz}$ can be attained. 155

6.8 Wafer-scale mapping of the free spectral range (FSR) for the fabricated CWDM-2 structures designed for $6.4\,\text{THz}$ operation. The measured FSR values range from $6.2\,\text{THz}$ to $6.44\,\text{THz}$, indicating good uniformity and process control across the wafer. 156

6.9 Schematic of the CWDM2 with a 120° bend and a minimum common arm length of L_0. The total arm length difference in this configuration is ΔL. The 120° bend has an effective arm length of $2\Delta L$. Each straight waveguide section connecting the bent DCs and the 120° bend has a length of L_0. The FSR of this MZ configuration can be manipulated by adjusting ΔL, where L_0 is always chosen as the minimum required value to minimize the common arm length. 157

6.10 The layout of the CWDM-2 $\times$ 6.4 THz system based on 120° bend using bent DCs. The design incorporates minimized common arm lengths to reduce phase errors. 158

6.11 The layout of the CWDM-2 $\times$ 6.4 THz system based on 120° bend using straight DCs. The design incorporates minimized common arm lengths to reduce phase errors. 158

6.12 Measured spectra of the CWDM-2 $\times$ 6.4 THz for bent DCs (a) and straight DCs (b). A significant improvement in the lowest extinction ratio (ER) is observed with the use of broadband bent DCs. The bent DC design achieves a better worst-case extinction ratio of 18.3 dB, compared to 7.8 dB for the straight DC configuration. The corresponding designs are shown in Fig. 6.10 and Fig. 6.11 for the bent and straight DCs, respectively. 159

6.13 Wafer mapping of extinction ratio (ER) for multiple dies, showing the improvement in ER with the use of bent DCs compared to straight DCs. The CWDM-2$\times$6.4 THz based on the bent DC demonstrates ER values ranging from 16.4 to 18.3 dB, while the straight DC shows ER values from 6.6 to 8.1 dB. 160

6.14 Linear fitting between the extra arm length difference and $(1/\text{FSR})$ for the CWDM-2 structure based on 120° WGM bend. This relationship is used to determine the arm length required to achieve an FSR of $12.8\,\text{THz}$. 161

6.15 Wafer-scale mapping of the free spectral range (FSR) for the fabricated CWDM-2 structures designed for $12.8\,\text{THz}$ operation. The measured FSR values range from $11.23\,\text{THz}$ to $12.99\,\text{THz}$, which should provide high quality filtering, indicating good uniformity and process control across the wafer. 162

6.16 Phase error characterization layout for CWDM-2 $\times$ based on regular MZ structure (a), the half ring based MZ structure (b), and the 120° bend MZ structure (c), where the same MZ design is replicated multiple times next to each other. Only a three duplicates are shown in this figure for each test site. 163

6.17 The cross power transmission spectra for identical MZI configurations: (a) traditional MZI structure, (b) half-ring based MZI structure, and (c) 120° bend MZI structure. Each panel shows 8 identical devices placed next to each other on the reticle to demonstrate phase error variations. Note the progressively reduced constructive interference wavelength shifts from (a) to (c), indicating decreasing phase errors as we move from traditional to more compact MZI configurations. The designs correspond to those shown in Fig. 6.16. 164

6.18 Standard deviation of phase error measured across 19 dies for various MZI configurations. The results highlight a substantial reduction in phase error for compact MZI designs, particularly those incorporating compact MZ structures including the half ring and the 120° bend. 165

6.19 The layout of the CWDM-4 $\times$ 3.2 THz system using bent DCs. The design incorporates CWDM-2 $\times$ 3.2 THz in the first stage and CWDM-2$\times$ 6.4 THz in the second stage. 166

6.20 Optical spectrum for the CWDM-4 $\times$ 3.2 THz system based on broadband bent DCs. The worst channel isolation (CI) is 25.9 dB covering a bandwidth$>$ 12.8 THz. The channel losses are minimal, where the loss is smaller than the measurement error. 166

6.21 Wafer mapping of the worst channel isolation (CI) over 12.8 THz band over a 300 mm wafer for the proposed CWDM-4 $\times$ 3.2 THz system. High values of CIs are observed across the wafer showing the robustness of the proposed design. 167

6.22 Transmission of CWDM-4 $\times$ 3.2 THz system based on bent DCs over 54 dies. Each color represents a different channel. The measurements show the robustness of the design to be used in mass manufacturing, where a channel spacing of 3.2 THz with each channel having a passband of 100 GHz showing a minimum CI of at least 13.5 dB. 167

6.23 Wafer mapping for the channel spacing in THz for the proposed CWDM-4$\times$3.2 THz system using bent DCs. The channel spacing ranges between 3.033 and 3.283 THz proving the robustness of the design over the whole wafer. 168

A.1 Extinction Ratio (ER) of the through port of a Mach-Zehnder Interferometer as a function of the DC's power coupling coefficient κ^2. The ER approaches infinity at $\kappa^2 = 0.5$ (perfect 3 dB coupling), and remains above 14 dB for κ^2 values in the range 0.4–0.6. This demonstrates the sensitivity of MZI performance to coupler balance and defines practical fabrication tolerance limits for high-extinction devices. 202

A.2 Transfer matrix method calculation for the transmission spectra comparison between cascaded MZI interleavers based on bent DCs: (a) four-channel configuration and (b) eight-channel configuration, showing wavelength-dependent response characteristics. In each graph, one color is given per output waveguide. The channel spacing is fixed as 100 GHz for both configurations. 208

A.3 Uncertainty comparison of the direct method, ring-based method, and the cutback method for extracting κ^2 in a directional coupler. The cutback method with 5 cascades exhibit the least uncertainty among all three methods. 215

List of Tables

3.1 Performance comparison table (a): Coupling variation and excess loss of various fabricated 2×2 splitters. 88

3.2 Performance comparison table (b): Device length and demonstrated coupling ratios of various fabricated 2×2 splitters. 90

4.1 Optimized parameters for arbitrary coupling ratios for the proposed adiabatic coupler based on optimizing ΔW and L via 3D FDTD simulations. The fixed parameters are $W_1 = 0.26\,\mu\mathrm{m}$, $g = 0.08\,\mu\mathrm{m}$, and t_p is the desired cross coupling ratio. 110

4.2 Optimization results for different W_1 values with a fixed gap of $0.08\ \mu m$ for the proposed adiabatic coupler based on optimizing ΔW and L via 3D FDTD simulations. The fixed parameters are $g = 0.08\ \mu m$, $t_p = 0.5\ \mu m$. 111

4.3 Optimization results for different gap values with a fixed waveguide width $W_1 = 0.26\,\mu\mathrm{m}$ for the proposed adiabatic coupler based on optimizing ΔW and L via 3D FDTD simulations. The fixed parameters are $W_1 = 0.26\,\mu\mathrm{m}$, $t_p = 0.5$. 111

5.1 Comparison of fabricated silicon DWDM-2 interleavers covering the C band. Overall, the proposed DWDM-2 $\times$100 GHz interleaver shows high ER values $\geq$18.4 dB without introducing further fabrication complexities as in [22], or compromising the excess loss as in [23]. 128

List of Acronyms

A

ADC	Adiabatic Directional Coupler
AI	Artificial Intelligence
AWG	Arrayed Waveguide Grating

B

BOX	Buried Oxide
BW	Bandwidth

C

C-band	Conventional Band (1530 – 1565 nm)
CI	Channel Isolation
CMOS	Complementary Metal-Oxide Semiconductor
CMT	Coupled Mode Theory
CS	Channel Spacing
CWDM	Coarse Wavelength Division Multiplexer

D

DC	Directional Coupler
DWDM	Dense Wavelength Division Multiplexer

E

ER	Extinction Ratio

F

FDTD	Finite Difference Time Domain
FEM	Finite Element Method
FSR	Free Spectral Range

H

HPC	High Performance Computing

I

IL	Insertion Loss
IP	Input

M

MMI	Multimode Interferometer
MRR	Microring Resonator
MZ	Mach Zehnder
MZI	Mach Zehnder Interferometer

O

O-band	Original Band (1260 – 1360 nm)
OP	Output

P

PIC	Photonic Integrated Circuit

S

SEM	Scanning Electron Microscope
Si	Silicon
SOI	Silicon on Insulator
SiO_2	Silicon Dioxide
SWG	Subwavelength grating

T

TE	Transverse Electric
TMM	Transfer Matrix Method
TOPIC	Third order polynomial interconnected circular

U

UCUT	Undercut

W

WDM	Wavelength Division Multiplexer
WG	Waveguide

X

XT	Crosstalk

0–9

2D	Two-Dimensional
3D	Three-Dimensional

Nederlandse Samenvatting

1 Inleiding

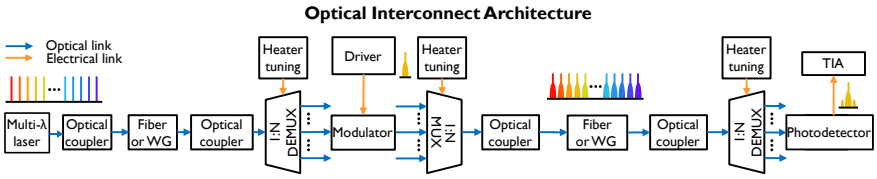

Figuur 1: Schematisch van een optische verbinding met de belangrijkste componenten: multi-golflengte laserbron, demultiplexerfilter voor kanaalscheiding, een modulator voor het coderen van data op het optische signaal, een multiplexer voor het combineren van meerdere golflengte kanalen, en een ontvanger met fotodetector voor signaalconversie. De WDM-filters maken parallelle transmissie van meerdere datastromen mogelijk, wat de primaire focus is van dit proefschrift.

De exponentiële groei in wereldwijd dataverkeer, gedreven door high-performance computing, cloud datacenters en toepassingen van kunstmatige intelligentie, heeft een ongekende vraag gecreëerd naar communicatiesystemen met hoge bandbreedte en energiezuinigheid [1, 2]. Fotonische interconnects zijn naar voren gekomen als een cruciale technologie om aan deze eisen te voldoen, met voordelen zoals hogere datasnelheden, lager energieverbruik en verminderde signaalverzwakking in vergelijking met elektronische connecties [3, 4]. Binnen dit landschap is golflengtemultiplexering (WDM) een hoeksteentechnologie geworden voor het schalen van bandbreedte door meerdere datakanalen gelijktijdig over verschillende optische golflengten te verzenden, waardoor de totale bandbreedte van een enkele optische verbinding effectief wordt vermenigvuldigd [5].

Siliciumfotonica heeft zich gevestigd als een veelbelovend platform voor het implementeren van WDM-systemen, waarbij gebruik wordt gemaakt van de maturiteit van CMOS-fabricageprocessen om fotonisch geïntegreerde circuits (PIC's) met hoge opbrengst, schaalbaarheid en kostenefficiëntie mogelijk te maken [6, 7]. Het hoge brekingsindexcontrast tussen silicium en silica maakt sterke optische modeopsluiting mogelijk, wat compacte bouwblockgeometrieën en efficiënte lichtmanipulatie mogelijk maakt [8, 9]. Bovendien maakt de compatibiliteit met CMOS-

technologie de co-integratie van optische en elektronische componenten op dezelfde chip mogelijk, wat energiezuinige systemen ondersteunt voor datacommunicatie en sensortoepassingen [10, 11].

Kernonderdelen van WDM-systemen zijn golflengte-selectieve filters, die de essentiële taken uitvoeren van het samenvoegen (multiplexen) en scheiden (demultiplexen) van afzonderlijke golflengtekanalen [9, 12]. Deze filters moeten voldoen aan strenge eisen om een hoge spectrale integriteit te waarborgen, waaronder lage transmissieverliezen en minimale overspraak tussen kanalen [13, 14]. Het realiseren van WDM-filters met hoge prestaties in siliciumfotonica is echter uitdagend vanwege de inherente dispersie (golflengte-afhankelijk gedrag) van het platform en fabricagevariaties, die de opbrengst en prestaties van WDM-circuits aanzienlijk kunnen beïnvloeden [15].

In een optische verbinding, zoals geïllustreerd in Fig. 1, zijn WDM-filters cruciaal voor het mogelijk maken van parallelle datatransmissie. De verbinding begint met een multi-golflengte laserbron die stabiele optische dragers levert. Deze dragers worden naar een demultiplexerfilter (DEMUX) geleid om de optische signalen in afzonderlijke kanalen te scheiden, die vervolgens worden gemoduleerd met behulp van elektro-optische modulatoren. De gemoduleerde kanalen worden opnieuw gecombineerd via een multiplexerfilter (MUX) om een signaal met hoge capaciteit te vormen. Bij de ontvanger wordt het signaal gedemultipexeerd, gedetecteerd door fotodetectoren en omgezet in elektrische signalen, die vervolgens worden versterkt en verwerkt door een transimpedantieversterker (TIA). Thermische afstemming zorgt voor nauwkeurige golflengte-uitlijning en stabiliteit. Deze golflengte-selectieve componenten zijn essentieel voor het vergroten van de totale bandbreedte van optische communicatiesystemen, omdat ze meerdere datastromen toestaan dezelfde fysieke golfgeleider te delen, wat de totale datacapaciteit van de verbinding aanzienlijk verhoogt zonder extra fysieke golfgeleiders te vereisen.

WDM-systemen kunnen grofweg worden ingedeeld in twee typen op basis van kanaalafstand:

- **Dense Wavelength Division Multiplexing (DWDM):** Deze systemen hebben een smalle kanaalafstand (meestal sub-nanometer), waardoor een aanzienlijk groter aantal kanalen binnen dezelfde spectrale bandbreedte mogelijk is. DWDM-systemen vereisen geavanceerde filterarchitecturen met hoge spectrale selectiviteit, lage overspraak en nauwkeurige golflengte-uitlijning.
- **Coarse Wavelength Division Multiplexing (CWDM):** Deze systemen hebben een bredere kanaalafstand (meestal ≈ 20 nm) en ondersteunen minder kanalen in vergelijking met DWDM-systemen. De grotere afstand vermindert de complexiteit van de componenten, waardoor CWDM-systemen kosteneffectiever en minder gevoelig voor fabricagetoleranties zijn.

Diverse architecturen voor WDM-filters in siliciumfotonica richten zich op het aan-

pakken van uitdagingen gerelateerd aan omvang, kanaalcapaciteit, kanaalisolatie, invoegverlies en fabricagetolerantie. Prominente types zijn onder andere Mach-Zehnder Interferometers (MZIs) [16], Mircoringresonatoren (MRR's) [17], Arrayed Waveguide Gratings (AWGs) [18], en Echelle Diffraction Gratings (EDGs) [19]. Echter, het bereiken van een WDM-architectuur die gelijktijdig aan al deze specificaties voldoet blijft een aanzienlijke uitdaging [5, 9].

Dit proefschrift pakt deze uitdagingen aan door robuuste, breedbandige optische componenten en WDM-architecturen voor zowel DWDM als CWDM systemen in siliciumfotonica te ontwikkelen. De focus ligt op MZI-gebaseerde WDM-architecturen vanwege hun hoge prestaties, schaalbaarheid, eenvoudige integratie en relatief compacte voetafdruk [20–23].

In een MZI verdeelt een optische splitter het inkomende licht in twee paden (armen), terwijl een optische combinator het licht aan de uitgang combineert, waardoor interferentie-gebaseerde golflengtefiltering mogelijk wordt. Traditionele MZI-architecturen maken vaak gebruik van rechte directionele koppelaars (DC's) als bundelsplitters en combinatoren. Echter, rechte DC's hebben last van golflengte-afhankelijke koppeling als gevolg van dispersie in het siliciumfotonica-platform. Een silicium rechte DC die is ontworpen voor een 0.5:0.5 splitsing kan bijvoorbeeld koppelingsvariaties vertonen die groter zijn dan 0.45 over een golflengtebereik van 80 nm, wat hun operationele bandbreedte beperkt en de signaalintegriteit aantast, vooral in breedband WDM-toepassingen [9, 24].

Dit proefschrift pakt deze beperkingen aan door de fundamentele bouwstenen van WDM-systemen te optimaliseren en breedbandige optische splitters en combinatoren te introduceren die breedbandwerking bij willekeurige koppelingsverhoudingen mogelijk maken. Deze componenten dienen als kritieke elementen voor geavanceerde WDM-filterarchitecturen, waardoor significante verbeteringen in het operationele golflengtegebied, invoegverlies en kanaalisolatie mogelijk worden gemaakt [23, 25, 26].

Dit werk draagt uiteindelijk bij aan de realisatie van zeer dichte WDM-systemen, waaronder een DWDM-systeem met 128 kanalen en 100 GHz kanaalafstand (DWDM-128$\times$100 GHz). De schematische weergave van een ontworpen DWDM-128$\times$100 GHz-systeem is te zien in Fig. 2. Het DWDM-128$\times$100 GHz-systeem combineert een MZI-interleaver, MRRs en MZI-gebaseerde CWDM-systemen om hoogdensiteits golflengte-demultiplexering te bereiken. De interleaver splitst het ingangsspectrum in 4 groepen van 32 kanalen, elk op 400 GHz afstand, en leidt ze naar 4 bus-golfgeleiders. Langs elke bus-golfgeleider worden 8 verschoven MRRs gebruikt om 4 kanalen per ring te extraheren. Deze geëxtraheerde signalen worden verder gedemultiplexed door CWDM-4-systemen. Deze hiërarchische architectuur maakt het mogelijk om 128 kanalen, elk op 100 GHz afstand, te demultiplexen naar 128 individuele uitgangsgolfgeleiders.

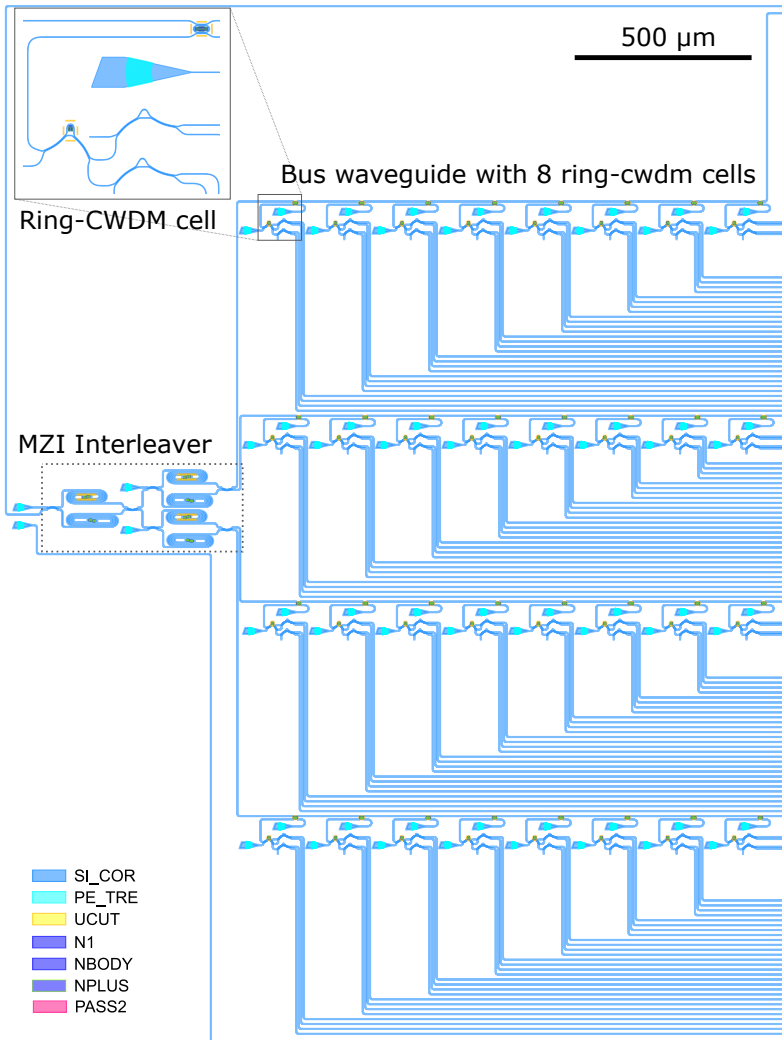

Figuur 2: Schematische weergave van het voorgestelde DWDM-128×100 GHz-systeem. De architectuur integreert een 4-kanaals MZI-stadium, microringresonatoren (MRRs), en CWDM-4-filters. Het MZI-stadium verdeelt de input in vier groepen, elk geleid naar een bus-golfgeleider met 8 verschoven MRRs (32 in totaal). Elke MRR drop-poort is in cascade geschakeld met een CWDM-4-filter, wat demultiplexing naar 128 kanalen met 100 GHz-afstand mogelijk maakt. De metalen routering en de uitgangstroosters worden hier niet getoond. De inzet toont een uitvergroot beeld van een van de ring-CWDM-eenheden.

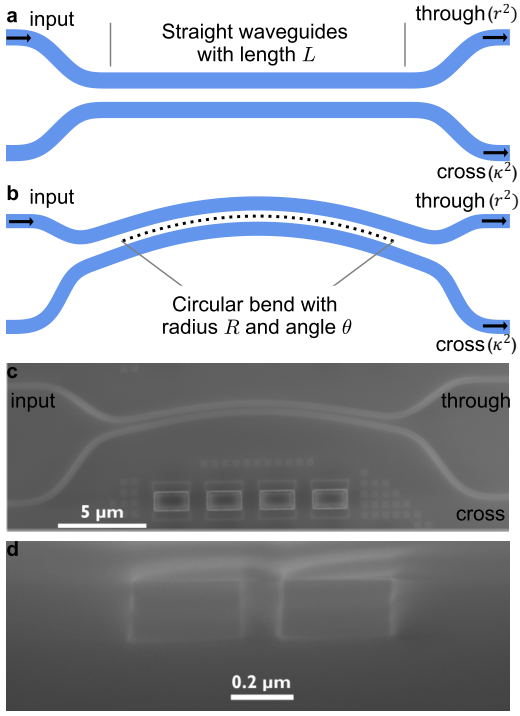

Figuur 3: Schematische weergave van de rechte DC (a), breedbandige gebogen DC (b), en SEM-afbeeldingen van de gefabriceerde gebogen DC (c, d), gefabriceerd met behulp van IMEC's iSiPP300-platform.

2 Breedband Gebogen Directionele Koppelaars

Om de prestaties van MZI-gebaseerde WDM-systemen te verbeteren en de breedbandbeperkingen van traditionele rechte DC's aan te pakken (Fig. 3 (a)), introduceert dit proefschrift breedbandige gebogen DC's (Fig. 3 (b, c, d)) door gebruik te maken van inzichten uit de gekoppelde-modetheorie (CMT) [27, 28]. De CMT-analyse toont aan dat gebogen DC's verbeterde ontwerpflexibiliteit bieden, waardoor golflengte-ongevoelige koppeling mogelijk wordt door dispersie-effecten te verminderen die verantwoordelijk zijn voor golflengte-afhankelijke koppelingsvariaties.

De sleutel tot het bereiken van breedbandkoppeling ligt in het analyseren van de afgeleide van het gekoppelde vermogen met betrekking tot golflengte. Twee kritieke parameters beïnvloeden het koppelingsgedrag: het groepsindexverschil (Δn_g) en de afgeleide van de effectieve index met betrekking tot golflengte ($d\Delta n_{eff}/d\lambda$). Deze parameters bepalen de dispersie-eigenschappen van de koppelaar.

In gebogen DC's kunnen deze twee parameters onafhankelijk worden afgestemd,

wat nauwkeurige controle over de koppelingskenmerken biedt. Deze afstemmingsmogelijkheid stelt de dispersietermen in staat elkaar effectief op te heffen, waardoor golflengte-afhankelijke koppelingsvariaties aanzienlijk worden verminderd. In tegenstelling tot rechte DC's, die inherent deze flexibiliteit missen, benutten gebogen DC's hun unieke geometrie om breedbandige werking te bereiken, waardoor ze geschikt zijn voor WDM-systemen.

Door het optimaliseren van belangrijke ontwerpparameters zoals de buigradius en koppelingshoek (Fig. 3 (b)), werd de golflengteafhankelijkheid van gebogen DC's aanzienlijk verminderd. Over het algemeen voldoen de gedemonstreerde gebogen DC's aan de essentiële vereisten van breedbandwerking, ondersteuning voor willekeurige koppelingsverhoudingen, laag invoegverlies, compacte voetafdruk en hoge fabricagetolerantie, waardoor ze geschikt zijn voor WDM-filters. De onderzoeksresultaten in de ontwikkeling van gebogen DC's omvatten:

- **Verminderde Koppelingsvariatie:** Bereikte een minimale koppelingsvariatie van slechts 0.051 over een golflengtebereik van 80 nm voor 0.5:0.5 gebogen DC's, wat een verbetering van 7.67$\times$ vertegenwoordigt in vergelijking met conventionele rechte DC's (Fig. 4 (a, b)).
- **Laag Invoegverlies:** Demonstreerde het laagste koppelingsverlies (0.006 ± 0.004 dB) onder alle gerapporteerde silicium 2×2 splitters, beperkt door de meetprecisie, bereikt door het gebruik van nieuwe lage-verlies bochten die zorgen voor continue kromming en krommingsafgeleide bij alle verbindingen [14].
- **Compacte Voetafdruk:** Deze verbeteringen werden gerealiseerd met een compacte lengte van slechts 27.5 μm, wat een kleine voetafdruk behoudt die cruciaal is voor dichte integratie.
- **Model voor Willekeurige Verhoudingen:** Ontwikkeld een model voor het bereiken van breedbandkoppeling bij willekeurige verhoudingen door de bochtstraal en koppelingshoek af te stemmen.
- **Robuustheid op Waferschaal:** Metingen op waferschaal over 63 dies op een 300 mm wafer, waarbij robuuste prestaties werden bevestigd met een maximale koppelingsvariatie van 0.112 en een gemiddelde koppelingsafwijking van 0.007 aan de uiterste rand van de wafer over een golflengtebereik van 80 nm (Fig. 5), wat geschiktheid voor massaproductie aantoont.
- **Platformcompatibiliteit:** Verschillende ontwerpen zijn gedemonstreerd die compatibel zijn met zowel 200 mm als 300 mm fabricageplatforms, wat hun praktische bruikbaarheid en commerciële levensvatbaarheid vergroot.

Deze vooruitgangen vestigen gebogen DC's als een robuuste oplossing voor breedband WDM-systemen, die een robuuste oplossing bieden voor breedbandwerking

die zich direct vertaalt naar hogere extinctieverhoudingen in MZI-gebaseerde WDM-filters en uiteindelijk de hoogwaardige DWDM- en CWDM-systemen mogelijk maakt die in latere hoofdstukken worden beschreven.

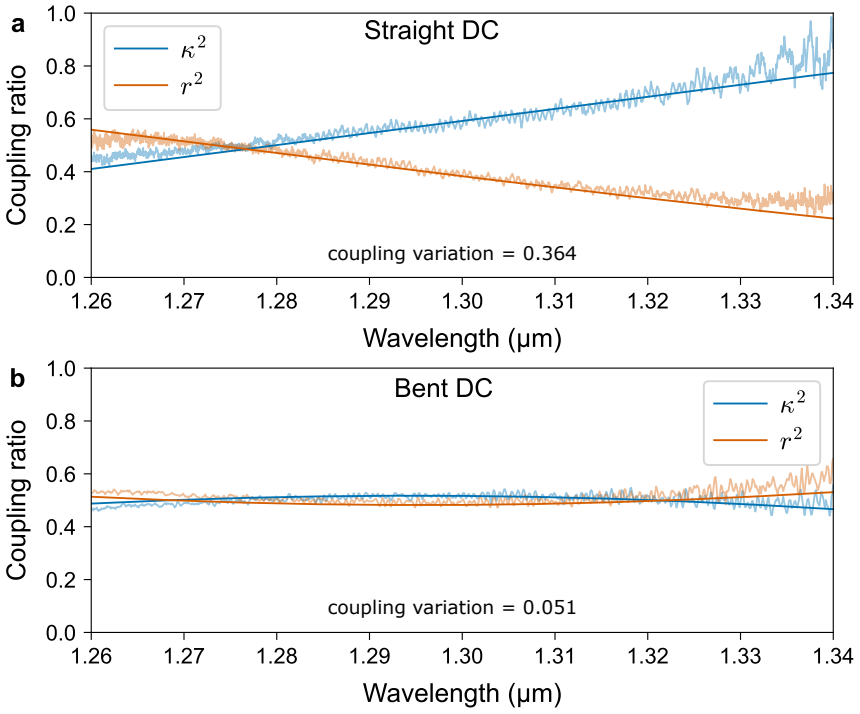

Figuur 4: Vergelijking van koppelingsverhoudingen tussen rechte DC's (a) en gebogen DC's (b) over een golflengtebereik van 80 nm, waarbij de aanzienlijk verbeterde golflengte-ongevoeligheid van het gebogen DC-ontwerp wordt aangetoond.

3 Breedband Adiabatische Koppelaars

Hoewel gebogen directionele koppelaars een verminderde koppelingsvariatie bieden in vergelijking met rechte DC's, is hun koppelingsvariatie niet volledig optimaal. Om de prestaties verder te verbeteren, introduceert dit proefschrift numeriek geoptimaliseerde adiabatische koppelaars (Fig. 6) die zijn ontworpen om de koppelingsvariatie over een breed golflengtebereik te minimaliseren op basis van een nieuwe ontwerpbenadering.

Adiabatische koppelaars werken volgens een fundamenteel ander principe dan conventionele directionele koppelaars [29, 30]. In symmetrische rechte DC's worden zowel even als oneven supermodi geëxciteerd vanwege structurele symme-

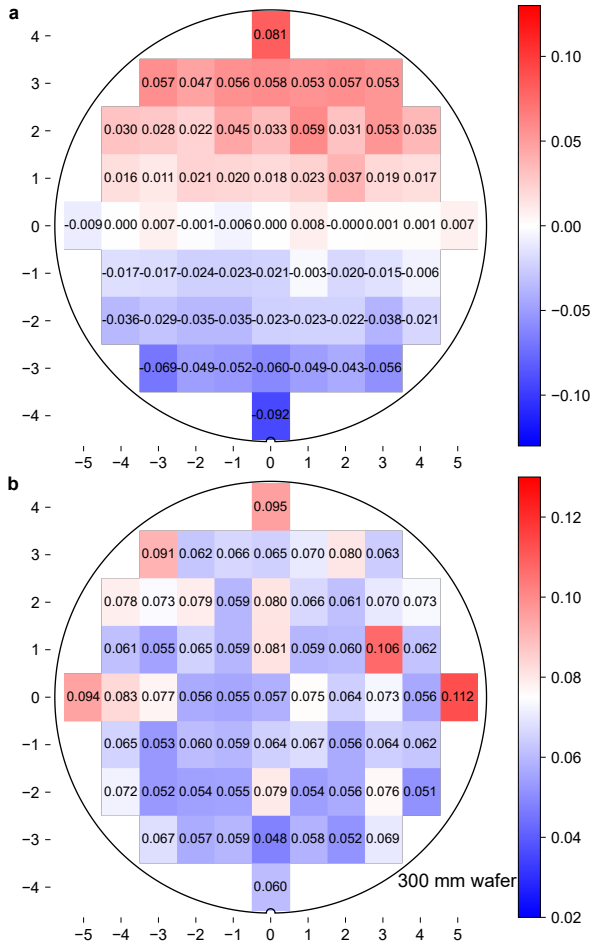

Figuur 5: Gemiddelde kruiskoppelingsafwijking ten opzichte van de centrale die (a) en kruiskoppelingsvariatie (b) over een golflengtebandbreedte van 80 nm voor de voorgestelde 0.5:0.5 gebogen DC-splitter over de 300 mm wafer, waarbij alle 63 dies worden gedekt.

trie, wat resulteert in een sinusvormige en golflengte-afhankelijke koppelingsrespons [31, 32]. Daarentegen zijn adiabatische koppelaars zo ontworpen dat slechts één mode voornamelijk wordt geëxciteerd (Fig. 7), wat breedbandige en robuuste vermogensoverdracht mogelijk maakt [33, 34]. Ze maken gebruik van geleidelijke veranderingen in golfgeleidergeometrie om ervoor te zorgen dat de optische mode continue evolueert van de ene golfgeleider naar de andere, waardoor verstrooiing en overmatig verlies worden geminimaliseerd [26, 35].

Dit proefschrift presenteert een nieuwe manier om adiabatische koppelaars (Fig. 6) te ontwerpen, gebaseerd op een minmax-optimalisatiebenadering om de koppe-

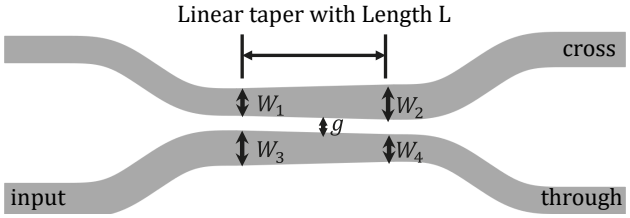

Figuur 6: Schematische weergave van de voorgestelde adiabatische koppelaar met de ontwerpparameters. Het ontwerp is niet op schaal en is uitsluitend bedoeld ter illustratie.

lingsvariatie over een doelgolflengtebereik te minimaliseren:

$$\min_{\Delta W, L} \left(\max_{\lambda \in [\lambda_1, \lambda_2]} |P_c(\lambda) - P_{c,\text{desired}}| \right)$$

waarbij ΔW de golfgeleiderbreedteverschillen aan het begin van de overgangsregio vertegenwoordigt, L de overgangslengte is, en $P_c(\lambda)$ het gekruiste gekoppelde vermogen is. De parameters worden weergegeven in Fig. 6. Deze aanpak levert een geoptimaliseerde oplossing die de maximale afwijking van de gewenste koppelingsverhouding over het gehele operationele golflengtebereik minimaliseert (Fig. 8), en kan worden gebruikt om te streven naar willekeurige koppelingsverhoudingen door de breedte van de uitgangsgolfgeleiders dienovereenkomstig aan te passen. Op basis van deze aanpak worden zowel breedbandige koppeling als ultracompacte lengtes bereikt.

De onderzoeksresultaten in de ontwikkeling van adiabatische koppelaars omvatten:

- **Lage Koppelingsvariatie:** De geoptimaliseerde 3-dB adiabatische koppelaar toont een koppelingsvariatie van slechts 0.02 over een golflengtebereik van 120 nm dat de O-band omvat, wat een 16.6× reductie vertegenwoordigt in vergelijking met traditionele rechte DC's (Fig. 9). Lage koppelingsvariatie is cruciaal voor het behouden van hoge kanaalisolatie in WDM-systemen.
- **Ultracompact Ontwerp:** Adiabatische koppelaars zijn meestal omvangrijk en kunnen honderden micrometers beslaan. De voorgestelde adiabatische koppelaar bereikt echter een ultracompacte tapsheidslengte van 1.44 μm, wat de kortste is die tot nu toe is gerapporteerd, voor zover bekend [26].
- **Willekeurige Koppelingsverhoudingen:** Breedbandkoppeling wordt aangetoond voor willekeurige koppelingsverhoudingen op basis van de minmax-optimalisatiebenadering.

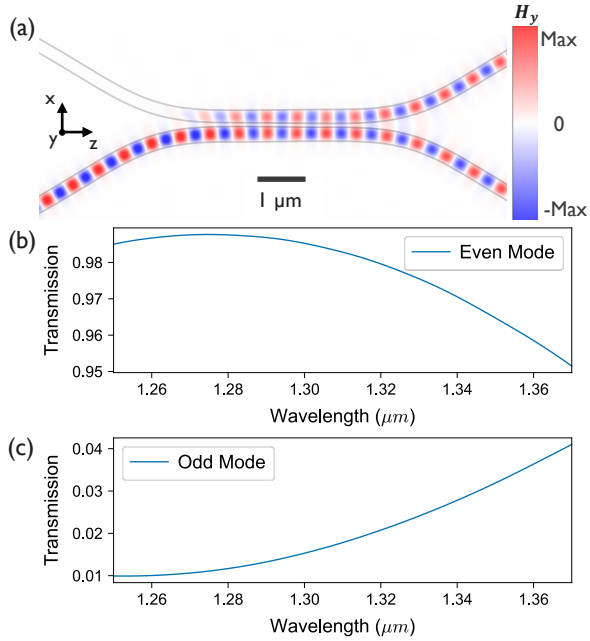

Figuur 7: H_y-veldplot van de voorgestelde 3-dB splitter bij λ=1.31 μm (a). TE even (b) en oneven (c) modusvermogensuitbreidingen in het midden van de koppelaar tonen aan dat het grootste deel van het vermogen (98.3% bij λ=1.31 μm) aanwezig is in de TE even modus, wat de adiabatische aard van de splitter bewijst.

- **Laag Invoegverlies:** Een laag invoegverlies van $\leq$ 0.03 dB wordt aangetoond dankzij het gebruik van lage-verlies bochten.

De ontwikkelde adiabatische koppelaars vertegenwoordigen een aanzienlijke vooruitgang ten opzichte van bestaande ontwerpen en bieden hoge prestaties op het gebied van bandbreedte, compactheid en invoegverlies. Toekomstige WDM-ontwerpiteraties kunnen profiteren van een dergelijk ontwerp om de systeemprestaties te verbeteren.

4 Dense Wavelength Division Multiplexing Systemen

De implementatie van breedband gebogen DC's ontwikkeld in dit werk heeft geleid tot aanzienlijke verbeteringen in de prestaties van DWDM-systemen, met name op het gebied van kanaalisolatie en operationeel golflengtebereik [23, 25].

MZI-gebaseerde interleavers spelen een cruciale rol in dit werk en dienen als

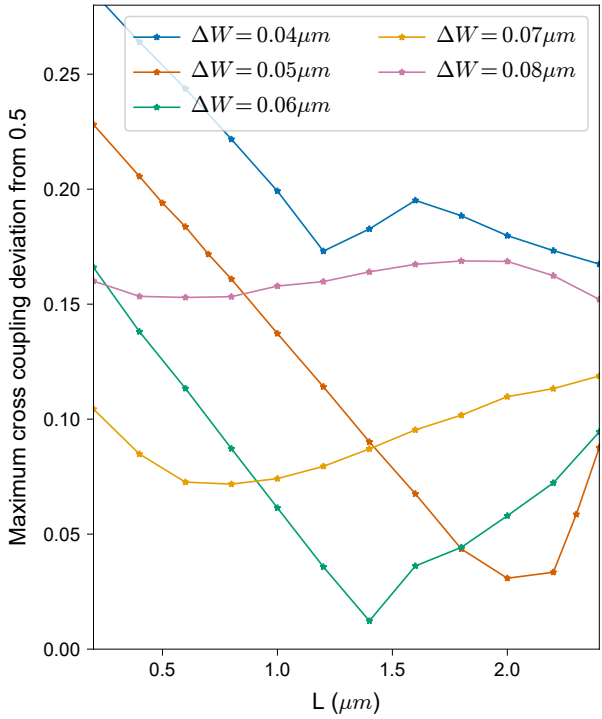

Figuur 8: Maximale kruiskoppelingsafwijking van 0.5 *over een* 120 nm *golflengtebereik als functie van de overgangslengte (L) en het initiële golfgeleiderbreedteverschil (ΔW).*

sleutelcomponenten in het DWDM-128× 100 GHz-systeem, zoals geïllustreerd in Fig. 10. Daarom worden DWDM-2×100 GHz- en DWDM-4×100 GHz-systemen met gebruik van breedband gebogen DC's gedemonstreerd.

Het proefschrift presenteert het ontwerp, de implementatie en de karakterisering van verschillende MZI-gebaseerde DWDM-systemen. De onderzoeksresultaten in DWDM-systemen omvatten:

- **Uitgebreide Operationele Bandbreedte:** De DWDM-2×100 GHz interleaver gebaseerd op breedband gebogen DC's toonde minstens een 2.7× toename in operationeel golflengtebereik (tot 100 nm) terwijl hoge extinctieverhoudingen (ER $\geq$ 18.4 dB) werden behouden in vergelijking met conventionele ontwerpen gebaseerd op rechte DC's (beperkt tot 36.7 nm), zoals weergegeven in Fig. 11. Vergelijkbare verbeteringen werden waargenomen in het DWDM-4×100 GHz-systeem via transfermatrixberekeningen, en het DWDM-16×800 GHz-systeem toonde aanzienlijk verbeterde werking over het doelgolflengtebereik, zoals geïllustreerd in Fig. 12.

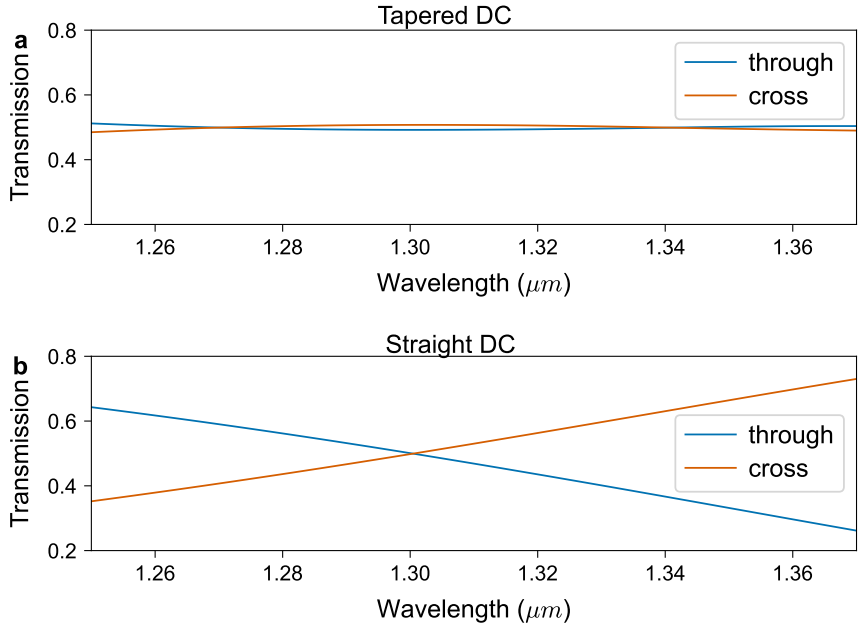

Figuur 9: 3-dB splitter optische transmissie met behulp van de voorgestelde adiabatische koppelaar (a) in vergelijking met de traditionele rechte koppelaar (b) over een golflengtebereik van 120 nm dat de O-band omvat. Een significante reductie van 16.6× in de koppelingsvariatie wordt bereikt met het voorgestelde ontwerp in vergelijking met de rechte DC-tegenhanger.

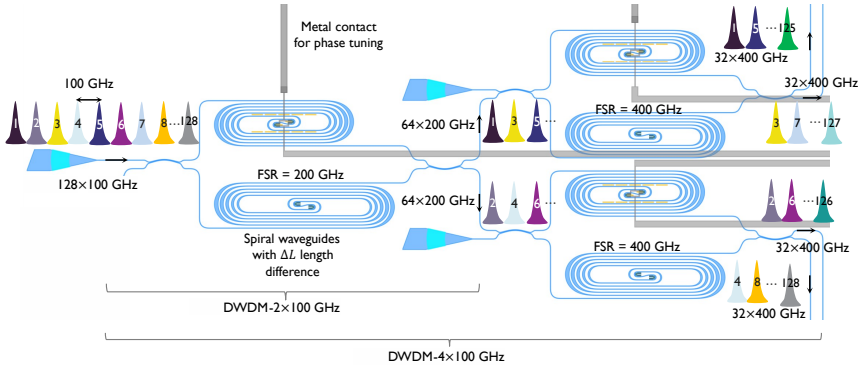

Figuur 10: Schematische weergave van de interleaver die wordt gebruikt in het WDM-128 × 100 GHz-systeem op basis van breedband gebogen DC's. De eerste MZI-fase interleaveert 128 kanalen in twee uitgangen van 64 kanalen. De tweede fase, met het dubbele van de FSR, interleaveert deze verder in vier golfgeleiders, elk met 32 kanalen.

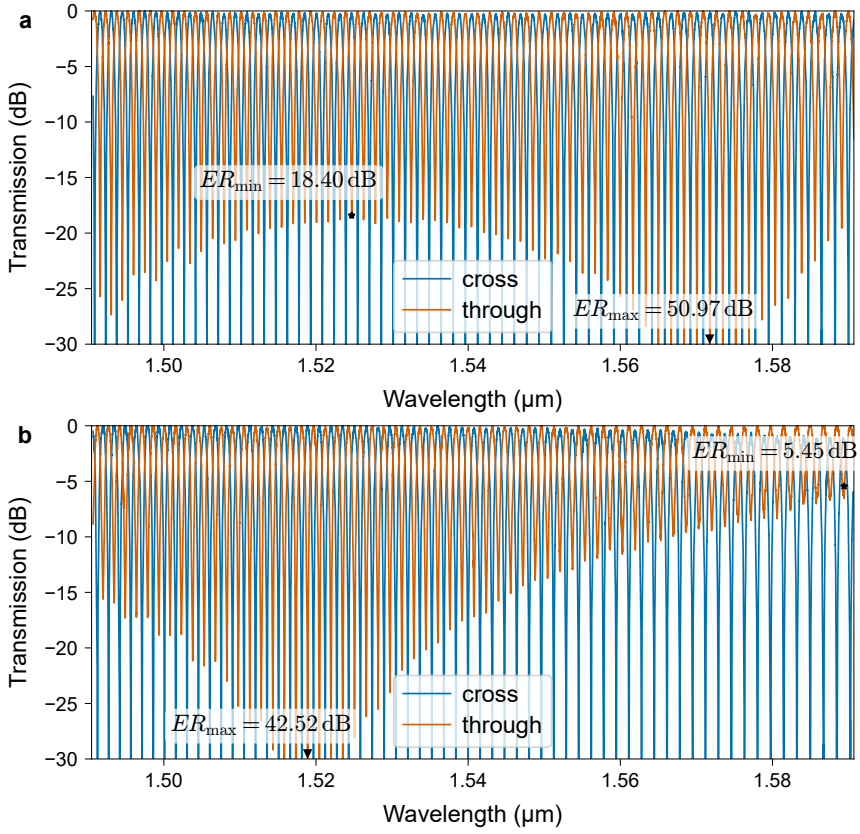

Figuur 11: Het voorgestelde DWDM-2 ×100 GHz interleaver-spectrum gebaseerd op gebogen DC's (a), en het traditionele DWDM-2-spectrum gebaseerd op rechte DC's (b). Minimale en maximale ER-waarden zijn gemarkeerd. Een verbetering van minstens 2.7× *in het ER-golflengte-werkingsbereik voor de voorgestelde interleaver wordt getoond.*

- **Hogere Kanaalisolatie:** De minimale extinctieverhouding van de DWDM-2×100 GHz interleaver werd verbeterd van 4.2-6.1 dB in traditionele ontwerpen tot 14.3-18.4 dB met de voorgestelde architectuur. Transfermatrixberekeningen voor het DWDM-4×100 GHz-systeem toonden een verbetering van de kanaalisolatie van 4.65 dB tot 16.77 dB, terwijl het DWDM-16×800 GHz-systeem verbeterde isolatie toonde van 5.42 dB tot 17.18 dB (Fig. 12). Deze verbeteringen verbeteren de signaalintegriteit aanzienlijk en verminderen overspraak over een grote bandbreedte, wat de effectiviteit van de voorgestelde architectuur voor schaalbare WDM-systemen bewijst.

- **Verminderd Invoegverlies:** Het gemiddelde invoegverlies werd aanzienlijk verminderd in alle DWDM-systemen bij gebruik van gebogen DC's in vergelijking met rechte DC's. In het DWDM-4×100 GHz-systeem daalde het

invoegverlies van 0.77 dB tot 0.18 dB, terwijl het in het DWDM-16×800 GHz-systeem verbeterde van 1.02 dB tot 0.30 dB, zoals duidelijk aangetoond in Fig. 12.

- **Robuustheid op Waferschaal:** Uitgebreide metingen over 63 dies op een 300 mm wafer bevestigden consistente prestaties met minimale variatie, wat de geschiktheid van het ontwerp voor massaproductie aantoont.

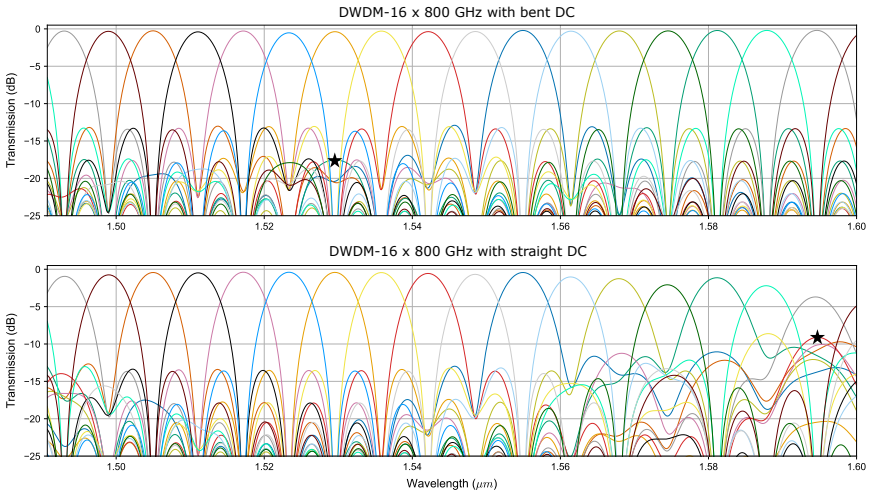

Figuur 12: DWDM-16 ×800 GHz-systeemspectra berekend met de transfermatrixmethode gebaseerd op (a) gebogen DC's en (b) rechte DC's. Het systeem gebaseerd op gebogen DC's toont aanzienlijke verbeteringen in kanaalisolatie en invoegverlies.

5 Coarse Wavelength Division Multiplexing Systemen

Als aanvulling op het werk aan DWDM-systemen richt dit proefschrift zich ook op de ontwikkeling van robuuste CWDM-systemen met gebruik van de breedband gebogen DC's. Het proefschrift presenteert het ontwerp en de implementatie van CWDM-2×3.2 THz- en CWDM-4×3.2 THz-systemen. CWDM-systemen zijn van groot belang voor het opschalen van het aantal kanalen in DWDM-systemen. In het bijzonder wordt voor het voorgestelde DWDM-128×100 GHz een CWDM-4×3.2 THz gebruikt om het aantal kanalen met een factor vier te vergroten, zoals weergegeven in Fig. 13.

Deze systemen zijn ontworpen met de nadruk op het minimaliseren van fasefouten door innovatieve architecturale benaderingen, zoals het toepassen van half-

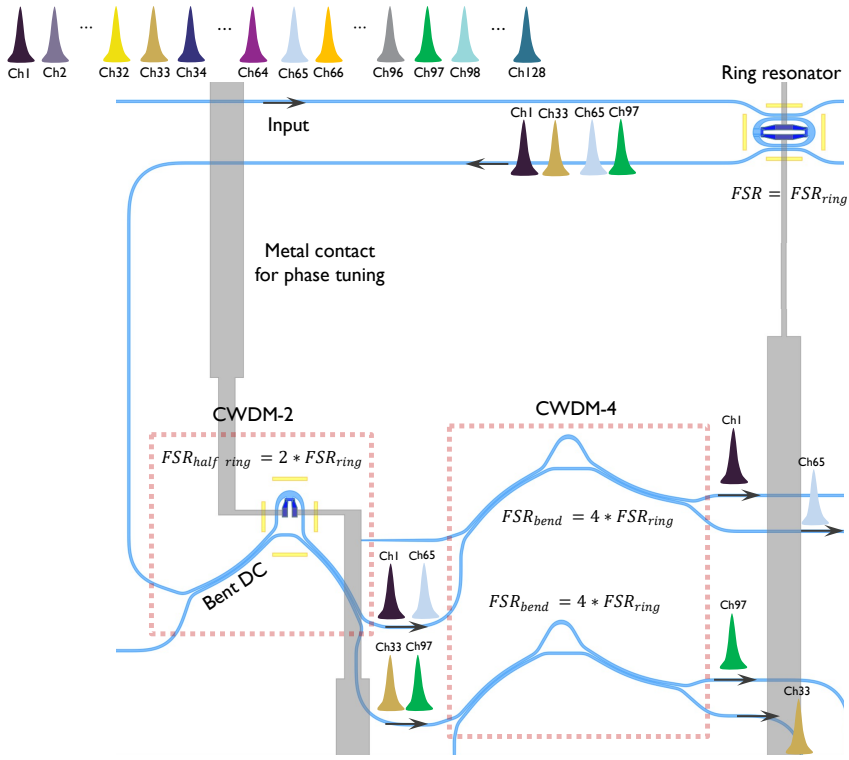

Figuur 13: Schematische weergave van de cascaded ring-CWDM-architectuur die DWDM-128 × 100 GHz mogelijk maakt. De drop-poort van een ringresonator met FSR = 3.2 THz *is verbonden met een CWDM-2 en vervolgens een CWDM-4, wat een viervoudige toename in het aantal kanalen mogelijk maakt.*

ringconfiguraties en whispering-gallery-mode (WGM) bochten die de gemeenschappelijke armlengtes minimaliseren. Deze aanpak adresseert een van de belangrijkste uitdagingen in siliciumfotonische WDM-systemen, namelijk golflengtedrift als gevolg van fasefouten door fabricagevariaties.

Belangrijke onderzoeksresultaten in CWDM-systeemontwerpen omvatten:

- **Verminderde Fasefouten:** Kwantitatief aangetoond dat significante fasefoutreductie in CWDM-filters wordt bereikt met behulp van half-ringconfiguraties en whispering-gallery-mode bochten. Metingen over 19 dies toonden aan dat de standaardafwijking van fasefouten afnam van 0.545 rad in conventionele MZI's tot 0.152 rad met half-ringconfiguraties, en verder tot slechts 0.040 rad met de 120° bochten. Dit maakt passieve werking zonder thermische afstemming mogelijk, wat een aanzienlijke energiebesparing vertegenwoordigt.
- **Kanaalisolatieverbetering:** Het CWDM-2×3.2 THz-systeem gebaseerd op

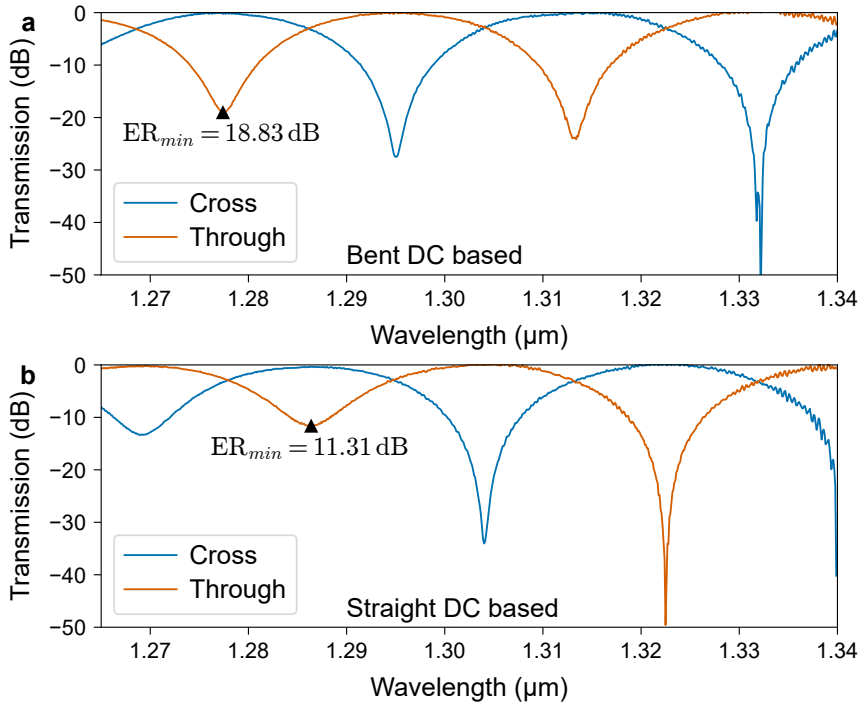

Figuur 14: Gemeten spectra van de CWDM-2 × 3.2 THz voor breedbandige gebogen directionele koppelaars (DC's) (a) en rechte gebogen DC's (b).

gebogen DC's behaalde extinctieverhoudingen van 16.5-18.8 dB in vergelijking met 10.9-11.7 dB voor implementaties met rechte DC's, terwijl het CWDM-2×6.4 THz-systeem een nog dramatischere verbetering liet zien van 6.6-8.1 dB tot 16.4-18.3 dB.

- **Hoogpresterende CWDM-4×3.2 THz:** Succesvol een CWDM-4-systeem gedemonstreerd dat essentieel is voor de DWDM-128×100 GHz-architectuur, met een slechtste geval kanaalisolatie van 25.9 dB over een bandbreedte van > 12.8 THz. Metingen op waferschaal over 54 dies bevestigden consistente prestaties met een minimale kanaalisolatie van 13.5 dB over een 100 GHz-bereik rond elk kanaalcentrum zonder thermische afstemming.

Deze CWDM-systemen vertegenwoordigen een significante vooruitgang in siliciumfotonische filtertechnologie, waardoor passieve werking mogelijk wordt gemaakt terwijl hoge prestatienormen worden gehandhaafd. De combinatie van nieuwe geometrische benaderingen met de eerder ontwikkelde breedband gebogen DC's resulteert in CWDM-systemen die conventionele ontwerpen overtreffen op het gebied van extinctieverhouding en operationele stabiliteit zonder gebruik van

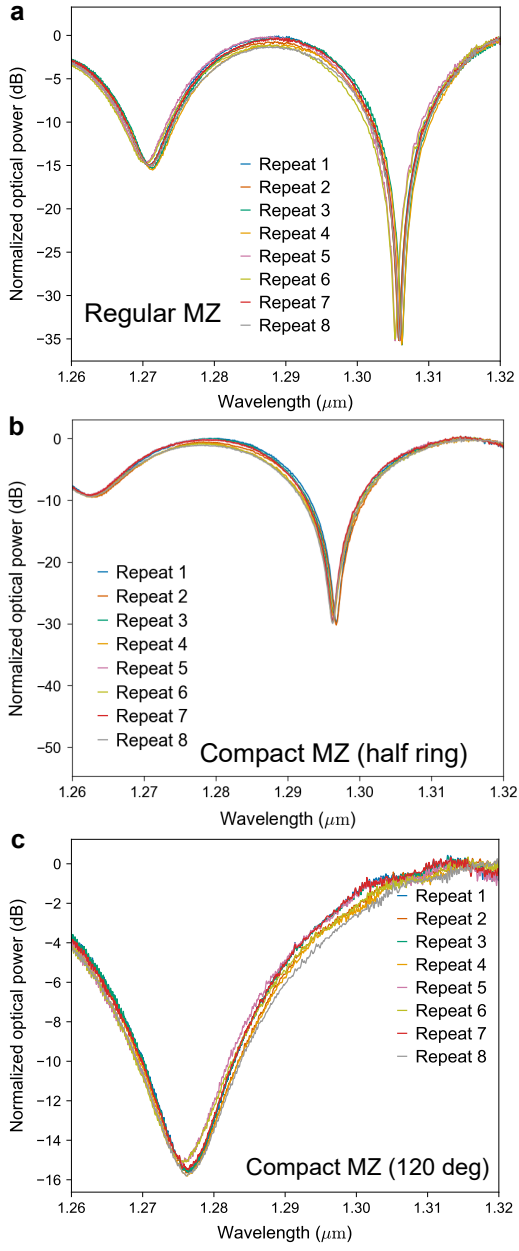

Figuur 15: De optische vermogenstransmissie in kruiskoppeling voor 8 identieke traditionele MZI's naast elkaar op de reticle, die de impact van fasefouten op de golflengterespons laat zien.

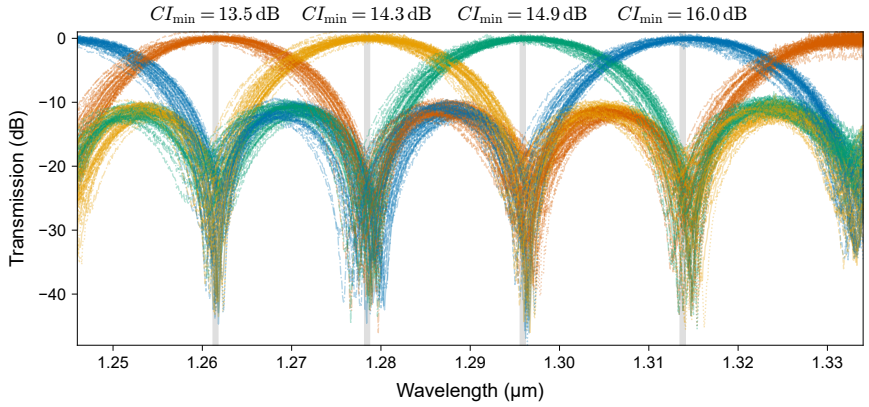

Figuur 16: Optisch spectrum voor het CWDM-4 × 3.2 THz-systeem gebaseerd op breedband gebogen DC's over 54 dies, waarbij elke kleur een ander kanaal vertegenwoordigt. De metingen tonen de robuustheid van het ontwerp voor gebruik in massaproductie.

thermo-optische afstemmingcircuits.

6 Conclusies

Dit proefschrift bevordert de siliciumfotonische WDM-technologie door drie belangrijke innovaties: (1) breedbandige gebogen en adiabatische directionele koppelaars met recordlage golflengtegevoeligheid en invoegverlies; (2) DWDM-systemen met uitgebreide operationele bandbreedte en hoge extinctieverhoudingen; en (3) CWDM-architecturen met lage fasefouten die betrouwbaar werken zonder thermische afstemming. Deze bijdragen pakken kritieke uitdagingen aan op het gebied van optische bandbreedteschaling, energie-efficiëntie en fabricagerobuustheid, en maken de volgende generatie optische interconnects met hoge capaciteit mogelijk.

Belangrijke bijdragen omvatten:

1. **Breedband Gebogen Directionele Koppelaars:** Bereikte lage koppelingsvariatie (0.051 over 80 nm, 7.67× verbetering) en minimaal invoegverlies (0.006 ± 0.004 dB), ondersteund door een uitgebreid analytisch model voor willekeurige koppelingsverhoudingen.

2. **Ultracompacte Adiabatische Koppelaars:** Ontwikkelde koppelaars met minimale koppelingsvariatie (0.02 over 120 nm) en ultracompacte overgangslengte (1.44 μm), orders van grootte korter dan conventionele ontwerpen.

3. **Hoogpresterende DWDM-Systemen:** Demonstreerde interleavers met 2.7× bredere operationele bandbreedte (100 nm) en extinctieverhoudingen $\geq$

18.4 dB, met verbeterde kanaalisolatie en verminderd transmissieverlies.

4. **Thermisch Afstemmingsvrije CWDM-Systemen:** Implementeerde CWDM-systemen met innovatieve technieken voor fasefoutminimalisatie, met verbeteringen in extinctieverhouding van 6.6-8.1 dB tot 16.4-18.3 dB.

5. **DWDM-**128×100 **GHz-Systeem:** Ontwierp een hoge-dichtheid DWDM-systeem dat gebogen DC's, DWDM-4 interleavers en CWDM-4 filters integreert, momenteel in fabricage.

Referenties

[1] Cisco. Cisco annual internet report (2018–2023). Technical report, Cisco Systems, 2020. https://www.cisco.com/c/en/us/solutions/executive-perspectives/annual-internet-report/index.html.

[2] NVIDIA Corporation. Nvidia spectrum-x photonics co-packaged optics networking switches to scale ai factories to millions of gpus. https://nvidianews.nvidia.com/news/nvidia-spectrum-x-co-packaged-optics-networking-switches-ai-factories/, 2025.

[3] D. Miller. Device requirements for optical interconnects to silicon chips. *Proceedings of the IEEE*, 97(7):1166–1185, July 2009. ISSN 1558-2256. doi: 10.1109/jproc.2009.2014298.

[4] Bahram Jalali and Sasan Fathpour. Silicon Photonics. *Journal of Lightwave Technology*, 24(12):4600–4615, 2006. ISSN 0277-786X. doi: 10.1016/B978-0-12-374171-4.00011-3. ISBN: 9780123741714.

[5] Nabarun Saha, Giuseppe Brunetti, Annarita di Toma, Mario Nicola Armenise, and Caterina Ciminelli. Silicon photonic filters: A pathway from basics to applications. *Advanced Photonics Research*, March 2024. ISSN 2699-9293. doi: 10.1002/adpr.202300343.

[6] S.K. Selvaraja, P. Jaenen, W. Bogaerts, D. Van Thourhout, P. Dumon, and R. Baets. Fabrication of photonic wire and crystal circuits in silicon-on-insulator using 193-nm optical lithography. *Journal of Lightwave Technology*, 27(18):4076–4083, September 2009. ISSN 1558-2213. doi: 10.1109/jlt.2009.2022282.

[7] F. J. Ferraro, P. De Heyn, M. Kim, N. Rajasekaran, M. Berciano, G. Muliuk, D. Bode, G. Lepage, S. Janssen, R. Magdziak, J. De Coster, H. Kobbi, S. Lardenois, N. Golshani, L. Shiramin, C. Marchese, S. Rajmohan, S. Nadarajan, N. Singh, S. Radhakrishnan, A. Tsiara, P. Xu, A. Karagoz, D. Yudistira, M. Martire, A. Shahar, M. Chakrabarti, D. Velenis, W. Guo, A. Miller, Kristof Croes, S. Balakrishnan, P. Verheyen, Y. Ban, J. Van Campenhout, and P. P. Absil. Imec silicon photonics platforms: performance overview and roadmap. In *Next-Generation Optical Communication: Components, Sub-Systems, and Systems XII*, volume 12429, pages 22–28. SPIE, March 2023. doi: 10.1117/12.2650579.

[8] D.A.B. Miller and H.M. Ozaktas. Limit to the bit-rate capacity of electrical interconnects from the aspect ratio of the system architecture. *Journal of Parallel and Distributed Computing*, 41(1):42–52, February 1997. ISSN 0743-7315. doi: 10.1006/jpdc.1996.1285.

[9] Dajian Liu, Hongnan Xu, Ying Tan, Yaocheng Shi, and Daoxin Dai. Silicon photonic filters. *Microwave and Optical Technology Letters*, 63(9):2252–2268, 2021. ISSN 1098-2760. doi: 10/gg6sj8.

[10] Elisabet A. Rank, Ryan Sentosa, Danielle J. Harper, Matthias Salas, Anna Gaugutz, Dana Seyringer, Stefan Nevlacsil, Alejandro Maese-Novo, Moritz Eggeling, Paul Muellner, Rainer Hainberger, Martin Sagmeister, Jochen Kraft, Rainer A. Leitgeb, and Wolfgang Drexler. Toward optical coherence tomography on a chip: in vivo three-dimensional human retinal imaging using photonic integrated circuit-based arrayed waveguide gratings. *Light: Science and Applications*, 10(1), January 2021. ISSN 2047-7538. doi: 10.1038/s41377-020-00450-0.

[11] NVIDIA Corporation. Nvidia and tsmc collaboration on photonics-enabled ai accelerators, 2025. Press Release. Available at: https://investor.nvidia.com/news/press-release-details/2025/NVIDIA-Announces-Spectrum-X-Photonics-Co-Packaged-Optics-Networking-Switches-to-Scale-AI-Factories-to-Millions-of-GPUs/default.aspx.

[12] Qixiang Cheng, Meisam Bahadori, Madeleine Glick, Sébastien Rumley, and Keren Bergman. Recent advances in optical technologies for data centers: a review. *Optica*, 5(11):1354, October 2018. ISSN 2334-2536. doi: 10.1364/optica.5.001354.

[13] Qingzhong Deng, Ahmed H. El-Saeed, Alaa Elshazly, Guy Lepage, Chiara Marchese, Hakim Kobbi, Rafal Magdziak, Jeroen De Coster, Neha Singh, Marko Ersek Filipcic, Kristof Croes, Dimitrios Velenis, Maumita Chakrabarti, Peter De Heyn, Peter Verheyen, Philippe Absil, Filippo Ferraro, Yoojin Ban, and Joris Van Campenhout. 32x100 GHz WDM filter based on ultra-compact silicon rings with a high thermal tuning efficiency of 5.85 mw/pi. In *Optical Fiber Communication Conference (OFC)*, page W1A, 2024.

[14] Qingzhong Deng, Ahmed H. El-Saeed, Alaa Elshazly, Guy Lepage, Chiara Marchese, Pieter Neutens, Hakim Kobbi, Rafal Magdziak, Jeroen De Coster, Javad Rahimi Vaskasi, Minkyu Kim, Yeyu Tong, Neha Singh, Marko Ersek Filipcic, Pol Van Dorpe, Kristof Croes, Maumita Chakrabarti, Dimitrios Velenis, Peter De Heyn, Peter Verheyen, Philippe Absil, Filippo Ferraro, Yoojin Ban, and Joris Van Campenhout. Low-loss and low-power silicon ring based WDM 32×100 GHz filter enabled by a novel bend design. *Laser & Photonics Reviews*, November 2024. ISSN 1863-8899. doi: 10.1002/lpor.202401357.

[15] Yikai Su, Yong Zhang, Ciyuan Qiu, Xuhan Guo, and Lu Sun. Silicon Photonic Platform for Passive Waveguide Devices: Materials, Fabrication, and Applications. *Advanced Materials Technologies*, 5(8):1901153, 2020. ISSN 2365-709X. doi: 10/gh3525. ZSCC: 0000015 _eprint: tex.ids= su_silicon_2020-1.

[16] Tzu-Hsiang Yen and Yung-Jr Hung. Fabrication-Tolerant CWDM (de)Multiplexer Based on Cascaded Mach–Zehnder Interferometers on Silicon-on-Insulator. *Journal of Lightwave Technology*, 39(1):146–153, January 2021. ISSN 1558-2213. doi: 10.1109/JLT.2020.3026314. Conference Name: Journal of Lightwave Technology.

[17] W. Bogaerts, P. De Heyn, T. Van Vaerenbergh, K. De Vos, S. Kumar Selvaraja, T. Claes, P. Dumon, P. Bienstman, D. Van Thourhout, and R. Baets. Silicon microring resonators. *Laser & Photonics Reviews*, 6(1):47–73, 2012. ISSN 1863-8899. doi: 10/cr3dtz. ZSCC: 0001902 _eprint:.

[18] S. Pathak, P. Dumon, D. Van Thourhout, and W. Bogaerts. Comparison of AWGs and echelle gratings for wavelength division multiplexing on silicon-on-insulator. *IEEE Photonics Journal*, 6(5):1–9, October 2014. ISSN 1943-0655. doi: 10.1109/jphot.2014.2361658.

[19] Yu Zheng, Yunming Li, Yixiong Yan, Pan Zhang, and Ji'an Duan. Compact low-loss low-crosstalk echelle grating demultiplexer on silicon-on-insulator for CWDM. *Optik*, 249:168236, January 2022. ISSN 0030-4026. doi: 10.1016/j.ijleo.2021.168236.

[20] Laiwen Yu, Jingshu Guo, Hengtai Xiang, Guojiang Yang, Yuqi Zhao, Yuanrong Li, and Daoxin Dai. Ultra-compact and high-performance four-channel coarse wavelength-division (de)multiplexing filters based on cascaded mach-zehnder interferometers with bezier-shape directional couplers. *Optics Express*, 32(5):7774, February 2024. ISSN 1094-4087. doi: 10.1364/oe.509936.

[21] Qiyuan Yi, Shuang Zheng, Zhiwei Yan, Guanglian Cheng, Fanglu Xu, Qiyuan Li, and Li Shen. Silicon photonic flat-top WDM (de)multiplexer based on cascaded mach-zehnder interferometers for the 2 μm wavelength band. *Optics Express*, 30(15):28232, July 2022. ISSN 1094-4087. doi: 10.1364/oe.467473.

[22] Zhizun Zhao, Zhen Li, Jiaqi Niu, Gaolu Zhang, Hongliang Chen, Xin Fu, and Lin Yang. Eight-Channel LAN WDM (De)Multiplexer Based on Cascaded Mach–Zehnder Interferometer on SOI for 400GbE. *Photonics*, 9(4):252, April 2022. ISSN 2304-6732. doi: 10.3390/photonics9040252. URL https://www.mdpi.com/2304-6732/9/4/252.

[23] Ahmed Bayoumi, Mehmet Oktay, Alaa Elshazly, Hakim Kobbi, Rafal Magdziak, Guy Lepage, Chiara Marchese, Javad Rahimi Vaskasi, Swetanshu Bipul, Dieter Bode, Dimitrios Velenis, Maumita Chakrabarti, Peter Verheyen, Philippe Absil, Filippo Ferraro, Yoojin Ban, Joris Van Campenhout, Wim Bogaerts, and Qingzhong Deng. Enhanced operation range of silicon MZI filters using a broadband bent directional coupler. *IEEE Photonics Technology Letters*, 37(9):500–503, May 2025. ISSN 1941-0174. doi: 10.1109/lpt.2025.3553059.

[24] Zeqin Lu, Han Yun, Yun Wang, Zhitian Chen, Fan Zhang, Nicolas A. F. Jaeger, and Lukas Chrostowski. Broadband silicon photonic directional coupler using asymmetric-waveguide based phase control. *Optics Express*, 23(3):3795–3808, February 2015. ISSN 1094-4087. doi: 10/gmf37j.

[25] Ahmed H. El-Saeed, Alaa Elshazly, Hakim Kobbi, Rafal Magdziak, Guy Lepage, Chiara Marchese, Javad Rahimi Vaskasi, Swetanshu Bipul, Dieter Bode, Marko Ersek Filipcic, Dimitrios Velenis, Maumita Chakrabarti, Peter De Heyn, Peter Verheyen, Philippe Absil, Filippo Ferraro, Yoojin Ban, Joris Van Campenhout, Wim Bogaerts, and Qingzhong Deng. Low-loss silicon directional coupler with arbitrary coupling ratios for broadband wavelength operation based on bent waveguides. *Journal of Lightwave Technology*, 42 (17):6011–6018, September 2024. ISSN 1558-2213. doi: 10.1109/jlt.2024.3407339.

[26] Ahmed Bayoumi, Ahmed Khalil, Pol Van Dorpe, Maumita Chakrabarti, Dimitrios Velenis, Philippe Absil, Filippo Ferraro, Yoojin Ban, Joris Van Campenhout, Wim Bogaerts, and Qingzhong Deng. Broadband and ultra-compact adiabatic coupler based on linearly tapered silicon waveguides, 2025. URL https://arxiv.org/abs/2504.20512.

[27] Ahmed H. El-Saeed, Alaa Elshazly, Hakim Kobbi, Rafal Magdziak, Guy Lepage, Chiara Marchese, Swetanshu Bipul, Dieter Bode, Marko E. Filipcic, Dimitrios Velenis, Maumita Chakrabarti, Peter De Heyn, Peter Verheyen, Philippe Absil, Filippo Ferraro, Yoojin Ban, Joris Van Campenhout, Wim Bogaerts, and Qingzhong Deng. Wavelength-insensitive and lossless 50:50 directional coupler based on silicon bent waveguides. In *2024 IEEE Silicon Photonics Conference*, 2024.

[28] Ahmed H. El-Saeed, Alaa Elshazly, Hakim Kobbi, Rafal Magdziak, Guy Lepage, Chiara Marchese, Swetanshu Bipul, Dieter Bode, Marko Ersek Filipcic, Dimitrios Velenis, Maumita Chakrabarti, Peter De Heyn, Peter Verheyen, Philippe Absil, Filippo Ferraro, Yoojin Ban, Joris Van Campenhout, Wim Bogaerts, and Qingzhong Deng. Wavelength-insensitive and lossless 50:50 directional coupler based on silicon bent waveguides. In *2024 IEEE Silicon Photonics Conference (SiPhotonics)*. IEEE, April 2024. doi: 10.1109/siphotonics60897.2024.10543882.

[29] J. S. Cook. Tapered velocity couplers. *Bell System Technical Journal*, 34(4): 807–822, July 1955. ISSN 0005-8580. doi: 10.1002/j.1538-7305.1955.tb03777.x.

[30] T.A. Ramadan, R. Scarmozzino, and R.M. Osgood. Adiabatic couplers: design rules and optimization. *Journal of Lightwave Technology*, 16(2):277–283, 1998. ISSN 0733-8724. doi: 10.1109/50.661021.

[31] Wei-Ping Huang. Coupled-mode theory for optical waveguides: an overview. *Journal of the Optical Society of America A*, 11(3):963, March 1994. doi: 10.1364/josaa.11.000963.

[32] L.B. Soldano and E.C.M. Pennings. Optical multi-mode interference devices based on self-imaging: principles and applications. *Journal of Lightwave Technology*, 13(4):615–627, April 1995. ISSN 0733-8724. doi: 10.1109/50.372474.

[33] Liang Cao, Ali Elshaari, Abdelsalam Aboketaf, and Stefan Preble. Adiabatic couplers in SOI waveguides. *Conference on Lasers and Electro-Optics 2010*, page CThAA2, 2010. doi: 10.1364/CLEO.2010.CThAA2.

[34] Hung-Ching Chung, Chih-Hsien Chen, Guan-Xun Lu, Yung-Jr Hung, and Shuo-Yen Tseng. Adiabaticity Engineered Silicon Polarization Independent 3-dB Coupler for the O-Band. *IEEE Photonics Journal*, 15(3):1–6, June 2023. doi: 10.1109/JPHOT.2023.3271320.

[35] Keun Il Kim, Dong Kim, Vinh Nguyen, Sangyoon Han, and Tae Seok. High-Performance and Compact Silicon Photonic 3-dB Adiabatic Coupler Based on Shortest Mode Transformer Method. *IEEE Photonics Journal*, August 2021. doi: 10.1109/JPHOT.2021.3107852.

English Summary

1 Introduction

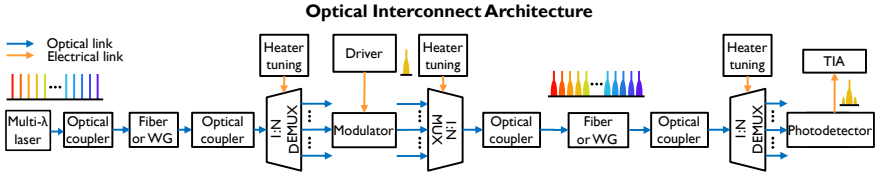

Figure 1: Schematic of an optical link showing the key components: multi-wavelength laser source, demultiplexing filter for channel separation, a modulator for encoding data onto the optical signal, a multiplexer for combining multiple wavelength channels, and receiver with photodetector for signal conversion. The WDM filters enable parallel transmission of multiple data streams, which is the primary focus of this thesis.

The exponential growth in global data traffic, driven by high-performance computing, cloud data centers, and artificial intelligence applications, has created an unprecedented demand for high-bandwidth, energy-efficient communication systems [1, 2]. Optical interconnects have emerged as a crucial technology for meeting these demands, offering advantages such as higher data rates, lower power consumption, and reduced signal attenuation compared to electronic systems [3, 4]. Within this landscape, wavelength division multiplexing (WDM) has become a cornerstone technology for scaling bandwidth by transmitting multiple data channels simultaneously over distinct optical wavelengths, effectively multiplying the aggregate bandwidth of a single optical link [5].

Silicon photonics has established itself as a promising platform for implementing WDM systems, leveraging the maturity of CMOS fabrication processes to enable high-yield, scalable, and cost-efficient photonic integrated circuits (PICs) [6, 7]. The high refractive index contrast between silicon and silica facilitates strong optical mode confinement, allowing for compact device geometries and efficient light manipulation [8, 9]. Furthermore, the compatibility with CMOS technology enables the co-integration of optical and electronic components on the same chip, supporting energy-efficient systems for data communications and sensing applications [10, 11].

At the core of WDM systems are wavelength-selective filters, which perform

the essential tasks of combining (multiplexing) and separating (demultiplexing) distinct wavelength channels [9, 12]. These filters must satisfy stringent requirements to ensure high spectral integrity including low insertion loss, and minimal crosstalk between channels [13, 14]. However, achieving high-performance WDM filters in silicon photonics is challenging due to the platform's inherent dispersion (wavelength-dependent behavior) and fabrication variabilities, which can significantly impact device yield and performance [15].

In an optical link, as illustrated in Fig. 1, WDM filters are pivotal for enabling parallel data transmission. The link begins with a multi-wavelength laser source providing stable optical carriers. These carriers are routed to a demultiplexing filter (DEMUX) to separate the optical signals into distinct channels, which are then modulated using electro-optic modulators. The modulated channels are recombined via a multiplexing filter (MUX) to form a high-capacity signal. At the receiver, the signal is demultiplexed, detected by photodetectors, and converted into electrical signals, which are subsequently amplified and processed by a transimpedance amplifier (TIA). Thermal tuning ensures precise wavelength alignment and stability. These wavelength-selective components are critical for increasing the aggregate bandwidth of optical communication systems, as they allow multiple data streams to share the same physical waveguide, significantly enhancing the total data capacity of the link without requiring additional physical waveguides.

WDM systems can be broadly categorized into two types based on channel spacing:

- **Dense Wavelength Division Multiplexing (DWDM):** These systems feature narrow channel spacing (typically sub-nanometer), allowing for a significantly higher number of channels within the same spectral bandwidth. DWDM systems require advanced filter architectures with high spectral selectivity, low crosstalk, and precise wavelength alignment.
- **Coarse Wavelength Division Multiplexing (CWDM):** These systems have wider channel spacing (typically $\approx$ 20 nm) and support fewer channels compared to DWDM systems. The wider spacing reduces component complexity, making CWDM systems more cost-effective and less sensitive to fabrication tolerances.

Various architectures for WDM filters in silicon photonics aim to address challenges related to footprint, channel count, channel isolation, insertion loss, and fabrication tolerance. Prominent types include Mach-Zehnder Interferometers (MZIs) [16], Microring Resonators (MRRs) [17], Arrayed Waveguide Gratings (AWGs) [18], and Echelle Diffraction Gratings (EDGs) [19]. However, achieving a WDM architecture that simultaneously satisfies all these specifications remains a significant challenge [5, 9].

This thesis addresses these challenges by developing robust, broadband optical components and WDM architectures for both DWDM and CWDM systems in

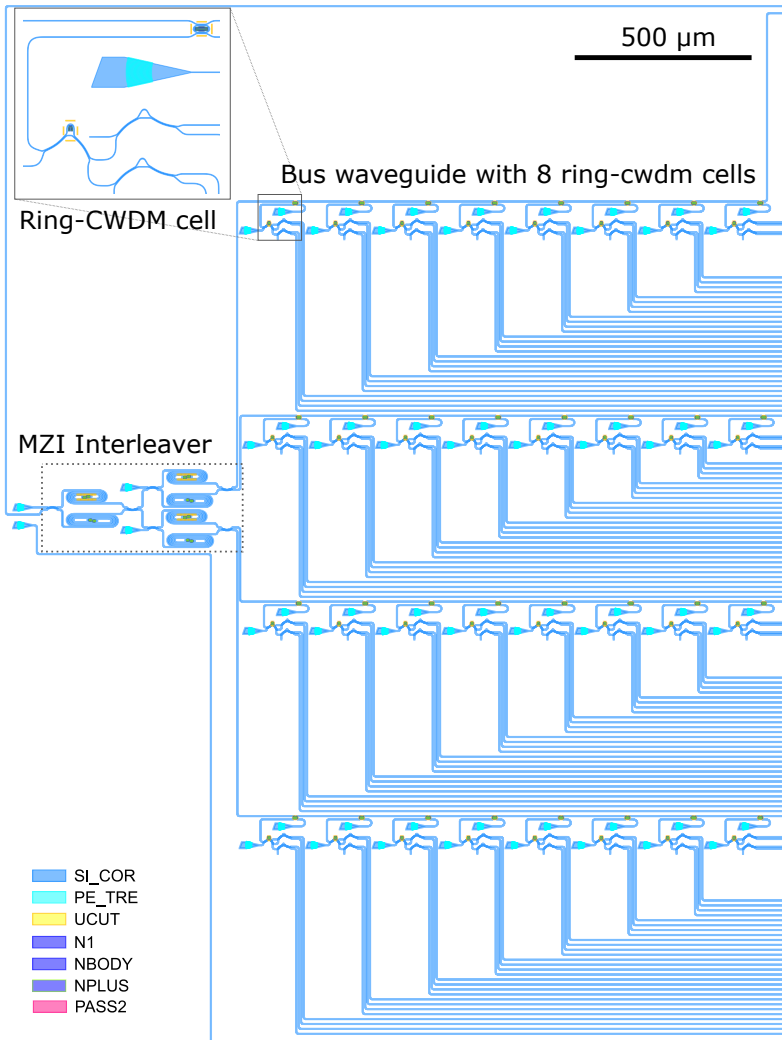

Figure 2: Schematic of the proposed DWDM-128×100 GHz system. The architecture integrates a 4-channel MZI stage, microring resonators (MRRs), and CWDM-4 filters. The MZI stage divides the input into four groups, each routed to a bus waveguide with 8 staggered MRRs (32 in total). Each MRR drop port is cascaded with a CWDM-4 filter, enabling demultiplexing into 128 channels with 100 GHz spacing. The metal routing and the output gratings are not shown here. The inset shows a zoomed-in image for one of the ring-CWDM units.

silicon photonics. The focus is on MZI-based WDM architectures due to their high performance, scalability, ease of integration, and relatively compact footprint [20–23].

In an MZI, an optical splitter divides the input light into two paths (arms), while an optical combiner combines the light at the output, enabling interference-based wavelength filtering. Traditional MZI architectures often rely on straight directional couplers (DCs) as beam splitters and combiners. However, straight DCs suffer from wavelength-dependent coupling due to dispersion in silicon photonics platform. For example, a silicon straight DC designed for 0.5:0.5 splitting can exhibit coupling variations exceeding 0.45 over an 80 nm wavelength range, limiting their operational bandwidth and compromising signal integrity, particularly in broadband WDM applications [9, 24].

This thesis addresses these limitations by optimizing the fundamental building blocks of WDM systems, introducing broadband optical splitters and combiners capable of achieving broadband operation at arbitrary coupling ratios. These components serve as critical elements for advanced WDM filter architectures, enabling significant improvements in operational wavelength range, insertion loss, and channel isolation [23, 25, 26].

This work eventually contributes to the realization of highly dense WDM systems, including a DWDM system with 128 channels and 100 GHz channel spacing (DWDM-128$\times$100 GHz). The schematic of a taped-out DWDM-128$\times$100 GHz system is shown in Fig. 2. The DWDM-128$\times$100 GHz system combines an MZI interleaver, MRRs, and MZI-based CWDM systems to achieve high-density wavelength demultiplexing. The interleaver splits the input spectrum into 4 groups of 32 channels, each spaced by 400 GHz, and routes them to 4 bus waveguides. Along each bus waveguide, 8 staggered MRRs are used to extract 4 channels per ring. These extracted signals are further demultiplexed by CWDM-4 systems. This hierarchical architecture enables the demultiplexing of 128 channels, each spaced by 100 GHz, into 128 individual output waveguides.

2 Broadband Bent Directional Couplers

In order to enhance the performance of MZI-based WDM systems and address the broadband limitations of traditional straight DCs (Fig. 3 (a)), this thesis introduces broadband bent DCs (Fig. 3 (b, c, d)) leveraging insights from coupled mode theory (CMT) [27, 28]. The CMT analysis reveals that bent DCs offer enhanced design flexibility, enabling wavelength-insensitive coupling by mitigating dispersion effects responsible for wavelength-dependent coupling variations.

The key to achieving broadband coupling lies in analyzing the derivative of the coupled power with respect to wavelength. Two critical parameters influence the coupling behavior: the group index difference (Δn_g) and the derivative of the effective index with respect to wavelength ($d\Delta n_{eff}/d\lambda$). These parameters govern the dispersion characteristics of the coupler.

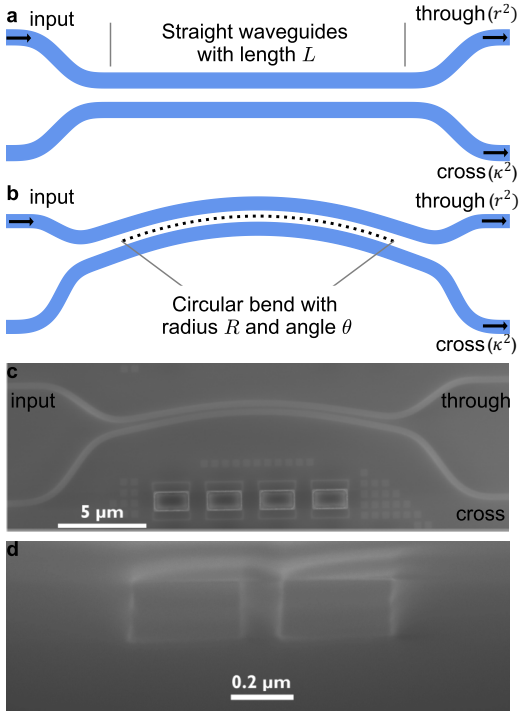

Figure 3: Schematic of the straight DC (a), broadband bent DC (b), and SEM images of the fabricated bent DC (c, d), fabricated using IMEC's iSiPP300 platform.

In bent DCs, these two parameters can be independently tuned, providing precise control over the coupling characteristics. This tunability allows the dispersion terms to effectively cancel each other, significantly reducing wavelength-dependent coupling variations. Unlike straight DCs, which inherently lack this flexibility, bent DCs exploit their unique geometry to achieve broadband operation, making them suitable for WDM systems.

By optimizing key design parameters such as bending radius and coupling angle (Fig. 3 (b)), the wavelength dependence of bent DCs was significantly reduced. Overall, the demonstrated bent DCs meet the essential requirements of broadband operation, support for arbitrary coupling ratio, low insertion loss, compact footprint, and high fabrication tolerance, making them suitable for WDM filters. The research achievements in bent DC development include:

- **Reduced Coupling Variation:** Achieved minimal coupling variation of only 0.051 over an 80 nm wavelength range for 0.5:0.5 bent DCs, representing a 7.67× improvement compared to conventional straight DCs (Fig. 4 (a, b)).
- **Low Insertion Loss:** Demonstrated the lowest coupling loss (0.006 ±

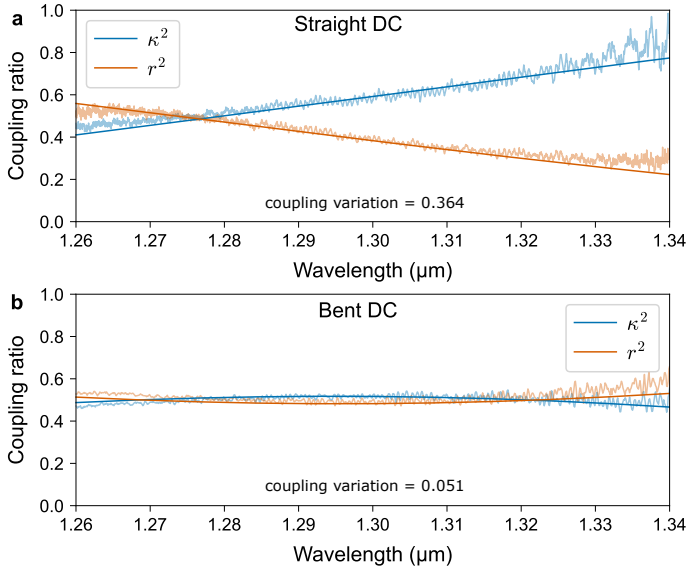

Figure 4: Coupling ratio comparison between straight DCs (a) and bent DCs (b) across 80 nm wavelength range, demonstrating the significantly improved wavelength insensitivity of the bent DC design.

0.004 dB) among all reported silicon 2×2 splitters, as limited by the measurement precision, achieved by incorporating novel low-loss bends that ensure continuous curvature and curvature derivative at all connections [14].

- **Compact Footprint:** Realized these improvements with a compact device length of just 27.5 μm, maintaining a small footprint critical for dense integration.
- **Model for Arbitrary Ratios:** Developed a model for achieving broadband coupling at arbitrary ratios by tuning the bending radius and coupling angle.
- **Wafer-Scale Robustness:** Wafer-scale measurements across 63 dies on a 300 mm wafer, confirming robust performance with a maximum coupling variation value of 0.112 and a corresponding average cross coupling deviation of 0.007 at the extreme edge of the wafer over 80 nm wavelength range (Fig. 5), demonstrating suitability for mass production.
- **Platform Compatibility:** Different designs are demonstrated that are compatible with both 200 mm and 300 mm fabrication platforms, enhancing their practical utility and commercial viability.

These advancements establish bent DCs as a robust solution for broadband WDM systems, providing a robust solution for broadband operation that directly translates

to higher extinction ratios in MZI-based WDM filters and ultimately enables the high-performance DWDM and CWDM systems described in later chapters.

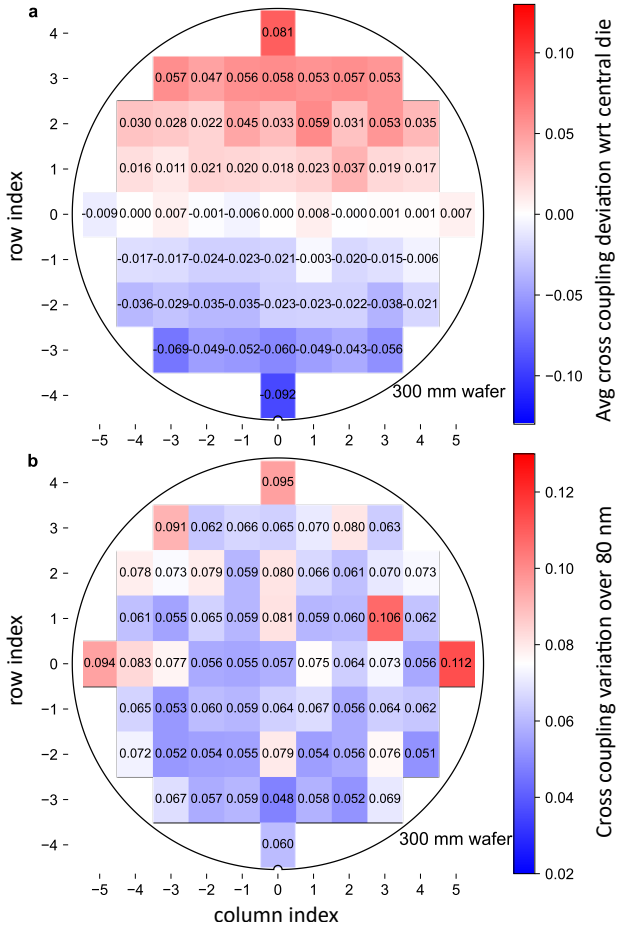

Figure 5: Average cross coupling deviation with respect to the central die (a) and cross coupling variation (b) over 80 nm bandwidth for the proposed 0.5:0.5 bent DC splitter over the 300 mm wafer, covering all 63 dies.

3 Broadband Adiabatic Couplers

While bent DCs offer reduced coupling variation compared to straight DCs, their coupling variation is not completely optimal. To further enhance the performance, this thesis numerically introduces optimized adiabatic couplers (Fig. 6) designed to minimize coupling variation over a broad wavelength range based on a novel

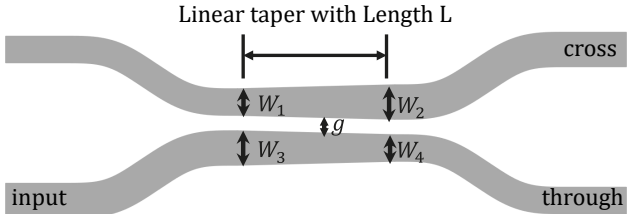

Figure 6: Schematic of the proposed adiabatic coupler showing the design parameters. The design is not to scale and is for illustration purposes.

design approach.

Adiabatic couplers operate on a fundamentally different principle compared to conventional DCs [29, 30]. In symmetric straight DCs, both even and odd supermodes are excited due to structural symmetry, resulting in a sinusoidal and wavelength-dependent coupling response [31, 32]. In contrast, adiabatic couplers are designed such that only a single mode is predominantly excited (Fig. 7), enabling broadband and robust power transfer [33, 34]. They leverage gradual changes in waveguide geometry to ensure the optical mode evolves smoothly from one waveguide to the other, minimizing scattering and excess loss [26, 35].

This thesis presents a novel way of designing adiabatic couplers (Fig. 6), based on a minmax optimization approach to minimize coupling variation across a target wavelength range:

$$\min_{\Delta W, L} \left(\max_{\lambda \in [\lambda_1, \lambda_2]} |P_c(\lambda) - P_{c,\text{desired}}| \right)$$

where ΔW represents the waveguide width difference at the taper start, L is the taper length, and $P_c(\lambda)$ is the the cross-coupled power, the parameters are depicted in Fig. 6. This approach yields an optimized solution that minimizes the maximum deviation from the desired coupling ratio across the entire operational wavelength band (Fig. 8), and can be used to aim for arbitrary coupling ratios by adjusting the taper output waveguides width accordingly. Based on this approach, both broadband coupling and ultra compact taper lengths are achieved.

The research achievements in adiabatic coupler development include:

- **Low Coupling Variation:** The optimized 3-dB adiabatic coupler demonstrates a coupling variation of only 0.02 over a 120 nm wavelength range covering the O-band, representing a 16.6× reduction compared to traditional straight DCs (Fig. 9). Low coupling variation is critical for maintaining high channel isolation in WDM systems.

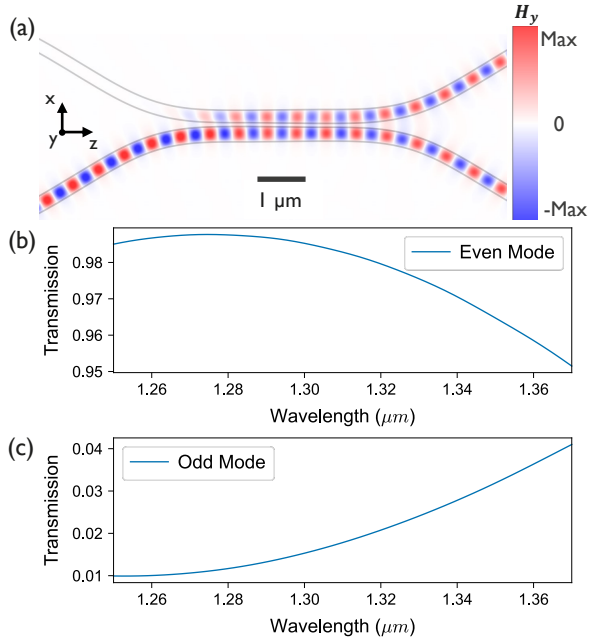

Figure 7: H_y field plot of the proposed 3-dB splitter at λ=1.31 μm (a). TE even (b) and odd (c) mode power expansions at the middle of the coupler showing most of the power (98.3% at λ=1.31 μm) existing in the TE even mode, proving the adiabatic nature of the splitter.

- **Ultra-Compact Design:** Adiabatic couplers are usually bulky that can span hundreds of micrometers. However, the proposed adiabatic coupler achieves an ultra-compact taper length of 1.44 μm, which is the shortest reported to date, to my best knowledge.
- **Arbitrary Coupling Ratios:** Broadband coupling is demonstrated for arbitrary coupling ratios based on the minmax optimization approach.
- **Low Insertion Loss** A low insertion loss of $\leq$ 0.03 dB is demonstrated thanks to the use of low-loss bends.

The developed adiabatic couplers represent a considerable advancement over existing designs, offering high performance in terms of bandwidth, compactness, and insertion loss. Future WDM design iterations can benefit from such a design to enhance the system performance.

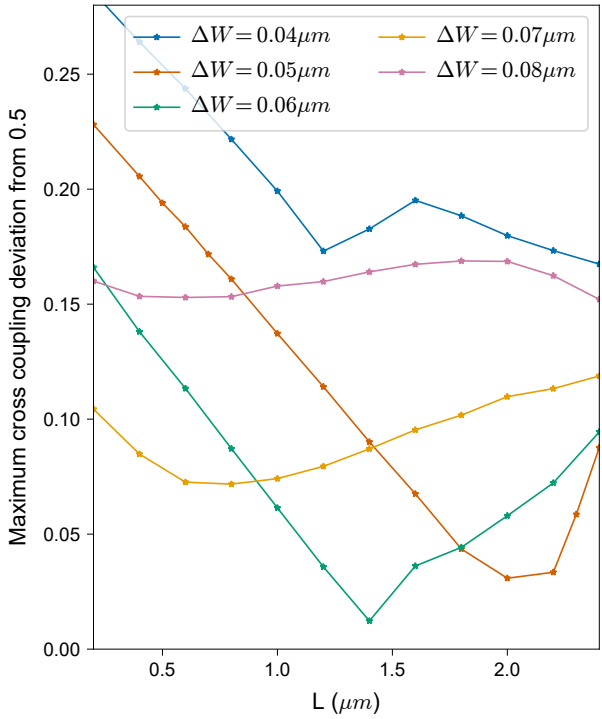

Figure 8: Maximum cross-coupling deviation from 0.5 *over a* $120\,\mathrm{nm}$ *wavelength range as a function of the taper length (L) and the initial waveguide width difference (*ΔW*), based on 3D finite-difference time-domain simulations.*

4 Dense Wavelength Division Multiplexing Systems

The implementation of broadband bent DCs developed in this work has led to substantial enhancements in DWDM system performance, particularly in terms of channel isolation and operational wavelength range [23, 25].

MZI-based interleavers play a pivotal role in this work, serving as key components in the DWDM-128$\times$ 100 GHz system, as illustrated in Fig. 10. Therefore, DWDM-2$\times$100 GHz and DWDM-4$\times$100 GHz systems using broadband bent DCs are demonstrated.

The thesis presents the design, implementation, and characterization of several MZI-based DWDM systems. The research achievements in DWDM systems include:

- **Extended Operational Bandwidth:** The DWDM-2$\times$100 GHz interleaver based on broadband bent DCs demonstrated at least a 2.7$\times$ increase in operational wavelength range (up to 100 nm) while maintaining high extinction

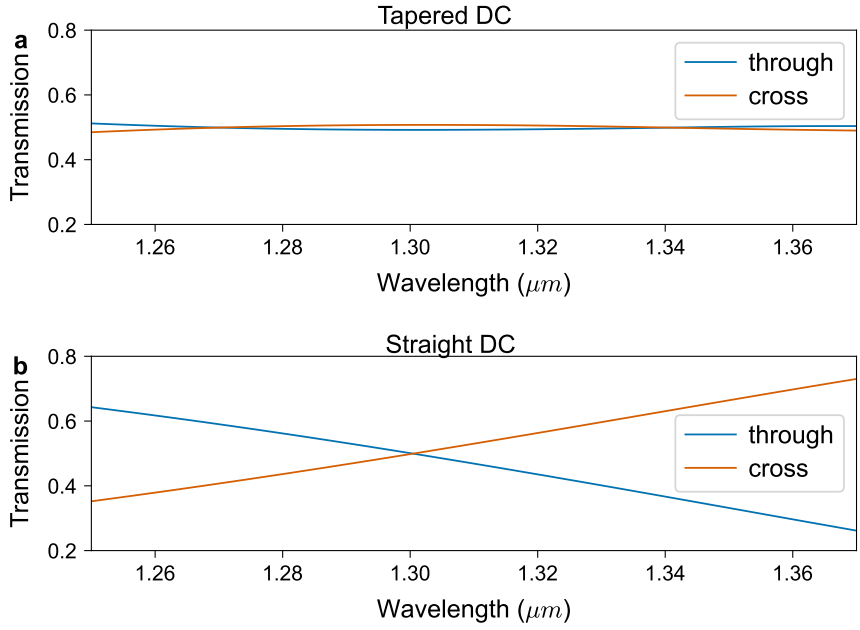

Figure 9: 3-dB splitter optical transmission using the proposed adiabatic coupler (a) as compared to the traditional straight coupler (b) over 120 nm wavelength range covering the O-band. Significant reduction of 16.6× in the coupling variation is achieved using the proposed design compared to the straight DC counterpart.

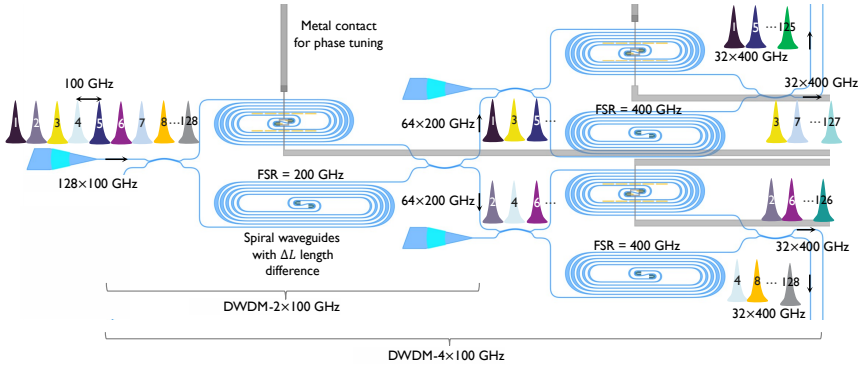

Figure 10: Schematic of the interleaver used in WDM-128 × 100 GHz system based on broadband bent DCs. The first MZI stage interleaves 128 channels into two outputs of 64 channels. The second stage, with double the FSR, further interleaves these into four waveguides, each with 32 channels.

ratios (ER $\geq$ 18.4 dB) compared to conventional designs based on straight

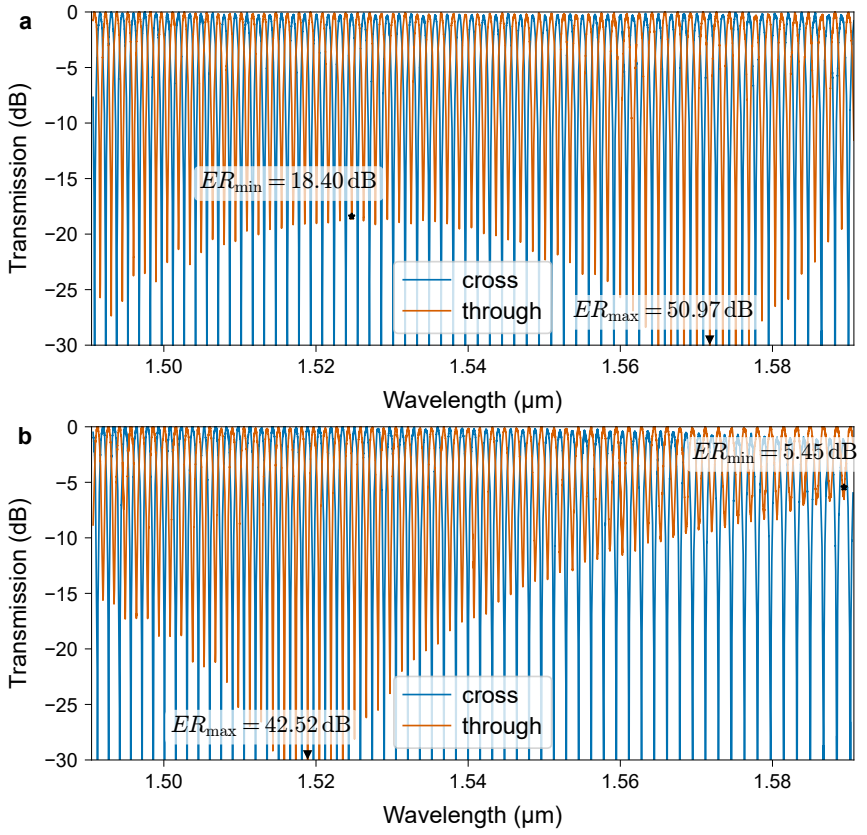

Figure 11: The proposed DWDM-2 ×100 GHz interleaver spectrum based on bent DCs (a), and the traditional DWDM-2 spectrum based on straight DCs (b). Minimum and maximum ER values are marked. At least 2.7× *improvement in the ER wavelength operational range for the proposed interleaver is shown.*

DCs (limited to 36.7 nm), as shown in Fig. 11. Similar improvements were observed in the DWDM-4×100 GHz system through transfer matrix calculations, and the DWDM-16×800 GHz system showed substantially improved operation across the target wavelength range, as illustrated in Fig. 12.

- **Higher Channel Isolation:** The minimum extinction ratio of the DWDM-2×100 GHz interleaver was improved from 4.2-6.1 dB in traditional designs to 14.3-18.4 dB with the proposed architecture. Transfer matrix calculations for the DWDM-4×100 GHz system showed channel isolation improvement from 4.65 dB to 16.77 dB, while the DWDM-16×800 GHz system demonstrated enhanced isolation from 5.42 dB to 17.18 dB (Fig. 12). These improvements significantly enhance signal integrity and reduce crosstalk over a wide bandwidth, proving the effectiveness of the proposed architecture for

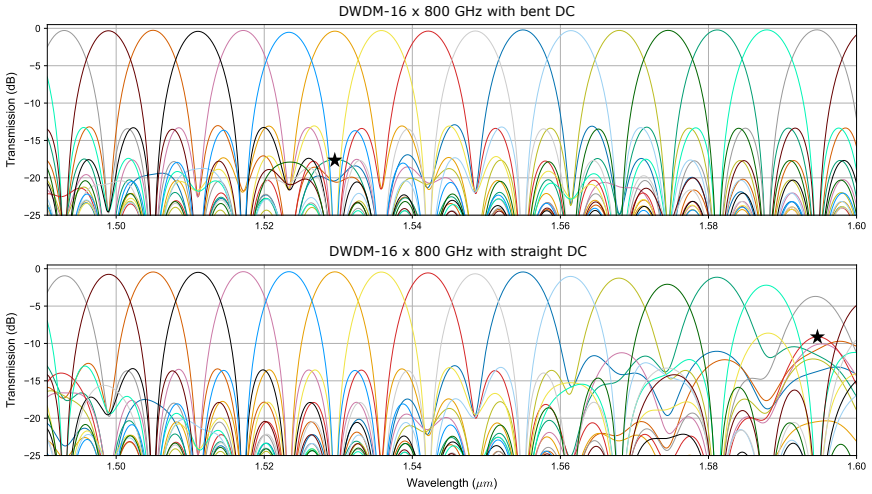

Figure 12: DWDM-16 ×800 GHz system spectra simulated using the transfer matrix method based on (a) bent DCs and (b) straight DCs. The bent DC-based system shows significant improvements in channel isolation and insertion loss.

scalable WDM systems.

- **Reduced Insertion Loss:** The average insertion loss was significantly reduced across all DWDM systems when using bent DCs compared to straight DCs. In the DWDM-4×100 GHz system, insertion loss decreased from 0.77 dB to 0.18 dB, while in the DWDM-16×800 GHz system, it improved from 1.02 dB to 0.30 dB as clearly demonstrated in Fig. 12.
- **Wafer-Scale Robustness:** Extensive measurements across 63 dies on a 300 mm wafer confirmed consistent performance with minimal variation, demonstrating the design's suitability for mass production.

5 Coarse Wavelength Division Multiplexing Systems

Complementing the work on DWDM systems, this thesis also focuses on the development of robust CWDM systems utilizing the broadband bent DCs. The thesis presents the design and implementation of CWDM-2×3.2 THz and CWDM-4×3.2 THz systems. CWDM systems are of a paramount importance in scaling the channel count of DWDM systems. In particular, for the proposed DWDM-128×100 GHz, a CWDM-4×3.2 THz is used to scale up the number of channels by a factor of four, as shown in Fig. 13.

These systems are designed with an emphasis on minimizing phase errors through innovative architectural approaches, by employing half-ring configurations and

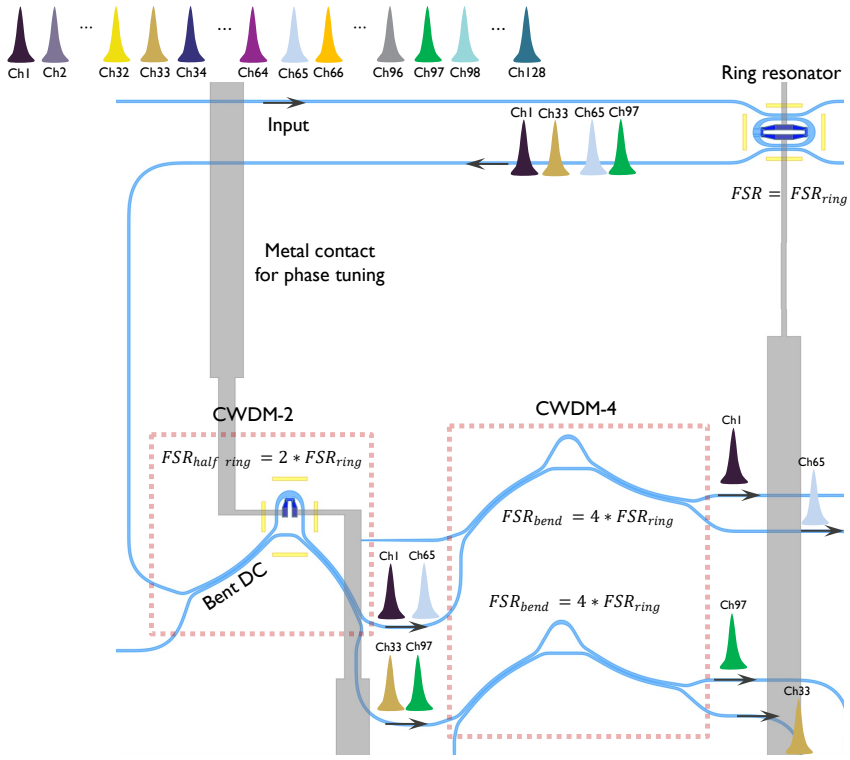

Figure 13: Schematic of the cascaded ring-CWDM architecture enabling DWDM-128 × 100 GHz. The drop port of a ring resonator with $\mathrm{FSR} = 3.2\,\mathrm{THz}$ *is connected to a CWDM-2 and subsequently a CWDM-4, enabling a fourfold increase in channel count.*

whispering-gallery-mode (WGM) bends that minimize common arm lengths. This approach addresses one of the significant challenges in silicon photonic WDM systems, namely, wavelength drift due to the phase error from fabrication variabilities.

Key research achievements in CWDM system designs include:

- **Reduced Phase Errors:** Quantitatively demonstrated significant phase error reduction in CWDM filters using the half-ring configurations and whispering-gallery-mode bends. Measurements across 19 dies showed the standard deviation of phase errors decreased from 0.545 rad in conventional MZIs to 0.152 rad with half-ring configurations, and further down to just 0.040 rad with the 120° bend bends. This enables passive operation without thermal tuning, representing significant power reduction.
- **Channel Isolation Enhancement:** The CWDM-2×3.2 THz system based on bent DCs achieved extinction ratios of 16.5-18.8 dB compared to 10.9-11.7 dB for straight DC implementations, while the CWDM-2×6.4 THz

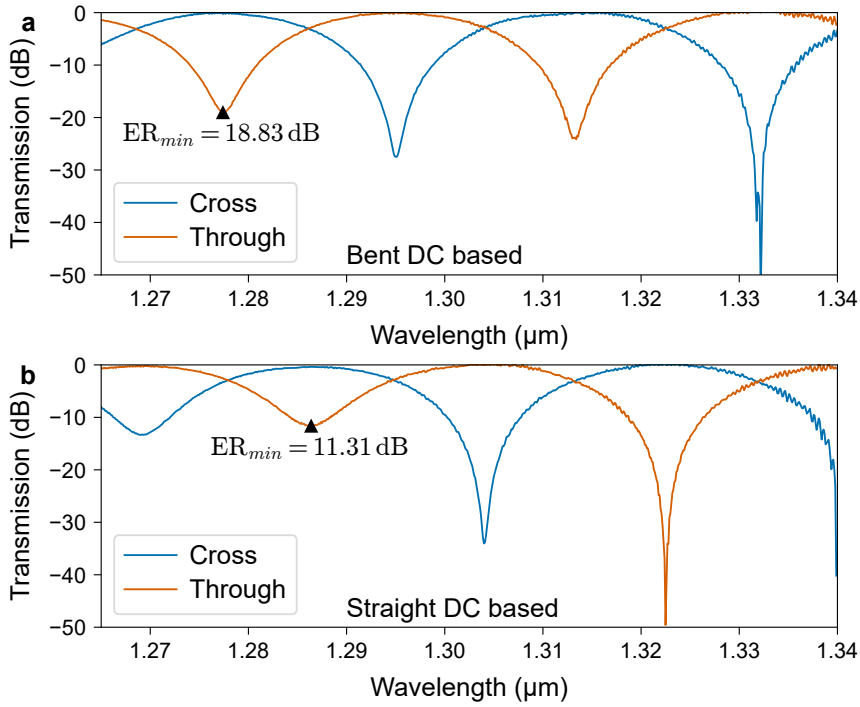

Figure 14: Measured spectra of the the CWDM-2 × 3.2 THz for broadband bent directional couplers (DCs) (a) and straight bent DCs (b).

showed an even more dramatic improvement from 6.6-8.1 dB to 16.4-18.3 dB.

- **High-Performance CWDM-4×3.2 THz:** Successfully demonstrated a CWDM-4 system essential for the DWDM-128×100 GHz architecture, achieving worst-case channel isolation of 25.9 dB across $>$ 12.8 THz bandwidth. Most notably, wafer-scale measurements across 54 dies confirmed consistent performance with a minimum channel isolation of 13.5 dB across a 100 GHz span around each channel center without requiring thermal tuning.

These CWDM systems represent a significant advancement in silicon photonic filter technology, enabling passive operation while maintaining high performance metrics. The combination of novel geometrical approaches with the broadband bent DCs developed earlier results in CWDM systems that outperform conventional designs in terms of extinction ratio, operational stability while working heater-free.

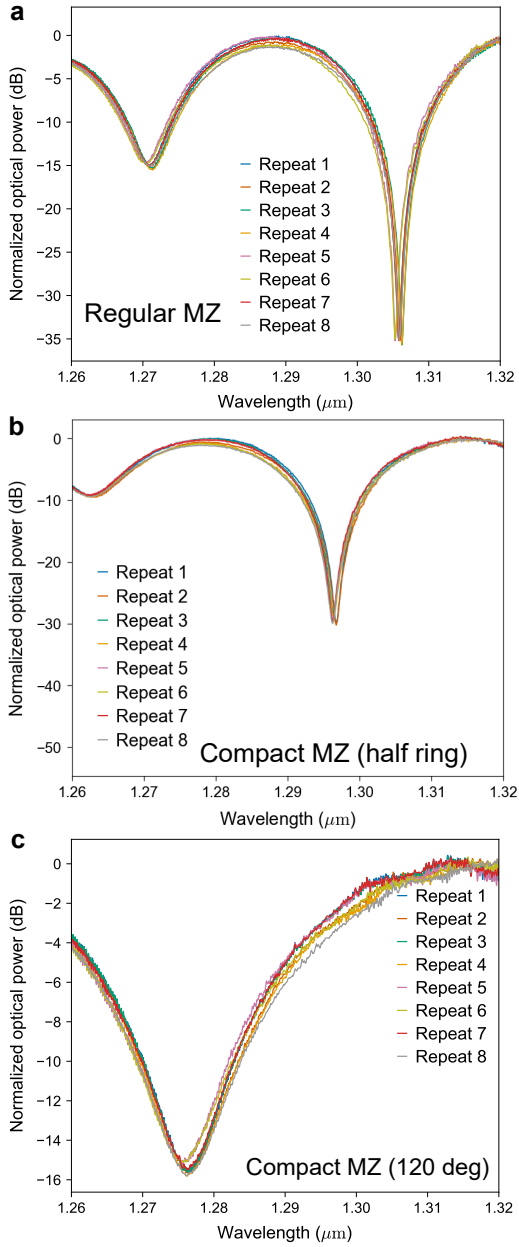

Figure 15: The cross power transmission for 8 identical traditional MZI next to each other on the reticle, showing the impact of phase errors on wavelength response.

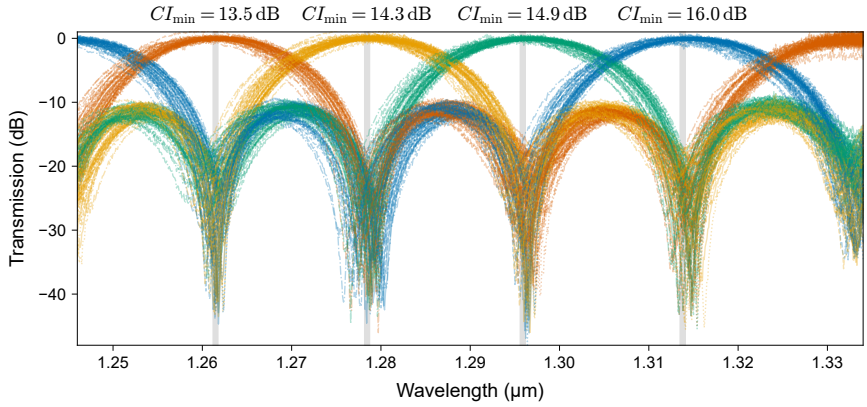

Figure 16: Optical spectrum for the CWDM-4 × 3.2 THz system based on broadband bent DCs over 54 dies, where each color represents a different channel. The measurements show the robustness of the design to be used in mass manufacturing.

6 Conclusions

This thesis advances silicon photonic WDM technology through three key innovations: (1) broadband bent and adiabatic directional couplers with record-low wavelength sensitivity and insertion loss; (2) DWDM systems with extended operational bandwidth and high extinction ratios; and (3) low-phase-error CWDM architectures operating reliably without thermal tuning. These contributions address critical challenges in optical bandwidth scaling, energy efficiency, and manufacturing robustness, enabling next-generation high-capacity optical interconnects.

Key contributions include:

1. **Broadband Bent Directional Couplers:** Achieved low coupling variation (0.051 over 80 nm, $7.67\times$ improvement) and minimal insertion loss (0.006 ± 0.004 dB), supported by a comprehensive analytical model for arbitrary coupling ratios.

2. **Ultra-Compact Adiabatic Couplers:** Developed couplers with minimal coupling variation (0.02 over 120 nm) and ultra-compact taper length (1.44 μm), orders of magnitude shorter than conventional designs.

3. **High-Performance DWDM Systems:** Demonstrated interleavers with $2.7\times$ wider operational bandwidth (100 nm) and extinction ratios ≥ 18.4 dB, with improved channel isolation and reduced insertion loss.

4. **Thermal Tuning-Free CWDM Systems:** Implemented CWDM systems with innovative phase error minimization techniques, achieving extinction ratio improvements from 6.6-8.1 dB to 16.4-18.3 dB.

5. **DWDM-**128×100 **GHz System:** Designed a high-density DWDM system integrating bent DCs, DWDM-4 interleavers, and CWDM-4 filters, currently under fabrication.

References

[1] Cisco. Cisco annual internet report (2018–2023). Technical report, Cisco Systems, 2020. https://www.cisco.com/c/en/us/solutions/executive-perspectives/annual-internet-report/index.html.

[2] NVIDIA Corporation. Nvidia spectrum-x photonics co-packaged optics networking switches to scale ai factories to millions of gpus. https://nvidianews.nvidia.com/news/nvidia-spectrum-x-co-packaged-optics-networking-switches-ai-factories/, 2025.

[3] D. Miller. Device requirements for optical interconnects to silicon chips. *Proceedings of the IEEE*, 97(7):1166–1185, July 2009. ISSN 1558-2256. doi: 10.1109/jproc.2009.2014298.

[4] Bahram Jalali and Sasan Fathpour. Silicon Photonics. *Journal of Lightwave Technology*, 24(12):4600–4615, 2006. ISSN 0277-786X. doi: 10.1016/B978-0-12-374171-4.00011-3. ISBN: 9780123741714.

[5] Nabarun Saha, Giuseppe Brunetti, Annarita di Toma, Mario Nicola Armenise, and Caterina Ciminelli. Silicon photonic filters: A pathway from basics to applications. *Advanced Photonics Research*, March 2024. ISSN 2699-9293. doi: 10.1002/adpr.202300343.

[6] S.K. Selvaraja, P. Jaenen, W. Bogaerts, D. Van Thourhout, P. Dumon, and R. Baets. Fabrication of photonic wire and crystal circuits in silicon-on-insulator using 193-nm optical lithography. *Journal of Lightwave Technology*, 27(18):4076–4083, September 2009. ISSN 1558-2213. doi: 10.1109/jlt.2009.2022282.

[7] F. J. Ferraro, P. De Heyn, M. Kim, N. Rajasekaran, M. Berciano, G. Muliuk, D. Bode, G. Lepage, S. Janssen, R. Magdziak, J. De Coster, H. Kobbi, S. Lardenois, N. Golshani, L. Shiramin, C. Marchese, S. Rajmohan, S. Nadarajan, N. Singh, S. Radhakrishnan, A. Tsiara, P. Xu, A. Karagoz, D. Yudistira, M. Martire, A. Shahar, M. Chakrabarti, D. Velenis, W. Guo, A. Miller, Kristof Croes, S. Balakrishnan, P. Verheyen, Y. Ban, J. Van Campenhout, and P. P. Absil. Imec silicon photonics platforms: performance overview and roadmap. In *Next-Generation Optical Communication: Components, Sub-Systems, and Systems XII*, volume 12429, pages 22–28. SPIE, March 2023. doi: 10.1117/12.2650579.

[8] D.A.B. Miller and H.M. Ozaktas. Limit to the bit-rate capacity of electrical interconnects from the aspect ratio of the system architecture. *Journal of Parallel and Distributed Computing*, 41(1):42–52, February 1997. ISSN 0743-7315. doi: 10.1006/jpdc.1996.1285.

[9] Dajian Liu, Hongnan Xu, Ying Tan, Yaocheng Shi, and Daoxin Dai. Silicon photonic filters. *Microwave and Optical Technology Letters*, 63(9):2252–2268, 2021. ISSN 1098-2760. doi: 10/gg6sj8.

[10] Elisabet A. Rank, Ryan Sentosa, Danielle J. Harper, Matthias Salas, Anna Gaugutz, Dana Seyringer, Stefan Nevlacsil, Alejandro Maese-Novo, Moritz Eggeling, Paul Muellner, Rainer Hainberger, Martin Sagmeister, Jochen Kraft, Rainer A. Leitgeb, and Wolfgang Drexler. Toward optical coherence tomography on a chip: in vivo three-dimensional human retinal imaging using photonic integrated circuit-based arrayed waveguide gratings. *Light: Science and Applications*, 10(1), January 2021. ISSN 2047-7538. doi: 10.1038/s41377-020-00450-0.

[11] NVIDIA Corporation. Nvidia and tsmc collaboration on photonics-enabled ai accelerators, 2025. Press Release. Available at: https://investor.nvidia.com/news/press-release-details/2025/NVIDIA-Announces-Spectrum-X-Photonics-Co-Packaged-Optics-Networking-Switches-to-Scale-AI-Factories-to-Millions-of-GPUs/default.aspx.

[12] Qixiang Cheng, Meisam Bahadori, Madeleine Glick, Sébastien Rumley, and Keren Bergman. Recent advances in optical technologies for data centers: a review. *Optica*, 5(11):1354, October 2018. ISSN 2334-2536. doi: 10.1364/optica.5.001354.

[13] Qingzhong Deng, Ahmed H. El-Saeed, Alaa Elshazly, Guy Lepage, Chiara Marchese, Hakim Kobbi, Rafal Magdziak, Jeroen De Coster, Neha Singh, Marko Ersek Filipcic, Kristof Croes, Dimitrios Velenis, Maumita Chakrabarti, Peter De Heyn, Peter Verheyen, Philippe Absil, Filippo Ferraro, Yoojin Ban, and Joris Van Campenhout. 32x100 GHz WDM filter based on ultra-compact silicon rings with a high thermal tuning efficiency of 5.85 mw/pi. In *Optical Fiber Communication Conference (OFC)*, page W1A, 2024.

[14] Qingzhong Deng, Ahmed H. El-Saeed, Alaa Elshazly, Guy Lepage, Chiara Marchese, Pieter Neutens, Hakim Kobbi, Rafal Magdziak, Jeroen De Coster, Javad Rahimi Vaskasi, Minkyu Kim, Yeyu Tong, Neha Singh, Marko Ersek Filipcic, Pol Van Dorpe, Kristof Croes, Maumita Chakrabarti, Dimitrios Velenis, Peter De Heyn, Peter Verheyen, Philippe Absil, Filippo Ferraro, Yoojin Ban, and Joris Van Campenhout. Low-loss and low-power silicon ring based WDM 32×100 GHz filter enabled by a novel bend design. *Laser & Photonics Reviews*, November 2024. ISSN 1863-8899. doi: 10.1002/lpor.202401357.

[15] Yikai Su, Yong Zhang, Ciyuan Qiu, Xuhan Guo, and Lu Sun. Silicon Photonic Platform for Passive Waveguide Devices: Materials, Fabrication, and Applications. *Advanced Materials Technologies*, 5(8):1901153, 2020. ISSN 2365-709X. doi: 10/gh3525. ZSCC: 0000015 _eprint: tex.ids= su_silicon_2020-1.

[16] Tzu-Hsiang Yen and Yung-Jr Hung. Fabrication-Tolerant CWDM (de)Multiplexer Based on Cascaded Mach–Zehnder Interferometers on Silicon-on-Insulator. *Journal of Lightwave Technology*, 39(1):146–153, January 2021. ISSN 1558-2213. doi: 10.1109/JLT.2020.3026314. Conference Name: Journal of Lightwave Technology.

[17] W. Bogaerts, P. De Heyn, T. Van Vaerenbergh, K. De Vos, S. Kumar Selvaraja, T. Claes, P. Dumon, P. Bienstman, D. Van Thourhout, and R. Baets. Silicon microring resonators. *Laser & Photonics Reviews*, 6(1):47–73, 2012. ISSN 1863-8899. doi: 10/cr3dtz. ZSCC: 0001902 _eprint:.

[18] S. Pathak, P. Dumon, D. Van Thourhout, and W. Bogaerts. Comparison of AWGs and echelle gratings for wavelength division multiplexing on silicon-on-insulator. *IEEE Photonics Journal*, 6(5):1–9, October 2014. ISSN 1943-0655. doi: 10.1109/jphot.2014.2361658.

[19] Yu Zheng, Yunming Li, Yixiong Yan, Pan Zhang, and Ji'an Duan. Compact low-loss low-crosstalk echelle grating demultiplexer on silicon-on-insulator for CWDM. *Optik*, 249:168236, January 2022. ISSN 0030-4026. doi: 10.1016/j.ijleo.2021.168236.

[20] Laiwen Yu, Jingshu Guo, Hengtai Xiang, Guojiang Yang, Yuqi Zhao, Yuanrong Li, and Daoxin Dai. Ultra-compact and high-performance four-channel coarse wavelength-division (de)multiplexing filters based on cascaded mach-zehnder interferometers with bezier-shape directional couplers. *Optics Express*, 32(5):7774, February 2024. ISSN 1094-4087. doi: 10.1364/oe.509936.

[21] Qiyuan Yi, Shuang Zheng, Zhiwei Yan, Guanglian Cheng, Fanglu Xu, Qiyuan Li, and Li Shen. Silicon photonic flat-top WDM (de)multiplexer based on cascaded mach-zehnder interferometers for the 2 μm wavelength band. *Optics Express*, 30(15):28232, July 2022. ISSN 1094-4087. doi: 10.1364/oe.467473.

[22] Zhizun Zhao, Zhen Li, Jiaqi Niu, Gaolu Zhang, Hongliang Chen, Xin Fu, and Lin Yang. Eight-Channel LAN WDM (De)Multiplexer Based on Cascaded Mach–Zehnder Interferometer on SOI for 400GbE. *Photonics*, 9(4):252, April 2022. ISSN 2304-6732. doi: 10.3390/photonics9040252. URL https://www.mdpi.com/2304-6732/9/4/252.

[23] Ahmed Bayoumi, Mehmet Oktay, Alaa Elshazly, Hakim Kobbi, Rafal Magdziak, Guy Lepage, Chiara Marchese, Javad Rahimi Vaskasi, Swetanshu Bipul, Dieter Bode, Dimitrios Velenis, Maumita Chakrabarti, Peter Verheyen, Philippe Absil, Filippo Ferraro, Yoojin Ban, Joris Van Campenhout, Wim Bogaerts, and Qingzhong Deng. Enhanced operation range of silicon MZI filters using a broadband bent directional coupler. *IEEE Photonics Technology Letters*, 37(9):500–503, May 2025. ISSN 1941-0174. doi: 10.1109/lpt.2025.3553059.

[24] Zeqin Lu, Han Yun, Yun Wang, Zhitian Chen, Fan Zhang, Nicolas A. F. Jaeger, and Lukas Chrostowski. Broadband silicon photonic directional coupler using asymmetric-waveguide based phase control. *Optics Express*, 23(3):3795–3808, February 2015. ISSN 1094-4087. doi: 10/gmf37j.

[25] Ahmed H. El-Saeed, Alaa Elshazly, Hakim Kobbi, Rafal Magdziak, Guy Lepage, Chiara Marchese, Javad Rahimi Vaskasi, Swetanshu Bipul, Dieter Bode, Marko Ersek Filipcic, Dimitrios Velenis, Maumita Chakrabarti, Peter De Heyn, Peter Verheyen, Philippe Absil, Filippo Ferraro, Yoojin Ban, Joris Van Campenhout, Wim Bogaerts, and Qingzhong Deng. Low-loss silicon directional coupler with arbitrary coupling ratios for broadband wavelength operation based on bent waveguides. *Journal of Lightwave Technology*, 42 (17):6011–6018, September 2024. ISSN 1558-2213. doi: 10.1109/jlt.2024.3407339.

[26] Ahmed Bayoumi, Ahmed Khalil, Pol Van Dorpe, Maumita Chakrabarti, Dimitrios Velenis, Philippe Absil, Filippo Ferraro, Yoojin Ban, Joris Van Campenhout, Wim Bogaerts, and Qingzhong Deng. Broadband and ultra-compact adiabatic coupler based on linearly tapered silicon waveguides, 2025. URL https://arxiv.org/abs/2504.20512.

[27] Ahmed H. El-Saeed, Alaa Elshazly, Hakim Kobbi, Rafal Magdziak, Guy Lepage, Chiara Marchese, Swetanshu Bipul, Dieter Bode, Marko E. Filipcic, Dimitrios Velenis, Maumita Chakrabarti, Peter De Heyn, Peter Verheyen, Philippe Absil, Filippo Ferraro, Yoojin Ban, Joris Van Campenhout, Wim Bogaerts, and Qingzhong Deng. Wavelength-insensitive and lossless 50:50 directional coupler based on silicon bent waveguides. In *2024 IEEE Silicon Photonics Conference*, 2024.

[28] Ahmed H. El-Saeed, Alaa Elshazly, Hakim Kobbi, Rafal Magdziak, Guy Lepage, Chiara Marchese, Swetanshu Bipul, Dieter Bode, Marko Ersek Filipcic, Dimitrios Velenis, Maumita Chakrabarti, Peter De Heyn, Peter Verheyen, Philippe Absil, Filippo Ferraro, Yoojin Ban, Joris Van Campenhout, Wim Bogaerts, and Qingzhong Deng. Wavelength-insensitive and lossless 50:50 directional coupler based on silicon bent waveguides. In *2024 IEEE Silicon Photonics Conference (SiPhotonics)*. IEEE, April 2024. doi: 10.1109/siphotonics60897.2024.10543882.

[29] J. S. Cook. Tapered velocity couplers. *Bell System Technical Journal*, 34(4): 807–822, July 1955. ISSN 0005-8580. doi: 10.1002/j.1538-7305.1955.tb03777.x.

[30] T.A. Ramadan, R. Scarmozzino, and R.M. Osgood. Adiabatic couplers: design rules and optimization. *Journal of Lightwave Technology*, 16(2):277–283, 1998. ISSN 0733-8724. doi: 10.1109/50.661021.

[31] Wei-Ping Huang. Coupled-mode theory for optical waveguides: an overview. *Journal of the Optical Society of America A*, 11(3):963, March 1994. doi: 10.1364/josaa.11.000963.

[32] L.B. Soldano and E.C.M. Pennings. Optical multi-mode interference devices based on self-imaging: principles and applications. *Journal of Lightwave Technology*, 13(4):615–627, April 1995. ISSN 0733-8724. doi: 10.1109/50.372474.

[33] Liang Cao, Ali Elshaari, Abdelsalam Aboketaf, and Stefan Preble. Adiabatic couplers in SOI waveguides. *Conference on Lasers and Electro-Optics 2010*, page CThAA2, 2010. doi: 10.1364/CLEO.2010.CThAA2.

[34] Hung-Ching Chung, Chih-Hsien Chen, Guan-Xun Lu, Yung-Jr Hung, and Shuo-Yen Tseng. Adiabaticity Engineered Silicon Polarization Independent 3-dB Coupler for the O-Band. *IEEE Photonics Journal*, 15(3):1–6, June 2023. doi: 10.1109/JPHOT.2023.3271320.

[35] Keun Il Kim, Dong Kim, Vinh Nguyen, Sangyoon Han, and Tae Seok. High-Performance and Compact Silicon Photonic 3-dB Adiabatic Coupler Based on Shortest Mode Transformer Method. *IEEE Photonics Journal*, August 2021. doi: 10.1109/JPHOT.2021.3107852.

1

Introduction

Photonics is the science and technology of generating, controlling, and utilizing light for information processing and transmission. It forms the backbone of modern high-speed optical communication systems, enabling efficient data transfer across local, metropolitan, and global networks. The widespread adoption of photonics stems from its key advantages over traditional electronic systems, including higher data rates, lower power consumption, and reduced signal attenuation over long distances. This chapter provides an overview of Photonic Integrated Circuits (PICs) and silicon photonics, establishing the context and motivation for the thesis. The focus is on advancing optical links through improved design of wavelength division multiplexing filters, which are critical for scaling bandwidth and enhancing system performance.

1.1 Silicon Photonics 2
Silicon Photonics Fabrication 3
Silicon Photonics Applications 5
Essential Building Blocks 7
1.2 Simulation methods 13
Finite-Difference Time-Domain Method (FDTD) 14
Finite Element Method (FEM) 15
Beam Propagation Method (BPM) 16
Eigenmode Expansion Method (EME) 16
Transfer Matrix Method (TMM) 17

1.3 Thesis Objectives 19
Optical Links and Wavelength Division Multiplexing 19
Challenges in Current WDM Architectures 20
Thesis Contributions and Outline 21
1.4 Publications 26
Journal Papers 26
International Conferences 27
References 28

1.1 Silicon Photonics

Photonics is a field of science focused on the generation, control, and utilization of light for processing and transmitting information [1]. In the modern era of high-speed communication, photonics plays a pivotal role as a significant portion of data transmission relies on light as the information carrier. Optical communication systems are now foundational technologies across a broad range of applications, from metropolitan networks and fiber-to-the-home deployments to transoceanic submarine cables that interconnect entire continents. The widespread adoption of optical communication stems from its advantages over traditional electronic systems [2, 3]. It enables higher data rates at lower costs and offers significantly reduced signal attenuation, allowing for long-distance transmission with minimal reliance on repeaters [3]. Furthermore, optical fibers consume substantially less power than electrical conductors, making them particularly well-suited for energy-efficient communication, which is an essential feature for interconnecting servers in large-scale data centers [4, 5].

Silicon photonics is a well-established platform for developing PICs, where silicon serves as the core material for fabricating optical components [4, 6]. A typical PIC integrates various photonic elements, such as waveguides [7], modulators [8], wavelength filters [9], and sensors [10], onto a single chip to perform complex optical functionalities. While silicon photonics has been predominantly utilized in optical fiber communications [2], it has also found applications in diverse domains, including sensing[11, 12], quantum computing [13, 14], and biomedical diagnostics [15].

One of the most significant advantages of silicon photonics is its compatibility with complementary metal-oxide-semiconductor (CMOS) fabrication processes. This compatibility enables leveraging the mature semiconductor manufacturing infrastructure to produce silicon photonic devices with high yield, scalability, and cost-efficiency [16]. Silicon, the core material of CMOS technology, is transparent at the infrared wavelengths commonly used in telecommunications, making

it appealing for integrated photonics. Additionally, silicon photonics enables the co-integration of optical and electronic components on the same chip, supporting compact and energy-efficient systems for data communications, sensing, and emerging quantum technologies [17].

Silicon Photonics Fabrication

Most nanophotonic waveguide circuits are fabricated using high-resolution lithography followed by dry etching, as illustrated in Fig. 1.1. The process begins with the deposition of a silicon layer on an insulator substrate, typically silicon dioxide (SiO_2). This is followed by photolithography, where a photoresist layer is applied and patterned using ultraviolet (UV) light. The exposed areas are then etched to create the desired waveguide structures. After etching, the photoresist is removed, and the device undergoes various post-processing steps such as annealing and passivation to enhance performance and reduce defects. Finally, the fabricated devices are characterized using techniques like scanning electron microscopy (SEM) and atomic force microscopy (AFM) to ensure quality and precision [18].

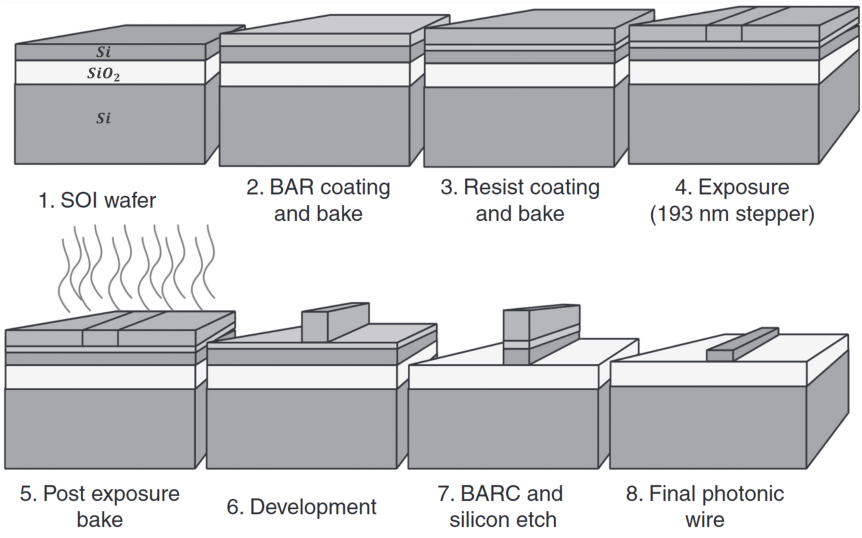

Figure 1.1: Fabrication flow for SOI nanophotonic waveguides, where BARC refers to Bottom Anti Reflective Coating [18, 19].

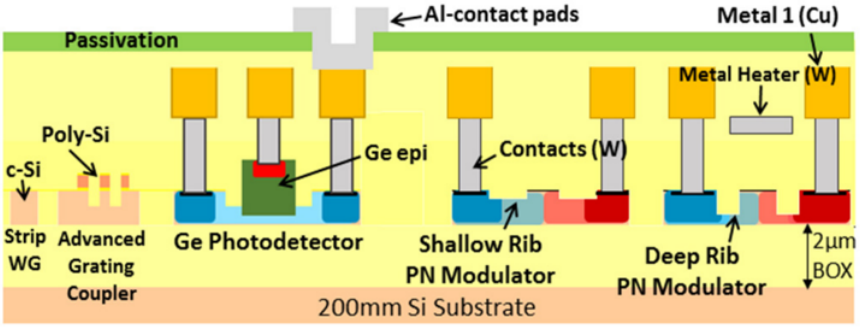

Figure 1.2: Schematic cross-section of IMEC's silicon photonics platform, showing fundamental passive and active building blocks and devices [17, 19].

IMEC Silicon Photonics Platform

The iSiPP300 (imec Silicon Photonics Platform) is a state-of-the-art silicon photonics technology that utilizes 300 mm SOI wafers and 193 nm immersion lithography. This platform offers a standardized, CMOS-compatible fabrication process for photonic integrated circuits (PICs) with sub-100 nm patterning precision. Its scalability and process maturity make it particularly attractive for applications such as optical transceivers and WDM systems [17, 19].

The iSiPP300 platform is based on 220 nm silicon and 2000 nm buried oxide (BOX) wafers, which are widely adopted industry standards for silicon photonics. It leverages the mature CMOS fabrication infrastructure, benefiting from high-volume and high-yield manufacturing processes originally developed for advanced electronic integrated circuits.

A schematic cross-section of imec's platform, illustrating some of the fundamental device layers and structures, is shown in Fig. 1.2. The platform supports a comprehensive set of passive and active photonic components, including low-loss waveguides, high-speed modulators, and photodetectors. The top silicon layer of the SOI wafer is employed to fabricate passive elements such as waveguides, multiplexers/demultiplexers, fiber-grating couplers, and silicon-based modulators. To realize a diverse range of optical functionalities, three silicon etch steps are implemented, corresponding to etch depths of 220 nm, 150 nm, and 70 nm. Following the waveguide definition, an oxide cladding layer is deposited to planarize the surface and encapsulate the photonic structures [18, 19].

Additional device capabilities are enabled through the deposition of a 160 nm-thick polysilicon layer, which is patterned in a single lithographic step. The silicon is doped via three implantation steps for p-type and three for n-type doping. After

oxide planarization of the polysilicon structures and an activation anneal, selective windows are opened in the planarized oxide. Germanium (Ge) or germanium-silicon (GeSi) is then selectively grown within these openings to form high-performance photodetectors and other optoelectronic structures [19].

For electrical interfacing, standard CMOS nickel silicide (Ni-silicide) and tungsten (W) contacts are employed to connect to the highly doped silicon regions. Thermal tuning of wavelength-sensitive components, such as silicon ring modulators, is facilitated by an integrated tungsten heater module. The electrical interconnects are fabricated using standard copper (Cu) damascene metallization, while aluminum-based bond pads and a silicon nitride (SiN) passivation layer enhance device reliability and support wire bonding on the copper lines [19].

Silicon Photonics Applications

Silicon photonics has transitioned from a research-driven field to a cornerstone of commercial innovation, enabling advancements in sensing, communications, and computing. Its compatibility with CMOS fabrication processes and potential for high-density integration have been instrumental in its widespread adoption.

The silicon photonics market has experienced remarkable growth, valued at approximately 68 million dollars in 2022, with projections estimating an increase to over 600 million dollars by 2028, reflecting a compound annual growth rate (CAGR) of 44% [20], as shown in Fig.1.3. This growth is largely driven by the rising demand for high-data-rate modules in data centers and the integration of optical I/O in machine learning (ML) servers, which require rapid and efficient data processing. In the broader context of PICs, the silicon PIC market is expected to grow from 95 million dollars in 2023 to 863 million dollars by 2029, marking a 45% CAGR [20]. This expansion highlights the critical role of silicon photonics in advancing optical communication technologies. While datacom and telecom remain the dominant applications, silicon photonics is also gaining traction in emerging fields such as biosensors, LiDAR, and optical and quantum computing.

Key application areas of silicon photonics include:

- **Data Communication and Data Centers:** Silicon photonics enables high-speed, energy-efficient optical interconnects with multi-Tb/s data rates essential for scaling modern data center infrastructure [21].
- **High Performance Computing (HPC) and AI:** Optical interconnects based on silicon photonics offer high bandwidth, low latency, and energy-efficient data transfer, which are essential for large-scale AI training and scientific

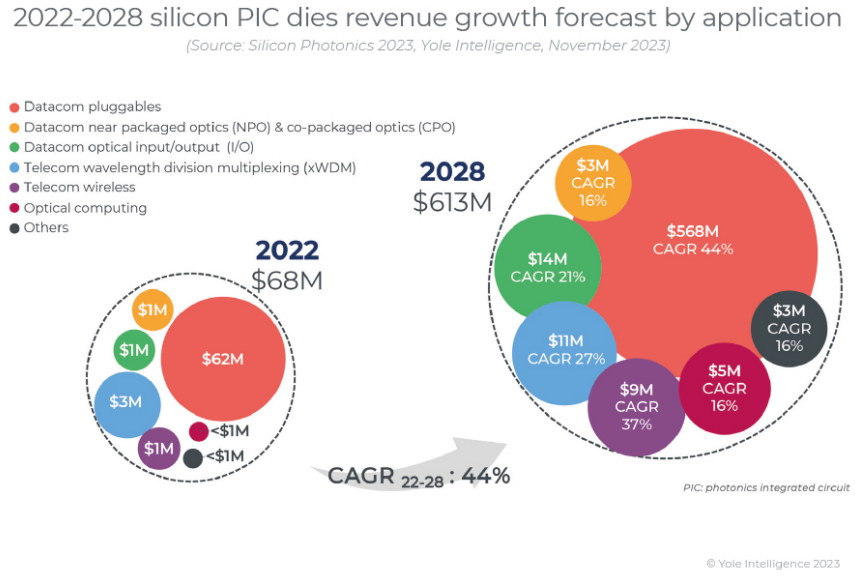

Figure 1.3: Silicon photonics market growth projections from 2022 to 2028, highlighting the compound annual growth rate (CAGR) of 44% driven by increasing demand for high-data-rate modules in data centers and machine learning servers [20].

computing [22].

- **LiDAR and Sensing:** Silicon photonics enables solid-state LiDAR with optical phased arrays, which are compact, robust, and capable of high-resolution beam steering, suitable for autonomous vehicles and industrial automation [23].

- **Biosensing:** Silicon photonic biosensors leverage evanescent field interactions in structures such as ring resonators and Mach Zehnder Interferometers (MZIs) to achieve label-free biomolecular detection with femtomolar sensitivity for diagnostic applications [24].

- **Quantum Technologies:** The high integration density of silicon photonics facilitates scaling of quantum photonic circuits for quantum computing, communication, and sensing applications requiring precise manipulation of single photons [14].

Silicon photonics is transitioning from research to commercialization, with both startups and established companies actively developing integrated photonic systems. A recent example is the introduction of silicon photonics-based networking

platforms by NVIDIA, which unveiled the *Spectrum-X Photonics* and *Quantum-X Photonics* switch architectures at GTC 2025. These systems are designed for exascale data center applications and achieve data rates of up to 1.6 Tb/s per port, with total switching capacities reaching 400 Tb/s, enabled by photonic integration with switch application-specific integrated circuits (ASICs) [25]. By incorporating photonics into networking hardware, such designs address fundamental limitations of traditional electrical interconnects, including signal attenuation and energy inefficiency. In collaboration with TSMC, NVIDIA is also exploring on-package optical I/O for chip-to-chip communication, indicating ongoing efforts to scale photonic integration for AI and high-performance computing workloads [26]. These trends highlight the growing relevance of silicon photonics in next-generation computing infrastructure.

Essential Building Blocks

Optical waveguide

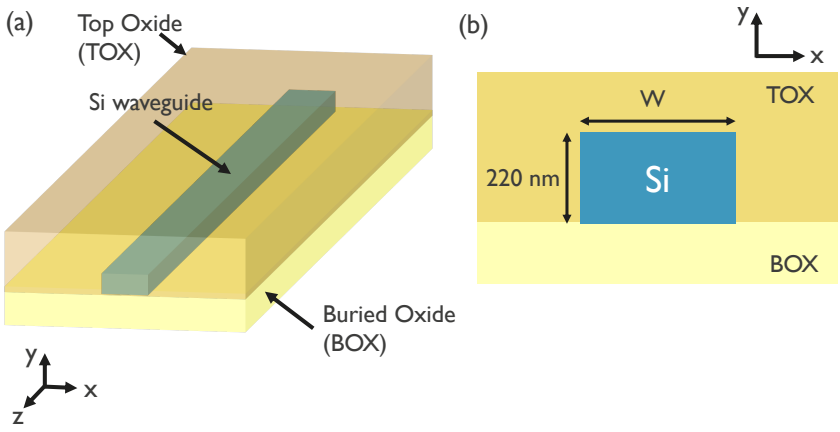

Figure 1.4: 3D schematic of a silicon waveguide with SiO_2 cladding (a) 2D cross section of the typical geometry and dimensions for a single mode silicon-on-insulator strip waveguide with silicon oxide cladding. W is for the width which is often 380 nm or 450 nm for O and C band based waveguides, respectively.

The waveguide is the most fundamental component of a PIC, serving as the pathway that guides light across the chip. In silicon photonics, a waveguide typically consists of a silicon core surrounded by a lower-refractive-index dielectric material, such as silicon oxide (SiO_2) or air. This structure confines light via total internal reflection. Usually, the waveguide is designed to operate in single-mode conditions to prevent

optical losses that are usually present with high-order modes.

Silicon's high refractive index ($n = 3.50$ at $\lambda = 1310\,\mathrm{nm}$) compared to its cladding materials (e.g., SiO_2, $n = 1.444$; air, $n \approx 1$) creates a strong optical confinement effect. This high index contrast enables sub-micrometer waveguide dimensions and tight bending radii, facilitating the miniaturization of photonic components and the dense integration of complex circuits in compact spaces, making silicon photonics a promising platform for large-scale systems.

Fabrication advancements reduced waveguide propagation losses to $0.2\,\mathrm{dB\,cm^{-1}}$ to $1.0\,\mathrm{dB\,cm^{-1}}$. The primary source of loss is sidewall roughness caused by manufacturing imperfections, as silicon itself exhibits minimal optical absorption at telecommunication wavelengths [27, 28].

The typical dimensions of a silicon photonic waveguide are illustrated in Fig.1.4. These compact structures enable both the miniaturization of photonic components and the high-density integration of numerous elements within a small footprint. This scaling capability is essential for realizing large-scale photonic systems.

Optical Waveguide Bends

Optical waveguide bends serve as essential components in PICs, facilitating compact routing and connections between optical elements. However, these bends introduce two primary loss mechanisms:

- **Mode mismatch losses** at straight-to-curved section interfaces, caused by the shift of the optical field distribution toward the outer waveguide boundary in curved sections
- **Increased sidewall scattering** due to heightened optical field intensity at the boundaries, particularly at the outer edge of the bend

These bend-induced losses become particularly significant in complex PICs containing numerous bends, where their cumulative effect can substantially degrade overall system performance.

This thesis employs Third-Order Polynomial Interconnected Circular (TOPIC) bends to minimize these losses [29, 30]. As illustrated in Fig. 1.5, TOPIC bends integrate three key segments:

- An initial third-order polynomial transition
- A central circular section

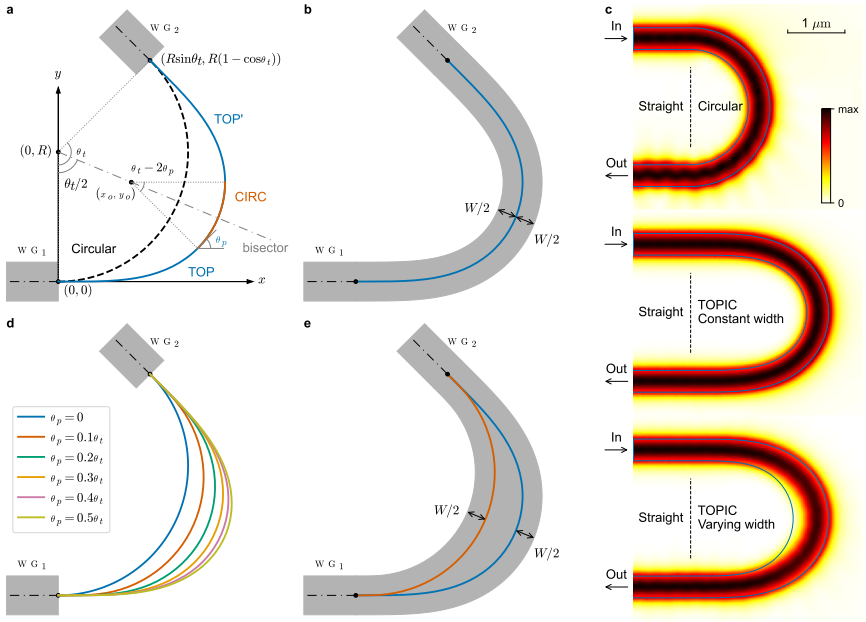

Figure 1.5: Schematic of the TOPIC bend design in comparison to the circular bend: (a) The baseline of the TOPIC and circular bends, (b) Schematic of a TOPIC bend with a fixed waveguide width, (c) Optical field evolutions ($|E|$) in circular and TOPIC bends, (d) Different TOPIC shapes based on manipulating parameter θ_p, and (e) TOPIC bend with varying waveguide width resulting in a whispering gallery mode (WGM) [29].

- A mirrored third-order polynomial transition

What distinguishes this architecture from other types of bends is that it ensures continuous curvature and curvature derivative across all interfaces, significantly reducing mode mismatch compared to conventional circular bends. Moreover, the TOPIC curve shape can be manipulated by varying the parameter θ_p, as depicted in Fig. 1.5 (d). The TOPIC bend design introduces an adjustable parameter (θ_p, shown in Fig. 1.5(a)) that effectively balances the inherent trade-off between sidewall scattering loss and mode transition loss. Sidewall scattering increases with longer paths and higher maximum curvature, while mode transition loss decreases with smoother transitions. Fig. 1.5(a) illustrates the comparison between the TOPIC baseline and a standard circular baseline.

TOPIC bends can be implemented in two configurations:

- **Constant-width TOPIC bends:** Created by generating the waveguide's inner and outer boundaries as parallel curves offset from a single baseline,

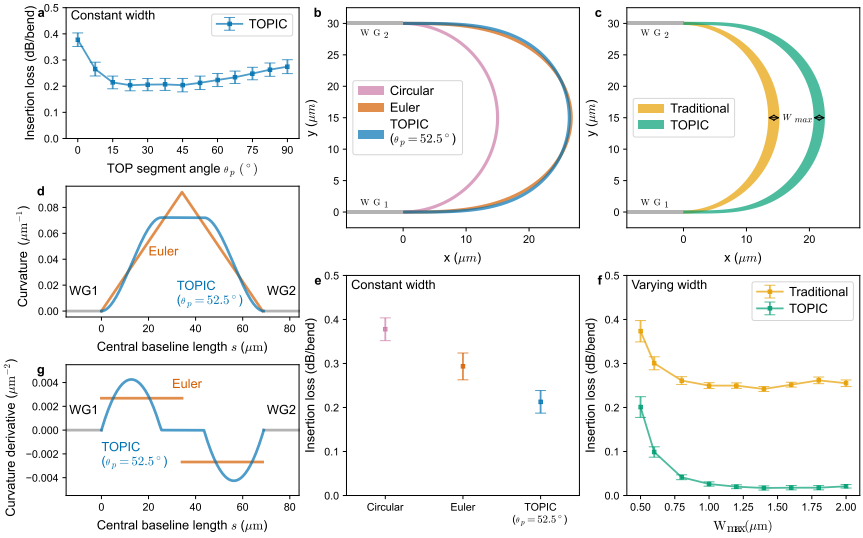

Figure 1.6: Measured insertion losses for different 180° waveguide bends. (a) Measured losses of constant-width TOPIC bends with varying θ_p. (b, c, e, f) Schematics (b, c) and corresponding measured losses (e, f) for waveguide bends with constant width (b, e) and varying width (c, f). (d, g) Comparison of curvature (d) and curvature derivative (g) between constant-width Euler and TOPIC bends. The waveguides consist of a silicon nitride (SiN) core clad in silicon oxide, operating at a wavelength of 638 nm. The SiN layer thickness is 150 nm, and the waveguide width, except in regions with varying width, is 500 nm. The bend radius is $R = 15$ μm. The parameter $W_{\max}$ represents the maximum waveguide width along a varying-width bend. In traditional varying-width designs, the outer boundary follows a circular arc, while the inner boundary is oval, adjusted via its semi-minor axis to achieve the target $W_{\max}$. For varying-width TOPIC bends, the outer boundary angle $\theta_{p,o}$ is fixed at 30°, and the inner boundary angle $\theta_{p,i}$ is tuned to obtain the desired $W_{\max}$. Loss measurements were performed using the cut-back method, with multiple identical bends cascaded to enable linear regression analysis of transmission data. The plotted loss values represent the mean and standard deviation across measurements from all dies on a 200 mm wafer fabricated using the imec pix4life platform. [29].

as depicted in Fig. 1.5(b). This configuration maintains uniform waveguide width throughout the bend while benefiting from the TOPIC curve's continuous curvature properties.

- **Varying-width TOPIC bends:** Formed by developing the waveguide's inner and outer boundaries as parallel curves of two distinct baselines with different θ_p values, as shown in Fig. 1.5(e). These designs can support whispering gallery modes (WGMs), which are optical modes confined near the curved waveguide boundary through total internal reflection.

WGMs offer several advantages, including:

- Enhanced optical confinement
- Reduced propagation loss
- High-quality factors in resonant structures
- Facilitated integration of thermal tuning elements within the waveguide

TOPIC bends substantially reduce mode transition loss compared to circular bends, as verified by the optical field evolution patterns shown in Fig. 1.5(c). This performance improvement becomes particularly valuable in complex PICs with numerous bends, where cumulative bend losses can significantly affect overall system performance. Furthermore, as indicated in Fig. 1.5(c), the varying-width TOPIC bend substantially reduces light intensity at the waveguide sidewalls, especially along the inner edge, effectively minimizing sidewall scattering loss in the presence of surface roughness.

To verify these theoretical findings, loss was experimentally evaluated for different silicon nitride TOPIC bends with varying θ_p values, as shown in Fig. 1.6(a). Various bend types were fabricated to connect two straight waveguides with fixed relative positions, marked as WG1 and WG2 in Fig. 1.6(b) and 1.6(c).

The experimental results reveal several key findings:

- At $\theta_p = 0^\circ$, the TOPIC bend defaults to a conventional circular bend, exhibiting minimal sidewall scattering but still showing high total loss (0.378 ± 0.026 dB) due to significant mode mismatch between straight and curved waveguide sections.
- As θ_p increases from 0° to 22.5°, the total loss decreases to 0.204 ± 0.021 dB, owing to smoother transitions between straight and curved waveguide modes.
- In the θ_p range of 22.5° to 45°, the loss remains relatively stable, indicating an optimal balance between sidewall scattering and mode transition losses.
- Further increasing θ_p toward 90° leads to higher losses, as mode transition loss becomes negligible but sidewall scattering increases due to longer waveguide paths and larger maximum curvature.

Of particular interest is the TOPIC bend with $\theta_p = 52.5^\circ$, which closely resembles an Euler bend in geometric configuration (Fig. 1.6(b)). These two bend types share similar total lengths and comparable average curvatures along their paths

(Fig. 1.6(d)), as well as continuous curvature profiles resulting in lower losses compared to conventional circular bends (Fig. 1.6(e)).

The critical distinction between TOPIC and Euler bends (and also the third order partial spline bends) lies in the curvature derivative. Only the TOPIC bend maintains a continuous curvature derivative along the entire waveguide path, as demonstrated in Fig. 1.6(g). This mathematical continuity translates to significantly lower insertion loss for the TOPIC bend (0.212 ± 0.026 dB) compared to the Euler bend (0.293 ± 0.030 dB). These results experimentally confirm that both continuous curvature and continuous curvature derivative are essential for minimizing waveguide bend losses.

Furthermore, varying-width TOPIC bends were fabricated and compared with traditional designs using circular outer and oval inner boundaries (Fig. 1.6(c)). The varying-width TOPIC bend achieved remarkably low loss (0.017 ± 0.005 dB), significantly outperforming the traditional approach (0.242 ± 0.006 dB at $W_{\text{max}} = 1.4$ μm, Fig. 1.6(f)).

Coupling and interference based devices

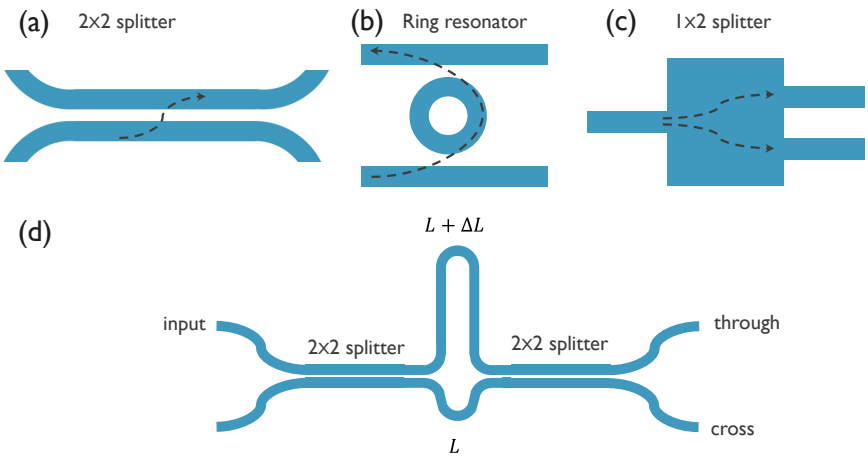

Figure 1.7: Several silicon photonic devices are based on coupling and/or interference mechanisms, including (a) directional coupler, (b) ring resonator, and (c) 1×2 splitter, (d) MZI.

Several silicon photonic devices rely on coupling and/or interference mechanisms, as illustrated in Fig. 1.7: (a) directional coupler (DC), (b) ring resonator, (c) 1×2 splitter, (d) MZI. Couplers are fundamental components in silicon photonics, facilitating efficient light transfer between waveguides or between waveguides and

free space. They are indispensable for various applications, including splitting, combining, and routing optical signals within integrated circuits [1, 31, 32].

DCs operate based on the principle of evanescent field coupling, where light propagating in one waveguide interacts with the evanescent field of an adjacent waveguide. The coupling efficiency depends on the gap between the waveguides, their refractive index contrast, and the coupling length. The power transfer between the waveguides can be controlled by adjusting these parameters, enabling precise control over the splitting ratio [1].

Ring resonators, on the other hand, rely on constructive and destructive interference of light circulating within a closed-loop waveguide. They are widely used for wavelength filtering, sensing, and modulation. The resonance condition is determined by the round-trip phase accumulation, which depends on the ring's geometry and the refractive index of the waveguide material. By coupling a ring resonator to a bus waveguide, specific wavelengths can be selectively dropped or added, making them essential components in wavelength-division multiplexing (WDM) systems [33].

The 1×2 splitter (Fig. 1.7c) is another critical device, designed to divide optical power equally or unequally between two output waveguides. These splitters are often implemented using multimode interference (MMI) structures or Y-branch configurations. MMIs leverage self-imaging effects in multimode waveguides to achieve compact and robust designs, while Y-branches rely on adiabatic tapering to minimize losses and ensure smooth power splitting [32].

MZIs are versatile components in silicon photonics, leveraging interference between two optical paths to achieve various functionalities such as filtering, modulation, and switching. An MZI consists of two couplers (splitters) connected by two arms of different lengths or refractive indices. The phase difference between the arms determines the interference pattern at the output, enabling precise control over the device's spectral response. MZIs are widely used in WDM systems [31].

Each of these devices plays a vital role in enabling the functionality and scalability of silicon PICs, supporting applications ranging from optical communication to sensing and quantum computing.

1.2 Simulation methods

The design and optimization of photonic components and WDM systems necessitate precise modeling of light propagation and interaction phenomena at micro and nanometer scales. Effective simulation tools must capture wavelength-dependent behavior, provide broadband spectral response, handle complex geometries with

high index contrasts, and ensure computational efficiency for iterative design and optimization. Additionally, system-level simulation tools are essential for analyzing WDM circuits. Various simulation methods offer distinct trade-offs in terms of accuracy, computational cost, and suitability for specific device geometries. This section provides an overview of key simulation approaches commonly employed in photonic device modeling.

Finite-Difference Time-Domain Method (FDTD)

The FDTD method is a full-wave numerical technique that directly solves Maxwell's equations in the time domain. One of its primary advantages is its excellent scalability with parallel computing architectures. Large simulation domains can be partitioned and distributed across multiple processors, significantly reducing overall simulation time [34].

FDTD simulates the propagation of a short optical pulse, typically lasting tens to hundreds of femtoseconds. Since such a pulse contains a broad spectral content, a single simulation can yield the transmission spectrum of the device across a wide range of wavelengths via Fourier transform analysis. This makes FDTD particularly powerful for broadband analysis.

The boundary conditions in FDTD are typically defined using Perfectly Matched Layers (PML), which effectively absorb outgoing waves and minimize artificial reflections at the simulation domain edges. FDTD is well-suited for arbitrary geometries and material distributions, and it exhibits good convergence as the spatial mesh is refined.

Despite these advantages, FDTD has several significant drawbacks. First, the computational cost scales steeply with mesh refinement. Second, the use of a Cartesian grid introduces numerical dispersion: waves propagating at different angles or polarizations experience slight variations in phase velocity, leading to phase errors unless a very fine mesh is used. Additionally, curved or oblique interfaces become "staircased", which can degrade accuracy unless subpixel smoothing or more advanced grid-fitting techniques are employed.

Further, resonant devices impose further challenges: resolving narrow spectral features demands very long simulation times, since the slowly decaying fields must be captured over extended time windows. This limitation makes FDTD less suitable for analyzing such devices, favoring alternative methods better optimized for resonant structures.

Finite Element Method (FEM)

The Finite Element Method (FEM) is a powerful and versatile numerical technique for solving partial differential equations (PDEs) over complex geometries. It is widely used across disciplines such as structural mechanics, electromagnetics, fluid dynamics, and thermal analysis. At its core, FEM approximates a continuous field (e.g., displacement, electric field) by dividing the problem domain into smaller subdomains called finite elements. Within each element, the field is represented using basis functions, typically low-order polynomials, whose coefficients are determined by enforcing the governing PDEs [35].

One of FEM's key strengths is its flexibility in handling arbitrary geometries and boundary conditions. Because it relies on a mesh of elements that conform to the geometry, it can accurately model curved boundaries and material inhomogeneities. Moreover, FEM allows for adaptive mesh refinement, where the mesh can be locally refined in regions requiring higher accuracy, thereby optimizing computational resources.

In the context of frequency-domain electromagnetic simulations, FEM solves Maxwell's equations by expanding the electric or magnetic field in terms of vector basis functions over each element. This leads to a sparse system of linear equations, which can be efficiently solved using modern numerical solvers. However, the method does require careful meshing, especially in regions with fine geometric features or high field gradients. Further, it is not the natural choice for broadband analysis, where the FEM simulations has to be repeated for each wavelength of interest. Further, when simulating devices with sharp spectral features, FEM requires multiple frequency-domain simulations to accurately resolve narrow resonances, dramatically increasing the overall computational cost.

FEM can also be implemented in the time domain as Finite Element Time Domain (FETD), which combines the geometric flexibility of FEM with the broadband capabilities of time-domain methods. In FETD, Maxwell's curl equations are discretized in both space and time, allowing for the modeling of complex electromagnetic wave propagation and interactions with a single simulation [36]. Commercial tools such as Omnisim by Photon Design implement FETD for photonic device simulation [37]. This approach is particularly advantageous for structures with complex geometries that would be difficult to handle with traditional FDTD methods, while still providing broadband spectral data through Fourier analysis of time-domain results. FETD also benefits from the use of unstructured or adaptive meshes, enabling accurate representation of curved surfaces without the staircase approximation issues that can affect FDTD simulations. However, this usually comes at the cost of a higher computational cost, greater memory requirements, and increased

implementation complexity.

Despite its computational cost in large three-dimensional problems, FEM is of high standard due to its generality, accuracy, and mature mathematical foundation. The method provides a systematic framework for error estimation, convergence analysis, and incorporation of complex material models, making it particularly suitable for high-fidelity simulations in advanced scientific and engineering applications.

Beam Propagation Method (BPM)

The Beam Propagation Method (BPM) is a numerical technique used to simulate the propagation of optical fields in waveguides and other photonic structures. It is particularly well-suited for analyzing devices with slowly varying refractive index profiles along the propagation direction, such as tapers, bends, and DCs [38].

BPM is based on solving the paraxial approximation of the Helmholtz equation, which assumes that the optical field primarily propagates in one direction and does not exhibit strong longitudinal field components (which represent high-angle waves). This approximation can be problematic for high-contrast waveguides like those in silicon photonics, which typically have large longitudinal fields at the sidewalls. The method discretizes the propagation axis into small steps and iteratively computes the field at each step (i.e. using finite-difference schemes).

One of the key advantages of BPM is its computational efficiency for long structures with gradual changes, as it avoids the need for a full-wave solution. It is also relatively straightforward to implement and can handle a wide range of refractive index profiles. However, BPM is less accurate for structures with sharp discontinuities, strong back-reflections, or highly multimode behavior, as the paraxial approximation breaks down in such cases.

Despite its limitations, BPM remains a widely used tool for the design and analysis of photonic devices, particularly in the early stages of development when rapid prototyping and parameter sweeps are required. Its simplicity and efficiency make it a valuable method for exploring design concepts and optimizing device performance.

Eigenmode Expansion Method (EME)

The Eigenmode Expansion (EME) method models light propagation by dividing a waveguide device into a series of uniform segments along the propagation direction. In each segment, the electromagnetic field is expanded as a linear combination of the local eigenmodes supported by that uniform cross-section. The propagation of

light through each segment is described by a transfer matrix that relates the mode amplitudes between interfaces. By cascading these matrices from input to output, the overall transmission and reflection characteristics of the device are computed [39].

EME method is particularly efficient for structures composed of straight or smoothly varying waveguide segments. Since only a limited number of eigenmodes are typically required in each segment, the method maintains low memory usage and achieves rapid convergence as additional modes are included. Unlike purely grid-based solvers, EME can represent straight angled interfaces exactly, though curved geometries still require appropriate discretization. Moreover, the method provides direct insight into which modes carry power and how energy is transferred between them through coupling.

However, the EME method is less well-suited for fully three-dimensional or continuously varying geometries unless the structure is discretized into many thin slices, an approach that increases computational cost. Additionally, regions with sharp discontinuities or strong multimode behavior may require dozens or even hundreds of modes to achieve accurate results, diminishing some of EME's computational advantages. Finally, because EME operates in the frequency domain, obtaining a broadband response necessitates repeating the calculation independently at each wavelength of interest.

Transfer Matrix Method (TMM)

The Transfer Matrix Method (TMM) is a powerful numerical technique for modeling electromagnetic wave propagation in layered or stratified media. It is particularly effective for simulating optical structures such as thin-film coatings, photonic crystals, and multilayer waveguides. In TMM, each optical layer or component is represented by a transfer matrix that relates the incident and transmitted fields at its boundaries. By cascading these matrices, the overall transmission and reflection properties of complex structures can be computed efficiently. It is worth mentioning that the EME method could be considered as a variation of the TMM method [40].

In the context of PICs, TMM enables circuit-level simulation by modeling interconnected components such as DCs, resonators, and filters as modular blocks. Each component's behavior is captured by its own transfer matrix, and the overall system response is obtained by matrix multiplication. This modularity allows for efficient scaling from single devices to full circuit simulations.

One of the key advantages of TMM is its ability to extract scattering parameters (S-parameters), which describe the reflection and transmission behavior of optical

components. For a two-port device, the reflection coefficient (r) corresponds to S_{11} and the transmission coefficient (t) corresponds to S_{21}:

$$S_{11} = r \quad \text{(input reflection)}, \tag{1.1}$$

$$S_{21} = t \quad \text{(forward transmission)}. \tag{1.2}$$

These S-parameters can be directly used in circuit-level simulation tools such as SPICE or Keysight ADS, enabling co-simulation with electronic components.

TMM offers several practical benefits. It significantly reduces computational cost compared to full-field simulations for compatible geometries, supports systematic construction of large photonic circuits, and provides outputs that are interoperable with standard electronic design automation (EDA) tools. As such, it serves as an efficient and scalable framework for the analysis and design of integrated photonic systems.

Design Automation

Automating the design process of photonic circuits is essential for enabling rapid prototyping, performance optimization, and large-scale integration. Manual design of components such as couplers, resonators, and multiplexers is time-consuming and prone to errors, particularly as device complexity increases. Python has emerged as a versatile and powerful platform for photonic design automation due to its rich ecosystem of scientific libraries and ease of integration with external tools [41].

Core Python libraries such as `NumPy` [42] and `SciPy` [43] are widely used for numerical computation and optimization, while `Matplotlib` [44] and `Pandas` [45] provides flexible plotting and data visualization capabilities. These tools support tasks such as parameter sweeps, data analysis, and curve fitting essential for analyzing device behavior and tolerances.

Moreover, Python supports automation and scripting interfaces for commercial photonic simulation software. For example, `LumAPI` allows direct control of Lumerical tools (e.g., FDTD, MODE) from Python [46], enabling batch simulations, parameterized design sweeps, and automatic extraction of performance metrics. Similarly, `MPh` provides a Python interface to COMSOL Multiphysics [47], allowing automated geometry generation, meshing, simulation, and post-processing within a unified workflow.

In addition to commercial tools, open-source frameworks such as `gdsfactory` [48] and `gdstk` [49] offer Python-based libraries for photonic layout generation, DRC-clean GDSII export, and hierarchical circuit design. These libraries enable users to create parameterized cells, assemble complex circuits programmatically,

and integrate directly with simulation backends. The combination of numerical analysis, design automation, and simulation scripting within Python provides a scalable approach to photonic device development. It empowers designers to explore large design spaces, implement optimization loops, and shorten development cycles significantly.

1.3 Thesis Objectives

Optical Links and Wavelength Division Multiplexing

The rampant adoption of the internet and the proliferation of online devices, cloud computing, and bandwidth-intensive applications such as video streaming and artificial intelligence, have brought about an unprecedented growth in data traffic, posing a significant challenge for service providers and network operators to keep pace with soaring bandwidth demands [50]. This trajectory underscores a critical challenge for network operators. Traditional electronic switching and copper-based interconnects, constrained by inherent limitations in speed, latency, and power consumption, are increasingly inadequate to meet these demands. Consequently, optical communication systems have emerged as the backbone of modern telecommunication networks, leveraging the light speed transmission and immense bandwidth of lightwave signals through fiber-optic cables [3, 5].

An optical interconnect is a communication system that transmits data using modulated light signals, typically through optical fibers. Optical interconnects are emerging as a key solution for overcoming the limitations of traditional electrical interconnects in high-speed data communication systems. Compared to traditional electrical links, optical links offer superior bandwidth, lower signal attenuation over long distances, and immunity to electromagnetic interference, making them highly suitable for applications in data centers, high-performance computing, and chip-to-chip communication [3].

A typical optical interconnect architecture integrates both photonic and electronic components to enable high-speed data transmission over optical links, as shown in the schematic in Fig.1.8. The system begins with a multi-wavelength continuous-wave (CW) laser source, which provides a stable optical carrier across multiple channels. This light is coupled into a waveguide or fiber and routed to a demultiplexing filter (DEMUX), which separates the wavelengths for individual data modulation. Each channel is subsequently modulated using an electro-optic modulator driven by high-speed electrical signals. The modulated channels are then recombined using a multiplexing filter (MUX) to produce a high-capacity optical

signal via dense wavelength division multiplexing (DWDM).

This signal is transmitted via optical fiber or waveguide to the receiver end, where it is again demultiplexed into individual wavelengths. Each channel is detected by a photodetector and converted into an electrical signal, which is then amplified and transformed to a voltage by a transimpedance amplifier (TIA) for further electronic processing. Thermal tuning elements integrated with the MUX and DEMUX components ensure accurate wavelength alignment and performance stability.

WDM filters, whether functioning as multiplexers (MUX) or demultiplexers (DEMUX), are critical components in optical interconnects. They enable the simultaneous transmission of multiple data channels over a single optical fiber, significantly enhancing bandwidth utilization. The design of WDM filters is crucial for scaling the channel count in optical links while maintaining high signal integrity, minimizing crosstalk between channels, and achieving low insertion loss [9, 51].

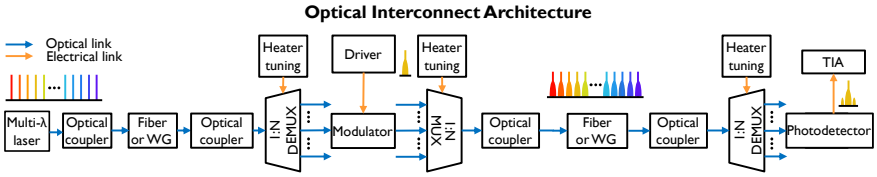

Figure 1.8: Schematic of a typical optical interconnect architecture. The system consists of a multi-wavelength CW laser source, a MUX, a DEMUX, and a TIA. The MUX and DEMUX enable simultaneous signals to be transmitted over a single optical fiber.

Challenges in Current WDM Architectures

The design of WDM filters is subject to stringent performance requirements, including high channel isolation, low insertion loss, thermal stability, and broadband operation [31]. These demands necessitate precise engineering of the filtering components within the DWDM system. In high-index contrast platforms such as silicon photonics, this challenge is further amplified. While silicon photonics offers significant advantages in terms of compactness and integration density, it also exhibits strong dispersion. As a result, WDM filters implemented in silicon are highly sensitive to wavelength variations and fabrication imperfections, making robust and reliable design particularly demanding.

Current implementations of DWDM components on silicon photonics utilize diverse architectures, including arrayed waveguide gratings (AWGs), Echelle gratings, micro-ring resonators (MRRs), and cascaded MZI filters, where each architecture presents unique trade offs. AWGs can achieve broad bandwidths and high channel counts but may introduce higher insertion losses and pose challenges in design and

fabrication complexity. Echelle gratings are capable of high channel counts and low insertion loss but demand high fabrication precision, making them challenging to implement. MRRs offer compactness and scalability but are sensitive to temperature variations and require precise tuning mechanisms to maintain performance. MZI filters are known for their high channel isolation and low insertion loss, however, they often exhibit limited bandwidth and sensitivity to fabrication tolerances.

Thesis Contributions and Outline

The objective of this thesis is to advance silicon photonic WDM systems by addressing key challenges in scaling channel counts, minimizing insertion loss, enhancing signal integrity, improving robustness to fabrication variations, and reducing overall system power consumption.

This work contributes to the realization of highly dense WDM systems, including a DWDM system with 128 channels and 100 GHz channel spacing (DWDM-128×100 GHz). The schematic of a taped-out DWDM-128×100 GHz system is shown in Fig. 1.9, while zoomed in views of building blocks of the system are shown in Fig .1.10, Fig.1.11, and Fig.1.12.

The proposed DWDM-128×100 GHz system is based on a combination of an MZI interleaver (Fig. 1.10), MRRs (Fig. 1.11), and MZI-based CWDM systems (Fig. 1.12). MZI interleavers are efficient, low-loss, and reliable, enabling scalable channel counts in DWDM systems while having the ability to provide flat-top passbands with lattice configurations [52]. Additionally, MRRs offer compactness and high spectral selectivity, making them attractive for DWDM systems [29]. MZI-CWDM systems can scale up the channel count leveraging their large free spectral range (FSR) to improve tolerance to fabrication variations [53]. Such a large scale DWDM system will eventually require temperature control to compensate for temperature drifts [9].

To achieve a high-performance DWDM-128×100 GHz WDM filter, the design incorporates 32 rings coupled with 4 parallel bus waveguides of the interleaver, where each ring drop port is coupled to a CWDM-4 system as depicted in Fig. 1.9. The MRRs have been already optimized in earlier work at IMEC [29].

Each bus waveguide is coupled to 8 rings, with a channel spacing of 400 GHz (Fig. 1.11). The working wavelengths of the rings are staggered by 100 GHz across the 4 bus waveguides. To divide the 128×100 GHz input signals into the 4 bus waveguides, spiral phase shifters are utilized to construct a 4-channel MZI interleaver, which separates the input into 4 groups of 32×400 GHz signals. The demultiplexing of the interleaver stage is illustrated in Fig. 1.10. Each ring drop

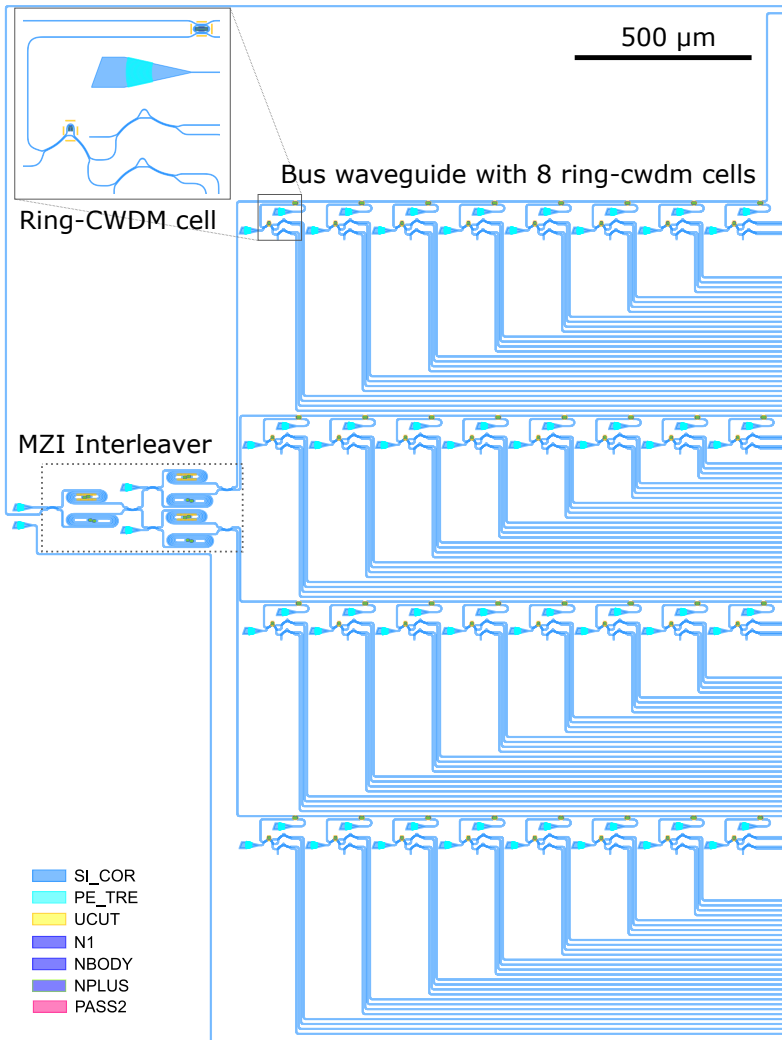

Figure 1.9: Schematic of the taped-out DWDM-128 × 100 GHz system. The architecture integrates a 4-channel MZI interleaver, microring resonators (MRRs), and CWDM-4 filters. The interleaver divides the input into four groups, each routed to a bus waveguide with 8 staggered MRRs (32 in total). Each MRR drop port is cascaded with a CWDM-4 filter, enabling demultiplexing into 128 channels with 100 GHz spacing. In the initial design run, the CWDM-4 filters are thermally tuned to compensate for fabrication variations; future iterations aim for heater-free operation. SI_COR represents fully etched silicon, PE_TRE partially etched silicon, N1 an N-type implant, NBODY an N-type body implant, and NPLUS an N-type contact implant.

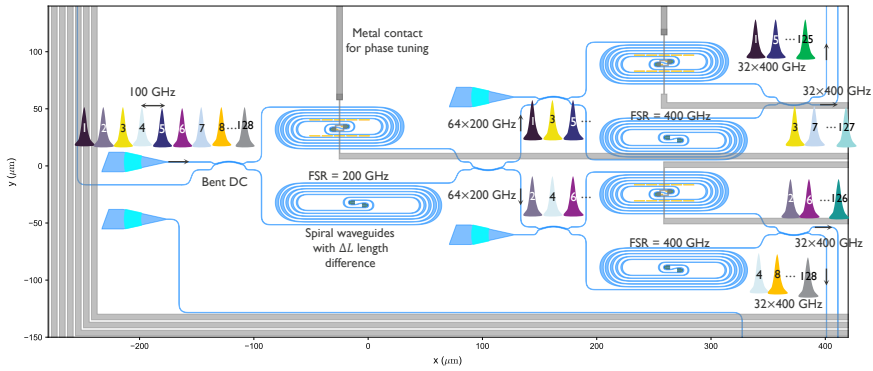

Figure 1.10: Zoomed in view of the interleaver used in the DWDM-128×100 GHz system in Fig. 1.9

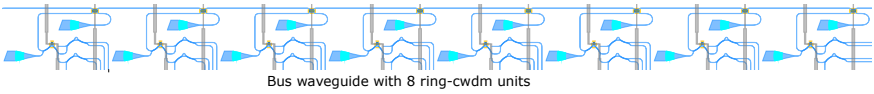

Figure 1.11: Zoomed in view of one of the ring racks used in the DWDM-128×100 GHz system in Fig. 1.9

port in the bus waveguides extracts four channels with a channel spacing of 3.2 THz. Subsequently, each ring drop port is cascaded with a CWDM-4 system featuring an FSR of 12.8 THz, enabling the final demultiplexing of signals into four outputs per ring. As an example, Fig. 1.12 illustrates the demultiplexing process for the first ring in the first bus waveguide. Overall, the proposed design eventually enables the 128 channels to be demultiplexed via 128 output waveguides. It is important to mention that such system would require active thermal tuning, in particular for the DWDM and the MRRs, to compensate for any possible drifts, and to compensate for fabrication variabilities. Further information regarding the thermo-optic phase shifters utilized in this thesis can be found in [29].

To realize such a complex system, several components must be developed and optimized. Among these, the broadband DC is of paramount importance. The DC is a critical element in both the interleaver and the CWDM-4 systems, necessitating a design with exceptionally low loss to prevent scaling up the system's overall insertion loss.

The DWDM-128×100 GHz WDM filter spans a spectral range of 12.8 THz, corresponding to approximately 72 nm in the O-band. Consequently, the broadband DC must exhibit minimal coupling variation across this entire wavelength range to ensure high signal integrity throughout the system. By leveraging the design of

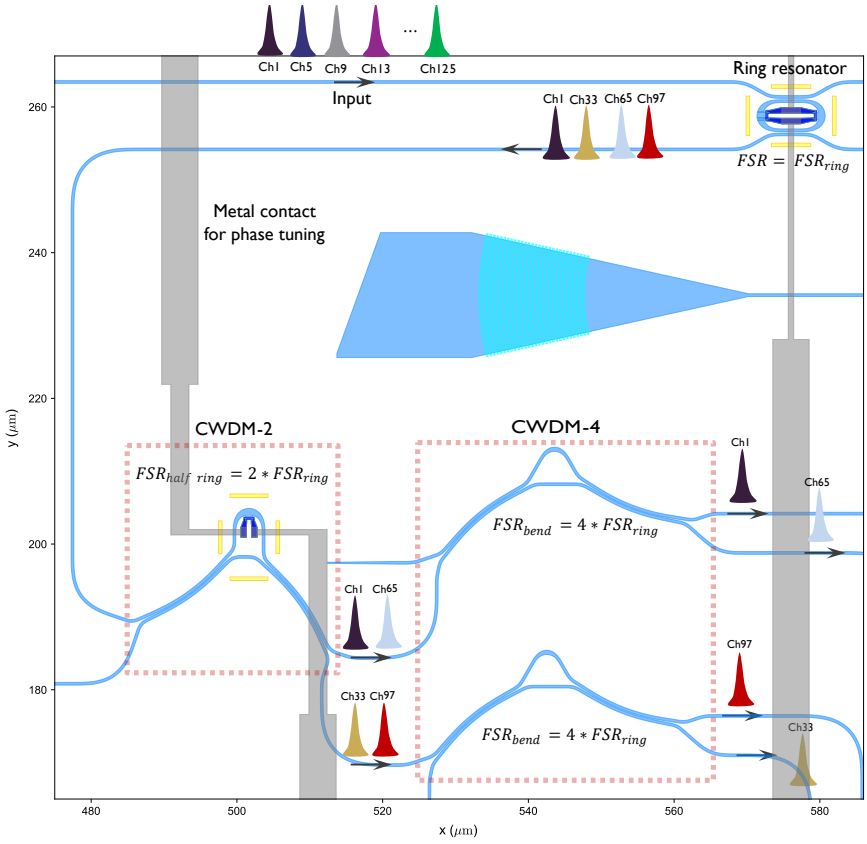

Figure 1.12: Zoomed in view of one of the CWDM-4 used in the DWDM-128×100 GHz system in Fig. 1.9

a broadband DC, a DWDM-4×100 GHz system can be developed, which serves as a foundational building block for scaling to the full DWDM-128×100 GHz architecture.

Additionally, CWDM systems play a critical role in this design. These systems must operate efficiently over a broad wavelength range, ideally without requiring thermal tuning to minimize power consumption, while maintaining low insertion loss and high channel isolation. The integration of robust CWDM systems ensures the scalability and energy efficiency of the overall WDM architecture.

By optimizing the aforementioned building blocks, significant improvements in DWDM and CWDM systems are achieved, particularly in channel isolation, insertion loss, and wavelength operation range. Additionally, novel CWDM system designs are introduced, minimizing phase errors and demonstrating robustness

across a 300 mm wafer. These systems exhibit high performance without requiring thermal tuning, significantly reducing the overall system power consumption.

The remainder of this thesis is structured as follows:

- **Chapter 2: Wavelength Filters Fundamentals:**

  This chapter reviews the principles of wavelength filters and evaluates state-of-the-art multiplexing architectures including Mach Zehnder Interferometers, Microring resonators, Arrayed waveguides and Echelle gratings. The key performance metrics and essential basics of WDM filters are also discussed. Further, we discuss the challenges in current WDM architectures and how this work addresses some of these challenges.

- **Chapter 3: Broadband Bent Directional Couplers:**

  Broadband couplers (splitters) are critical for scaling channel counts while maintaining high channel isolation and low excess loss in WDM filters. Conventional designs based on straight DCs often degrade the performance of WDM filters. This chapter presents the design of broadband, low-loss, and compact bent DCs, along with a model to achieve arbitrary coupling ratios. A bent DC is demonstrated with a 7.67$\times$ reduction in coupling variation compared to conventional designs, while maintaining compactness and low loss. The proposed design is validated through measurements across 63 dies on a 300 mm wafer, showcasing its robustness. The bent DC is subsequently employed in later sections to enhance the performance of WDM systems.

- **Chapter 4: Broadband Adiabatic Couplers:**

  While bent DCs offer broadband operation, they still exhibit non-negligible coupling variation, indicating the potential for further performance enhancement. This chapter introduces a novel design methodology for adiabatic couplers, which achieves ultra-low coupling variation and ultra compact taper lengths through a min-max optimization framework. Utilizing this approach, coupling variation is reduced by over $16\times$ compared to conventional designs, and the shortest taper length reported in the literature for an adiabatic coupler is achieved, to our best knowledge. This design can be used in future design iterations in highly dense WDM systems.

- **Chapter 5: Dense Wavelength Division Multiplexing Systems:**

  This chapter demonstrates DWDM systems with enhanced operation range and channel isolation based on broadband DCs. The proposed design of a DWDM-2$\times$100 GHz achieves a 2.7$\times$ improvement in operational wavelength range compared to straight-coupler-based architectures, while also showcasing robustness across fabrication variations as proved by wafer-scale measurements.

The chapter also demonstrates more complex DWDM systems such as DWDM-16×800 GHz based on transfer matrix method. Finally, the measurement results of DWDM-16×200 GHz are discussed.

- **Chapter 6: Coarse Wavelength Division Multiplexing Systems:**

  This chapter presents a novel design approach for coarse wavelength division multiplexing (CWDM) systems that significantly reduces sensitivity to fabrication variations and minimizes excess loss, while having large channel isolation over broad wavelength range. The design is based on employing minimal common arm lengths in MZI architectures, resulting in improved uniformity and robustness across the entire wafer. By addressing key limitations of traditional MZI-based systems, the proposed approach also offers the potential to eliminate the need for thermal tuning, thereby reducing power consumption, which is an increasingly critical metric in modern WDM systems.

- **Chapter 7: Conclusions:**

  This chapter summarizes the key contributions of the thesis and discusses possible future directions for this research. The work presented in this thesis provides a foundation for scaling WDM channel counts while overcoming known limitations in bandwidth and fabrication sensitivity.

1.4 Publications[1]

Journal Papers

- **A. Bayoumi*** et al., Low-Loss Silicon Directional Coupler with Arbitrary Coupling Ratios for Broadband Wavelength Operation Based on Bent Waveguides, *Journal of Lightwave Technology*, 2024.
- **A. Bayoumi** et al., Enhanced Operation Range of Silicon MZI Filters Using a Broadband Bent Directional Coupler , *IEEE Photonics Technology Letters*, 2025.
- **A. Bayoumi** et al., Broadband and Ultra-Compact Adiabatic Coupler Based on Linearly Tapered Silicon Waveguides , *arXiv (preprint)*, 2025.
- **A. Bayoumi** et al., Robust and Low-Loss Coarse Wavelength Division Multiplexing Filters in Silicon Photonics , *Manuscript In preparation*, 2025.

[1] Ahmed Bayoumi has publication names of A. Bayoumi and A. H. El-Saeed

- Q. Deng, **A. Bayoumi*** et al., Low-Loss and Low-Power Silicon Ring-Based WDM 32 × 100 GHz Filter Enabled by a Novel Bend Design, *Laser and Photonics Reviews*, 2024.
- A. Elshazly, **A. Bayoumi** et al., Silicon Photonic Polarization Beam Splitter with Low Loss and High Extinction Ratio Enabled by TOPIC Bends, *Submitted*, 2025.
- A. Elshazly, **A. Bayoumi** et al., Silicon Photonic S-Bent Directional Coupler with Low Wavelength-Dependent Coupling Variation , *Manuscript In preparation*, 2025.

International Conferences

- **A. Bayoumi*** et al., Wavelength-insensitive and lossless 50: 50 directional coupler based on silicon bent waveguides , *IEEE Silicon Photonics Conference*, 2024.
- Q. Deng, J.Coster, R. Magdziak, **A. Bayoumi*** et al., Ultra-compact silicon rings with high thermal tuning efficiency demonstrated as an 8x 400 GHz WDM filter , *Optical Fiber Communication Conference (OFC)*, 2025.
- Q. Deng, **A. Bayoumi*** et al., 32x 100 GHz WDM filter based on ultra-compact silicon rings with a high thermal tuning efficiency of 5.85 mW/π , *Optical Fiber Communication Conference (OFC)*, 2024.
- Q.Deng , J. De Coster, R. Magdziak, **A. Bayoumi*** et al., Silicon Ring Based Wavelength Division Multiplexing With an Ultra-wide Spectral Range of 6.4 THz , *IEEE Silicon Photonics Conference*, 2024.
- Q.Deng , P. Neutens, R. Magdziak, **A. Bayoumi*** et al., Low-loss waveguide bend supporting a whispering gallery mode , *IEEE Silicon Photonics Conference*, 2023.

References

[1] Jia ming Liu. *Photonic Devices*. Cambridge University Press, April 2005. ISBN 9780521551953. doi: 10.1017/cbo9780511614255.

[2] Cyriel Minkenberg, Nathan Farrington, Aaron Zilkie, David Nelson, Caroline P. Lai, Dan Brunina, Jerry Byrd, Bhaskar Chowdhuri, Nick Kucharewski, Karl Muth, Amit Nagra, German Rodriguez, David Rubi, Thomas Schrans, Pradeep Srinivasan, Yeong Wang, Chiang Yeh, and Andrew Rickman. Reimagining datacenter topologies with integrated silicon photonics. *Journal of Optical Communications and Networking*, 10(7):B126, June 2018. ISSN 1943-0639. doi: 10.1364/jocn.10.00b126.

[3] D. Miller. Device requirements for optical interconnects to silicon chips. *Proceedings of the IEEE*, 97(7):1166–1185, July 2009. ISSN 1558-2256. doi: 10.1109/jproc.2009.2014298.

[4] Bahram Jalali and Sasan Fathpour. Silicon Photonics. *Journal of Lightwave Technology*, 24(12):4600–4615, 2006. ISSN 0277-786X. doi: 10.1016/B978-0-12-374171-4.00011-3. ISBN: 9780123741714.

[5] D.A.B. Miller and H.M. Ozaktas. Limit to the bit-rate capacity of electrical interconnects from the aspect ratio of the system architecture. *Journal of Parallel and Distributed Computing*, 41(1):42–52, February 1997. ISSN 0743-7315. doi: 10.1006/jpdc.1996.1285.

[6] Wim Bogaerts and Lukas Chrostowski. Silicon photonics circuit design: Methods, tools and challenges. *Laser and Photonics Reviews*, 12(4), March 2018. ISSN 1863-8899. doi: 10.1002/lpor.201700237.

[7] Wim Bogaerts, Pieter Dumon, Dries Van Thourhout, and Roel Baets. Low-loss, low-cross-talk crossings for silicon-on-insulator nanophotonic waveguides. *Optics Letters*, 32(19):2801, 2007. ISSN 0146-9592. doi: 10.1364/OL.32.002801. URL http://ol.osa.org/abstract.cfm?URI=ol-32-19-2801. Publisher: OSA.

[8] R. Palmer, L. Alloatti, D. Korn, P. C. Schindler, R. Schmogrow, W. Heni, S. Koenig, J. Bolten, T. Wahlbrink, M. Waldow, H. Yu, W. Bogaerts, P. Verheyen, G. Lepage, M. Pantouvaki, J. Van Campenhout, P. Absil, R. Dinu, W. Freude, C. Koos, and J. Leuthold. Silicon-Organic Hybrid MZI Modulator Generating OOK, BPSK and 8-ASK Signals for Up to 84 Gbit/s. *IEEE Photonics Journal*, 5(2):6600907–6600907, April 2013. ISSN 1943-0655. doi: 10.1109/JPHOT.2013.2258142. URL http://ieeexplore.ieee.org/document/6502647/.

[9] Dajian Liu, Hongnan Xu, Ying Tan, Yaocheng Shi, and Daoxin Dai. Silicon photonic filters. *Microwave and Optical Technology Letters*, 63(9):2252–2268, 2021. ISSN 1098-2760. doi: 10/gg6sj8.

[10] Lei Jin, Mingyu Li, and Jian-Jun He. Highly-sensitive silicon-on-insulator sensor based on two cascaded micro-ring resonators with vernier effect. *Optics Communications*, 284(1):156–159, January 2011. ISSN 0030-4018. doi: 10.1016/j.optcom.2010.08.035. URL https://www.sciencedirect.com/science/article/pii/S0030401810008904.

[11] Huang Zengzhi, Yong Zhang, Cheng Zeng, Danping Li, Muhammad Shemyal Nisar, Jinzhong Yu, and Jinsong Xia. High confinement factor ridge slot waveguide for optical sensing. *IEEE Photonics Technology Letters*, 27(22): 2395–2398, 2015. doi: 10.1109/LPT.2015.2466595.

[12] C. Ciminelli, F. Dell'Olio, D. Conteduca, C.M. Campanella, and M.N. Armenise. High performance SOI microring resonator for biochemical sensing. *Optics & Laser Technology*, 59:60–67, July 2014. ISSN 0030-3992. doi: 10.1016/j.optlastec.2013.12.011.

[13] Nicholas C. Harris, Darius Bunandar, Mihir Pant, Greg R. Steinbrecher, Jacob Mower, Mihika Prabhu, Tom Baehr-Jones, Michael Hochberg, and Dirk Englund. Large-scale quantum photonic circuits in silicon. *Nanophotonics*, 5 (3):456–468, August 2016. ISSN 2192-8606. doi: 10.1515/nanoph-2015-0146.

[14] Gaolu Zhang, Zhizun Zhao, Jincheng Dai, Shanglin Yang, Xin Fu, and Lin Yang. Polarization-based Quantum Key Distribution Encoder and Decoder on Silicon Photonics. *Journal of Lightwave Technology*, pages 1–1, 2021. ISSN 1558-2213. doi: 10.1109/JLT.2021.3131193. Conference Name: Journal of Lightwave Technology.

[15] A.S. Jugessur, J. Dou, J.S. Aitchison, R.M. De La Rue, and M. Gnan. A photonic nano-bragg grating device integrated with microfluidic channels for bio-sensing applications. *Microelectronic Engineering*, 86(4–6):1488–1490, April 2009. ISSN 0167-9317. doi: 10.1016/j.mee.2008.12.002.

[16] Wim Bogaerts, Daniel Pérez, José Capmany, David A. B. Miller, Joyce Poon, Dirk Englund, Francesco Morichetti, and Andrea Melloni. Programmable photonic circuits. *Nature*, 586(7828):207–216, October 2020. ISSN 1476-4687. doi: 10.1038/s41586-020-2764-0.

[17] F. J. Ferraro, P. De Heyn, M. Kim, N. Rajasekaran, M. Berciano, G. Muliuk, D. Bode, G. Lepage, S. Janssen, R. Magdziak, J. De Coster, H. Kobbi, S. Lardenois, N. Golshani, L. Shiramin, C. Marchese, S. Rajmohan, S. Nadarajan,

N. Singh, S. Radhakrishnan, A. Tsiara, P. Xu, A. Karagoz, D. Yudistira, M. Martire, A. Shahar, M. Chakrabarti, D. Velenis, W. Guo, A. Miller, Kristof Croes, S. Balakrishnan, P. Verheyen, Y. Ban, J. Van Campenhout, and P. P. Absil. Imec silicon photonics platforms: performance overview and roadmap. In *Next-Generation Optical Communication: Components, Sub-Systems, and Systems XII*, volume 12429, pages 22–28. SPIE, March 2023. doi: 10.1117/12.2650579.

[18] S.K. Selvaraja, P. Jaenen, W. Bogaerts, D. Van Thourhout, P. Dumon, and R. Baets. Fabrication of photonic wire and crystal circuits in silicon-on-insulator using 193-nm optical lithography. *Journal of Lightwave Technology*, 27(18):4076–4083, September 2009. ISSN 1558-2213. doi: 10.1109/jlt.2009.2022282.

[19] M. Pantouvaki, S. A. Srinivasan, Y. Ban, P. De Heyn, P. Verheyen, G. Lepage, H. Chen, J. De Coster, N. Golshani, S. Balakrishnan, P. Absil, and J. Van Campenhout. Active components for 50 gb/s nrz-ook optical interconnects in a silicon photonics platform. *Journal of Lightwave Technology*, 35(4): 631–638, February 2017. ISSN 1558-2213. doi: 10.1109/jlt.2016.2604839.

[20] Yole Group. 2023 silicon photonics outlook. https://www.yolegroup.com/yole-group-actuality/2023-silicon-photonics-outlook/, 2023. Accessed: 2025-05-17.

[21] Chen Sun, Mark T. Wade, Yunsup Lee, Jason S. Orcutt, Luca Alloatti, Michael S. Georgas, Andrew S. Waterman, Jeffrey M. Shainline, Rimas R. Avizienis, Sen Lin, Benjamin R. Moss, Rajesh Kumar, Fabio Pavanello, Amir H. Atabaki, Henry M. Cook, Albert J. Ou, Jonathan C. Leu, Yu-Hsin Chen, Krste Asanović, Rajeev J. Ram, Miloš A. Popović, and Vladimir M. Stojanović. Single-chip microprocessor that communicates directly using light. *Nature*, 528(7583):534–538, December 2015. ISSN 1476-4687. doi: 10.1038/nature16454.

[22] Yichen Shen, Nicholas C. Harris, Scott Skirlo, Mihika Prabhu, Tom Baehr-Jones, Michael Hochberg, Xin Sun, Shijie Zhao, Hugo Larochelle, Dirk Englund, and Marin Soljačić. Deep learning with coherent nanophotonic circuits. *Nature Photonics*, 11(7):441–446, June 2017. ISSN 1749-4893. doi: 10.1038/nphoton.2017.93.

[23] Christopher V. Poulton, Ami Yaacobi, David B. Cole, Matthew J. Byrd, Manan Raval, Diedrik Vermeulen, and Michael R. Watts. Coherent solid-state LIDAR with silicon photonic optical phased arrays. *Optics Letters*, 42(20): 4091, October 2017. ISSN 1539-4794. doi: 10.1364/ol.42.004091.

[24] M.C. Estevez, M. Alvarez, and L.M. Lechuga. Integrated optical devices for lab-on-a-chip biosensing applications. *Laser and Photonics Reviews*, 6(4): 463–487, September 2011. ISSN 1863-8899. doi: 10.1002/lpor.201100025.

[25] NVIDIA Corporation. Nvidia spectrum-x photonics co-packaged optics networking switches to scale ai factories to millions of gpus. https://nvidianews.nvidia.com/news/nvidia-spectrum-x-co-packaged-optics-networking-switches-ai-factories/, 2025.

[26] NVIDIA Corporation. Nvidia and tsmc collaboration on photonics-enabled ai accelerators, 2025. Press Release. Available at: https://investor.nvidia.com/news/press-release-details/2025/NVIDIA-Announces-Spectrum-X-Photonics-Co-Packaged-Optics-Networking-Switches-to-Scale-AI-Factories-to-Millions-of-GPUs/default.aspx.

[27] Minh A. Tran, Duanni Huang, Tin Komljenovic, Jonathan Peters, Aditya Malik, and John E. Bowers. Ultra-low-loss silicon waveguides for heterogeneously integrated silicon/iii-v photonics. *Applied Sciences*, 8(7):1139, July 2018. ISSN 2076-3417. doi: 10.3390/app8071139.

[28] Ang Li, Yufei Xing, Raphael Van Laer, Roel Baets, and Wim Bogaerts. Extreme spectral transmission fluctuations in silicon nanowires induced by backscattering. In *2016 IEEE 13th International Conference on Group IV Photonics (GFP)*, pages 160–161. IEEE, August 2016. doi: 10.1109/group4.2016.7739068.

[29] Qingzhong Deng, Ahmed H. El-Saeed, Alaa Elshazly, Guy Lepage, Chiara Marchese, Pieter Neutens, Hakim Kobbi, Rafal Magdziak, Jeroen De Coster, Javad Rahimi Vaskasi, Minkyu Kim, Yeyu Tong, Neha Singh, Marko Ersek Filipcic, Pol Van Dorpe, Kristof Croes, Maumita Chakrabarti, Dimitrios Velenis, Peter De Heyn, Peter Verheyen, Philippe Absil, Filippo Ferraro, Yoojin Ban, and Joris Van Campenhout. Low-loss and low-power silicon ring based WDM 32×100 GHz filter enabled by a novel bend design. *Laser & Photonics Reviews*, November 2024. ISSN 1863-8899. doi: 10.1002/lpor.202401357.

[30] Qingzhong Deng, Pieter Neutens, Rafal Magdziak, Ahmed H. El-Saeed, Yoojin Ban, Filippo Ferraro, Guy Lepage, Jeroen De Coster, Dimitrios Velenis, Maumita Chakrabarti, Peter De Heyn, Peter Verheyen, Pol Van Dorpe, and Joris Van Campenhout. Low-loss Waveguide Bend Supporting a Whispering Gallery Mode. In *2023 IEEE Silicon Photonics Conference*, pages 1–2, April 2023. doi: 10.1109/SiPhotonics55903.2023.10141913. ISSN: 1949-209X.

[31] Govind P. Agrawal. *Fiber-optic communication systems*. Wiley series in microwave and optical engineering. Wiley, Hoboken, NJ, fifth edition edition, 2021. ISBN 9781119737391. Includes bibliographical references and index.

[32] Bahaa E. A. Saleh and Malvin Carl Teich. *Fundamentals of Photonics*. Wiley, second edition edition, 2007. ISBN 978-0471358329.

[33] W. Bogaerts, P. De Heyn, T. Van Vaerenbergh, K. De Vos, S. Kumar Selvaraja, T. Claes, P. Dumon, P. Bienstman, D. Van Thourhout, and R. Baets. Silicon microring resonators. *Laser & Photonics Reviews*, 6(1):47–73, 2012. ISSN 1863-8899. doi: 10/cr3dtz. ZSCC: 0001902 _eprint:.

[34] Karl S. Kunz and Raymond J. Luebbers. *The Finite Difference Time Domain Method for Electromagnetics*. CRC Press, May 2018. ISBN 9780203736708. doi: 10.1201/9780203736708.

[35] Susanne C. Brenner and L. Ridgway Scott. *The Mathematical Theory of Finite Element Methods*. Springer New York, 2008. ISBN 9780387759340. doi: 10.1007/978-0-387-75934-0.

[36] Jin-Fa Lee, R. Lee, and A. Cangellaris. Time-domain finite-element methods. *IEEE Transactions on Antennas and Propagation*, 45(3):430–442, March 1997. ISSN 0018-926X. doi: 10.1109/8.558658.

[37] Photon Design. Omnisim FETD engine. https://photond.com/omnisim/features/fetd-engine. Accessed: 2025-07-06.

[38] J. Van Roey, J. van der Donk, and P. E. Lagasse. Beam-propagation method: analysis and assessment. *Journal of the Optical Society of America*, 71(7): 803, July 1981. ISSN 0030-3941. doi: 10.1364/josa.71.000803.

[39] Dominic F. G. Gallagher and Thomas P. Felici. Eigenmode expansion methods for simulation of optical propagation in photonics: pros and cons. In Yakov S. Sidorin and Ari Tervonen, editors, *Integrated Optics: Devices, Materials, and Technologies VII*. SPIE, June 2003. doi: 10.1117/12.473173.

[40] Charalambos C. Katsidis and Dimitrios I. Siapkas. General transfer-matrix method for optical multilayer systems with coherent, partially coherent, and incoherent interference. *Applied Optics*, 41(19):3978, July 2002. ISSN 1539-4522. doi: 10.1364/ao.41.003978.

[41] Python Software Foundation. Python programming language. https://www.python.org/, 2024. https://www.python.org/.

[42] NumPy Developers. NumPy: The fundamental package for scientific computing with python. https://numpy.org/, 2024.

[43] SciPy Developers. SciPy: Scientific computing tools for python. https://scipy.org/, 2024.

[44] Matplotlib Development Team. Matplotlib: Visualization with python. https://matplotlib.org/, 2024.

[45] The pandas development team. pandas: Python data analysis library. https://pandas.pydata.org/, 2024.

[46] Ansys Lumerical. LumAPI - python scripting interface. https://optics.ansys.com, 2024. https://optics.ansys.com/hc/en-us/articles/360034494114-LumAPI-Python-Scripting-Interface.

[47] MPh Developers. Mph: Python interface for comsol multiphysics. https://mph.readthedocs.io, 2024. https://mph.readthedocs.io.

[48] GDSFactory Developers. gdsfactory: Photonic integrated circuit layout generator. https://gdsfactory.github.io/, 2024.

[49] gdstk: Python library for gdsii manipulation. https://github.com/heitzmann/gdstk, 2021. Accessed: 2025-05-17.

[50] Cisco. Cisco annual internet report (2018–2023). Technical report, Cisco Systems, 2020. https://www.cisco.com/c/en/us/solutions/executive-perspectives/annual-internet-report/index.html.

[51] Nabarun Saha, Giuseppe Brunetti, Annarita di Toma, Mario Nicola Armenise, and Caterina Ciminelli. Silicon photonic filters: A pathway from basics to applications. *Advanced Photonics Research*, March 2024. ISSN 2699-9293. doi: 10.1002/adpr.202300343.

[52] Qingzhong Deng, Lu Liu, Rui Zhang, Xinbai Li, Jurgen Michel, and Zhiping Zhou. Athermal and flat-topped silicon mach-zehnder filters. *Optics Express*, 24(26):29577, December 2016. ISSN 1094-4087. doi: 10.1364/OE.24.029577. URL https://www.osapublishing.org/abstract.cfm?URI=oe-24-26-29577.

[53] Hongnan Xu and Yaocheng Shi. Flat-Top CWDM (De)Multiplexer Based on MZI With Bent Directional Couplers. *IEEE Photonics Technology Letters*, 30 (2):169–172, January 2018. ISSN 1941-0174. doi: 10.1109/LPT.2017.2779489.

2

Wavelength Filters Fundamentals

This chapter is structured as follows: It begins with an introduction to the principles of wavelength division multiplexing (WDM) and its importance in optical communication systems. The chapter then delves into the critical performance metrics for WDM filters, followed by a detailed review of different WDM filter architectures in silicon photonics. Challenges in WDM filter design are subsequently explored, along with ongoing research directions.

2.1 Introduction 36
2.2 Optical Filters in Communication Systems 37
2.3 WDM Key Performance Metrics 41
2.4 WDM Filter Architectures in Silicon Photonics 44
Finite impulse response (FIR) filters 44
Microring Resonators (MRRs) 49
Arrayed Waveguide Gratings (AWGs) 52
Echelle Diffraction Gratings (EDGs) 54
2.5 Challenges in WDM Filters and Research Directions . . . 56
Fabrication Variability and Tolerance 56
Thermal Sensitivity and Power Consumption 56
Spectral Density and Scalability 57
2.6 Conclusion 57
References 59

2.1 Introduction

The relentless growth in global data traffic, driven by applications such as high performance computing (HPC), cloud data centers, and artificial intelligence (AI), demands photonic interconnects that are both highly scalable and energy efficient [1]. Wavelength Division Multiplexing (WDM) addresses this requirement by transmitting multiple data channels concurrently over distinct optical wavelengths, thereby multiplying the aggregate bandwidth of a single waveguide. Silicon photonics, leveraging mature CMOS compatible fabrication techniques, provides an attractive platform for realizing dense, low cost photonic integrated circuits (PICs) tailored to WDM applications [2–4].

At the heart of any WDM link lies the wavelength selective filter, whose role is to combine (multiplex) or separate (demultiplex) distinct wavelength channels with stringent requirements of high spectral resolution, minimal insertion loss, and low crosstalk [5, 6]. WDM systems can be broadly categorized based on channel spacing into two types: dense WDM (DWDM) systems and coarse WDM (CWDM) systems.

DWDM systems are designed for high-capacity, long-haul optical communication. They feature much narrower channel spacing, typically in the range of 0.8 nm to 0.4 nm (100 GHz to 50 GHz in frequency spacing), allowing for a significantly higher number of channels within the same spectral bandwidth. DWDM systems require advanced filter architectures with high spectral selectivity, low crosstalk, and precise wavelength alignment. These systems are well-suited for long-haul and high-capacity networks. However, due to silicon's high thermo-optic coefficient ($\mathrm{d}n/\mathrm{d}T \approx 1.8 \times 10^{-4}\,\mathrm{K}^{-1}$), DWDM systems in silicon photonics necessitate precise temperature control to maintain wavelength stability and minimize thermal drift [3, 5].

CWDM systems, on the other hand, typically have wider channel spacing, ranging from 10 nm to 20 nm, and support fewer channels compared to DWDM systems. The wider spacing reduces the complexity of the optical components, making CWDM systems more cost-effective and less sensitive to fabrication tolerances. CWDM is commonly used in short-reach applications, such as metropolitan area networks (MANs) and access networks, where high spectral efficiency is not a primary requirement. Most importantly, the wide channel spacing of CWDM filters enhances tolerance to wavelength drifts and reduces the need for precise wavelength alignment and stringent environmental temperature control. This enables the use of uncooled lasers, significantly simplifying system design and reducing overall complexity [5].

In silicon photonics, various architectures of WDM filters have been demonstrated

[2–5, 7], each offering a unique trade-off between footprint, channel count, spectral performance, insertion loss, and fabrication tolerance. This chapter reviews several principal classes of WDM silicon photonic filters: Mach-Zehnder Interferometers (MZIs) [8, 9], Microring Resonators (MRRs) [10, 11], Arrayed Waveguide Gratings (AWGs) [12–14], and Echelle Diffraction Gratings (EDGs) [15, 16]. Their operating principles, key performance metrics, and practical considerations, such as thermal tuning and process variation, are compared.

2.2 Optical Filters in Communication Systems

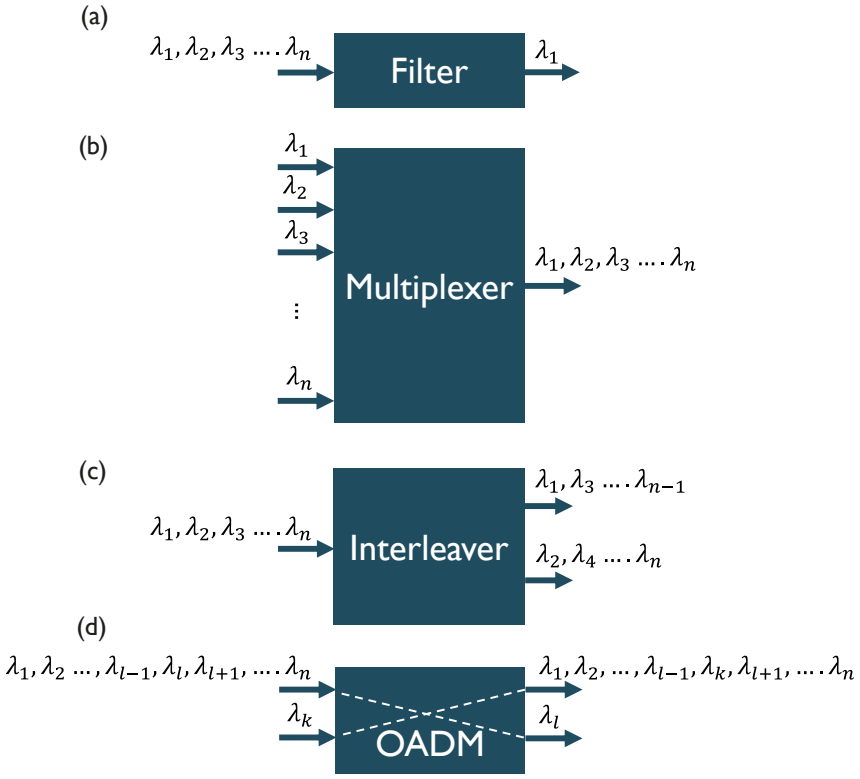

Figure 2.1: Different types of optical filters. (a) Filtering of a specific wavelength. (b) Multiplexer combining multiple wavelengths into a single output; the reverse operation is called demultiplexing. (c) Interleaver used to interleave or separate wavelength channels. (d) Optical add-drop multiplexer (OADM) where channel λ_k is added and channel λ_1 is dropped from the WDM spectrum.

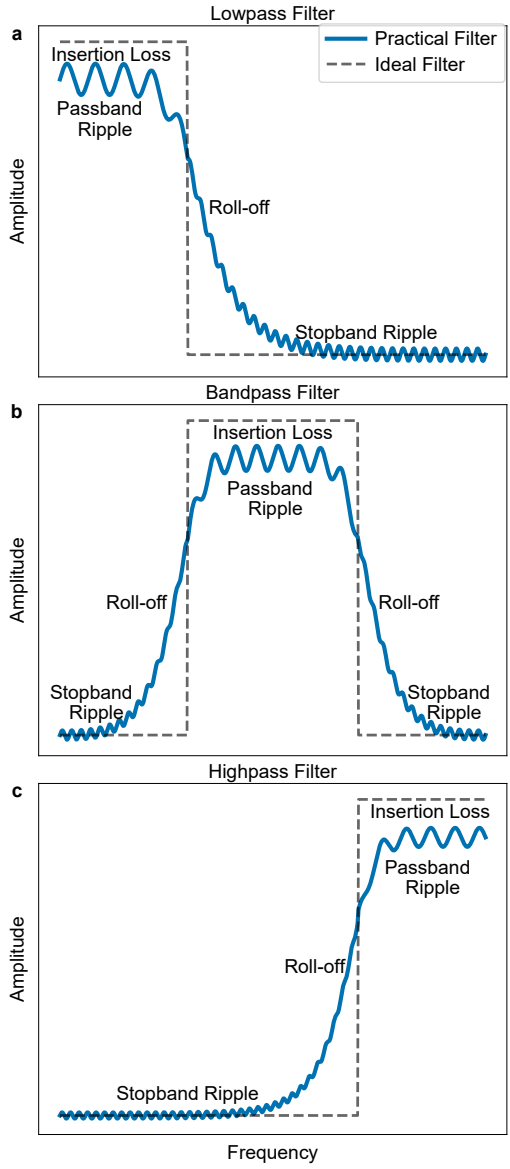

Figure 2.2: Comparison of low pass (a), band pass (b), and high pass (c) filter responses. The low-pass filter transmits longer wavelengths (lower frequencies) while blocking shorter ones. The bandpass filter allows transmission of light within a specific wavelength range while attenuating light outside this range. The high-pass filter transmits shorter wavelengths while blocking longer ones. The ideal filter response is shown in dashed grey, while the non-ideal filter response is shown in blue.

Optical filters are indispensable components in various applications, including telecommunications [17], spectroscopy [18], and optical signal processing [19]. Fundamentally, optical filters are often four-port devices consisting of an *input port*, *pass port*, *drop port*, and optionally, an *add port*. Their primary function is to selectively transmit signals of specific wavelengths while attenuating or rejecting others. In certain designs, the drop port may account for intrinsic losses, and the add port may not always be utilized.

Optical filters play a pivotal role in WDM systems and other optical communication technologies. The primary types of optical filters include:

- **Bandpass, Low pass, and High pass filters:** These filters allow transmission of light within a specified wavelength window while attenuating light outside this range. In single-channel systems, band pass filters improve the signal-to-noise ratio (SNR) by reducing noise introduced by optical amplifiers. They are also critical in multiplexing and demultiplexing operations in WDM systems. An example of a band filtering is shown in Fig. 2.1(a). Low-pass filters transmit longer wavelengths while blocking shorter ones. Conversely, high-pass filters transmit shorter wavelengths and block the longer ones. These filters are useful in isolating specific wavelength bands [6]. A simple comparison between the bandpass, low pass and high pass filters responses is shown in Fig. 2.2, where some nonidealities such as insertion loss, passband ripples, stopband ripples, and roll-off are annotated. Filter nonidealities are discussed in a later section. The most simple bandpass filter in photonics is a waveguide, where it is a two-port band pass filter with input and output ports.

- **Multiplexers and Demultiplexers:** Multiplexers combine multiple wavelength channels into a single output stream, while demultiplexers perform the reverse operation: separating the combined stream into distinct wavelength channels. These components are essential for WDM transmitters, receivers, and optical cross-connects (OXCs), where they enable routing of individual wavelength channels to specific output ports. The schematic for multiplexing operation is depicted in Fig. 2.1(b) [3].

- **Interleavers:** These are a special class of periodic bandpass filters used to interleave or separate wavelength channels at regular intervals. They are often used in DWDM systems to increase channel capacity by allowing closely spaced channels to be multiplexed and demultiplexed. Interleavers can be implemented using various architectures, including MZIs [20].

- **Optical Add-Drop Multiplexers (OADMs):** OADMs are key devices in reconfigurable WDM networks. They enable selective addition and removal of individual wavelength channels from a multi-channel optical signal. The

principle of OADM operation is shown in Fig. 2.1(d). OADMs can be implemented using MRRs [10].

These diverse filter architectures enable dynamic configuration, efficient multiplexing, and reliable management of optical networks, supporting high-capacity and high-speed data transmission over fiber-optic links.

The port configuration of a bandpass filter in PICs is a critical determinant of its functionality, particularly in signal routing and management. The number and arrangement of ports define the pathways for light propagation, governing how transmitted and rejected wavelength components are handled. This directly impacts device performance metrics such as insertion loss and determines the filter's suitability for specific applications. For wavelength-selective systems, such as OADMs, the port configuration is especially significant as it dictates whether unwanted spectral components are dissipated or redirected for further use within the network.

In the context of optical communications, bandpass filters can be categorized into three primary types based on their port configuration: two-port filters, three- or four-port filters, and multiple-port filters. Each configuration offers distinct operational characteristics and is tailored to specific application domains.

Two-port bandpass filters consist of a single input and a single output port. In these structures, wavelengths outside the passband are typically attenuated through radiation modes, scattering losses, or absorption. While these filters can effectively transmit desired wavelengths, they offer no means to collect or redirect the rejected wavelengths, which are simply lost as insertion loss. This fundamental limitation makes two-port filters unsuitable for applications requiring wavelength routing or channel add-drop functionality, despite their simplicity and compact footprint.

Three- or Four-port bandpass filters (input, passband output, rejection-band output, and optionally an add port) provide significantly enhanced functionality for wavelength management in complex photonic networks. The key advantage of this configuration is the ability to route different spectral components to physically separate ports, ensuring that both the passband and rejection band signals remain accessible within the waveguide network. This capability is particularly crucial for OADM applications, where specific wavelengths must be selectively dropped from or added without disrupting other channels.

Two filter architectures that inherently support three- or four-port operation and are therefore widely used in OADM applications are:

- **Mach-Zehnder Interferometers (MZIs):** In a properly designed MZI,

wavelengths that constructively interfere are routed to one output port (the 'bar' state), while wavelengths that destructively interfere are directed to the other output port (the 'cross' state). This wavelength-dependent routing enables simultaneous management of both transmitted and 'rejected' spectral components through distinct physical paths.

- **Microring Resonators (MRRs):** When coupled to two bus waveguides, MRRs naturally implement a four-port configuration. At resonant wavelengths, light couples into the ring and is transferred to the drop port of the second waveguide, while non-resonant wavelengths continue through the pass port with minimal attenuation. This intrinsic spectral separation mechanism makes MRRs particularly effective for wavelength-selective add-drop operations.

Multiple-port filters feature multiple output ports. Arrayed Waveguide Gratings (AWGs) and Echelle Diffraction Gratings (EDGs) are both planar waveguide devices that spatially separate wavelengths through optical path differences. However, AWGs and EDGs differ in the way these phase shifts are implemented: AWGs use an array of waveguides with incrementally increasing lengths, while EDGs rely on diffraction off a blazed grating. These devices typically feature 1 input port and N output ports, with each output port corresponding to a specific wavelength channel. Later sections will discuss these architectures in further detail.

2.3 WDM Key Performance Metrics

WDM systems require filters with specific performance characteristics to ensure efficient operation. A summary of commonly-used metrics in the literature are summarized in Fig. 2.3. The key performance metrics for WDM filters include:

- **Insertion loss (IL):** The loss of signal power due to the filter, measured as the ratio of input power to output power in the passband. Lower insertion loss is desirable for efficient signal transmission.
- **Free spectral range (FSR):** The wavelength spacing between adjacent transmission peaks in periodic filters. A larger FSR reduces channel overlap.
- **Full width at half maximum (FWHM):** The wavelength range over which the filter's transmission is at least 50% of its peak value. This metric characterizes the filter's bandwidth.

- **Intra-band and out of band ripple:** The variation in transmission within the passband and stopband, respectively. Ideally, the passband should be flat, but practical filters exhibit some ripple due to imperfections in design or fabrication.
- **Channel isolation:** The ability to separate adjacent channels without interference, typically measured as the difference in power between the peak of the desired channel and the maximum power leakage from adjacent channels at that wavelength. Higher channel isolation ensures better signal quality and reduces bit error rates.
- **Crosstalk:** The leakage of power from one channel into adjacent channels. Crosstalk is typically expressed in decibels (dB) and should be minimized for high channel isolation.
- **Roll off rate:** The steepness of the transition between the passband and stopband. A steeper roll-off rate indicates better spectral selectivity.
- **Temperature drift**: A wavelength drift in the filter performance due to temperature variations. Filters should be designed to minimize sensitivity to temperature changes, or include active tuning mechanisms to compensate for drift.

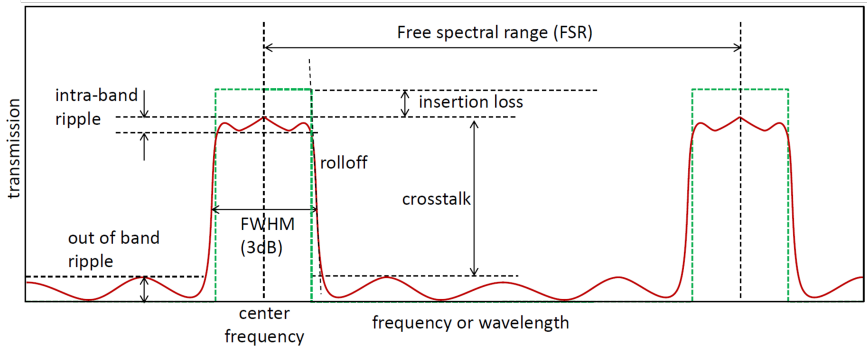

Figure 2.3: Key performance metrics for WDM filters including insertion loss (IL), free spectral range (FSR), full width at half maximum (FWHM), Intra-band and out-of-band ripple, crosstalk, and roll-off rate. The green dotted curves are ideal filters, while the red lines indicate typical actual performance of practical designs [21].

The performance metrics of WDM filters are intrinsically linked to the overall functionality and reliability of WDM communication systems. Understanding how these specifications impact system-level performance is essential for designing robust optical networks that comply with telecommunications standards, such as those defined by the International Telecommunication Union (ITU-T G.694.1) [22].

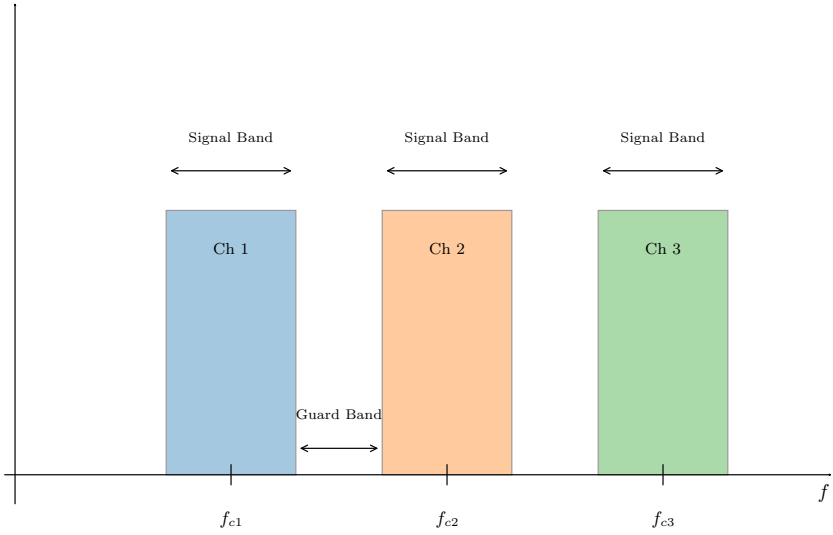

Figure 2.4: Schematic illustrating the signal band and the guard band in a WDM system. The signal band is the central spectral region where the modulated optical signal carries information, while the guard band is the spectral region between adjacent channels that prevents inter-channel interference.

In WDM system design, careful spectral allocation is required for each channel to ensure reliable operation. The definition of signal band and guard band (Fig. 2.4) is critical to understand how WDM filters metrics affect the overall system:

- **Signal band:** The central spectral region where the modulated optical signal carries information. The required signal bandwidth depends on the modulation format, data rate, and encoding scheme [6]. The filter's passband must fully encompass the signal bandwidth with minimal amplitude and phase distortion to maintain signal integrity. Excessive insertion loss or passband ripple can degrade performance and may necessitate optical amplification. Temperature-induced wavelength drift can also impact the signal, often requiring active thermal control.
- **Guard band:** The spectral region between adjacent channels that prevents inter-channel interference. The width of the guard band is determined by the filter's roll-off characteristics, wavelength stability, and standardized channel spacing (e.g., ITU-T: 100, 50, or 25 GHz) [22]. Sufficient guard bands are essential to minimize crosstalk and ensure channel isolation and high signal integrity.

A well-designed WDM filter must balance a sufficiently wide and flat passband for the signal, steep roll-off to minimize the guard band, and high wavelength stability to prevent channel overlap. These requirements directly influence system capacity, spectral efficiency, and overall network robustness.

2.4 WDM Filter Architectures in Silicon Photonics

WDM filters utilize multi-path interference to achieve wavelength selectivity. In its most basic form, this means splitting an optical signal into multiple paths with different optical lengths, and then recombining them so that constructive or destructive interference occurs at specific wavelengths. This principle underpins all major WDM filter architectures. In silicon photonics, these filters leverage the material properties of the silicon-on-insulator (SOI) platform. The high refractive index contrast between silicon ($n \approx 3.5$ at 1310 nm) and silica ($n \approx 1.44$) enables strong optical confinement and sub-micrometer waveguide dimensions. This allows for compact, densely integrated photonic circuits. However, the same high index contrast also increases sensitivity to fabrication imperfections, temperature variations, and high dispersion, which can degrade filter performance if not carefully managed. To leverage silicon's advantages while addressing its challenges, several silicon photonics filter architectures have been developed in the literature:

Finite impulse response (FIR) filters

Optical filters fundamentally operate on multi-path interference principles. This mechanism involves:

1. Splitting an input optical signal across multiple delay lines
2. Creating controlled optical path differences between these paths
3. Recombining the signals to produce wavelength-dependent interference patterns

The output of such an interferometric filter $y(t)$ (Fig. 2.5) can be mathematically represented as a weighted sum of delayed input samples:

$$y(t) = \sum_{k=0}^{M} b_k x(t - k\Delta t) \tag{2.1}$$

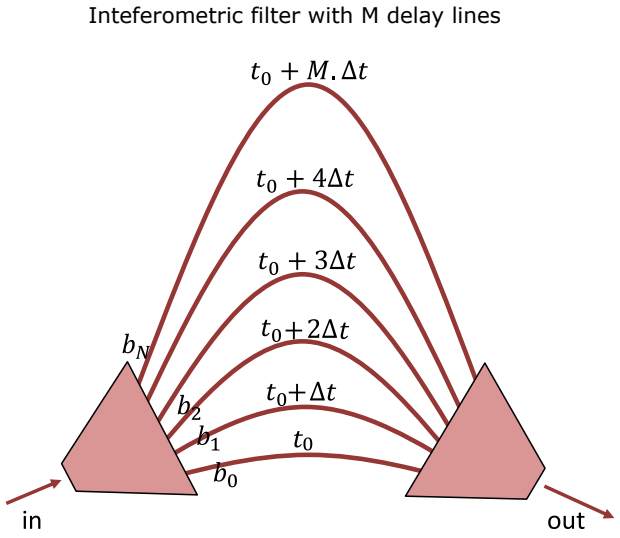

Figure 2.5: Schematic of an optical filter with M delay lines. The filter consists of an input port, M delay lines with different lengths, and an output port. The output signal is a superposition of the delayed signals from each delay line, resulting in a wavelength-dependent interference pattern. The transfer function of the filter can be expressed as a finite impulse response (FIR) filter in the time domain.

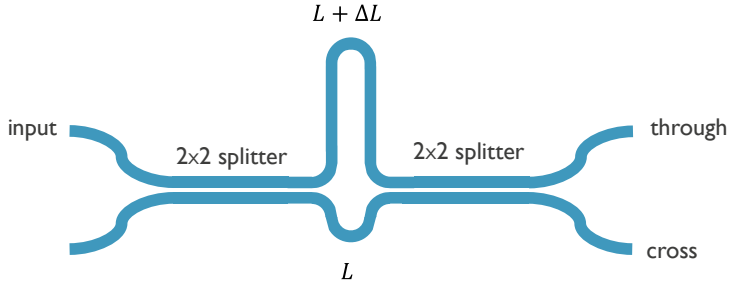

Figure 2.6: Schematic of an MZI filter. The MZI consists of an optical splitter, two waveguide arms with a length difference, allowing for wavelength-selective interference, and an optical combiner. The output is determined by the relative phase difference between the two arms, which can be tuned using thermal or electro-optic methods.

where $x(t)$ is the input signal at time t, Δt represents the time delay between adjacent paths, b_k are the tap coefficients controlling the contribution of each path, and M is the number of delay lines.

In the Z-domain, where $z^{-1} = e^{-j\omega\Delta t}$, this system transfer function $H(z)$ be-

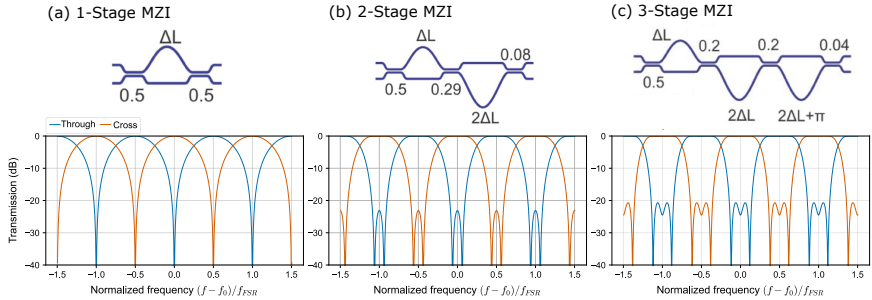

Figure 2.7: Schematic of cascaded MZI systems and their effect on passband flatness. The figure shows one-stage, two-stage, and three-stage MZI filters. The one-stage MZI uses two $0.5 : 0.5$ *couplers. The two-stage MZI uses three couplers with cross coupling ratios of 0.5, 0.29, and 0.08. The three-stage MZI uses four couplers with cross coupling ratios of 0.5, 0.2, 0.2, and 0.04. The MZI spectra are simulated with transfer matrix method. The MZI diagrams are adapted from [23].*

comes:

$$H(z) = \sum_{k=0}^{M} b_k z^{-k} \tag{2.2}$$

This can be equivalently expressed in factored form:

$$H(z) = k \prod_{i=0}^{M} (z - z_i) \tag{2.3}$$

where $z_i = e^{-j\omega_i \Delta t}$ are the complex zeros of the transfer function and k is a scaling factor. This implementation contains only zeros (no poles), constituting a finite impulse response (FIR) filter.

Mach-Zehnder Interferometer (MZI)

The Mach-Zehender interferometer (MZI) represents the simplest case: a single-zero FIR filter with two optical paths differing in length by ΔL (Fig. 2.6). Its transfer function in the Z-domain is:

$$H(z) = b_0 + b_1 z^{-1} \tag{2.4}$$

In the Fourier domain (evaluating on the unit circle $z = e^{j\omega}$), this becomes:

$$H(f) = b_0 + b_1 e^{-j2\pi f \Delta t} \tag{2.5}$$

where f represents the optical frequency and Δt is the relative time delay between interferometer arms. This function describes a periodic response with period equal to the Free Spectral Range (FSR) (see Appendix A.2.2 - A.2.4):

$$\text{FSR} = \frac{c}{n_g \Delta L} \approx \frac{\lambda_0^2}{n_g \Delta L} \tag{2.6}$$

where c is the speed of light in vacuum and n_g is the group index of the waveguide. The FSR defines the spectral spacing between adjacent transmission peaks.

The time delay Δt between optical paths relates to the physical path length difference ΔL by:

$$\Delta t = \frac{n_g \Delta L}{c} \tag{2.7}$$

Similarly, the phase delay $\Delta \phi$ is given by:

$$\Delta \phi = \frac{2\pi n_{eff} \Delta L}{\lambda} = \frac{2\pi n_{eff} \Delta L \cdot f}{c} \tag{2.8}$$

where n_{eff} is the effective refractive index of the waveguide mode. Both n_g and n_{eff} are generally wavelength-dependent, which affects the filter response across the spectrum.

For a wavelength λ_1 where $n_{eff}(\lambda_1)\Delta L = m\lambda_1$ (with m being an integer), light waves from both paths arrive in phase, resulting in constructive interference. Conversely, at wavelength λ_2 where $n_{eff}(\lambda_2)\Delta L = (m + \frac{1}{2})\lambda_2$, the waves arrive out of phase, producing destructive interference. This wavelength-selective behavior creates the periodic frequency response that characterizes MZI filters.

Several nonidealities can degrade filter performance in practical implementations:

- **Group Index Dispersion**: The wavelength dependence of n_g causes Δt to vary with wavelength, shifting the interference pattern and producing a non-uniform FSR across the spectrum.
- **Coupling Deviations**: Imperfections in power splitters lead to deviations from the designed coupling ratios, altering the b_k coefficients and introducing amplitude and phase errors in the filter response.
- **Phase Errors**: Fabrication variations, temperature fluctuations, or material inhomogeneities can introduce unintended phase shifts, misaligning the filter's resonant wavelengths. Active phase shifters are commonly integrated to compensate for these errors.

Precise control of the coupling ratios in the power splitter/coupler is crucial for achieving an accurate MZI filter response. Directional couplers (DCs) are commonly employed for this purpose; however, their coupling ratios are often wavelength-dependent due to dispersion effects. This wavelength sensitivity can adversely impact the performance of MZI filters, leading to degraded spectral characteristics [24].

MZI-based WDM filters can be designed for both DWDM and CWDM operation. By adjusting the path length difference, ΔL, the FSR can be tailored to meet the requirements of either CWDM or DWDM systems. Additionally, the resonance (operating) wavelength can be dynamically tuned using integrated thermo-optic phase shifters, as detailed in Appendix A.2.3 and A.2.4.

Higher-order filtering functions can be realized by cascading multiple MZIs or by configuring them in lattice topologies [23, 25], as demonstrated in Fig. 2.7. These advanced architectures enable precise spectral shaping, including flat-top passbands and steep roll-off transitions. As a result, MZI-based filters offer significant flexibility and performance in WDM systems.

Overall, the advantages and disadvantages of MZI-based WDM filters can be summarized as follows:

Advantages

- **Flat, wide passbands with low insertion loss:** Cascaded lattice MZIs can achieve flat-top passbands with low IL, making them attractive for high-performance WDM applications. For example, an 8-channel DWDM filter with a channel spacing of 3.2 nm was demonstrated using cascaded MZIs, achieving an IL of less than 1.6 dB and a flat passband with an ER of approximately 15 dB [23].
- **Dynamic reconfigurability:** The integration of thermo-optic phase shifters allows real-time tuning of the central wavelength, enabling adaptability to varying system requirements and enhancing operational flexibility.
- **Scaling WDM system channel count:** Cascaded MZI filters can function as standalone WDM filters or as interleavers to scale up DWDM systems. For example, a recent study demonstrated a four-channel interleaver based on cascaded MZIs, which successfully scaled a DWDM system's channel count by a factor of four [26].

Disadvantages

- **Large footprint:** Cascaded MZI systems often require long waveguide arm lengths and multiple phase shifters, resulting in a significant footprint. This can limit integration density and increase manufacturing complexity. For example, an 8-channel MZI-based DWDM filter was demonstrated with a footprint of 1.9 mm^2 [27].
- **Phase errors and high tuning power:** The long common arm lengths in MZIs can introduce phase errors, causing shifts in the operating wavelength. The problem gets even worse with high-order architectures as each stage experiences its own uncorrelated phase errors. Active tuning mechanisms are necessary to compensate for these drifts. Additionally, the typically long interferometer arms often require substantial heating power for precise phase control, which can limit energy efficiency and scalability. For instance, a recent study reported that MZI-based WDM filters required 23.2 mW/FSR power consumption to tune the MZIs [28].

Microring Resonators (MRRs)

MRRs are compact, wavelength-selective filters that are usually composed of circular waveguide cavities that couple resonantly to adjacent bus waveguides, as shown in Fig. 2.8. When the resonance condition is satisfied (Fig. 2.8(a)), light is efficiently coupled into the ring, resulting in a sharp drop in the transmission through the bus waveguide at the resonant wavelength. This resonance condition is governed by:

$$m\lambda_{res} = n_{\text{eff}} L,$$

where m is the mode number, λ_{res} is the resonant wavelength, n_{eff} is the effective refractive index, and L is the optical round-trip length of the ring. The filter characteristics of MRRs, such as bandwidth, ER, and FSR, are determined by design parameters including ring radius and coupling coefficient [10]. Further, it is essential in an MRR to have precise control of the coupling values (i.e. between the ring and the bus waveguide) to have accurate MRR filter response. Similar to MZIs, MRRs typically employ DCs to control the coupling between the ring and bus waveguides, and the wavelength dependence of these DCs directly impacts the spectral response of the resonator.

Due to their compact size and high spectral selectivity, MRRs are particularly suitable for DWDM systems [26]. However, their performance is highly sensitive to fabrication tolerances and thermal variations, often necessitating active tuning to maintain alignment with the desired spectral channels [10].

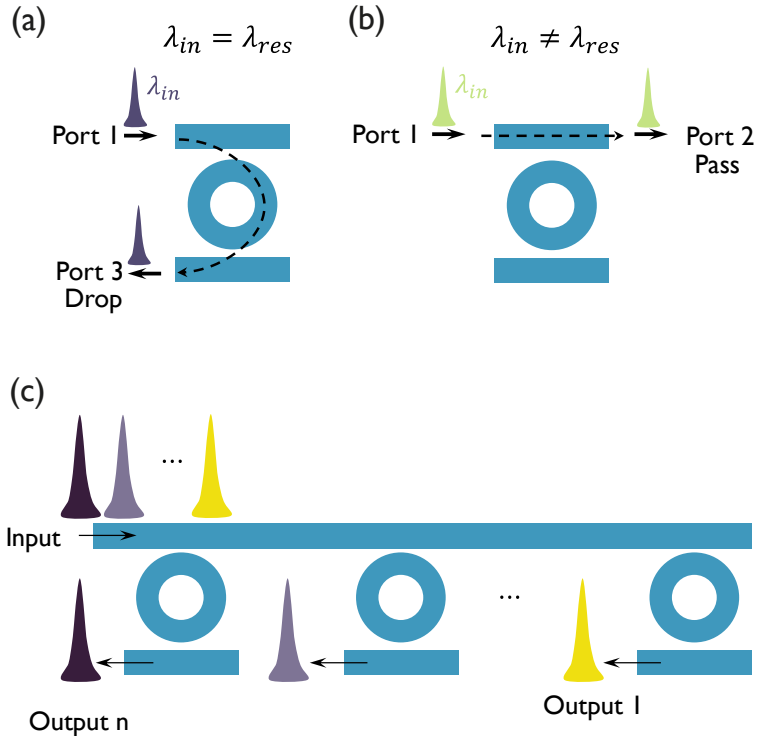

Figure 2.8: Schematics of microring resonator (MRR) filters. The MRR consists of a circular waveguide that is coupled to a bus waveguide. Light is coupled into the ring and can be dropped or added at specific wavelengths based on the resonance condition. Resonance wavelength condition is satisfied (a). Resonance wavelength condition is not satisfied (b). Example of MRR-based WDM filter based on cascaded ring resonators on a shared bus waveguide (c).

Types of MRR Filters MRR filters can be classified into several categories based on their design and operational principles. The most common types include:

- **Single-ring filters (Add-drop ring resonators):** Basic configuration in which each ring is designed to drop or add a single wavelength channel (Fig. 2.8 (a, b)) [10]. The transmission spectrum of a single ring is Lorentzian (or Airy function for low-finesse rings), resulting in a limited useful bandwidth compared to the channel spacing. This could lead to high nearest-neighbour crosstalk and could require a large guard band between channels.
- **Coupled-Resonator Optical Waveguides (CROWs):** Multiple cascaded rings (Fig. 2.9 (a)) produce flat-top passbands and steep spectral transitions,

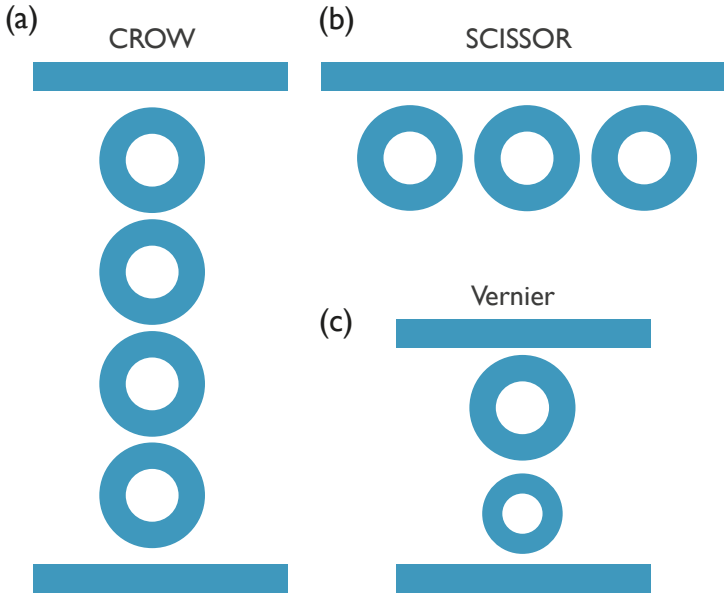

Figure 2.9: Schematics of different MRR-based filter architectures including Coupled-Resonator Optical Waveguides (CROWs) (a), Side-Coupled Integrated Spaced Sequence of Optical Resonators (SCISSOR) (b), and Vernier filters (c).

enhancing channel isolation, albeit usually on the expense of low fabrication tolerance [29].

- **Side-Coupled Integrated Spaced Sequence of Optical Resonators (SCISSOR):** A series of identical rings all side-coupled to a single bus waveguide (Fig. 2.9 (b)). The resulting constructive and destructive interference produces very sharp spectral features with high extinction ratios and low crosstalk. However, SCISSOR filters are generally not useful for channel drop filters [30].

- **Vernier filters:** Vernier filters use rings with slightly different radii to exploit the Vernier effect (Fig. 2.9 (c)), increasing the effective FSR and improving wavelength selectivity [31]. These filters, however, usually exhibit side bands within the FSR, which could lead to crosstalk depending on the application requirements.

Overall, the advantages and disadvantages of MRR-based WDM filters can be summarized as follows:

Advantages

- **Ultra-compact footprint:** MRRs typically have diameters on the order of tens of micrometers or even sub-micrometer, enabling high integration density (i.e. multiple MRRs can be cascaded in an array in DWDM systems). For instance, a recent study demonstrated an MRR with a radius of 0.7 μm while still maintaining single-mode operation [26].
- **High spectral selectivity:** Narrow resonance linewidths and sharp roll-off make MRRs well-suited for DWDM applications. For example, a recent study demonstrated a DWDM system with 32 channels and 100 GHz spacing based on MRRs [26].

Disadvantages

- **Fabrication sensitivity:** Variations in waveguide width, sidewall roughness, and etch depth can significantly shift resonance wavelengths and degrade performance (similar to MZIs) [10].
- **Limited FSR:** The relatively small FSR of individual rings restricts the number of usable channels unless advanced configurations are implemented. This limitation arises due to constraints on how small the bend radius can be [26].
- **Narrow bandwidth:** The spectral response of MRRs is inherently an Airy function, which may not be ideal for certain applications requiring flat top passbands. Advanced designs, such as coupled ring configurations, are often required to address this limitation [10].

Arrayed Waveguide Gratings (AWGs)

AWGs are probably the most well-known WDM filter architecture in silicon photonics [13, 33, 34]. AWGs have been commercialized for many years already [5]. AWGs are passive multi-path interferometric devices that spatially separate optical wavelengths based on differential phase accumulation, as shown in Fig. 2.10 [32]. A typical AWG consists of three main components: an input free-propagation region (FPR), an array of waveguides with linearly incremented path lengths, and an output FPR. When light enters the input FPR, it diffracts into the waveguide array, where it accumulates wavelength-dependent phase delays. These phase-shifted signals then interfere constructively at specific positions in the output FPR, enabling spatial demultiplexing of individual wavelength channels [13].

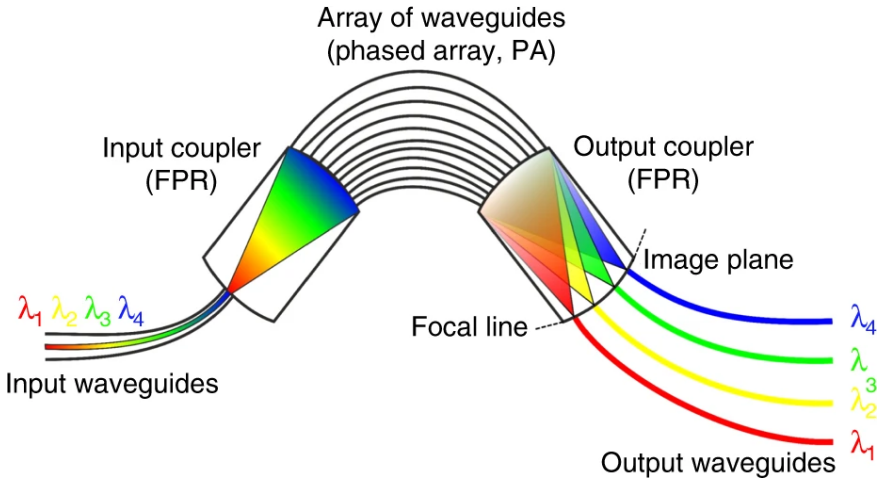

Figure 2.10: Schematic of an Arrayed Waveguide Grating (AWG) filter [32]. The AWG consists of an input free-propagation region (FPR), a waveguide array with linearly incremented path lengths, and an output FPR. Light entering the input FPR is diffracted into the waveguide array, where it accumulates wavelength-dependent phase delays. The phase-shifted signals interfere constructively at specific positions in the output FPR, enabling spatial demultiplexing of individual wavelength channels

AWGs are widely used in DWDM systems due to their ability to support high channel counts, small channel spacing, and passive, athermal operation. However, their relatively large footprint and sensitivity to fabrication-induced phase errors often present design and integration challenges [35].

Overall, the advantages and disadvantages of AWG-based WDM filters can be summarized as follows:

Advantages

- **High channel count:** Silicon photonic AWGs can support a large channel count. For instance, a recent study based on AWGs demonstrated 512 channels with 25 GHz channel spacing, albeit with high channel cross talk of -4 dB [36].
- **Low crosstalk and flat-top passbands:** Advanced AWG designs can achieve inter-channel crosstalk levels below −20 dB and flat-top spectral response (albeit with extra design modifications). For example, a 16-channel AWG-based DWDM filter demonstrated crosstalk as low as −31.7 dB [37].

Disadvantages

- **Large footprint:** High-channel-count AWGs require millimeter-scale areas on-chip, which limits integration density. For example, a 64-channel AWG-based WDM filter was demonstrated with a footprint of 2.3 mm $\times$ 2 mm [38].
- **Stringent fabrication tolerances:** Accurate control of waveguide length increments and minimization of sidewall roughness are critical to suppress phase errors and maintain low crosstalk [36].
- **High insertion loss:** AWGs can exhibit insertion losses $\geq$ 3 dB, depending on the design and fabrication quality. This can limit their efficiency in low-power applications [37, 38]. Overall, AWGs exhibit inherent losses, which tend to increase towards the outer channels, further complicating their use in high-density applications.

Echelle Diffraction Gratings (EDGs)

EDGs, also referred to as planar concave gratings (PCGs), are diffractive optical elements that integrate a blazed grating onto a concave slab waveguide structure, as shown in Fig. 2.11. These devices operate based on angular dispersion within a free-space propagation region, enabling different wavelengths to be diffracted and focused onto discrete output ports. The concave geometry provides a natural focusing mechanism, yielding a compact, folded design [39].

In contrast to AWGs, EDGs eliminate the need for a path-length-incremented waveguide array and instead utilize a single free-space slab for both diffraction and spatial separation. This simplifies the overall layout and improves channel uniformity by averaging out localized fabrication variations. Additionally, the ability to align angled output facets with standard fiber array geometries facilitates efficient fiber-to-chip coupling [15].

Overall, the advantages and disadvantages of EDG-based WDM filters can be summarized as follows:

Advantages

- **Compact folded geometry for CWDM filters:** The concave slab design combined with angular dispersion could enable a reduced footprint compared to AWGs, particularly for low channel count filters. Overall, Echelle gratings tend to have better performance for CWDM applications, while AWGs are

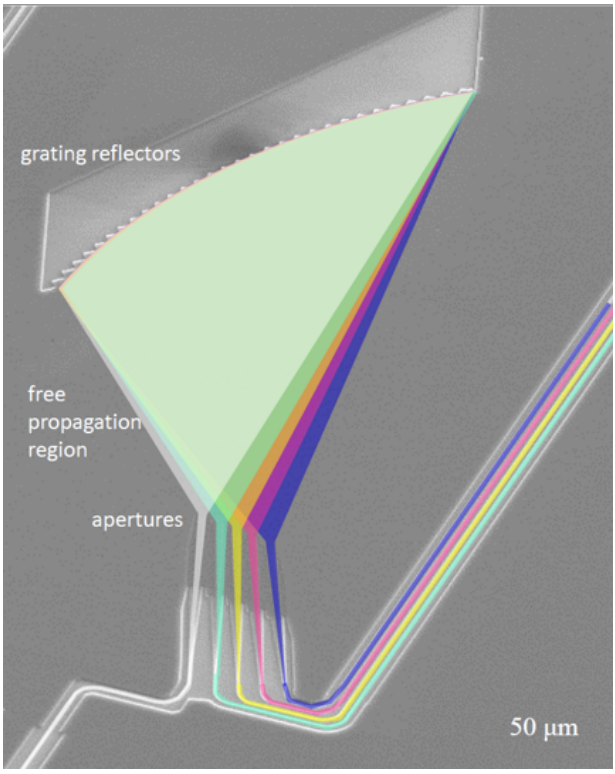

Figure 2.11: Echelle diffraction grating (EDG) filter [39]. The EDG consists of a concave slab waveguide with a blazed grating structure. Light entering the slab is diffracted by the grating, and different wavelengths are focused onto discrete output ports based on their diffraction angles. The concave geometry provides natural focusing, enabling compact designs for coarse wavelength-division multiplexing (CWDM) applications.

often preferred for DWDM applications [15]. For instance, a CWDM-4 filter based on an EDG design demonstrated a footprint of $140 \times 100\,\mu\mathrm{m}^2$ [40]. However, AWGs are often prefered for applications with low FSR values.

- **Enhanced crosstalk uniformity:** The free-space slab averages out waveguide imperfections, improving spectral uniformity and channel isolation. For example, an EDG-based WDM filter achieved crosstalk levels below $-20\,\mathrm{dB}$ [40].

Disadvantages

- **Fabrication complexity:** Achieving high-precision grating etching and facet definition is critical to minimize scattering losses and ensure efficient

diffraction, particularly for the groove structure. Having a (very) large unetched free propagation region can disrupt pattern density control, leading to uneven etching and degraded device performance [39].

- **Insertion loss:** Grating and waveguide losses, exacerbated by fabrication imperfections, can result in higher insertion losses compared to other WDM architectures [15].
- **Limited channel density:** The angular dispersion mechanism imposes constraints on the maximum achievable channel count, especially in dense spacing regimes where diffraction order overlap may occur [15].

2.5 Challenges in WDM Filters and Research Directions

The development of WDM filters in silicon photonics faces several challenges that must be addressed to enable their widespread adoption in high-performance photonic systems. This section discusses key challenges and outlines potential future directions for advancing WDM filter technologies.

Fabrication Variability and Tolerance

The high refractive index contrast in silicon photonics amplifies the impact of fabrication imperfections, such as sidewall roughness, dimensional variations, and lithographic errors. These imperfections can lead to performance degradation, including resonance shifts in microring resonators, phase errors in MZIs and AWGs, and increased crosstalk in MZIs. To mitigate these effects, it is essential to develop silicon photonic components that are highly tolerant to fabrication variations and exhibit broadband operation.

Thermal Sensitivity and Power Consumption

Silicon's strong thermo-optic coefficient makes WDM filters highly sensitive to temperature variations, resulting in wavelength shifts that can degrade performance. While thermal tuning can compensate for these shifts, it increases power consumption and introduces thermal crosstalk in densely integrated photonic circuits. Designs that minimize the power consumption of thermal tuning or eliminate the need for active thermal control are essential for energy-efficient WDM systems.

Spectral Density and Scalability

As WDM systems evolve to support higher channel counts and narrower channel spacings, achieving low crosstalk and high spectral selectivity becomes increasingly challenging. Next-generation WDM systems should aim to utilize a broader wavelength range while maintaining minimal insertion loss and ensuring high channel isolation.

2.6 Conclusion

In this chapter, we examined the fundamental principles and architectures of Wavelength Division Multiplexing (WDM) filters in silicon photonics. A comprehensive overview of key filter types was presented, including Mach-Zehnder Interferometers (MZIs), Microring Resonators (MRRs), Arrayed Waveguide Gratings (AWGs), and Echelle diffraction gratings (EDGs). Each architecture was analyzed in terms of its performance metrics, such as insertion loss, crosstalk, footprint, and fabrication tolerance.

The selection of a suitable filter architecture is inherently application-specific, depending on factors such as channel count, channel spacing, and integration density. As WDM systems advance toward higher spectral efficiency and integration, overcoming challenges such as fabrication variability, thermal sensitivity, and spectral density becomes increasingly crucial.

This thesis addresses some of these challenges through the development of robust WDM filter designs with consistent performance across an entire wafer. We also explore enhancing the wavelength operation range of WDM filters with broadband coupler designs. Furthermore, we explore novel strategies for realizing CWDM architectures that eliminate the need for active thermal tuning, thereby reducing power consumption and improving the scalability of silicon photonic systems. Ultimately, the work presented herein contributes to the realization of high performance, energy-efficient, and scalable WDM filters, paving the way for their deployment in next generation optical communication and computing platforms.

References

[1] Cisco. Cisco annual internet report (2018–2023). Technical report, Cisco Systems, 2020. https://www.cisco.com/c/en/us/solutions/executive-perspectives/annual-internet-report/index.html.

[2] Yikai Su, Yong Zhang, Ciyuan Qiu, Xuhan Guo, and Lu Sun. Silicon Photonic Platform for Passive Waveguide Devices: Materials, Fabrication, and Applications. *Advanced Materials Technologies*, 5(8):1901153, 2020. ISSN 2365-709X. doi: 10/gh3525. ZSCC: 0000015 _eprint: tex.ids= su_silicon_2020-1.

[3] Nabarun Saha, Giuseppe Brunetti, Annarita di Toma, Mario Nicola Armenise, and Caterina Ciminelli. Silicon photonic filters: A pathway from basics to applications. *Advanced Photonics Research*, March 2024. ISSN 2699-9293. doi: 10.1002/adpr.202300343.

[4] Yaocheng Shi, Yong Zhang, Yating Wan, Yu Yu, Yuguang Zhang, Xiao Hu, Xi Xiao, Hongnan Xu, Long Zhang, and Bingcheng Pan. Silicon photonics for high-capacity data communications. *Photonics Research*, 10(9):A106, August 2022. ISSN 2327-9125. doi: 10.1364/prj.456772.

[5] Dajian Liu, Hongnan Xu, Ying Tan, Yaocheng Shi, and Daoxin Dai. Silicon photonic filters. *Microwave and Optical Technology Letters*, 63(9):2252–2268, 2021. ISSN 1098-2760. doi: 10/gg6sj8.

[6] Govind P. Agrawal. *Fiber-optic communication systems*. Wiley series in microwave and optical engineering. Wiley, Hoboken, NJ, fifth edition edition, 2021. ISBN 9781119737391. Includes bibliographical references and index.

[7] Wei Shi, Ye Tian, and Antoine Gervais. Scaling capacity of fiber-optic transmission systems via silicon photonics. *Nanophotonics*, 9(16):4629–4663, October 2020. ISSN 2192-8606. doi: 10.1515/nanoph-2020-0309.

[8] Mi Wang, Xiangfeng Chen, Umar Khan, and Wim Bogaerts. Programmable wavelength filter with double ring loaded MZI. *Scientific Reports*, 12(1), January 2022. ISSN 2045-2322. doi: 10.1038/s41598-021-04598-6.

[9] Qingzhong Deng, Lu Liu, Rui Zhang, Xinbai Li, Jurgen Michel, and Zhiping Zhou. Athermal and flat-topped silicon mach-zehnder filters. *Optics Express*, 24(26):29577, December 2016. ISSN 1094-4087. doi: 10.1364/OE.24.029577. URL https://www.osapublishing.org/abstract.cfm?URI=oe-24-26-29577.

[10] W. Bogaerts, P. De Heyn, T. Van Vaerenbergh, K. De Vos, S. Kumar Selvaraja, T. Claes, P. Dumon, P. Bienstman, D. Van Thourhout, and R. Baets. Silicon microring resonators. *Laser & Photonics Reviews*, 6(1):47–73, 2012. ISSN 1863-8899. doi: 10/cr3dtz. ZSCC: 0001902 _eprint:.

[11] Qingzhong Deng, Jeroen De Coster, Rafal Magdziak, Ahmed H. El-Saeed, Alaa Elshazly, Guy Lepage, Chiara Marchese, Hakim Kobbi, Neha Singh, Marko Ersek Filipcic, Kristof Croes, Dimitrios Velenis, Maumita Chakrabarti, Peter De Heyn, Peter Verheyen, Philippe Absil, Filippo Ferraro, Yoojin Ban, and Joris Van Campenhout. Silicon ring based wavelength division multiplexing with an ultra-wide spectral range of 6.4 thz. In *2024 IEEE Silicon Photonics Conference (SiPhotonics)*, pages 1–2. IEEE, April 2024. doi: 10.1109/siphotonics60897.2024.10543750.

[12] P. Dumon, W. Bogaerts, D. Van Thourhout, D. Taillaert, R. Baets, J. Wouters, S. Beckx, and P. Jaenen. Compact wavelength router based on a silicon-on-insulator arrayed waveguide grating pigtailed to a fiber array. *Optics Express*, 14(2):664, 2006. ISSN 1094-4087. doi: 10.1364/opex.14.000664.

[13] Nebiyu Adello Yebo, Wim Bogaerts, Zeger Hens, and Roel Baets. On-chip arrayed waveguide grating interrogated silicon-on-insulator microring resonator-based gas sensor. *IEEE Photonics Technology Letters*, 23(20): 1505–1507, October 2011. ISSN 1941-0174. doi: 10.1109/lpt.2011.2162825.

[14] Tatsuhiko Fukazawa, Fumiaki Ohno, and Toshihiko Baba. Very compact arrayed-waveguide-grating demultiplexer using Si photonic wire waveguides. *Japanese Journal of Applied Physics*, 43(5B):L673, 2004. ISSN 0021-4922. doi: 10.1143/jjap.43.l673.

[15] S. Pathak, P. Dumon, D. Van Thourhout, and W. Bogaerts. Comparison of AWGs and echelle gratings for wavelength division multiplexing on silicon-on-insulator. *IEEE Photonics Journal*, 6(5):1–9, October 2014. ISSN 1943-0655. doi: 10.1109/jphot.2014.2361658.

[16] F. Horst, W.M.J. Green, B.J. Offrein, and Y.A. Vlasov. Silicon-on-insulator echelle grating WDM demultiplexers with two stigmatic points. *IEEE Photonics Technology Letters*, 21(23):1743–1745, December 2009. ISSN 1941-0174. doi: 10.1109/lpt.2009.2032151.

[17] D. Sadot and E. Boimovich. Tunable optical filters for dense WDM networks. *IEEE Communications Magazine*, 36(12):50–55, 1998. ISSN 0163-6804. doi: 10.1109/35.735877.

[18] Nahum Gat. Imaging spectroscopy using tunable filters: a review. In Harold H. Szu, Martin Vetterli, William J. Campbell, and James R. Buss, editors, *Wavelet Applications VII*. SPIE, April 2000. doi: 10.1117/12.381686.

[19] Christi K. Madsen and Jian H. Zhao. *Optical Filter Design and Analysis: A Signal Processing Approach*. Wiley, June 1999. ISBN 9780471213758. doi: 10.1002/0471213756.

[20] Zhizun Zhao, Zhen Li, Jiaqi Niu, Gaolu Zhang, Hongliang Chen, Xin Fu, and Lin Yang. Eight-Channel LAN WDM (De)Multiplexer Based on Cascaded Mach–Zehnder Interferometer on SOI for 400GbE. *Photonics*, 9(4):252, April 2022. ISSN 2304-6732. doi: 10.3390/photonics9040252. URL https://www.mdpi.com/2304-6732/9/4/252.

[21] Wim Bogaerts. Photonic integrated circuits M.Sc. course. Lecture notes, 2020. Ghent University, Belgium.

[22] CW-WDM MSA (Continuous-Wave Wavelength Division Multiplexing Multi-Source Agreement). URL https://cw-wdm.org/.

[23] Folkert Horst, William M. J. Green, Solomon Assefa, Steven M. Shank, Yurii A. Vlasov, and Bert Jan Offrein. Cascaded mach-zehnder wavelength filters in silicon photonics for low loss and flat pass-band WDM (de-)multiplexing. *Optics express*, 21(10):11652–11658, 2013. doi: 10.1364/OE.21.011652.

[24] Ahmed H. El-Saeed, Alaa Elshazly, Hakim Kobbi, Rafal Magdziak, Guy Lepage, Chiara Marchese, Javad Rahimi Vaskasi, Swetanshu Bipul, Dieter Bode, Marko Ersek Filipcic, Dimitrios Velenis, Maumita Chakrabarti, Peter De Heyn, Peter Verheyen, Philippe Absil, Filippo Ferraro, Yoojin Ban, Joris Van Campenhout, Wim Bogaerts, and Qingzhong Deng. Low-loss silicon directional coupler with arbitrary coupling ratios for broadband wavelength operation based on bent waveguides. *Journal of Lightwave Technology*, 42 (17):6011–6018, September 2024. ISSN 1558-2213. doi: 10.1109/jlt.2024.3407339.

[25] Hongnan Xu and Yaocheng Shi. Flat-Top CWDM (De)Multiplexer Based on MZI With Bent Directional Couplers. *IEEE Photonics Technology Letters*, 30 (2):169–172, January 2018. ISSN 1941-0174. doi: 10.1109/LPT.2017.2779489.

[26] Qingzhong Deng, Ahmed H. El-Saeed, Alaa Elshazly, Guy Lepage, Chiara Marchese, Pieter Neutens, Hakim Kobbi, Rafal Magdziak, Jeroen De Coster, Javad Rahimi Vaskasi, Minkyu Kim, Yeyu Tong, Neha Singh, Marko Ersek Filipcic, Pol Van Dorpe, Kristof Croes, Maumita Chakrabarti, Dimitrios

Velenis, Peter De Heyn, Peter Verheyen, Philippe Absil, Filippo Ferraro, Yoojin Ban, and Joris Van Campenhout. Low-loss and low-power silicon ring based WDM 32×100 GHz filter enabled by a novel bend design. *Laser & Photonics Reviews*, November 2024. ISSN 1863-8899. doi: 10.1002/lpor.202401357.

[27] Qiyuan Yi, Shuang Zheng, Zhiwei Yan, Guanglian Cheng, Fanglu Xu, Qiyuan Li, and Li Shen. Silicon photonic flat-top WDM (de)multiplexer based on cascaded mach-zehnder interferometers for the 2 μm wavelength band. *Optics Express*, 30(15):28232, July 2022. ISSN 1094-4087. doi: 10.1364/oe.467473.

[28] Yunhong Ding, Minhao Pu, Liu Liu, Jing Xu, Christophe Peucheret, Xinliang Zhang, Dexiu Huang, and Haiyan Ou. Bandwidth and wavelength-tunable optical bandpass filter based on silicon microring-MZI structure. *Optics Express*, 19(7):6462, March 2011. ISSN 1094-4087. doi: 10.1364/oe.19.006462.

[29] Joyce Poon, Jacob Scheuer, Shayan Mookherjea, George T. Paloczi, Yanyi Huang, and Amnon Yariv. Matrix analysis of microring coupled-resonator optical waveguides. *Optics Express*, 12(1):90, 2004. ISSN 1094-4087. doi: 10.1364/opex.12.000090.

[30] Mattia Mancinelli, Romain Guider, Marco Masi, Paolo Bettotti, Manga Rao Vanacharla, Jean-Marc Fedeli, and Lorenzo Pavesi. Optical characterization of a SCISSOR device. *Optics Express*, 19(14):13664, June 2011. ISSN 1094-4087. doi: 10.1364/oe.19.013664.

[31] Lei Jin, Mingyu Li, and Jian-Jun He. Highly-sensitive silicon-on-insulator sensor based on two cascaded micro-ring resonators with vernier effect. *Optics Communications*, 284(1):156–159, January 2011. ISSN 0030-4018. doi: 10.1016/j.optcom.2010.08.035. URL https://www.sciencedirect.com/science/article/pii/S0030401810008904.

[32] Elisabet A. Rank, Ryan Sentosa, Danielle J. Harper, Matthias Salas, Anna Gaugutz, Dana Seyringer, Stefan Nevlacsil, Alejandro Maese-Novo, Moritz Eggeling, Paul Muellner, Rainer Hainberger, Martin Sagmeister, Jochen Kraft, Rainer A. Leitgeb, and Wolfgang Drexler. Toward optical coherence tomography on a chip: in vivo three-dimensional human retinal imaging using photonic integrated circuit-based arrayed waveguide gratings. *Light: Science and Applications*, 10(1), January 2021. ISSN 2047-7538. doi: 10.1038/s41377-020-00450-0.

[33] K. Sasaki, F. Ohno, A. Motegi, and T. Baba. Arrayed waveguide grating of 70×60 [micro sign]m2 size based on Si photonic wire waveguides. *Electronics Letters*, 41(14):801–801, 2005. doi: 10.1049/el:20051541.

[34] Óscar M. Matos, María L. Calvo, Pavel Cheben, Siegfried Janz, José A. Rodrigo, Dan-Xia Xu, and André Delâge. Arrayed waveguide grating based on group-index modification. *Journal of Lightwave Technology*, 24(3):1551–1551, 2006.

[35] Jun Zou, Fangyuan Sun, Changhui Wang, Ming Zhang, Junnan Wang, Tingting Lang, Xuyang Wang, Zichun Le, and Jian-Jun He. Silicon-based arrayed waveguide gratings for WDM and spectroscopic analysis applications. *Optics and Laser Technology*, 147:107656, March 2022. ISSN 0030-3992. doi: 10.1016/j.optlastec.2021.107656.

[36] Stanley Cheung, Tiehui Su, Katsunari Okamoto, and S. J. B. Yoo. Ultra-compact silicon photonic 512 × 512 25 GHz arrayed waveguide grating router. *IEEE Journal of Selected Topics in Quantum Electronics*, 20(4):310–316, July 2014. ISSN 1558-4542. doi: 10.1109/jstqe.2013.2295879.

[37] Xiaowan Shen, Chenlei Li, Weike Zhao, Huan Li, Yaocheng Shi, and Daoxin Dai. Ultra-low-crosstalk silicon arrayed-waveguide grating (de)multiplexer with 1.6-nm channel spacing. *Laser and Photonics Reviews*, 18(1), October 2023. ISSN 1863-8899. doi: 10.1002/lpor.202300617.

[38] Yingjie Liu, Xi Wang, Yong Yao, Jiangbing Du, Qinghai Song, and Ke Xu. Silicon photonic arrayed waveguide grating with 64 channels for the 2 μm spectral range. *Optics Letters*, 47(5):1186, February 2022. ISSN 1539-4794. doi: 10.1364/ol.452476.

[39] Joost Brouckaert, Wim Bogaerts, Pieter Dumon, Dries Van Thourhout, and Roel Baets. Planar concave grating demultiplexer fabricated on a nanophotonic silicon-on-insulator platform. *Journal of Lightwave Technology*, 25(5):1269–1275, 2007. doi: 10.1109/JLT.2007.893025.

[40] Yu Zheng, Yunming Li, Yixiong Yan, Pan Zhang, and Ji'an Duan. Compact low-loss low-crosstalk echelle grating demultiplexer on silicon-on-insulator for CWDM. *Optik*, 249:168236, January 2022. ISSN 0030-4026. doi: 10.1016/j.ijleo.2021.168236.

3

Broadband Bent Directional Couplers

Directional couplers are an important building block in many wavelength division multiplexing (WDM) filters. In order to improve the performance of those WDM architectures, broadband 2×2 couplers (and splitters) must be demonstrated. Optimal 2×2 couplers for WDM filters must exhibit minimal coupling variation across a broad wavelength range, maintain a compact footprint, and support arbitrary broadband coupling ratios. Furthermore, they should demonstrate low-loss performance and high tolerance to fabrication variations, as they are usually used multiple times in WDM circuits. This chapter demonstrates the use of bent directional couplers (DCs) to fulfill these requirements. A coupled mode theory-based analysis is conducted to characterize the coupling behavior of bent DCs, with straight DCs serving as a benchmark for comparison and to further understand the broadband behavior of bent DCs. The bent DCs developed in this chapter will serve as critical building blocks for subsequent chapters on WDM filters.

3.1 Introduction 66
Operational principle of directional couplers 66
Performance metrics for 2×2 splitters 68
State of the art 68
Bent directional coupler 71
3.2 Proposed design and analysis 72
Coupled mode theory analysis 72
Optical characterization methodology 77

3.3 3-dB coupler results and wafer mapping 81
3.4 Model for arbitrary broadband coupling ratios 86
3.5 Compatibility with 200 mm and 300 mm platforms 89
3.6 Conclusion 90
References 93

3.1 Introduction

Operational principle of directional couplers

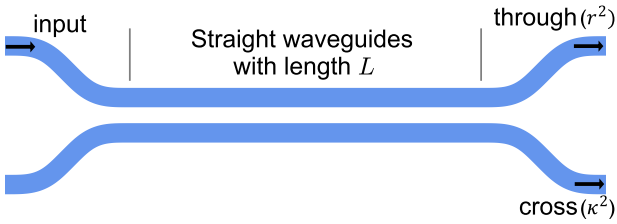

Figure 3.1: Schematic of the traditional straight directional coupler (DC) with L representing the coupling length. The DC consists of three sections: the input, coupling region, and output. Optical power remaining in the same waveguide as the input is often termed as 'through', while power transferred to the adjacent waveguide is often termed as 'cross'.

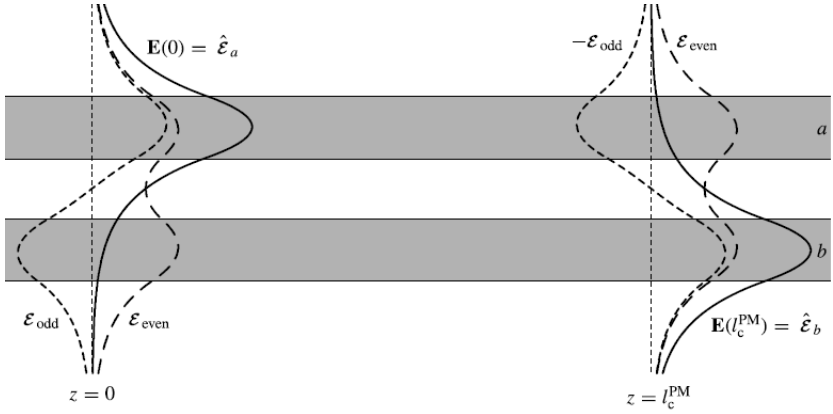

Figure 3.2: Evolution of supermodes in a symmetric directional coupler. Dashed curves indicate the even and odd supermodes, while solid curves show the total fields. As the supermodes propagate in the coupler, the power is coupled from waveguide 'a' to waveguide 'b'. Figure is adapted from [1].

Within the realm of photonic integrated circuits (PICs), optical power splitters serve as indispensable components. Among these, the 2×2 splitters emerge as fundamental building blocks with significant applications such as wavelength division multiplexing (WDM) [2, 3], modulation [4], and signal switching [5].

The directional coupler (DC) has traditionally served as the primary 2×2 splitter owing to its simplicity and ease of fabrication (Fig. 3.1). The DC operates through wavelength-dependent evanescent coupling between two closely spaced waveguides, allowing the oscillation of light between these waveguides. This ultimately enables the splitting of incident light into the through and cross ports. Alternatively, the DC can be understood in terms of supermodes: when two identical waveguides are brought close together, even and odd supermodes with slightly different propagation constants are formed. As light propagates, these supermodes accumulate a phase difference, leading to a periodic exchange of power between the waveguides. This beating between the two uncoupled supermodes provides an equivalent description of the light transfer mechanism in the coupler, as demonstrated in Fig. 3.2 (see Appendix A.1).

Although DCs are theoretically lossless, support arbitrary splitting ratios, and possess a compact design, their performance undergoes significant degradation owing to their inherent wavelength dependence due to dispersion. For instance, a simple silicon DC designed for $0.5 : 0.5$ splitting has more than 0.45 coupling variation over an 80 nm wavelength span [6], as shown in Fig. 3.3 [6].

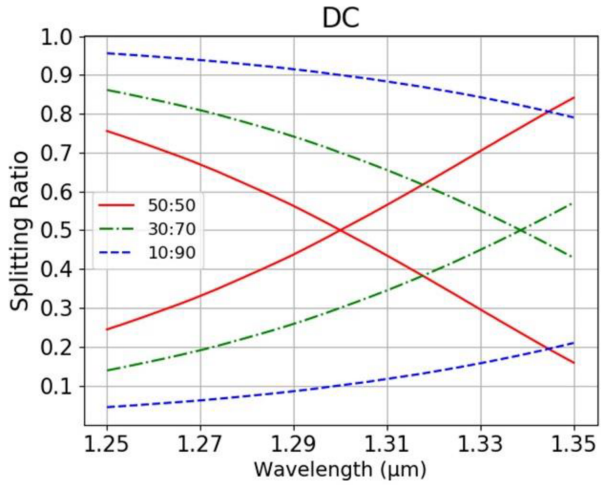

Figure 3.3: Coupling behavior of a straight symmetric silicon directional coupler with variation more than 0.45 for $0.5 : 0.5$ *splitting. The figure is from [6].*

Performance metrics for 2×2 splitters

For 2×2 splitters to be effectively utilized in PICs, particularly within WDM filters, several key performance metrics must be satisfied:

- **Broadband operation:** The splitter should exhibit minimal coupling variation across a wide operational bandwidth. The operational bandwidth is usually defined by the application. For WDM filters, it is usually the spectral wavelength range that is used by the WDM filter. Wavelength-dependent coupling limits the usable bandwidth, which is critical in broadband applications. For instance, a straight DC designed for 0.5 cross coupling may shift to 0.8 due to dispersion, reducing the extinction ratio (ER) of a Mach-Zehnder interferometer (MZI) from its theoretical value of ∞ to about 4.5 dB (see Appendix A.2.2), thereby severely degrading its performance.
- **Arbitrary coupling ratios:** In many applications, particularly within WDM systems, coupling ratios other than $0.5 : 0.5$ are often required. For instance, flat-top passbands in MZIs, as discussed in Chapter 2, necessitate other coupling ratios than $0.5 : 0.5$. Therefore, it is essential for 2×2 splitters to support broadband operation across a range of coupling ratios.
- **Robustness and fabrication tolerance:** The splitter should maintain consistent performance across the wafer, with low sensitivity to fabrication variations. A simple fabrication process is also preferred.
- **Low excess loss and compact footprint:** Since many splitters are typically used in PICs and in particular in WDMs, splitters must have minimal excess loss and occupy a small footprint.

State of the art

In the pursuit for an arbitrary-splitting-ratio, broadband, low-loss, robust, and compact splitter, various design schemes have been investigated in the literature. Multi mode interferometers (MMIs) are commonly used as broadband 2×2 splitters, where the wavelength dependence is averaged out through the different dispersion profiles of the high order modes propagating through the MMI [7]. However, MMIs only allow for a few discrete coupling ratio choices, and more complex configurations are a must to enable arbitrary splitting ratios [8]. Further, MMIs often suffer from high excess loss and are quite sensitive to the position of the input and output ports [9].

Adiabatic DCs (ADCs) are another common approach to achieve broadband coupling with arbitrary coupling ratios [10–12]. Unlike DCs, only one mode is excited in adiabatic couplers, and this mode evolutes adiabatically through the coupler and therefore broadband coupling could take place [13]. ADCs are, however, inherently long devices that could be longer than 240 μm and often exhibit high excess loss [12, 14].

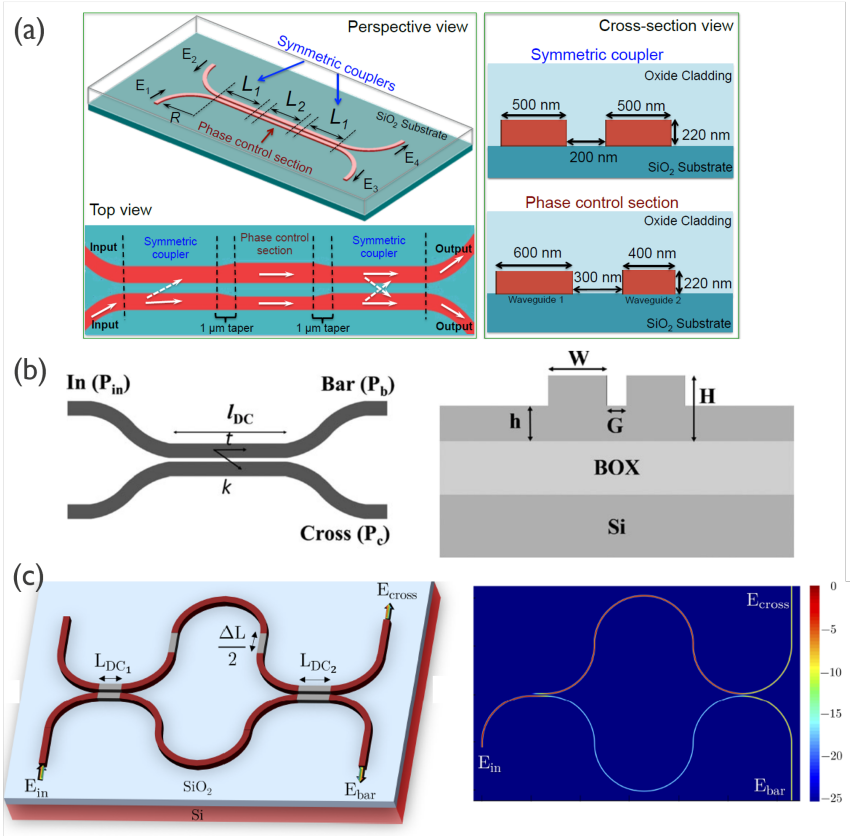

Figure 3.4: Various examples on demonstrations of broadband 2×2 splitters based on manipulating the directional coupler (DC), including DC with phase compensation section (a) [15], rib-waveguide based DC (b) [16], and MZI-based 2×2 splitter (c) [17]. It is worth noting that the DC with phase compensation section has the same working principle as the MZI-based 2×2 splitter.

On the other hand, several attempts have been made to adapt the traditional DC for broadband operation as shown in Fig. 3.4. For instance, DCs based on rib waveguides have shown broadband coupling through dispersion engineering of the geometrical parameters. However, their input and output ports require large bending

radii, as large as 180 μm, in order to minimize the bending loss, resulting in a large footprint [16]. Another approach is based on incorporating phase-compensation sections to the DC design. However, despite their broadband coupling, these designs are sensitive to linewidth variations and further design considerations are a must to make them fabrication tolerant [15, 18]. Another strategy is to cascade DCs in an MZI configuration, where an optical path length difference is introduced to compensate for the wavelength dependence of the DC. Arbitrary coupling ratios are possible via the optimization of the DC coupling ratios and the MZI arms lengths [17, 19]. However, precise control over the DC coupling ratios and the phase difference of the MZI arms is a necessity and ultimately complicates the design process. Further, subwavelength gratings (SWGs) have shown the capability to render the DC broadband by means of fine tuning the periodic SWG structures incorporated into the DC [20]. However, the fabrication of the SWGs is complex and unreliable specifically with feature sizes as small as 70 nm [21, 22].

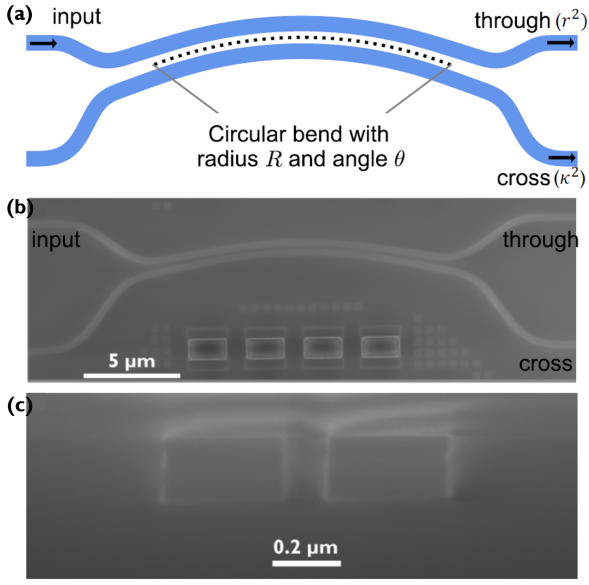

Figure 3.5: Schematic (a) and scanning electron microscope (SEM) image (b) of the proposed bent DC with R as the coupling radius, and θ as the coupling angle. All bent DC curves are designed with low-loss bends [23], while the straight DC input and output ports have traditional circular bends with a bending radius of 5 μm. SEM image of the cross section of the proposed bent DC in the coupling region (c). The waveguide material stacks are SOI with silicon oxide as top cladding, using IMEC iSiPP300 platform. All DCs are based on strip waveguides with nominal silicon thickness of 220 nm, and waveguide width of 380 nm. The coupling gap is nominally 100 nm.

Bent directional coupler

By bending the waveguides in the DC, a seven-fold enhancement in the operational bandwidth of the $0.5 : 0.5$ coupler was possible as compared to the traditional straight DC, all while maintaining a compact footprint, being fabrication tolerant and insensitive to temperature variations [24, 25]. It should be noted that with the introduced asymmetry, the $\pi/2$ phase difference between the through and cross ports is not necessarily satisfied anymore. Overall, for DCs with identical waveguides, $\pi/2$ phase difference between the output ports is satisfied as long as there is negligible loss. In bent DCs, the introduction of asymmetry, through bending waveguides with different bending radii, eliminates the need for different waveguide widths. This eventually addresses the fabrication sensitivity observed in DCs with different waveguide widths [24]. Several studies employed the bent DC to achieve broadband coupling with different approaches, including using the transfer matrix method to solve for the design parameters [26], using a cascade of bent DCs to achieve polarization insensitive and broadband coupling response [27], and using a semi-inverse design method to optimize freely-shaped waveguide section shapes [28]. Nonetheless, a detailed analysis of the bent DC wavelength dependence and an experimental-based coupling model for achieving broadband coupling at arbitrary coupling ratios have not yet been developed.

This chapter begins with an analytical model based on coupled mode theory (CMT) to describe the coupling behavior of both bent and straight DCs. Using this model, the CMT parameters are extracted. Given that the $0.5 : 0.5$ coupling ratio is the most commonly used ratio for WDM filters, a broadband $0.5 : 0.5$ bent DC is demonstrated with minimal coupling variation. The power coupling coefficients are determined using the cutback method, and the loss is extracted through sinusoidal fitting of the CMT equations. To assess the robustness and practical usability of the broadband $0.5 : 0.5$ bent DC in complex WDM systems, coupling measurements were performed across 63 dies on a 300 mm wafer, showing low coupling variation across the wafer. Further, a model is proposed to achieve broadband coupling at arbitrary ratios by tuning the bending radius and coupling angle of the bent DC. Finally, bent DC designs compatibility with IMEC's 200 mm and 300 mm platforms are discussed.

To benchmark the demonstrated results with the literature, the presented 0.5:0.5 bent DC has a compact length of 27.5 μm and a coupling variation of 0.051 over an 80 nm wavelength range, which is the lowest coupling variation reported for bent DCs to the best of my knowledge. Lower coupling variation directly translates to a higher extinction ratio (ER) for MZI filters (see Appendix A.2.2). Additionally, the incorporation of low-loss bends [23], which ensure continuous curvature and curvature derivative at all connections, has resulted in significantly low coupling

loss of 0.006 ± 0.004 dB, as limited by the precision of the measurements. Finally, the proposed DCs demonstrate robustness and suitability for mass production, as evidenced by wafer-scale measurements conducted on IMEC's 300 mm platform. This chapter is primarily based on the results published in [29, 30].

3.2 Proposed design and analysis

Coupled mode theory analysis

According to CMT (see Appendix A.1) [1], the through (r^2) and cross (κ^2) coupling ratio of a directional coupler (Fig. 3.5) can be expressed as:

$$\begin{cases} r^2 = 1 - m\sin^2(\beta_c l + \phi), \\ \kappa^2 = m\sin^2(\beta_c l + \phi), \end{cases} \tag{3.1}$$

where the excess loss is ignored, m is the matching coefficient and determines the maximum coupling ratio which is inversely correlated with the asymmetry, i.e. $m < 1$ for a DC with non-negligible asymmetry, and $m = 1$ for a symmetric straight DC. $\beta_c = \pi(n_{eff,even} - n_{eff,odd})/\lambda$ denotes the coupling strength per unit length or angle, where $n_{eff,even}$ and $n_{eff,odd}$ denote the effective refractive indices of the even or odd supermodes in the DC, respectively. Further, $l = L$ is the coupling length in a straight DC (Fig. 3.1), and $l = \theta$ is the coupling angle in a bent DC (Fig. 3.5a, b). Additionally, ϕ accounts for the coupling contributed from the input and output connection bends. Note that the effective refractive indices related to bent waveguides should be calculated with Maxwell's equations expressed in a cylindrical coordinate system.

The wavelength dependence for the cross coupling of a directional coupler can be calculated by taking the derivative of κ^2 (Eq. 3.1), as shown:

$$\begin{aligned} \frac{d\kappa^2}{d\lambda} &= \frac{dm}{d\lambda}\sin^2(\beta_c l + \phi) \\ &\quad + m(l\frac{d\beta_c}{d\lambda} + \frac{d\phi}{d\lambda})\sin(2(\beta_c l + \phi)). \end{aligned} \tag{3.2}$$

Notably,

$$\frac{dm}{d\lambda} \propto \frac{d\Delta n_{eff}}{d\lambda} = \frac{d(n_{eff,1} - n_{eff,2})}{d\lambda}, \tag{3.3}$$

where $n_{eff,1}$ and $n_{eff,2}$ denote the individual effective refractive indices of the two waveguides being coupled respectively. Further,

$$\frac{d\beta_c}{d\lambda} = -\frac{\pi}{\lambda^2}\Delta n_g, \tag{3.4}$$

where $\Delta n_g = n_{g,even} - n_{g,odd}$. n_g is the group refractive index, $n_{g,*} = n_{eff,*} - \lambda \partial n_{eff,*}/\partial\lambda$ (* is even or odd).

According to Eq. 3.2, and ignoring the bends coupling contribution (ϕ) in the subsequent analysis, in order to achieve a broadband response for a directional coupler (i.e. $d\kappa^2/d\lambda = 0$), one would aim to achieve two criteria simultaneously, namely $dm/d\lambda = 0$ and $\Delta n_g = 0$. The $dm/d\lambda = 0$ criterion is automatically satisfied in the symmetric straight DC. This is because $n_{eff,1} = n_{eff,2}$ for all wavelengths so that $dm/d\lambda = 0$ according to Eq. 3.3. Nevertheless, a parameter sweep for the gaps and waveguide widths of the symmetric straight DC reveals that the $\Delta n_g = 0$ criterion is not possible, i.e. Δn_g is consistently positive, as depicted in Fig. 3.6(a). This outcome underscores that the remaining second term of Eq. 3.2 will only be nullified at the zeros of the sinusoid (i.e. at 0 or 1 cross coupling values). Therefore, achieving broadband behavior at an arbitrary coupling ratio with a straight symmetric DC, based on strip waveguides, is not possible.

A similar analysis was made for the bent DC. In order to achieve broadband coupling Δn_g and $d\Delta n_{eff}/d\lambda$ are evaluated across various gaps and bending radii, as depicted in Fig. 3.6(b) and Fig. 3.6(c), respectively. In contrast to the straight DC, the bent DC can achieve $\Delta n_g = 0$ by tuning the design parameters as shown in Fig. 3.6(b). Further, the $d\Delta n_{eff}/d\lambda = 0$ criterion is no longer automatically satisfied due to the asymmetry, in contrast to the straight symmetric DC. Only at a specific combination of gap-radius pairs that $d\Delta n_{eff}/d\lambda = 0$, as shown in Fig 3.6(c). However, $\Delta n_g = 0$ and $d\Delta n_{eff}/d\lambda = 0$ cannot be achieved with the same device parameters. On the other hand, it is observed that both Δn_g and $d\Delta n_{eff}/d\lambda$ can take on negative, zero, or positive values in the bent DC. This indicates the feasibility of fine tuning the design parameters in order to operate in a region where both terms of Eq. 3.2 cancel each other out and eventually achieve broadband coupling, i.e. $d\kappa^2/d\lambda = 0$.

In summary, the modal analysis reveals that the straight DC cross coupling wavelength derivative is primarily governed by Δn_g, i.e., $d\kappa^2/d\lambda_{\text{str DC}} = f(\Delta n_g)$. For the given parameters, this term cannot be nullified, making broadband coupling unattainable. Conversely, the bent DC introduces an additional term, $dm/d\lambda$, to the derivative, resulting in $d\kappa^2/d\lambda_{\text{bent DC}} = f(\Delta n_g) + f(dm/d\lambda)$. The presented analysis demonstrates that these two terms can independently assume negative, zero, or positive values. This flexibility allows them to cancel each other out, enabling broadband coupling under specific design conditions.

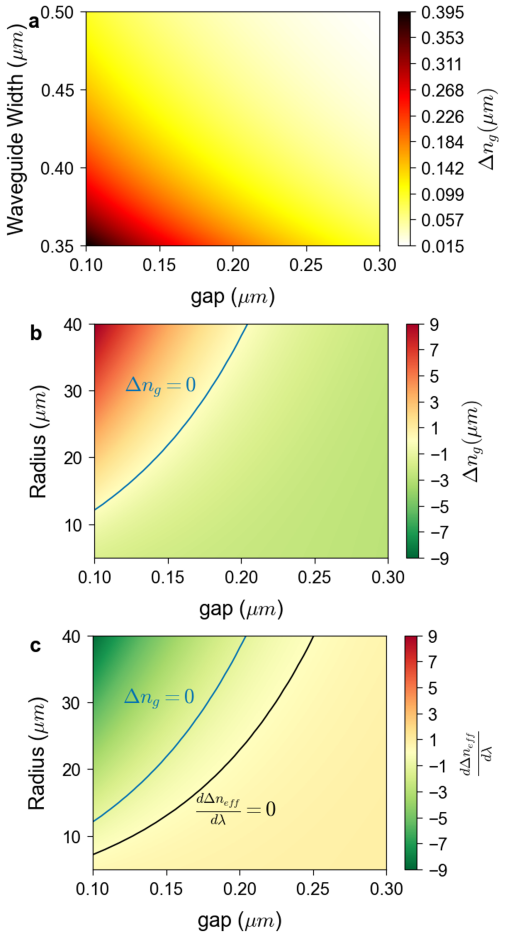

Figure 3.6: Wavelength dependence analysis for the straight and bent DC with lines showing broadband criteria. Contour plot of Δn_g as a function of the gap and the waveguide width for the straight symmetric DC (a). Contour plots of Δn_g (b) and $d\Delta n_{eff}/d\lambda$ (c) for the bent DC as a function of gap and radius, where the waveguide widths are fixed as 0.38 μm, along with lines showing where $\Delta n_g = 0$ (blue) and $d\Delta n_{eff}/d\lambda = 0$ (black). The results are based on finite element method simulations using COMSOL Multiphysics in cylindrical coordinates for bent waveguides.

In order to build the coupling model of the straight symmetric DC and the bent DC experimentally, Eq. 3.1 is rewritten as:

$$\begin{cases} r^2 = A_t(1 - m\sin^2(\beta_c l + \phi)), \\ \kappa^2 = A_c m \sin^2(\beta_c l + \phi), \end{cases} \tag{3.5}$$

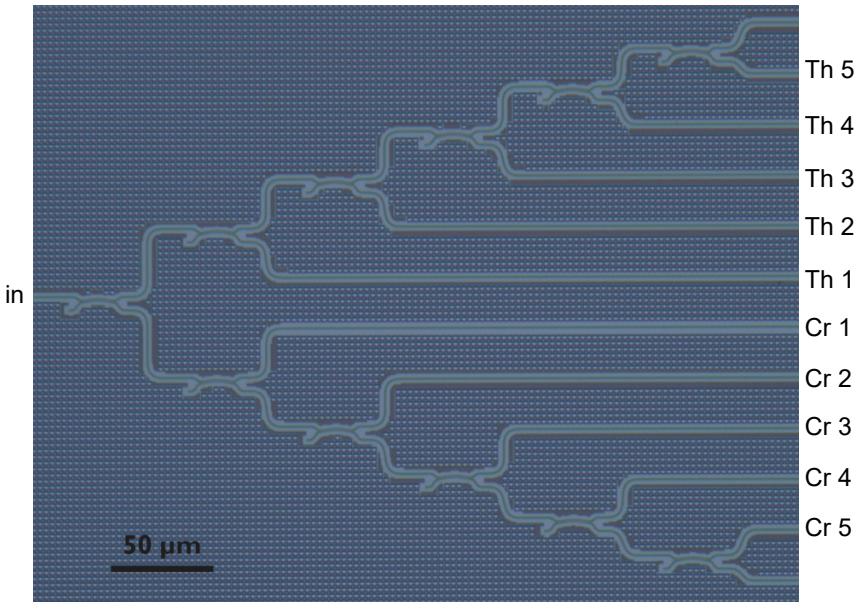

Figure 3.7: Microscope image of the cascaded identical bent DCs used for robust measurements. The power is input at the port (in) and measured at all the cascaded output stages. The labels determine whether the cascaded through (Th) or cascaded cross (Cr) coupled power is extracted, and the number indicates the number of times the measured value (through or cross) was repeated for that measurement. The proposed 0.5:0.5 broadband bent DC has a bending radius of $25\ \mu\mathrm{m}$*, a gap of* $0.1\ \mu\mathrm{m}$*, and a coupling angle of* 8.5 degrees.

where A_t and A_c are introduced to address the coupling loss of the through and cross ports respectively. Several straight DCs and bent DCs were fabricated and measured. The fabrication is done using IMEC's most advanced iSiPP300 platform allowing high waveguide quality and access to feature dimensions well below 100 nm thanks to the 193 nm immersion lithography [31]. All the waveguides are strip-based silicon waveguides with nominal silicon thickness of 220 nm and width of 380 nm.

Overall, the bent DC design procedure can be summarized as follows:

- Based on CMT analysis, it was revealed that broadband coupling is feasible with the bent DC. However, 3D finite-difference time-domain (FDTD) simulations are still needed to be able to accurately extract the design parameters that achieve broadband coupling.
- The design parameters are the inner and outer waveguide widths, the waveg-

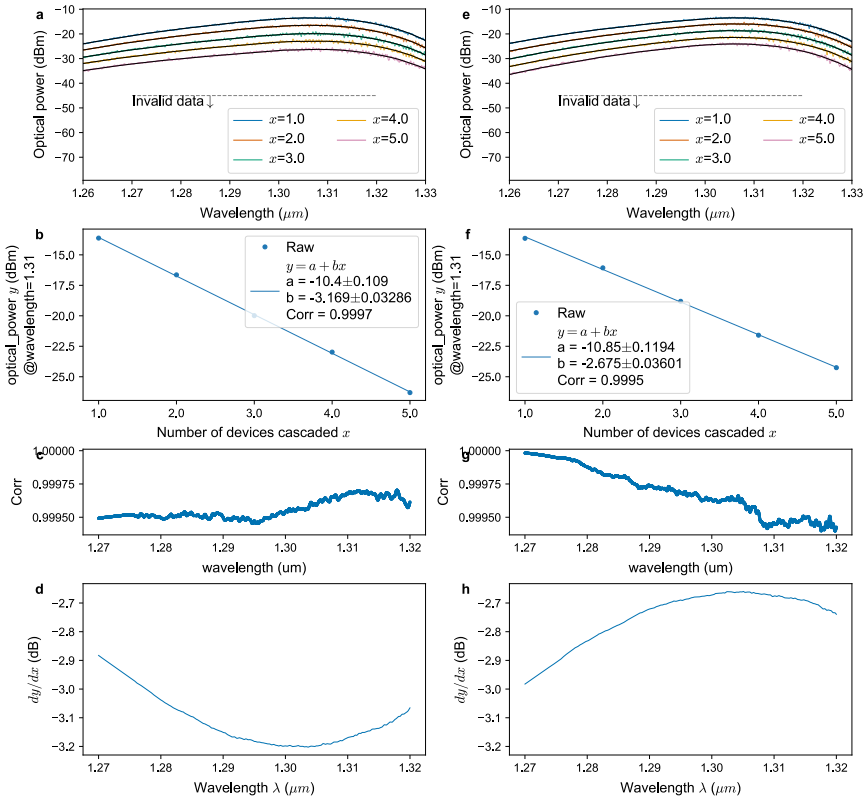

Figure 3.8: Data processing for coupling ratio extraction of the proposed 0.5:0.5 bent DC. The device has a bending radius of $25\ \mu$m*, a gap of* $0.1\ \mu$m*, and a coupling angle of* 8.5 degrees*. (a) Power at the through ports as a function of wavelength, where Savitzky-Golay filter is utilized to get rid of the noise (shown in black lines). (b) Linear regression between the power and the number of cascaded devices. (c) Correlation of the linear regression as a function of wavelength. (d) Extracted power from the slope of the linear regression as a function of wavelength. (e-h) Corresponding analysis for the cross ports.*

uide thickness, the coupling gap, the bending radius, and the coupling angle.

- The waveguide thickness is nominally fixed to 220 nm, as dictated by IMEC's iSiPP300 platform.
- The waveguide widths are nominally fixed to 380 nm as commonly used for devices in the O band.
- The coupling gap is chosen as 100 nm which is the minimum stable gap allowed in IMEC's iSiPP300 platform. The minimum value is chosen as the lower gap leads to higher coupling strength which leads to a more

compact design and lower sensitivity to wavelength variations.

– The free design parameters are the bending radius and the coupling angle, which are optimized through 3D FDTD simulations to achieve broadband coupling at a desired coupling ratio. Further, various bent DCs are fabricated with a sweep of bending radii and coupling angles values to experimentally build the coupling model.

Optical characterization methodology

To extract coupling coefficients for the bent DC, the cutback method was employed using cascaded identical devices. Fig. 3.7 shows the measurement setup where six identical bent DCs were cascaded in sequence. The measurements were conducted according to the following procedure:

- Light was input at the designated input port (labeled 'in' in Fig. 3.7)
- Output powers were measured at multiple stages along the cascade
- Port labels in Fig. 3.7 follow this convention:
  - 'Th' indicates power measured at a through port
  - 'Cr' indicates power measured at a cross port
  - The number indicates how many identical bent DCs with the same coupling state (i.e. through or cross) the light has traversed
- For example:
  - Port 'Th5' represents light that passed through five identical bent DCs via the through port, then coupled via the cross port in the sixth bent DC
  - Port 'Cr3' represents light that passed through three identical bent DCs via the cross port, then coupled via the through port in the fourth bent DC

According to the cutback method, when plotted on a logarithmic scale, the measured power at each (through or cross) output should decrease linearly with the number of cascaded identical bent DCs. By applying linear regression to these measurements, the through and cross coupling ratios can be reliably extracted from the slopes of the resulting lines. It is worth mentioning that the alignment of the pigtail fibers on top of the grating couplers is done at the same wavelength for all measurements. Further practical details on this implementation are shown in the following paragraphs.

Alternative methods for extracting DC coupling powers include direct measurement of the powers normalized to a reference waveguide or incorporating the DC into a ring resonator and determining the coupling from the ring's transmission spectrum. Each approach introduces its own sources of uncertainty. A mathematical analysis of error propagation reveals that the cutback method, particularly with a high number of cascades (i.e., ≥ 5), generally yields the lowest uncertainty (see Appendix A.3). Consequently, the cutback method is considered a reliable technique for extracting DC power coefficients.

The data processing for one of the bent DC devices is shown in Fig. 3.8, where the measured optical spectrum is presented in Fig. 3.8(a) and Fig. 3.8(e) for the through and cross ports, respectively. Before further analysis, Savitzky-Golay filter is applied to the measured optical powers to get rid of the noise, as shown in black lines in Fig. 3.8(a) and (e). The Savitzky-Golay filter is a digital smoothing filter that fits successive subsets of adjacent data points with a low-degree polynomial by the method of least squares. This approach is particularly effective for preserving the underlying trend of the signal while reducing noise, making it ideal for applications where signal integrity is crucial. By applying the Savitzky-Golay filter, the measured optical powers are smoothed from the interference patterns on the grating couplers without introducing significant uncertainty, ensuring that the extracted coupling coefficients remain accurate and reliable. The filter's ability to maintain the signal's tendency while minimizing noise has been widely demonstrated and highly adopted in signal processing literature, further validating its use in this context [32]. The through port data processing graphs are displayed in the left column, while the cross port graphs are in the right column of the figure. The corresponding linear regressions are depicted in Fig. 3.8(b) and Fig. 3.8(f). The correlations of the linear regressions, shown in Fig. 3.8(c) and Fig. 3.8(g), indicate high correlation values, demonstrating the reliability of the linear regression. Finally, the extracted power coupling coefficients are illustrated in Fig. 3.8(d) and Fig. 3.8(h) as a function of wavelength.

In order to reliably extract the excess loss and the other CMT parameters (i.e. A_t,A_c, m, β_c, and ϕ, as shown in Eq. 3.5), the coupling ratios are fitted into the CMT sinusoidal functions with respect to the coupling length or angle at each measured wavelength as shown in Fig. 3.9(a) for the straight DC, and in Fig. 3.9(b) for the bent DC. The sinusoidal curve fitting is performed with constraints to ensure the extracted CMT parameters remain within the range of physically plausible values. It is worth noting that the bent DC gap of 0.1 μm and bending radius of 25 μm are chosen in the analysis as they enable broadband coupling at 0.5:0.5 splitting ratio as will be demonstrated. The sinusoidal fitting (depicted as a solid line) is shown to be in good agreement with the experimental data (shown in dots). Through the fitting of the sinusoidal model as shown in Fig. 3.9, the model parameters were

extracted, where a significant improvement in the excess loss in the bent DC with low-loss bends is shown (Fig. 3.10(e)) as compared to the traditional straight DC design with traditional circular bends (bending radius of 5 μm, Fig. 3.10(a)), where the worst transmission improved from -0.128 ± 0.098 dB to -0.006 ± 0.004 dB (see Appendix A.3), due to the use of the low-loss bends, where the bends have both continuous curvature and curvature derivative at all connections [23]. The rest of the parameters are linearly fitted with respect to the working wavelength as shown in Fig. 3.10(b-d) for the straight DC and in Fig. 3.10(f-h) for the bent DC.

This low loss shows a substantially promising prospect for this device to be used in highly dense PICs like in dense WDM architectures. Further, as expected, $m \approx 1$ for the straight symmetric DC, while it is 0.704 at the wavelength of 1.31 μm for the bent DC due to the asymmetry. m (of the bent DC), β_c, and ϕ exhibit wavelength dependence that could be represented by a linear fitting as shown in Fig. 3.10(f-h). The wavelength dependence of the bent DC's parameters will be shown to cancel each other out at a specific regime in the following analysis.

Based on the experimentally extracted parameters of the bent DC (Fig. 3.10(e-h)), the two terms of the cross coupling derivative (Eq. 3.2) are plotted in Fig. 3.11. It is

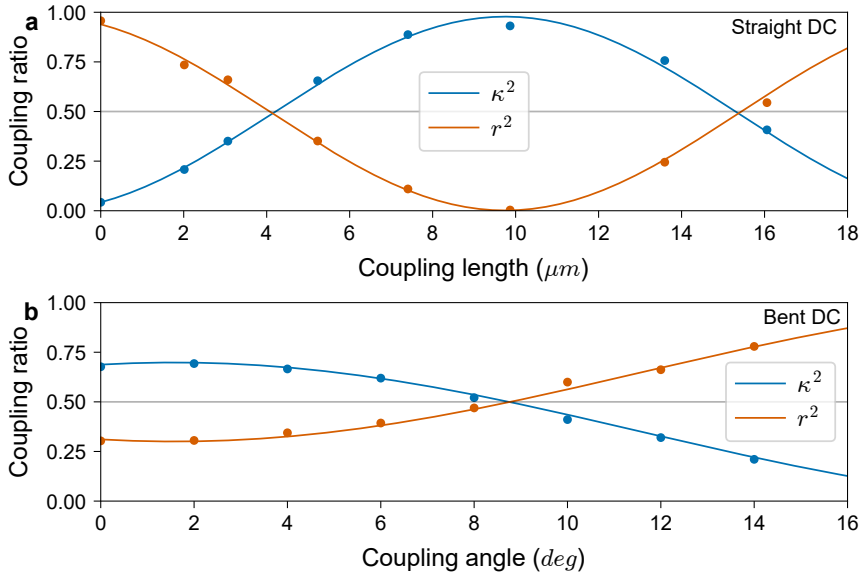

Figure 3.9: Sinusoidal fitting of the cross coupling (κ^2) and through coupling (r^2) with the coupling length for the straight DC (a) and with the coupling angle for the bent DC (b) at $\lambda = 1.31$ μm for the proposed devices. Both designs have a gap of 0.1 μm. The bent DC has a bending radius of 25 μm. Dots represent measured values, and lines depict the fitting.

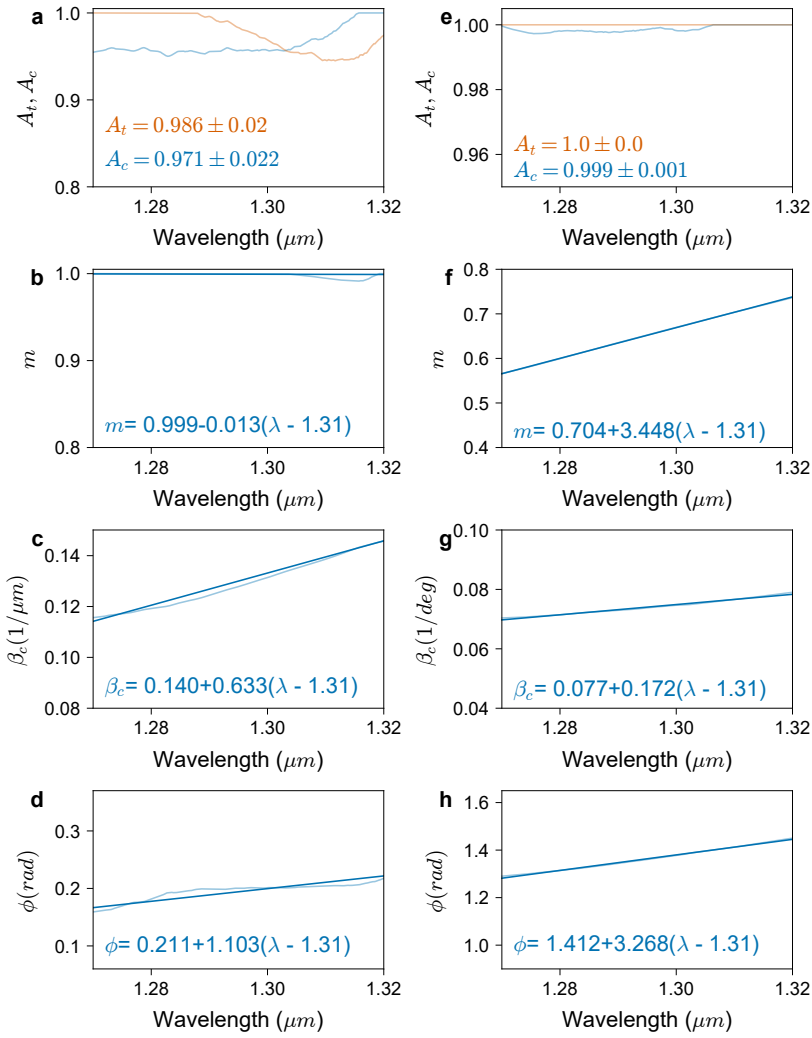

Figure 3.10: Extracted model parameters wavelength response with linear fitting based on experimental data. A_t, A_c, m, β_c, and ϕ for the 0.5:0.5 straight DC (a-d) and for the proposed 0.5:0.5 bent DC (e-h). The mean and standard deviation values for A_t and A_c for the straight (a) and bent DC (e) show the reduction of the loss by the introduction of the low-loss bends in the bent DC as compared to the traditional circular bends in the straight DC. The model parameters show expected wavelength dependence of the parameters. The symmetric straight DC has a matching coefficient, $\mathrm{m} \approx 1$, as expected (b), while the bent DC has a wavelength dependent matching coefficient with $m = 0.704$ at $\lambda = 1.31$. The straight DC has a coupling length of 5.23 μm and a gap of 0.1 μm. The bent DC has a bending radius of 25 μm, a gap of 0.1 μm, and a coupling angle of 8.5 degrees.

shown that a broadband response for the bent DC (i.e. $d\kappa^2/d\lambda = 0$) is feasible at the intersection of the positive part of the first term (plotted in blue) and the negative part of the second term (plotted in orange). At this intersection point (marked by stars for both terms), the wavelength dependence of the parameters cancel each other out. This implies the satisfaction of the broadband condition:

$$\frac{dm}{d\lambda}\sin^2(\beta_c l + \phi) = -m(l\frac{d\beta_c}{d\lambda} + \frac{d\phi}{d\lambda})\sin(2(\beta_c l + \phi)) \tag{3.6}$$

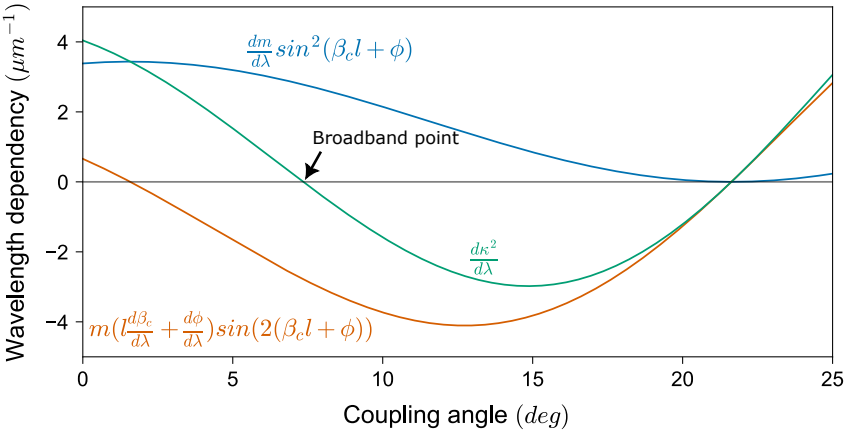

Figure 3.11: Cross coupling wavelength derivative ($d\kappa^2/d\lambda$, Eq. 3.2) of the bent DC, along with its constituent terms, demonstrating that broadband coupling (i.e. $d\kappa^2/d\lambda = 0$) can take place at the intersection of the positive and negative parts (marked by stars) of the sinusoid terms at a specific design regime. The black stars indicate points where the terms cancel each other. The proposed 0.5:0.5 bent DC has a bending radius of $25\ \mu$m *and a gap of* $0.1\ \mu$m.

3.3 3-dB coupler results and wafer mapping

After identifying the design point where broadband coupling occurs, as illustrated in Fig. 3.11, it is valuable to analyze the relationship between the coupling length (or angle), the cross coupling, and its wavelength derivative. This interplay is depicted in Fig. 3.12. To highlight the broadband coupling behavior and examine the influence of asymmetry on wavelength dependence, the cross coupling and its derivative are presented for fabricated 0.5:0.5 splitters using both straight and bent DCs. These results are shown in Fig. 3.12(a) for varying coupling lengths in straight DCs and Fig. 3.12(b) for varying coupling angles in bent DCs. In the case of the straight DC (Fig. 3.12(a)), $d\kappa^2/d\lambda = 0$ only at the valley and the peak

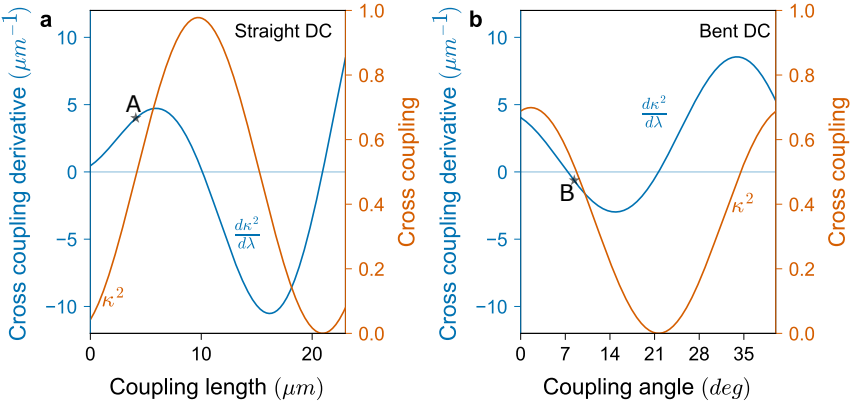

Figure 3.12: The cross coupling (κ^2) and the cross coupling derivative $(d\kappa^2/d\lambda)$ as a function of the coupling length for the straight DC (a) and as a function of the coupling angle for the bent DC (b). The introduced asymmetry presented in the bent DC shifted the broadband cross coupling point ($\kappa^2|_{d\kappa^2/d\lambda=0}$) from $\kappa^2|_{d\kappa^2/d\lambda=0} = 1$ to $\kappa^2|_{d\kappa^2/d\lambda=0} \sim 0.5$, this idea makes it possible to have broadband coupling at distinct coupling ratios based on the bending radius value. Points A and B represent the coupling derivative at 0.5 coupling. All the designs have a gap of 0.1 μm. The bent DC has a bending radius of 25 μm and a gap of 0.1 μm.

of the sinusoid (i.e. at 0 and 1 cross coupling ratios, respectively). Further, at the 0.5:0.5 point, $d\kappa^2/d\lambda \approx 4\ \mu m^{-1}$, very close to the peak of the derivative, showing high wavelength dependence (marked by A). Conversely, in the case of the bent DC (Fig. 3.12(b)), a cross coupling value of ~ 0.5 is achieved (marked by B) at a low cross coupling derivative of $d\kappa^2/d\lambda = -0.73$ with the proposed design parameters of a bending radius of 25 μm and a coupling angle of 8.5 degrees.

The coupling length and the coupling angle corresponding to 0.5 coupling ratio were extracted from Fig. 3.12 for both the straight and bent DC, respectively. Further, their coupling spectrum is depicted in Fig. 3.13(a) for the straight DC and in Fig. 3.13(b) for the bent DC, showing consistency with the presented analysis. In particular, in Fig. 3.13(a), the straight DC demonstrates high wavelength dependence, recording 0.391 coupling variation over 80 nm wavelength range. In contrast, the bent DC (Fig. 3.13(b)) exhibits broadband coupling and showcased a minimal cross coupling variation of 0.051. Quantitatively, the coupling variation of the proposed bent DC is 7.67 times lower than that of the straight DC. For the bent DC, around $\lambda = 1.3$ μm, $\kappa^2 \approx 0.5$ where $d\kappa^2/d\lambda$ is substantially reduced to zero enabling the broadband behavior of the coupler, in contrast to a highly variant coupling behavior of the straight DC. Furthermore, the model presented in Fig. 3.10 for the straight and bent DC was used to fit the experimental coupling data, as

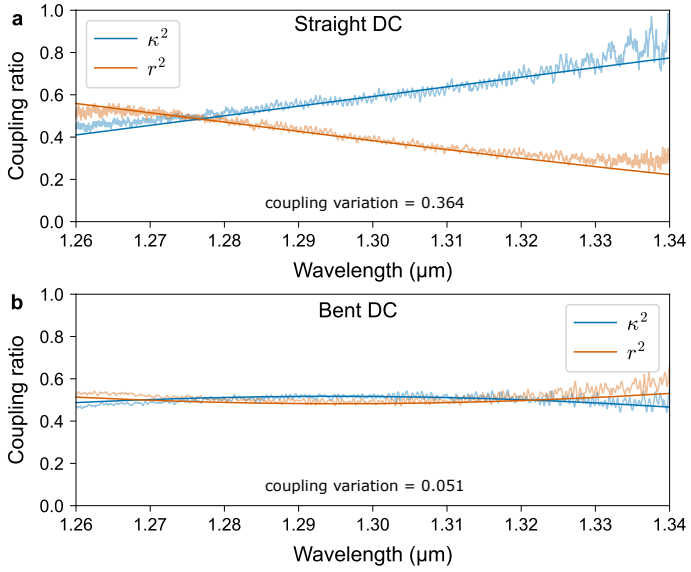

Figure 3.13: The measured coupling ratios of the traditional straight DC (a) and the proposed bent DC (b) at $0.5:0.5$ *coupling. The straight DC has a coupling length of 5.23* μm *and a gap of 0.1* μm*. The bent DC has a bending radius of 25* μm*, a gap of 0.1* μm*, and a coupling angle of* 8.5 degrees*. The bent DC shows broadband coupling with a minimal variation of 0.051 achieving 7.67 times reduction in coupling variation as compared to the straight DC. Non transparent lines show the model fitting, while the transparent lines show the measured experimental data.*

shown in Fig. 3.13 by solid curves with deeper colors, showing agreement with the experimental data. It is worth mentioning that the oscillations in the transmission spectrum are due to the measurement setup and working close to the edge of the grating coupler operating wavelength range.

To assess the fabrication tolerance of the proposed $0.5:0.5$ bent DC and benchmark it with that of the straight DC, the coupling behavior of devices with waveguide width deviations (δw) of $-20,\ -10,\ 0,\ 10,\ 20$ nm are simulated using 3D-FDTD model for both the straight DC (Fig. 3.14(a)) and the bent DC (Fig. 3.14(b)). Over the presented wavelength range, the bent DC shows low coupling variations and still performs well even with $\delta \mathrm{w} = \pm 20$ nm, showcasing the tolerance of the proposed device, while the straight DC shows high coupling variations overall. For instance, with a deviation of $\delta \mathrm{w} = \pm 10$ nm, the straight DC exhibited maximum cross coupling variations around the $0.5:0.5$ point of 0.035 , whereas the bent DC exhibited less variations of 0.011.

Furthermore, the robustness of the proposed design across the 300 mm wafer is

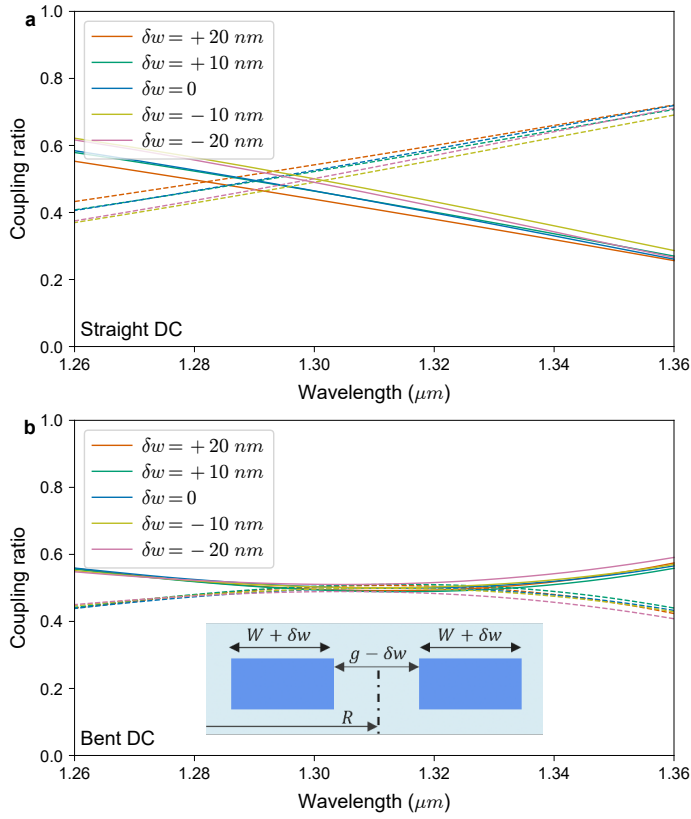

Figure 3.14: Fabrication tolerance analysis based on 3D FDTD simulations of the traditional straight DC (a) and the proposed $0.5 : 0.5$ *bent DC (b). Coupling spectrum simulation results of the nominal design (*$\delta w = 0$*) along with waveguide width deviations of -20, -10, 10, 20 nm. Through couplings are shown in solid lines and the cross couplings are shown in dashed lines. The inset figure depicts the waveguide width (*W*) deviation and the corresponding gap deviation for the SOI-based DCs. The nominal straight DC design has a coupling length of 5.23* μm *and a gap (*g*) of* $0.1\ \mu m$*. The nominal bent DC design has a bending radius (*R*) of* $25\ \mu$m*, a g of* $0.1\ \mu m$*, and a coupling angle of* 8.5 degrees*.*

also investigated. Complete wafer measurements were conducted for two metrics, namely the cross coupling deviation, averaged over 80 nm wavelength range, with respect to the central die (Fig. 3.15(a)) and the cross coupling variation (Fig. 3.15(b)) over 80 nm wavelength range, covering all 63 dies. It can be shown that over the wafer and in particular around the nine central dies, low average cross coupling deviations and cross coupling variations are observed. Overall, the die with the largest coupling variation was die (5, 0) at the extreme edge of the wafer where process variations are usually high. Die (5,0) has 0.112 maximum cross

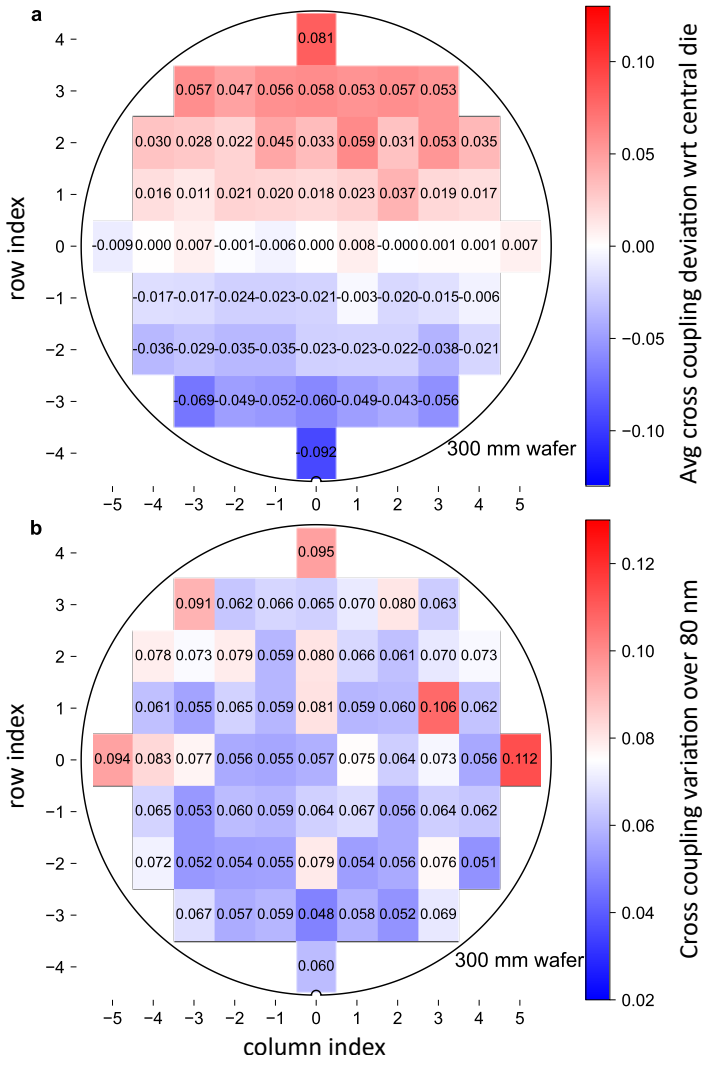

Figure 3.15: Average cross coupling deviation with respect to the central die (a) and cross coupling variation (b) over 80 nm bandwidth for the proposed 0.5:0.5 bent DC splitter over the 300 mm wafer, covering all 63 dies. Low variation is shown over all dies except a relatively higher variation at the edges of the wafer, as expected due to process variation. The bent DC has a bending radius of 25 μm*, a gap of* 0.1 μm*, and a coupling angle of* 8.5 degrees.

coupling variation over 80 nm wavelength range. In general, the results indicate low variations across most dies, with a relatively high value observed only at the extreme edges of the wafer. This further illustrates the potential of the proposed

bent DCs to be used in Dense WDM systems reliably.

3.4 Model for arbitrary broadband coupling ratios

In many WDM architectures, coupling ratios different from 0.5 are often required. Therefore, a reliable model for achieving broadband coupling at arbitrary ratios would be highly beneficial. The cross coupling wavelength derivative ($d\kappa^2/d\lambda$) and the cross coupling (κ^2) are plotted in Fig. 3.16(a) and Fig. 3.16(b), respectively, as a function of the bending radius and the coupling angle while maintaining a fixed gap of 0.1 μm and waveguide widths of 0.38 μm. A line is drawn indicating points where $d\kappa^2/d\lambda = 0$ in both plots, which is the condition for broadband coupling. This indicates the possibility of achieving broadband coupling at arbitrary coupling ratios by tuning the bending radius and the coupling angle.

In the bent DC, the asymmetry is inversely proportional to the bending radius (R), with higher asymmetry, higher phase mismatch takes place and the maximum coupling ratio goes down. A comprehensive fitting was conducted for broadband coupling ratios (red contour in Fig. 3.16), as shown in Fig. 3.17. As depicted in Fig. 3.17(a), with the increase of the bending radius, the mismatch decreases and higher cross coupling values are achieved. Additionally, the increase of the bending radius (i.e. decrease in the mismatch) implies a decrease in the required coupling angle to achieve a specific coupling value, as illustrated in Fig. 3.17(b). This fitting provides a valuable tool for achieving broadband coupling for arbitrary coupling ratios.

The fitting depicted in Fig. 3.17 is subsequently employed to extract broadband splitters with arbitrary coupling ratios. As illustrated in Fig. 3.18, multiple examples of devices with broadband cross coupling ratios of 0.4 (a), 0.5 (b), 0.6 (c), and 0.7 (d) are shown. The corresponding cross coupling variations over 50 nm wavelength range for these ratios are minimally equal to 0.023, 0.023, 0.038, and 0.034, respectively. This affirms the potential of the proposed methodology for designing broadband coupling ratios with flexibility.

Compared to the results existing in literature (Tab. 3.1 and Tab.3.2), the proposed splitter stands out as a high-performance design that simultaneously meets all essential criteria of low wavelength dependence, ultra low-loss coupling, compact footprint, support for arbitrary coupling ratios, and high fabrication tolerance. Specifically, the proposed model represents the first demonstration of an experimental-based model to achieve broadband coupling with arbitrary coupling ratios using the bent DC. On that basis, a compact 2×2 splitter with low coupling variation and excess loss is presented. Furthermore, the proposed device exhibits

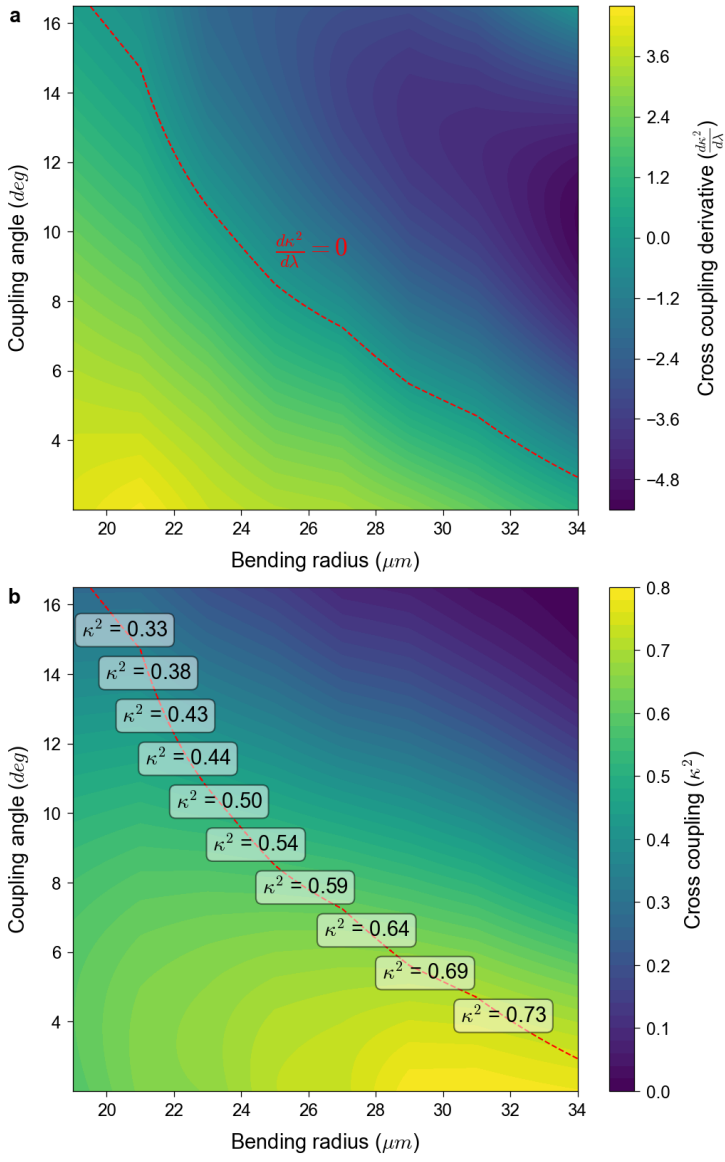

Figure 3.16: Contour plot for the cross coupling wavelength derivative (a) and the cross coupling (b) as a function of the design parameters (bending radius and coupling angle). A few cross coupling values are plotted along the zero derivative contour in (b). The coupling gap and waveguides widths are fixed as 0.1 μm *and* 0.38 μm*, respectively.*

consistently low variations across the 300 mm wafer, indicating its fabrication tolerance. The wafer measurements are augmented with waveguides width variations

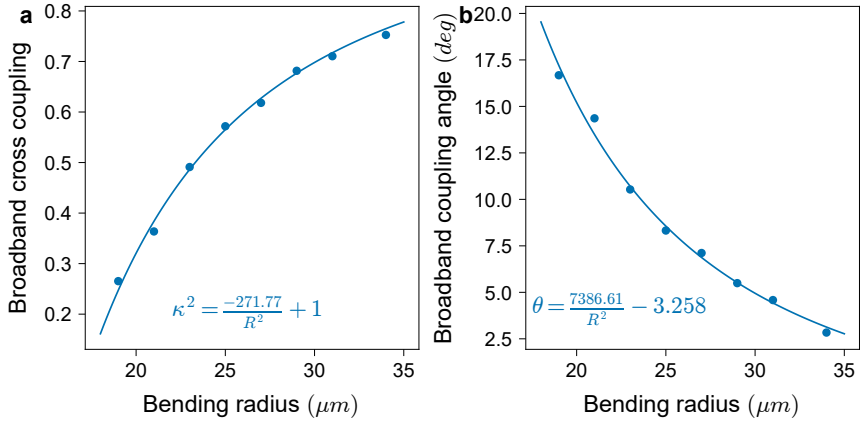

Figure 3.17: The proposed model for extracting broadband bent DCs with arbitrary coupling ratios. Broadband cross coupling values as a function of the bending radius (a). The corresponding coupling angle as a function of bending radius (b). The experimental data is shown in dots while the fitting model is depicted as a solid line. The coupling gap and waveguides widths are fixed as 0.1 μm *and* 0.38 μm*, respectively.*

Reference	Structure	0.5:0.5 coupling variation (over 80 nm)	Excess loss (dB)
[8]	MMI	> 0.037	< 1.3
[10]	Rib-waveguide ADC	0.082	< 0.22
[11]	Rib-waveguide ADC	0.038	< 0.18
[13]	ADC	> 0.1	-
[15]	MZI	0.11	< 1
[17]	MZI circuit	0.051	< 0.38
[22]	SWG-assisted ADC	0.039	< 0.11
[26]	Bent DC	0.18	-
[27]	Bent DC	0.13	< 1
[28]	Inverse designed bent DC	0.106	< 0.05
This work	Bent DC	0.051	0.006 ± 0.004

Table 3.1: Performance comparison table (a): Coupling variation and excess loss of various fabricated 2×2 *splitters.*

study, where the proposed device showed a cross coupling variation away from 0.5 of 0.061 over the proposed wavelength range for $\delta \mathrm{w} = \pm 20$ nm. These features highlight the potential of the proposed device to be used in mass production reliably. Future designs could use the findings of this chapter and the proposed model to design more broadband bent DCs.

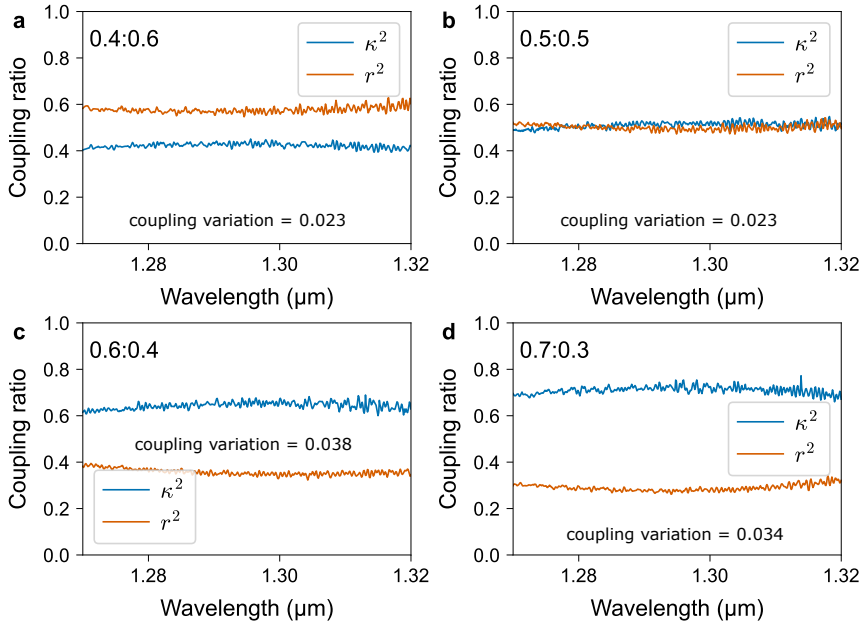

Figure 3.18: Examples of broadband bent DCs with arbitrary coupling ratios in accordance with the proposed model, where the through and cross coupling are shown as a function of wavelength. Devices with broadband 0.4 (a), 0.5 (b), 0.6 (c), and 0.7 (d) cross coupling values are presented. The bending radii and the coupling angles of the devices are: 23 μm *and* 12 degrees *(a),* 25 μm *and* 8.5 degrees *(b),* 29 μm *and* 6 degrees *(c), and* 34 μm *and* 4 degrees *(d). All the designs have a gap of* 0.1 μm.

3.5 Compatibility with 200 mm and 300 mm platforms

The proposed 3-dB bent DC was initially designed with a gap of 100 nm, which is incompatible with most 200 mm platforms that typically impose a minimum gap limitation of 150 nm. To address this limitation, a 3-dB bent DC was designed with a gap of 150 nm to ensure compatibility with 200 mm platforms. This design features a bending radius of 47 μm and a coupling angle of 8.8 degrees. The measured coupling spectrum of the 150 nm gap device is illustrated in Fig. 3.19. While this design achieves compatibility with 200 mm platforms, it exhibits a slightly higher coupling variation compared to the 100 nm gap design. This observation aligns with the general trend that smaller coupling gaps typically result in lower coupling variations, as confirmed by both simulations and experimental measurements.

Furthermore, bent DC devices with a gap of 80 nm have been investigated. Focused

Reference	Structure	Device length (μm)	Coupling ratios
[8]	MMI	75	0.07, 0.15, 0.3, 0.4, 0.5, 0.6, 0.7, 0.8, 0.9
[10]	Rib-waveguide ADC	79	0.5, 0.7, 0.9
[11]	Rib-waveguide ADC	108	0.5
[13]	ADC	67	0.5
[15]	MZI	31.4	0.1, 0.2, 0.3, 0.4, 0.5
[17]	MZI circuit	60	0.05, 0.2, 0.3, 0.5
[22]	SWG-assisted ADC	35	0.5
[26]	Bent DC	> 20	0.5
[27]	Bent DC	50	0.5
[28]	Inverse designed bent DC	28.8	0.5
This work	Bent DC	27.5	0.4, 0.5, 0.6, 0.7 with model

Table 3.2: Performance comparison table (b): Device length and demonstrated coupling ratios of various fabricated 2×2 *splitters.*

ion beam (FIB) analysis was performed on the gap of one such device to examine potential abnormalities. Some cross sections revealed what appeared to be uneven gap filling, as shown in Fig. 3.20. However, optical characterization of the device did not reveal any resonances indicative of significant scattering, as demonstrated in Fig. 3.21. In the subsequent chapter, ultra-broadband designs with a coupling gap of 80 nm are explored, which have been taped out for the 300 mm platform.

3.6 Conclusion

In conclusion, this chapter presented a comprehensive CMT-based and experimental analysis for a bent DC with low wavelength sensitivity. Leveraging this analysis, a model was derived in order to achieve broadband bent DCs with arbitrary coupling ratios. In particular, the proposed model is used to verify the broadband bent DCs at a few coupling ratios including 0.4, 0.5, 0.6, and 0.7. As a benchmark, a 0.5:0.5 splitter is demonstrated showcasing the least coupling variation in a bent DC to my best knowledge with 0.051 cross coupling variation over 80 nm wavelength range. Additionally, the proposed 0.5:0.5 splitter exhibited low excess loss of 0.006 ± 0.004 dB, along with the capability of achieving arbitrary coupling ratios, compactness (with a length of 27.5 μm), and high fabrication tolerance (with a cross coupling variation of 0.061 with $\delta \mathrm{w} = \pm 20$ nm over 80 nm wavelength range). Wafer mapping analysis confirmed the robustness of the proposed device for practical applications, with low variation observed over a 300 mm wafer, exhibiting a maximum coupling variation value of 0.112 at the extreme edge of the

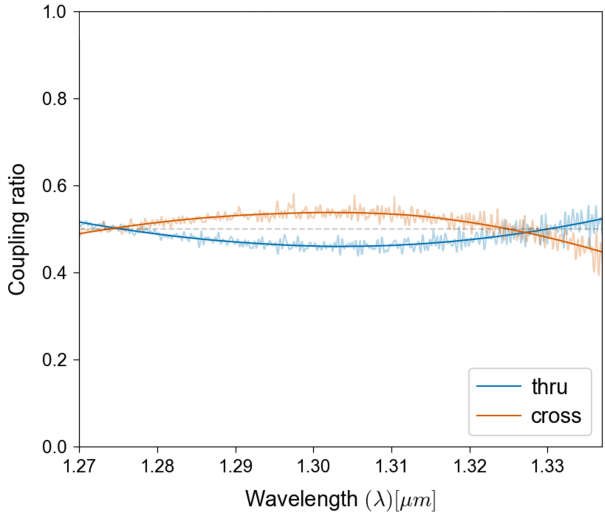

Figure 3.19: The coupling spectrum of the proposed 3-dB bent DC with a gap of 150 nm, designed for compatibility with 200 mm platforms. The device features a bending radius of 47 μm and a coupling angle of 8.8 degrees. Transparent lines represent the measured data, while solid lines depict the smoothed data.

wafer over 80 nm wavelength range. Overall, the proposed bent DCs meet all the aforementioned essential requirements and exhibit reliability for integration into highly dense PICs, and can be used as a building block in WDM systems, as will be demonstrated in the following chapters. Additionally, a more 'relaxed' design with a 150 nm gap is presented, ensuring compatibility with the 200 mm platform. Finally, FIB analysis is conducted for a bent DC with an 80 nm gap to investigate the feasibility of smaller gaps in future iterations, as smaller gaps have been shown to reduce wavelength sensitivity and coupling variations.

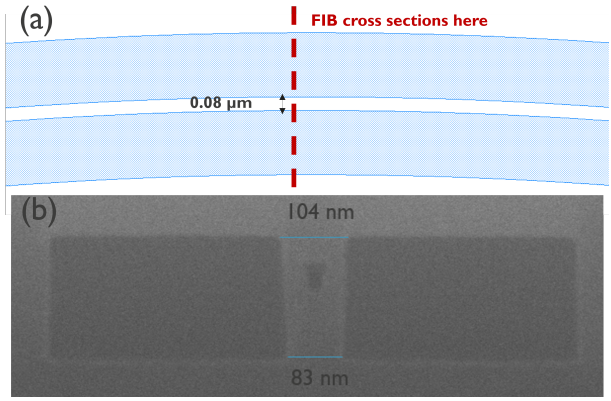

Figure 3.20: Schematic illustrating the FIB cross section taken from the fabricated bent DC with an 80 nm gap (a). Multiple FIB cross sections were analyzed around the region highlighted in red. The resulting FIB image at the indicated cross section (b) reveals minor unevenness in the gap filling observed in certain cross sections. The cross section shows a typical sloped sidewall of the waveguides with a base gap of ≈ 83 nm, and a top gap of ≈ 104 nm.

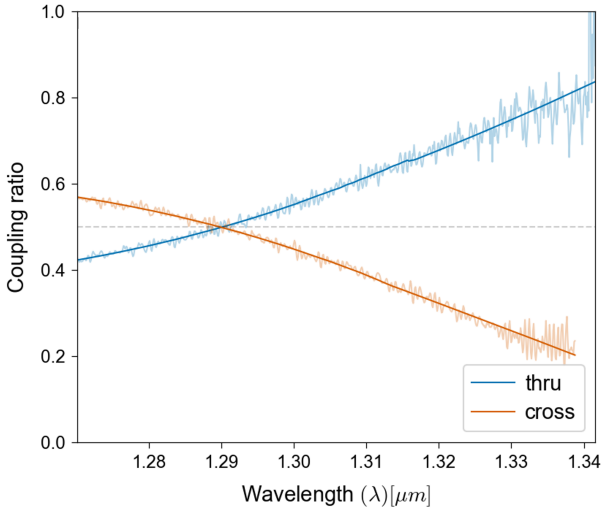

Figure 3.21: The coupling spectrum of a bent DC device with an 80 nm gap, demonstrating normal optical behavior without any resonances indicative of significant scattering. Transparent lines represent the measured data, while solid lines depict the smoothed data.

References

[1] Jia ming Liu. *Photonic Devices*. Cambridge University Press, April 2005. ISBN 9780521551953. doi: 10.1017/cbo9780511614255.

[2] Qingzhong Deng, Ahmed H. El-Saeed, Alaa Elshazly, Guy Lepage, Chiara Marchese, Hakim Kobbi, Rafal Magdziak, Jeroen De Coster, Neha Singh, Marko Ersek Filipcic, Kristof Croes, Dimitrios Velenis, Maumita Chakrabarti, Peter De Heyn, Peter Verheyen, Philippe Absil, Filippo Ferraro, Yoojin Ban, and Joris Van Campenhout. 32x100 GHz WDM filter based on ultra-compact silicon rings with a high thermal tuning efficiency of 5.85 mw/pi. In *Optical Fiber Communication Conference (OFC)*, page W1A, 2024.

[3] Ahmed Bayoumi, Mehmet Oktay, Alaa Elshazly, Hakim Kobbi, Rafal Magdziak, Guy Lepage, Chiara Marchese, Javad Rahimi Vaskasi, Swetanshu Bipul, Dieter Bode, Dimitrios Velenis, Maumita Chakrabarti, Peter Verheyen, Philippe Absil, Filippo Ferraro, Yoojin Ban, Joris Van Campenhout, Wim Bogaerts, and Qingzhong Deng. Enhanced operation range of silicon MZI filters using a broadband bent directional coupler. *IEEE Photonics Technology Letters*, 37(9):500–503, May 2025. ISSN 1941-0174. doi: 10.1109/lpt.2025.3553059.

[4] Shihao Sun, Mingbo He, Mengyue Xu, Shengqian Gao, Siyuan Yu, and Xinlun Cai. Hybrid Silicon and Lithium Niobate Modulator. *IEEE Journal of Selected Topics in Quantum Electronics*, 27(3):1–12, May 2021. ISSN 1558-4542. doi: 10.1109/JSTQE.2020.3036059.

[5] Sitao Chen, Yaocheng Shi, Sailing He, and Daoxin Dai. Low-loss and broadband 2x2 silicon thermo-optic mach-zehnder switch with bent directional couplers. *Optics Letters*, 41(4):836, February 2016. doi: 10.1364/ol.41.000836.

[6] Yi-Ting Lu, Benedictus Yohanes Bagus Widhianto, Shih-Hsiang Hsu, and Che-Chang Chang. Tandem mach zehnder directional coupler design and simulation on silicon platform for optical coherence tomography applications. *Sensors*, 20(4):1054, February 2020. ISSN 1424-8220. doi: 10.3390/s20041054.

[7] L.B. Soldano and E.C.M. Pennings. Optical multi-mode interference devices based on self-imaging: principles and applications. *Journal of Lightwave Technology*, 13(4):615–627, April 1995. ISSN 0733-8724. doi: 10.1109/50.372474.

[8] Jin Zhang, Liangshun Han, Bill Ping-Piu Kuo, and Stojan Radic. Broadband angled arbitrary ratio SOI MMI couplers with enhanced fabrication tolerance.

Journal of Lightwave Technology, 38(20):5748–5755, October 2020. ISSN 1558-2213. doi: 10.1109/jlt.2020.3004424.

[9] Devendra Chack and Shamsul Hassan. Design and experimental analysis of multimode interference-based optical splitter for on-chip optical interconnects. *Optical Engineering*, 59(10):105102, October 2020. ISSN 0091-3286, 1560-2303. doi: 10.1117/1.OE.59.10.105102. Publisher: SPIE.

[10] Xiang Liu, Zhen Sheng, Yingxuan Zhao, and Fuwan Gan. Ultra-broadband on-chip power splitters for arbitrary ratios on silicon-on-insulator. *Optics Express*, 32(2):2029, January 2024. ISSN 1094-4087. doi: 10.1364/oe.508058.

[11] Xiang Liu, Yingxuan Zhao, Zhen Sheng, and Fuwan Gan. Compact and ultra-broadband silicon photonic adiabatic directional coupler using rib waveguides. *IEEE Photonics Technology Letters*, 36(10):1–1, May 2024. ISSN 1941-0174. doi: 10.1109/LPT.2024.3381826.

[12] Deng Mao, Yun Wang, Eslam El-Fiky, Luhua Xu, Amar Kumar, Maxime Jaques, Alireza Samani, Olivier Carpentier, Santiago Bernal, Md Samiul Alam, Jinsong Zhang, Mingyue Zhu, Ping-Chiek Koh, and David V. Plant. Adiabatic Coupler With Design-Intended Splitting Ratio. *Journal of Lightwave Technology*, 37(24):6147–6155, December 2019. ISSN 1558-2213. doi: 10.1109/JLT.2019.2946948.

[13] Hung-Ching Chung, Chih-Hsien Chen, Guan-Xun Lu, Yung-Jr Hung, and Shuo-Yen Tseng. Adiabaticity Engineered Silicon Polarization Independent 3-dB Coupler for the O-Band. *IEEE Photonics Journal*, 15(3):1–6, June 2023. doi: 10.1109/JPHOT.2023.3271320.

[14] Jiejiang Xing, Kang Xiong, Hao Xu, Zhiyong Li, Xi Xiao, Jinzhong Yu, and Yude Yu. Silicon-on-insulator-based adiabatic splitter with simultaneous tapering of velocity and coupling. *Optics Letters*, 38(13):2221–2223, July 2013. ISSN 1539-4794. doi: 10/gnsck5. URL https://opg.optica.org/ol/abstract.cfm?uri=ol-38-13-2221. Publisher: Optical Society of America.

[15] Zeqin Lu, Han Yun, Yun Wang, Zhitian Chen, Fan Zhang, Nicolas A. F. Jaeger, and Lukas Chrostowski. Broadband silicon photonic directional coupler using asymmetric-waveguide based phase control. *Optics Express*, 23(3):3795–3808, February 2015. ISSN 1094-4087. doi: 10/gmf37j.

[16] Ramesh K. Gupta, Sujith Chandran, and Bijoy Krishna Das. Wavelength-Independent Directional Couplers for Integrated Silicon Photonics. *Journal of Lightwave Technology*, 35(22):4916–4923, November 2017.

[17] Marios Papadovasilakis, Sujith Chandran, Yonas Gebregiorgis, Yusheng Bian, Michal Rakowski, Subramanian Krishnamurthy, Abdelsalam Aboketaf, Rod Augur, and Jaime Viegas. Fabrication tolerant and wavelength independent arbitrary power splitters on a monolithic silicon photonics platform. *Optics Express*, 30(19):33780, August 2022. ISSN 1094-4087. doi: 10.1364/oe.463721.

[18] Qiuyang Jiang, Guangfan Tao, and Xiangning Chen. Comparison of fabrication tolerance of broadband silicon photonic directional couplers. In *Optoelectronic Devices and Integration VIII*, volume 11184, pages 27–34. SPIE, November 2019. doi: 10.1117/12.2537596.

[19] Mi Wang, Mi Wang, Antonio Ribero, Antonio Ribero, Yufei Xing, Yufei Xing, and Wim Bogaerts. Tolerant, broadband tunable 2x2 coupler circuit. *Optics Express*, 28(4):5555–5566, February 2020. ISSN 1094-4087. doi: 10/gj6sv7.

[20] Xiang Liu, Yingxuan Zhao, Zhen Sheng, and Fuwan Gan. Ultra-Broadband, Compact Arbitrary Ratio Power Splitters Enabled by Adiabatic Sub-Wavelength Grating. *Photonics*, 10(5):578, May 2023. ISSN 2304-6732. doi: 10.3390/photonics10050578. URL https://www.mdpi.com/2304-6732/10/5/578.

[21] Heng Xie, Jiajiu Zheng, Peipeng Xu, Jianting Yao, James Whitehead, and Arka Majumdar. Ultra-Compact Subwavelength-Grating-Assisted Polarization-Independent Directional Coupler. *IEEE Photonics Technology Letters*, 31(18):1538–1541, September 2019. ISSN 1941-0174. doi: 10.1109/LPT.2019.2937890.

[22] Han Yun, Lukas Chrostowski, and Nicolas A. F. Jaeger. Ultra-broadband 2×2 adiabatic 3 dB coupler using subwavelength-grating-assisted silicon-on-insulator strip waveguides. *Optics Letters*, 43(8):1935–1938, April 2018. ISSN 1539-4794. doi: 10/gmqffw. Publisher: Optical Society of America.

[23] Qingzhong Deng, Pieter Neutens, Rafal Magdziak, Ahmed H. El-Saeed, Yoojin Ban, Filippo Ferraro, Guy Lepage, Jeroen De Coster, Dimitrios Velenis, Maumita Chakrabarti, Peter De Heyn, Peter Verheyen, Pol Van Dorpe, and Joris Van Campenhout. Low-loss Waveguide Bend Supporting a Whispering Gallery Mode. In *2023 IEEE Silicon Photonics Conference*, pages 1–2, April 2023. doi: 10.1109/SiPhotonics55903.2023.10141913. ISSN: 1949-209X.

[24] C.R. Doerr, M. Cappuzzo, E. Chen, A. Wong-Foy, L. Gomez, A. Griffin, and L. Buhl. Bending of a planar lightwave circuit 2×2 coupler to desensitize it to wavelength, polarization, and fabrication changes. *IEEE Photonics Technology Letters*, 17(6):1211–1213, June 2005. ISSN 1941-0174. doi: 10.1109/LPT.2005.846922.

[25] Hisayasu Morino, Takeo Maruyama, and Koichi Iiyama. Reduction of Wavelength Dependence of Coupling Characteristics Using Si Optical Waveguide Curved Directional Coupler. *Journal of Lightwave Technology*, 32(12):2188–2192, June 2014. ISSN 1558-2213. doi: 10.1109/JLT.2014.2321660.

[26] George F. R. Chen, Jun Rong Ong, Thomas Y. L. Ang, Soon Thor Lim, Ching Eng Png, and Dawn T. H. Tan. Broadband Silicon-On-Insulator directional couplers using a combination of straight and curved waveguide sections. *Scientific Reports*, 7(1):7246, August 2017. ISSN 2045-2322. doi: 10.1038/s41598-017-07618-6.

[27] Xun Chen, Weixi Liu, Yuguang Zhang, and Yaocheng Shi. Polarization-insensitive broadband 2 × 2 3 dB power splitter based on silicon-bent directional couplers. *Optics Letters*, 42(19):3738, September 2017. doi: 10.1364/ol.42.003738.

[28] Laiwen Yu, Jingshu Guo, Hengtai Xiang, Chaoyue Liu, Yuqi Zhao, and Daoxin Dai. High-performance 2×2 bent directional couplers designed with an efficient semi-inverse design method. *Journal of Lightwave Technology*, 42(2):1–8, January 2024. ISSN 1558-2213. doi: 10.1109/JLT.2023.3315214.

[29] Ahmed H. El-Saeed, Alaa Elshazly, Hakim Kobbi, Rafal Magdziak, Guy Lepage, Chiara Marchese, Javad Rahimi Vaskasi, Swetanshu Bipul, Dieter Bode, Marko Ersek Filipcic, Dimitrios Velenis, Maumita Chakrabarti, Peter De Heyn, Peter Verheyen, Philippe Absil, Filippo Ferraro, Yoojin Ban, Joris Van Campenhout, Wim Bogaerts, and Qingzhong Deng. Low-loss silicon directional coupler with arbitrary coupling ratios for broadband wavelength operation based on bent waveguides. *Journal of Lightwave Technology*, 42 (17):6011–6018, September 2024. ISSN 1558-2213. doi: 10.1109/jlt.2024.3407339.

[30] Ahmed H. El-Saeed, Alaa Elshazly, Hakim Kobbi, Rafal Magdziak, Guy Lepage, Chiara Marchese, Swetanshu Bipul, Dieter Bode, Marko E. Filipcic, Dimitrios Velenis, Maumita Chakrabarti, Peter De Heyn, Peter Verheyen, Philippe Absil, Filippo Ferraro, Yoojin Ban, Joris Van Campenhout, Wim Bogaerts, and Qingzhong Deng. Wavelength-insensitive and lossless 50:50 directional coupler based on silicon bent waveguides. In *2024 IEEE Silicon Photonics Conference*, 2024.

[31] F. J. Ferraro, P. De Heyn, M. Kim, N. Rajasekaran, M. Berciano, G. Muliuk, D. Bode, G. Lepage, S. Janssen, R. Magdziak, J. De Coster, H. Kobbi, S. Lardenois, N. Golshani, L. Shiramin, C. Marchese, S. Rajmohan, S. Nadarajan, N. Singh, S. Radhakrishnan, A. Tsiara, P. Xu, A. Karagoz, D. Yudistira, M. Martire, A. Shahar, M. Chakrabarti, D. Velenis, W. Guo, A. Miller,

Kristof Croes, S. Balakrishnan, P. Verheyen, Y. Ban, J. Van Campenhout, and P. P. Absil. Imec silicon photonics platforms: performance overview and roadmap. In *Next-Generation Optical Communication: Components, Sub-Systems, and Systems XII*, volume 12429, pages 22–28. SPIE, March 2023. doi: 10.1117/12.2650579.

[32] Abraham. Savitzky and M. J. E. Golay. Smoothing and Differentiation of Data by Simplified Least Squares Procedures. *Analytical Chemistry*, 36(8): 1627–1639, July 1964. ISSN 0003-2700, 1520-6882. doi: 10/dktbw4. ZSCC: 0017054.

4

Broadband Adiabatic Couplers

In the previous chapter, bent directional couplers (DCs) were introduced as a broadband 2×2 splitter to be used in wavelength division multiplexing (WDM) systems. However, bent DCs still exhibit a sinusoidal coupling response, and their coupling variation is not completely optimal. To further enhance the performance, minimizing the deviation from the desired coupling ratio is essential for designing better WDM filters. This chapter focuses on adiabatic couplers, presenting a new optimization strategy based on a minmax approach to minimize coupling variation. By optimizing the adiabatic coupler design parameters, a 3 dB adiabatic coupler is numerically demonstrated with a coupling variation of only 0.02 over a 120 nm wavelength range covering the O-band, representing a 16.6$\times$ reduction compared to traditional straight DCs. The proposed 3 dB coupler also achieves an insertion loss of $\leq$0.03 dB and an ultra-compact taper length of 1.44 μm, the shortest reported to date to my best knowledge. Arbitrary coupling ratios are attainable by adjusting the final taper widths and the taper length. Overall, the proposed coupler and design methodology enable highly optimized 2×2 couplers for next-generation photonic integrated circuits, particularly benefiting WDM filters requiring broad wavelength operation.

4.1 State of the art 100
4.2 Design and optimization scheme for the 3 dB splitter . . . 102
4.3 Broadband coupling and arbitrary coupling ratios 108

4.4 Impact of the waveguide width and coupling gap 110
4.5 Conclusions 112
References 115

4.1 State of the art

2×2 splitters are essential in photonic integrated circuits (PICs) for wavelength division multiplexing (WDM) [1, 2], modulation [3], and switching [4]. While symmetric directional couplers (DCs) are commonly used, their wavelength sensitivity often degrades performance. Ideal splitters should be broadband, compact, low-loss, and support arbitrary coupling ratios. Proposed solutions include multi-mode interferometers [5], phase-compensated DCs [6], subwavelength grating DCs [7], rib waveguide DCs [8], bent DCs [9], and adiabatic couplers [10].

Several issues persist in current designs: high insertion loss [5–8, 10], which is problematic for dense WDM systems with cascaded splitters, large footprints [8, 9], and fabrication challenges [10]. Further improvements in coupling variation and performance remain needed for silicon photonic splitters.

In symmetric straight DCs, both even and odd supermodes are excited due to structural symmetry, resulting in a sinusoidal and wavelength-dependent coupling response as described by coupled mode theory (CMT) (see Appendix A.1.1) [11]. In contrast, adiabatic couplers are designed such that only a single mode is predominantly excited, enabling broadband and robust power transfer. Adiabatic couplers leverage gradual changes in waveguide geometry to ensure the optical mode evolves smoothly from one waveguide to the other, minimizing scattering and excess loss [12, 13]. The adiabatic principle ensures that the system remains in its instantaneous eigenmode throughout the transition, which is key to achieving efficient and broadband coupling.

In the existing literature, the design parameters of adiabatic couplers are typically chosen to ensure a large asymmetry, maintaining single-mode operation throughout the device. This is often achieved by optimizing the asynchronicity parameter ($X \equiv \frac{\Delta\beta}{2\kappa}$), where $\Delta\beta$ is the difference in propagation constants of two isolated waveguides, and κ is the coupling strength between two waveguides with a certain gap (see Appendix A.1.1) [11]. Researchers often choose to focus on increasing $\Delta\beta$, as its variation is more significant compared to κ.

The optimized design parameters to enhance asynchronicity include the taper length, input and output waveguide widths, coupling gap, and the S-bend parameters of the input and output coupling/decoupling sections. A few adiabatic coupler examples

are shown in Fig. 4.1 [14, 15], where the taper length is $\geq 165\,\mu m$. Arbitrary coupling ratios are typically achieved by adjusting only the output waveguide widths [15, 16]. However, this approach often results in non-optimized wavelength dependence of the coupling and large taper lengths in reported adiabatic couplers [7, 10, 14–26].

In this chapter, a new scheme for the design of adiabatic couplers is proposed. In particular, the wavelength sensitivity of the coupling ratio in adiabatic couplers is significantly reduced by solving a minmax optimization problem, with the taper length and the waveguide width difference at the taper start as the free parameters. This approach also reduces the asymmetry in the design, enabling faster mode evolution and dramatically reducing the footprint. It should be noted that results in this chapter are purely based on 3D finite-difference time-domain (FDTD) simulations, as the fabrication of the proposed devices is currently in progress.

Using this methodology, a 3 dB adiabatic coupler is numerically demonstrated with an exceptionally low coupling variation of 0.02 over a 120 nm wavelength range covering the O-band. To the best of my knowledge, this represents the low-

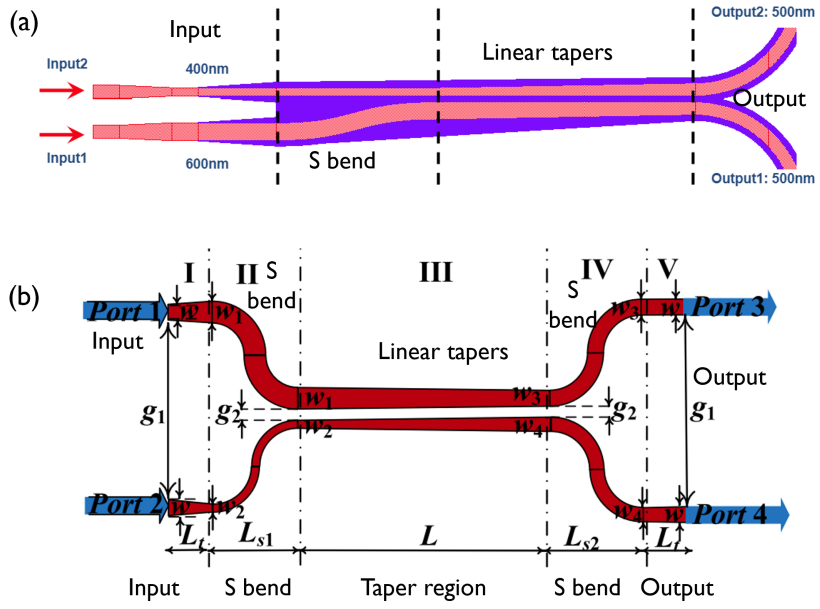

Figure 4.1: Examples of existing adiabatic couplers in the literature. (a) Adiabatic coupler with a total length of 165 μm [14]. (b) Adiabatic coupler with a total length of 240 μm [15].

est coupling variation reported for silicon adiabatic couplers over the presented wavelength range, while maintaining compatibility with standard silicon photonics fabrication platforms. Compared to the traditional straight DC counterpart, the proposed coupler achieves a 16.6× reduction in coupling variation. Further, the optimization results in an ultra-compact taper length of 1.44 μm, which is the shortest mode evolution length for silicon 3 dB couplers reported in the literature to my best knowledge. Moreover, novel low loss third-order polynomial interconnected circular (TOPIC) bends that attain continuous curvature and curvature derivative [1] were exploited in the design to achieve an insertion loss of $\leq$0.03 dB over the presented 120 nm wavelength range. Overall, the presented device is broadband, ultra-compact, can enable arbitrary coupling ratios, and is low-loss, rendering it a highly competitive 2×2 coupler to be used in next-generation PIC applications and an excellent candidate for WDM filters with large wavelength operation range.

This chapter is structured as follows. First, the design principles and optimization strategies for the proposed adiabatic coupler are introduced, emphasizing the broadband 0.5:0.5 splitter with minimal coupling variation and a compact footprint. Next, broadband arbitrary coupling ratios are demonstrated for the adiabatic coupler. Subsequently, the effects of the coupling gap and waveguide width are examined. Finally, a more robust design is proposed to address potential challenges such as uneven gap filling or sidewall scattering losses that comes with small gaps or waveguides widths. This chapter is partially based on the results published in [23]. Cascaded adiabatic couplers and Mach-Zehnder interferometers utilizing adiabatic couplers have already been taped out in a 300 mm fabrication run, with fabrication currently in progress.

4.2 Design and optimization scheme for the 3 dB splitter

The proposed adiabatic coupler consists of two linearly tapered waveguides whose width variations have opposite signs, with a taper length of L, which are connected to low-loss TOPIC S-bends at the input/output sections (Fig. 4.2(a)). The traditional DC counterpart is shown in Fig. 4.2(b) for benchmarking. The adiabatic coupler waveguides widths can be described as in Eq. 4.1 and Eq. 4.2.

$$W_2 = W_1 + \Delta W \cdot t_p \tag{4.1}$$

$$W_4 = W_3 - \Delta W \cdot t_p \tag{4.2}$$

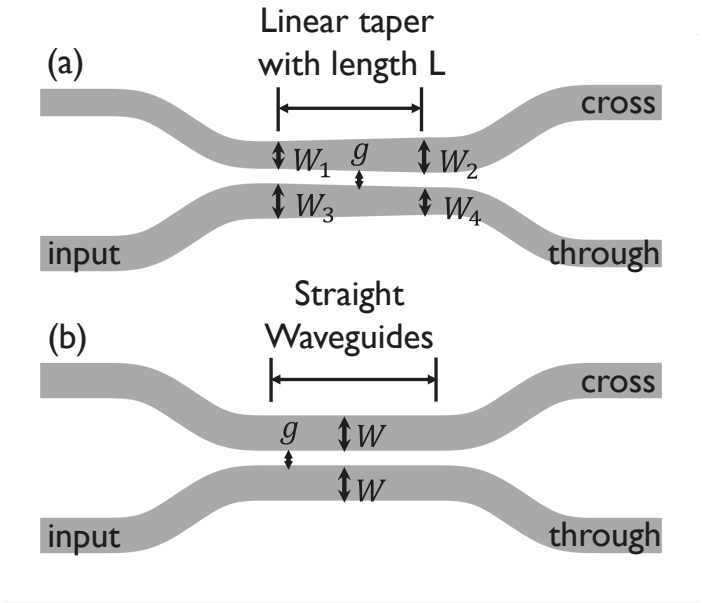

Figure 4.2: Schematic of the proposed adiabatic coupler (a), where the top waveguide width increases in the propagation direction, while the bottom waveguide width decreases. The schematic of the traditional straight directional coupler (b) with fixed waveguide width of W which is used as a benchmark for comparison. Both designs have a fixed gap of g. The schematic is for illustration purposes and is not intended to be in scale.

$$W_2 = W_4 \quad \text{if} \quad t_p = 0.5 \tag{4.3}$$

where the top and bottom waveguides are linear tapers with initial and final waveguide widths of (W_1, W_2) and (W_3, W_4), respectively. $\Delta W = W_3 - W_1$ is the waveguide width difference at the taper start. $t_p \in [0, 1]$ is the taper percentage ratio that controls the waveguide width difference at the taper end, which affects the coupling ratio significantly. In adiabatic couplers, the coupling ratio is largely controlled by adjusting the output waveguide widths. For a 50:50 splitting ratio, equal output waveguide widths should be used to ensure smooth and equal mode evolution between the waveguides. This is achieved by setting $t_p = 0.5$, which ensures $W_2 = W_4$ as shown in Eq. 4.3. Different coupling ratios can be obtained by adjusting t_p, where values closer to 0 or 1 result in asymmetric output waveguide widths and consequently uneven power splitting.

The complementary tapering in the top and bottom waveguides facilitates efficient energy transfer between the waveguides because the optical mode preferentially remains confined in the region with the higher effective refractive index. Further, the

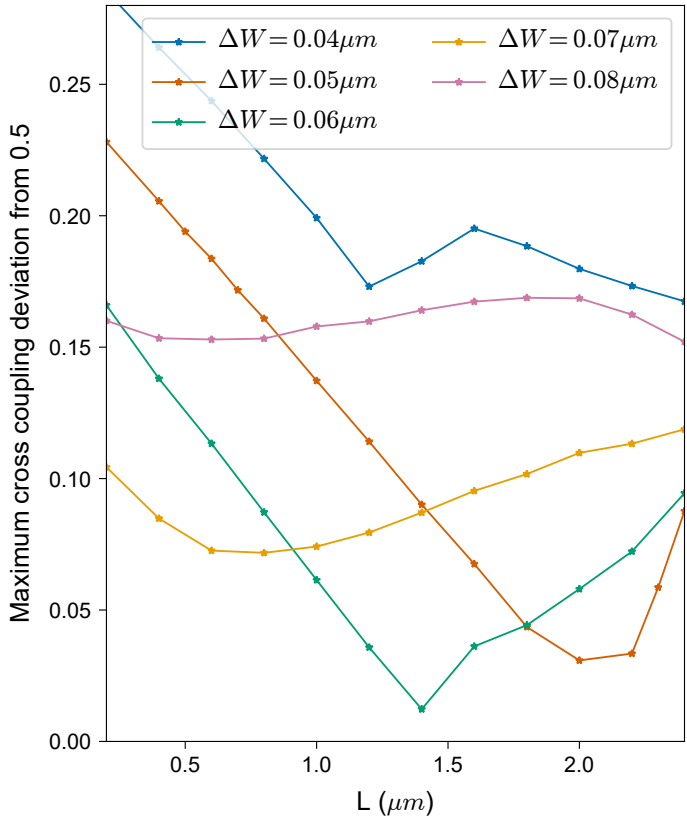

Figure 4.3: Maximum cross-coupling deviation from 0.5 *over a* 120 nm *wavelength range as a function of the taper length (*L*), and the initial waveguide width difference (*ΔW*), based on 3D FDTD simulations. The fixed design parameters are* $W_1 = 0.26\,\mu$m, $g = 0.08\,\mu$m, *and* t_p *= 0.5. Each line represents the coupling deviation at a certain* ΔW. *The coupling deviation is minimized at* $\Delta W = 0.06\,\mu$m *with a compact* $L = 1.44\,\mu$m.

gradual variation in dimensions minimizes scattering and reflection losses, ensuring robust mode conversion and improved coupling efficiency between the waveguides [27].

As depicted by CMT, the narrower waveguide width has less mode confinement with a larger coupling strength allowing a shorter coupler length [27]. W_1 is chosen to be 0.26 μm to achieve higher coupling strength without introducing additional excess loss according to 3D FDTD simulations. To achieve broadband coupling at a specific ratio, ΔW and L must be optimized to minimize the coupling deviation from the desired coupling ratio over a broad wavelength range. This can be formulated as a minmax optimization problem,

$$\min_{\Delta W, L} \left(\max_{\lambda \in [\lambda_1, \lambda_2]} |P_c(\lambda) - P_{c,\text{desired}}| \right) \tag{4.4}$$

where $\lambda_1 = 1.25\,\mu\text{m}$, $\lambda_2 = 1.37\,\mu\text{m}$, $P_c(\lambda)$ is the cross-coupled power as a function of wavelength, and $P_{c,\text{desired}}$ is the desired cross-coupled power value. By solving the optimization problem in Eq. 4.4, a $(\Delta w, L)$ pair can be determined that minimizes the coupling variation. For instance, for the 3 dB coupler, the coupling variation could be minimized to merely 0.02 over the presented wavelength range with $\Delta w = 0.06\,\mu\text{m}$ and an ultra- compact taper length of $L = 1.44\,\mu\text{m}$, as shown in Fig. 4.4. The coupling spectrum of the proposed 3 dB splitter is shown in Fig. 4.4(a) with a 16.6× reduction in the coupling variation as compared to the traditional straight DC in Fig. 4.4(b).

To illustrate the adiabatic nature of the proposed coupler, the power confinement ratio in the TE even and odd modes were extracted at the middle of the taper region for the proposed 3 dB splitter. Figure 4.5(a) shows the H_y field plot representing the TE mode of the splitter, where 98.3 % of the power remains in the TE even

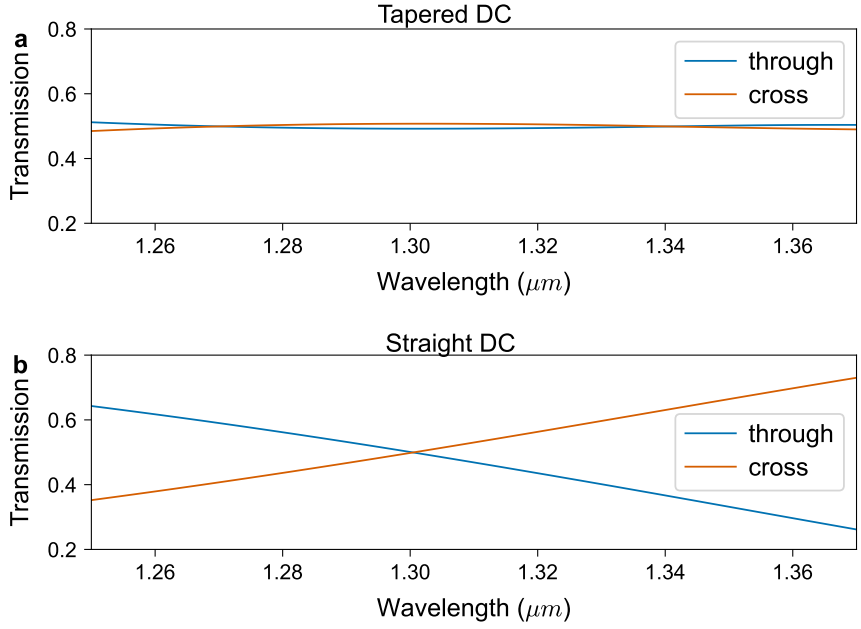

Figure 4.4: 3 dB splitter optical transmission using the proposed adiabatic coupler (a) as compared to the traditional straight coupler (b) over 120 nm wavelength range covering the O-band, based on 3D FDTD simulations. Significant reduction of 16.6x in the coupling variation is achieved using the proposed design compared to the straight DC counterpart.

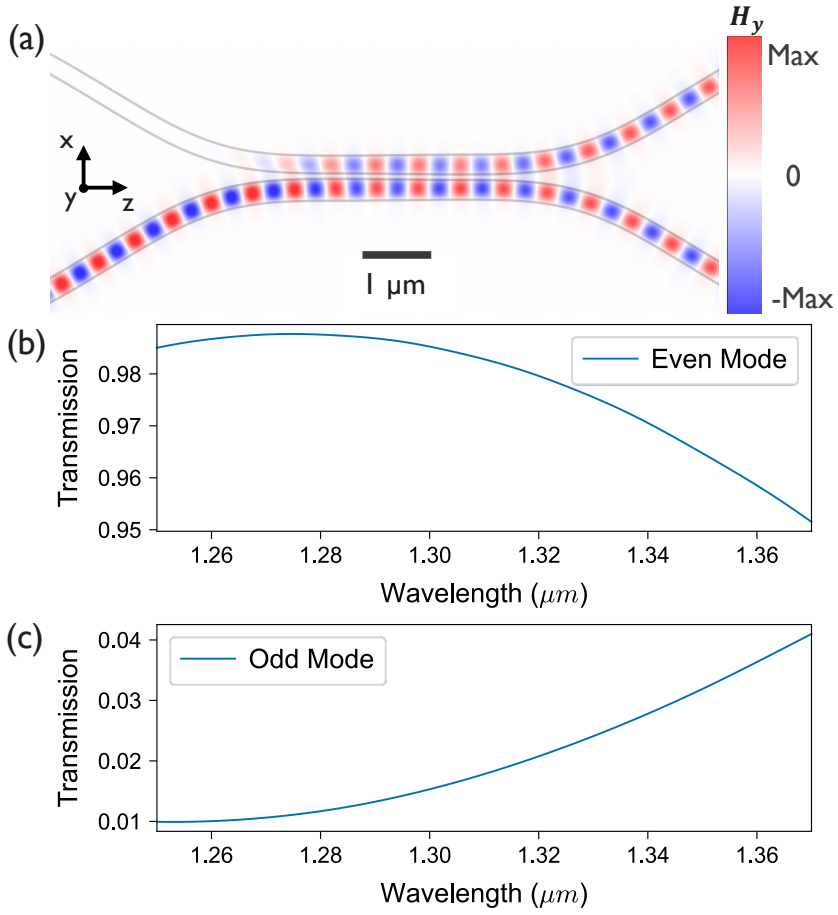

Figure 4.5: H_y field plot of the proposed 3 dB splitter at λ=1.31 μm (a). TE even (b) and odd (c) mode power expansions at the middle of the coupler showing most of the power (98.3% at λ=1.31 μm) existing in the TE even mode, proving the adiabatic nature of the splitter.

mode as shown in Fig. 4.5(b) and merely 1.7% of the power is in the TE odd mode at λ=1.31 μm, which shows the smooth mode evolution taking place in this design and confirms the adiabatic nature of the tapering.

Overall, the adiabatic DC design parameters and their effects can be summarized as follows:

- The key design parameters include the waveguide widths at the start of the tapers (W_1 and W_3), the coupling gap (g), the taper percentage (t_p), and the

taper length (L).

- The waveguide widths W_1 and W_3 are selected to be sufficiently low to avoid significant excess loss, as verified by 3D FDTD simulations (e.g., $W_1 = 0.26, \mu\text{m}$). Reducing the waveguide width increases the coupling strength, enabling a shorter coupler length. Additionally, several designs with larger W_1 values are evaluated both in simulation and fabrication, as discussed in subsequent sections.
- The coupling gap g is set to $0.08, \mu\text{m}$ and $0.1, \mu\text{m}$. A smaller gap enhances coupling strength, which results in a shorter coupler and reduced wavelength-dependent coupling variation. The minimum gap of $0.08, \mu\text{m}$ is used to test the fabrication limits of the iSiPP300 platform; however, such a small gap may introduce fabrication challenges, including uneven gap filling or sidewall scattering losses. Therefore, a more robust variant with $g = 0.1, \mu\text{m}$ is also proposed.
- The taper percentage t_p serves as a convenient parameter to control the output waveguide widths, which strongly influence the coupling ratio. In line with previous studies [15, 18], t_p is set equal to the desired coupling ratio (e.g., $t_p = 0.5$ for a 3 dB coupler), facilitating smooth mode evolution. It should be noted, however, that there is no one-to-one correspondence between t_p and the coupling ratio, as the latter also depends on the other design parameters.
- The taper length L determines the amount of power transferred between the two waveguides; a longer taper allows for stronger coupling.

It is important to highlight that the adiabatic coupler designs currently under fabrication include a comprehensive design of experiments. These experiments encompass variations in waveguide widths and taper lengths to ensure robust performance and adaptability to potential fabrication variations.

The design procedure of the adiabatic couplers can be summarized as follows:

- Specific values of W_1 and g are chosen based on the design objectives (either to push the fabrication limits of the platform or to realize a more robust and manufacturable design).
- The taper percentage t_p is chosen to match the desired coupling ratio (e.g., $t_p = 0.5$ for a 3 dB coupler).
- The waveguide width difference ΔW and the taper length L are optimized by solving the the minmax optimization problem defined in Eq. 4.4 to minimize the coupling variation over the desired wavelength range via 3D FDTD simulations.

It is important to distinguish the adiabatic coupler presented in this thesis from most designs reported in the literature. Conventional adiabatic couplers typically exhibit strong structural asymmetry, where the coupling ratio quickly saturates beyond a certain coupling length due to weak coupling strength. In contrast, the proposed design features a significantly higher coupling strength, enabled by a smaller coupling gap and reduced waveguide widths. As a result, the coupling ratio continues to vary with increasing taper length, unlike in conventional designs. While the overall architecture of the proposed coupler resembles previously reported adiabatic couplers, hence the use of the same terminology, the underlying design methodology and optimization strategy differ substantially.

4.3 Broadband coupling and arbitrary coupling ratios

Achieving broadband coupling at arbitrary ratios is of utmost importance for some WDM filters (i.e. MZI-based WDMs). Therefore, in this section, broadband coupling is demonstrated at arbitrary coupling ratios. In an adiabatic coupler, t_p facilitates the mode evolution to achieve the corresponding splitting ratio; for instance, 3 dB splitting can be achieved by maintaining equal output waveguide width (i.e. $W_2 = W_4$ as in Fig. 4.2). Furthermore, L affects the amount of coupling that takes place and has a direct control on the cross-coupled value. Finally, ΔW has a significant impact on the asymmetry of the design, where a larger ΔW value allows for lower cross-coupling values, while smaller ΔW values allow for larger cross-coupling values. Nonetheless, with a fixed $\Delta W = 0.06\,\mu\mathrm{m}$, broadband coupling can still take place at coupling ratios of 0.2, 0.3, 0.4, 0.5, and 0.55 as presented in Fig. 4.6(a), where $W_1 = 0.26\,\mu\mathrm{m}$ and t_p is set to be equal to the desired cross-coupling ratio. Furthermore, it is shown that for broadband coupling, there exists a quadratic relationship between the taper length, L, and the taper percentage, t_p (and the cross-coupling value), as shown in Fig. 4.6(b) for the presented coupling ratios, at a fixed ΔW, where a larger taper length is required to achieve a larger cross-coupling ratio as expected. It is important to note that the coupling variation in this configuration is not fully optimized for all coupling ratios, as illustrated in Fig. 4.6(a), due to the fixed ΔW value of $0.06\,\mu\mathrm{m}$. To overcome this limitation, the subsequent paragraph focuses on optimizing ΔW to achieve ultra-low coupling variation across a broader range of arbitrary coupling ratios.

To further enhance the performance and achieve precise control over the coupling ratios, the taper length and the waveguide width difference at the taper start are optimized for a range of coupling ratios, as summarized in Tab. 4.1. The presented coupling ratios span from 0 to 1 in increments of 0.1, along with additional values

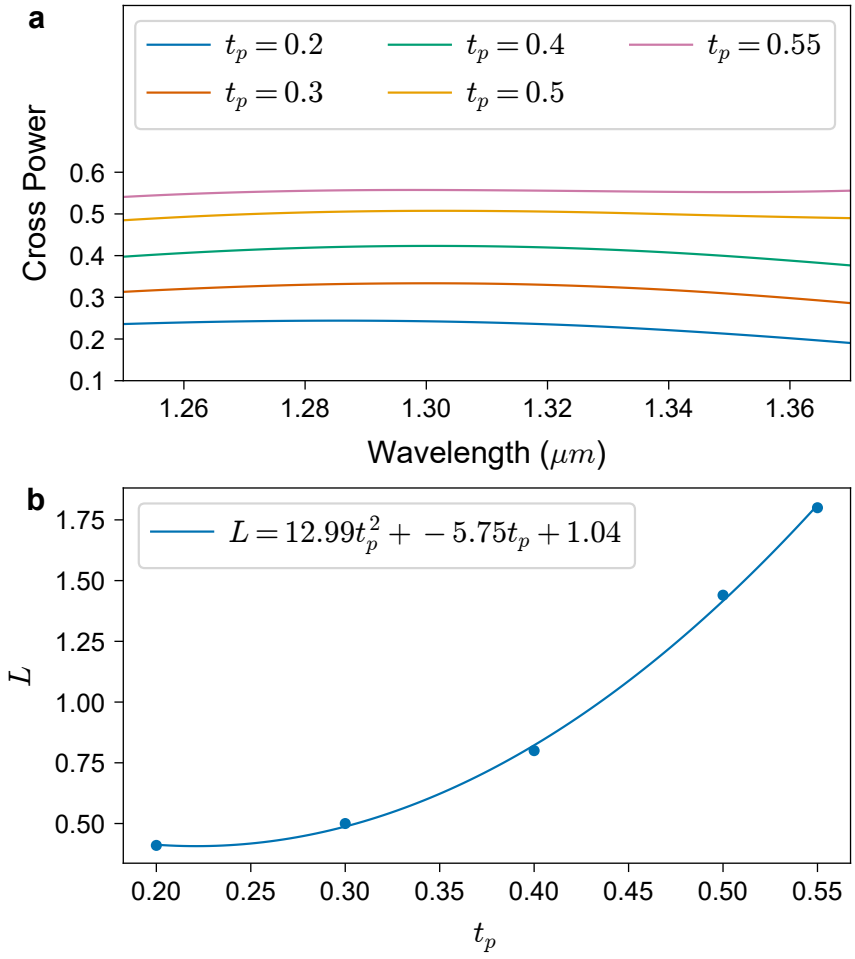

Figure 4.6: Demonstration of broadband coupling using the proposed tapered DC for cross-coupling values of 0.2, 0.3, 0.4, 0.5, *and* 0.55 *over a* 120 nm *wavelength range (a). Taper length (L) as a function of the taper percentage (t_p) (b). t_p is chosen to have the same value as the required cross-coupling value. Dots represent the data while the line is a quadratic fitting. All the presented devices have the same parameters except for t_p and L. The results are based on 3D FDTD simulations.*

commonly employed in WDM filter designs, such as 0.29, 0.08, and 0.04. This optimization ensures minimal coupling variation across the 120 nm wavelength range. The optimization results show minimal coupling variation for all presented cross coupling ratios highlighting the effectiveness of the proposed design methodology. In particular, the coupling variation ranged between 0.002 for cross coupling ratio

of 0.04 and 0.06 for cross coupling ratio of 0.8. Overall, larger broadband cross coupling values tend to have a smaller ΔW and larger L values, as expected, where a smaller ΔW is needed to allow for less asymmetry to increase the cross coupled power. Further, longer taper lengths provide sufficient interaction length to achieve higher power transfer.

Cross coupling ratio	ΔW (μm)	L (μm)	Max coupling deviation (from λ = 1.25 μm to 1.37 μm)
0.04	0.085	0.05	0.006
0.08	0.080	0	0.006
0.10	0.075	0.1	0.010
0.20	0.070	0.2	0.019
0.29	0.065	0.4	0.022
0.30	0.065	0.5	0.032
0.40	0.065	0.6	0.029
0.50	0.055	1.8	0.011
0.60	0.060	1.8	0.042
0.70	0.040	2.6	0.058
0.80	0.035	2.7	0.060
0.90	0.040	2.87	0.045
1.00	0.045	2.9	0.011

Table 4.1: Optimized parameters for arbitrary coupling ratios for the proposed adiabatic coupler based on optimizing ΔW and L via 3D FDTD simulations. The fixed parameters are $W_1 = 0.26\,\mu\mathrm{m}$, $g = 0.08\,\mu\mathrm{m}$, and t_p is the desired cross coupling ratio.

4.4 Impact of the waveguide width and coupling gap

To better understand the impact of waveguide width, an optimization was conducted for varying W_1 values, ranging from $0.26\,\mu\mathrm{m}$ to $0.38\,\mu\mathrm{m}$ in increments of $0.02\,\mu\mathrm{m}$. The other parameters were kept fixed at $g = 0.08\,\mu\mathrm{m}$ and $t_p = 0.5$, while ΔW and L were optimized to achieve a broadband cross-coupling ratio of 0.5. This analysis is particularly important because smaller waveguide widths are more susceptible to higher losses due to amplified effects of sidewall roughness and fabrication imperfections, specially at the bends sections.

The results are summarized in Tab. 4.2, which lists the optimized W_1, ΔW, and L values required to achieve broadband cross-coupling of 0.5. The maximum cross-coupling deviation from 0.5 over the 120 nm wavelength range is also presented. The findings indicate that small coupling deviations can still be achieved with larger waveguide widths, albeit at the cost of a longer taper length.

W_1 (μm)	ΔW (μm)	L (μm)	Max coupling deviation (from λ = 1.25 μm to 1.37 μm)
0.26	0.055	1.8	0.011
0.28	0.06	1.8	0.029
0.30	0.055	2.9	0.030
0.32	0.055	3.8	0.031
0.34	0.05	5.4	0.035
0.36	0.05	6.7	0.028
0.38	0.045	8.2	0.035

Table 4.2: Optimization results for different W_1 values with a fixed gap of 0.08 μm for the proposed adiabatic coupler based on optimizing ΔW and L via 3D FDTD simulations. The fixed parameters are $g = 0.08$ μm, $t_p = 0.5$ μm.

In the previous optimizations, a gap of $0.08\,\mu\mathrm{m}$ was used. However, such a gap is typically achievable only on a 300 mm platform, whereas 200 mm platforms usually have a minimum gap limitation of $0.15\,\mu\mathrm{m}$. To ensure compatibility with 200 mm platforms, it is crucial to evaluate the impact of the coupling gap and identify suitable design parameters. To investigate this, the coupling gap was varied from $0.08\,\mu\mathrm{m}$ to $0.16\,\mu\mathrm{m}$ in increments of $0.02\,\mu\mathrm{m}$ while keeping W_1 fixed at $0.26\,\mu\mathrm{m}$ for the 3 dB coupler design. The optimization results are summarized in Tab. 4.3, which presents the gap, ΔW, and L values required to achieve broadband cross-coupling of 0.5. The maximum cross-coupling deviation from 0.5 over the 120 nm wavelength range is also included. The results show that while the coupling deviation decreases slightly with larger gaps, the optimized parameters consistently achieve a coupling variation of less than 0.05 for all evaluated gaps. This demonstrates that the proposed design is adaptable for use in 200 mm platforms with larger gaps while maintaining low coupling variation. However, it is important to note that the taper length increases with larger gaps, leading to a larger footprint. This behavior aligns with CMT, as couplers with smaller gaps exhibit higher coupling coefficients [11].

Gap (μm)	ΔW (μm)	L (μm)	Max coupling deviation (from λ = 1.25 μm to 1.37 μm)
0.08	0.055	1.8	0.011
0.1	0.05	1.8	0.023
0.12	0.08	6.8	0.046
0.14	0.07	8	0.043
0.16	0.07	15.3	0.032

Table 4.3: Optimization results for different gap values with a fixed waveguide width $W_1 = 0.26\,\mu\mathrm{m}$ for the proposed adiabatic coupler based on optimizing ΔW and L via 3D FDTD simulations. The fixed parameters are $W_1 = 0.26\,\mu\mathrm{m}$, $t_p = 0.5$.

To address potential challenges associated with small coupling gaps and narrow waveguide widths, a "less risky" adiabatic coupler design is proposed. This design features a larger waveguide width of $0.34\,\mu\mathrm{m}$ and a coupling gap of $0.1\,\mu\mathrm{m}$. The coupling spectrum, shown in Fig. 4.7, demonstrates a coupling variation of only 0.037 over the 120 nm wavelength range, with a taper length of 6.7 μm.

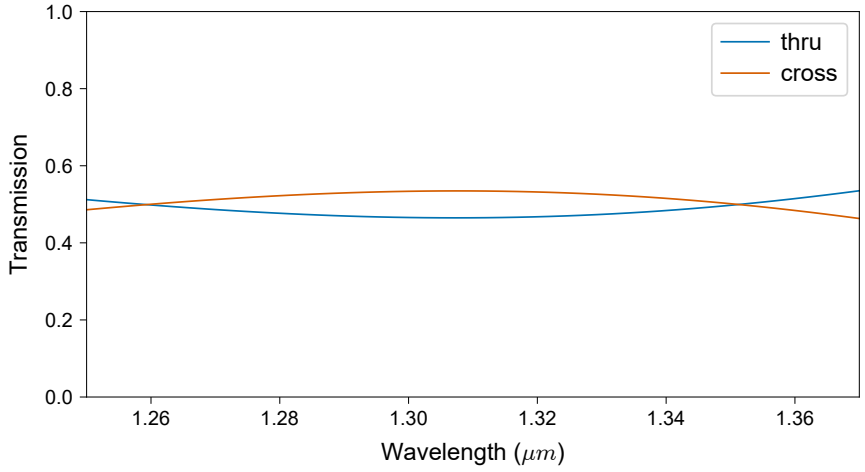

Figure 4.7: Coupling spectrum of the proposed adiabatic coupler with a larger waveguide width of $0.34\,\mu\mathrm{m}$ *and a larger gap of* $0.1\,\mu\mathrm{m}$ *based on 3D FDTD simulations. The coupling deviation is 0.037 over the 120 nm wavelength range.*

4.5 Conclusions

In this chapter, a new optimization scheme for adiabatic couplers is demonstrated. Solving a minmax optimization problem for the coupling deviation of adiabatic couplers significantly minimizes coupling variation by optimizing the taper length and the waveguide width difference at the taper start. Using this approach, a 3 dB adiabatic coupler is numerically demonstrated with a coupling variation of 0.02 over a $120\,\mathrm{nm}$ wavelength range covering the O-band, achieving a $16.6\times$ reduction in coupling variation compared to traditional straight DCs. In theory, this means that the worst extinction ratio of a Mach–Zehnder interferometer (MZI) filter using the proposed coupler would be 27.96 dB over 120 nm wavelength range (see Appendix 2.2). The proposed coupler also achieves an ultra-compact taper length of $1.44\,\mu\mathrm{m}$, the shortest reported to date to my best knowledge. Arbitrary coupling ratios are achieved by adjusting the final taper waveguide widths. The proposed coupler has a low insertion loss of $\leq 0.03\,\mathrm{dB}$ over the presented wavelength range,

making it suitable for dense WDM applications where multiple 2×2 splitters are used, leading to loss accumulation. Additionally, the impact of waveguide width and coupling gap on the design of broadband adiabatic couplers was demonstrated. A design with a larger waveguide width of $0.34\,\mu\mathrm{m}$ and a gap of $0.1\,\mu\mathrm{m}$ was also proposed. This design achieves a coupling variation of 0.037 over the $120\,\mathrm{nm}$ wavelength range with a taper length of $6.7\,\mu\mathrm{m}$.

Overall, the proposed coupler and design methodology enable highly optimized 2×2 couplers for next-generation photonic applications, particularly benefiting WDM filters requiring broad wavelength operation with high extinction ratios. Experimental validation of the proposed coupler is currently underway, where a recent tapeout included design of experiments (DoEs) on cascaded adiabtic couplers and MZIs based on adiabatic couplers as shown in the layouts of Fig. 4.8 and Fig. 4.9.

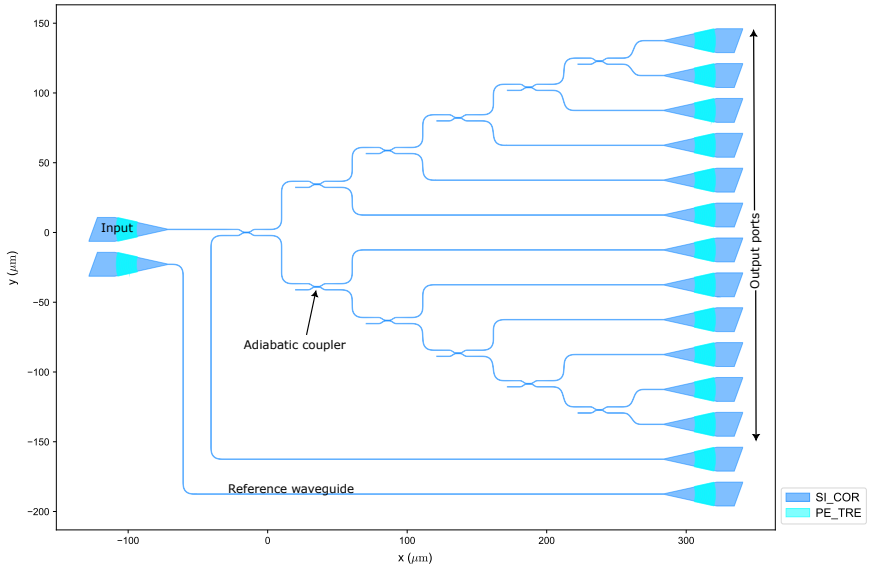

Figure 4.8: Layout of the cascaded adiabatic coupler, which has been taped out and is currently under fabrication.

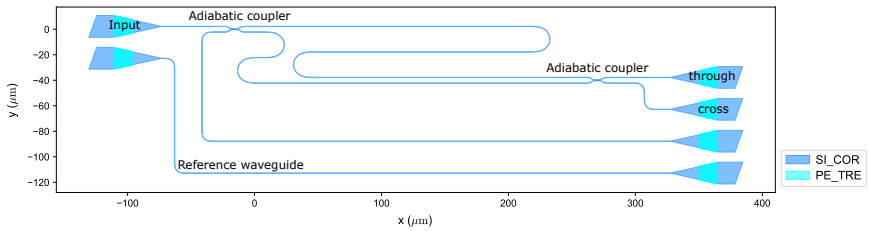

Figure 4.9: Layout of the MZI based on adiabatic couplers, which has been taped out and is currently under fabrication.

References

[1] Qingzhong Deng, Ahmed H. El-Saeed, Alaa Elshazly, Guy Lepage, Chiara Marchese, Pieter Neutens, Hakim Kobbi, Rafal Magdziak, Jeroen De Coster, Javad Rahimi Vaskasi, Minkyu Kim, Yeyu Tong, Neha Singh, Marko Ersek Filipcic, Pol Van Dorpe, Kristof Croes, Maumita Chakrabarti, Dimitrios Velenis, Peter De Heyn, Peter Verheyen, Philippe Absil, Filippo Ferraro, Yoojin Ban, and Joris Van Campenhout. Low-loss and low-power silicon ring based WDM 32×100 GHz filter enabled by a novel bend design. *Laser & Photonics Reviews*, November 2024. ISSN 1863-8899. doi: 10.1002/lpor.202401357.

[2] Ahmed Bayoumi, Mehmet Oktay, Alaa Elshazly, Hakim Kobbi, Rafal Magdziak, Guy Lepage, Chiara Marchese, Javad Rahimi Vaskasi, Swetanshu Bipul, Dieter Bode, Dimitrios Velenis, Maumita Chakrabarti, Peter Verheyen, Philippe Absil, Filippo Ferraro, Yoojin Ban, Joris Van Campenhout, Wim Bogaerts, and Qingzhong Deng. Enhanced operation range of silicon MZI filters using a broadband bent directional coupler. *IEEE Photonics Technology Letters*, 37(9):500–503, May 2025. ISSN 1941-0174. doi: 10.1109/lpt.2025.3553059.

[3] Shihao Sun, Mingbo He, Mengyue Xu, Shengqian Gao, Siyuan Yu, and Xinlun Cai. Hybrid Silicon and Lithium Niobate Modulator. *IEEE Journal of Selected Topics in Quantum Electronics*, 27(3):1–12, May 2021. ISSN 1558-4542. doi: 10.1109/JSTQE.2020.3036059.

[4] Sitao Chen, Yaocheng Shi, Sailing He, and Daoxin Dai. Low-loss and broadband 2x2 silicon thermo-optic mach-zehnder switch with bent directional couplers. *Optics Letters*, 41(4):836, February 2016. doi: 10.1364/ol.41.000836.

[5] Devendra Chack and Shamsul Hassan. Design and experimental analysis of multimode interference-based optical splitter for on-chip optical interconnects. *Optical Engineering*, 59(10):105102, October 2020. ISSN 0091-3286, 1560-2303. doi: 10.1117/1.OE.59.10.105102. Publisher: SPIE.

[6] Zeqin Lu, Han Yun, Yun Wang, Zhitian Chen, Fan Zhang, Nicolas A. F. Jaeger, and Lukas Chrostowski. Broadband silicon photonic directional coupler using asymmetric-waveguide based phase control. *Optics Express*, 23(3):3795–3808, February 2015. ISSN 1094-4087. doi: 10/gmf37j.

[7] Han Yun, Lukas Chrostowski, and Nicolas A. F. Jaeger. Ultra-broadband 2×2 adiabatic 3 dB coupler using subwavelength-grating-assisted silicon-on-insulator strip waveguides. *Optics Letters*, 43(8):1935–1938, April 2018. ISSN 1539-4794. doi: 10/gmqffw. Publisher: Optical Society of America.

[8] Ramesh K. Gupta, Sujith Chandran, and Bijoy Krishna Das. Wavelength-Independent Directional Couplers for Integrated Silicon Photonics. *Journal of Lightwave Technology*, 35(22):4916–4923, November 2017.

[9] Ahmed H. El-Saeed, Alaa Elshazly, Hakim Kobbi, Rafal Magdziak, Guy Lepage, Chiara Marchese, Javad Rahimi Vaskasi, Swetanshu Bipul, Dieter Bode, Marko Ersek Filipcic, Dimitrios Velenis, Maumita Chakrabarti, Peter De Heyn, Peter Verheyen, Philippe Absil, Filippo Ferraro, Yoojin Ban, Joris Van Campenhout, Wim Bogaerts, and Qingzhong Deng. Low-loss silicon directional coupler with arbitrary coupling ratios for broadband wavelength operation based on bent waveguides. *Journal of Lightwave Technology*, 42 (17):6011–6018, September 2024. ISSN 1558-2213. doi: 10.1109/jlt.2024.3407339.

[10] Keun Il Kim, Dong Kim, Vinh Nguyen, Sangyoon Han, and Tae Seok. High-Performance and Compact Silicon Photonic 3-dB Adiabatic Coupler Based on Shortest Mode Transformer Method. *IEEE Photonics Journal*, August 2021. doi: 10.1109/JPHOT.2021.3107852.

[11] Jia ming Liu. *Photonic Devices*. Cambridge University Press, April 2005. ISBN 9780521551953. doi: 10.1017/cbo9780511614255.

[12] J. S. Cook. Tapered velocity couplers. *Bell System Technical Journal*, 34(4): 807–822, July 1955. ISSN 0005-8580. doi: 10.1002/j.1538-7305.1955.tb03777.x.

[13] A. G. Fox. Wave coupling by warped normal modes. *Bell System Technical Journal*, 34(4):823–852, July 1955. ISSN 0005-8580. doi: 10.1002/j.1538-7305.1955.tb03778.x.

[14] Han Yun, Wei Shi, Yun Wang, Lukas Chrostowski, and Nicolas A. F. Jaeger. 2×2 adiabatic 3-dB coupler on silicon-on-insulator rib waveguides. pages 89150V–89150V. International Society for Optics and Photonics, 2013.

[15] Deng Mao, Yun Wang, Eslam El-Fiky, Luhua Xu, Amar Kumar, Maxime Jaques, Alireza Samani, Olivier Carpentier, Santiago Bernal, Md Samiul Alam, Jinsong Zhang, Mingyue Zhu, Ping-Chiek Koh, and David V. Plant. Adiabatic Coupler With Design-Intended Splitting Ratio. *Journal of Lightwave Technology*, 37(24):6147–6155, December 2019. ISSN 1558-2213. doi: 10.1109/JLT.2019.2946948.

[16] Hung-Ching Chung, Chih-Hsien Chen, Guan-Xun Lu, Yung-Jr Hung, and Shuo-Yen Tseng. Adiabaticity Engineered Silicon Polarization Independent 3-dB Coupler for the O-Band. *IEEE Photonics Journal*, 15(3):1–6, June 2023. doi: 10.1109/JPHOT.2023.3271320.

[17] Jiejiang Xing, Kang Xiong, Hao Xu, Zhiyong Li, Xi Xiao, Jinzhong Yu, and Yude Yu. Silicon-on-insulator-based adiabatic splitter with simultaneous tapering of velocity and coupling. *Optics Letters*, 38(13):2221–2223, July 2013. ISSN 1539-4794. doi: 10/gnsck5. URL https://opg.optica.org/ol/abstract.cfm?uri=ol-38-13-2221. Publisher: Optical Society of America.

[18] Xiang Liu, Yingxuan Zhao, Zhen Sheng, and Fuwan Gan. Ultra-Broadband, Compact Arbitrary Ratio Power Splitters Enabled by Adiabatic Sub-Wavelength Grating. *Photonics*, 10(5):578, May 2023. ISSN 2304-6732. doi: 10.3390/photonics10050578. URL https://www.mdpi.com/2304-6732/10/5/578.

[19] Xiang Liu, Yingxuan Zhao, Zhen Sheng, and Fuwan Gan. Compact and ultra-broadband silicon photonic adiabatic directional coupler using rib waveguides. *IEEE Photonics Technology Letters*, 36(10):1–1, May 2024. ISSN 1941-0174. doi: 10.1109/LPT.2024.3381826.

[20] Liang Cao, Ali Elshaari, Abdelsalam Aboketaf, and Stefan Preble. Adiabatic couplers in SOI waveguides. *Conference on Lasers and Electro-Optics 2010*, page CThAA2, 2010. doi: 10.1364/CLEO.2010.CThAA2.

[21] Han Yun, Wei Shi, Yun Wang, Lukas Chrostowski, and Nicolas A. F. Jaeger. 2×2 adiabatic 3-dB coupler on silicon-on-insulator rib waveguides. In Pavel Cheben, Jens Schmid, Caroline Boudoux, Lawrence R. Chen, André Delâge, Siegfried Janz, Raman Kashyap, David J. Lockwood, Hans-Peter Loock, and Zetian Mi, editors, *Photonics North 2013*. SPIE, October 2013. doi: 10.1117/12.2037968.

[22] Han Yun, Yun Wang, Fan Zhang, Zeqin Lu, Stephen Lin, Lukas Chrostowski, and Nicolas A. F. Jaeger. Broadband 2 x 2 adiabatic 3 dB coupler using silicon-on-insulator sub-wavelength grating waveguides. *Optics Letters*, 41 (13):3041, June 2016. ISSN 1539-4794. doi: 10.1364/ol.41.003041.

[23] Ahmed Bayoumi, Ahmed Khalil, Pol Van Dorpe, Maumita Chakrabarti, Dimitrios Velenis, Philippe Absil, Filippo Ferraro, Yoojin Ban, Joris Van Campenhout, Wim Bogaerts, and Qingzhong Deng. Broadband and ultra-compact adiabatic coupler based on linearly tapered silicon waveguides, 2025. URL https://arxiv.org/abs/2504.20512.

[24] Deng Mao, Yun Wang, Luhua Xu, Eslam El-Fiky, Maxime Jacques, Jinsong Zhang, Md Samiul Alam, Amar Kumar, Yannick D Mello, and David V. Plant. Adiabatic coupler with nonlinearly tapered mode-evolution region. *IEEE Photonics Technology Letters*, 33(16):840–843, August 2021. ISSN 1941-0174. doi: 10.1109/lpt.2021.3072787.

[25] Yung-Jr Hung, Chih-Hsien Chen, Guan-Xun Lu, Fu-Chieh Liang, Hung-Ching Chung, and Shuo-Yen Tseng. Compact and robust 2x2 fast quasi-adiabatic 3-dB couplers on SOI strip waveguides. *Optics & Laser Technology*, 145: 107485, January 2022. ISSN 0030-3992. doi: 10.1016/j.optlastec.2021.107485.

[26] Han Yun, Wei Shi, Yun Wang, Lukas Chrostowski, and Nicolas A. F. Jaeger. 2×2 adiabatic 3-dB coupler on silicon-on-insulator rib waveguides. page 89150V, Ottawa, Canada, October 2013. doi: 10.1117/12.2037968.

[27] Wei-Ping Huang. Coupled-mode theory for optical waveguides: an overview. *Journal of the Optical Society of America A*, 11(3):963, March 1994. doi: 10.1364/josaa.11.000963.

5

Dense Wavelength Division Multiplexing Systems

Broadband directional couplers (DCs) have been developed in the previous chapters showing significant reduction in coupling variation over a wide wavelength range. The presented broadband DCs have shown very low loss, a compact footprint, and the ability to achieve broadband coupling at arbitrary ratios. In this chapter, dense wavelength division multiplexing (DWDM) systems based on broadband bent DCs are demonstrated showing a considerable improvement in the operational wavelength range and channel isolation compared to traditional straight DC based DWDM systems. The DWDM systems presented herein are paramount in scaling the channel count of DWDM systems by working as interleavers.

5.1 State of the art 120
5.2 DWDM-2 ×100 GHz 122
Design and Results 122
Wafer mapping 127
Comparison with the state of the art 128
5.3 DWDM-4 ×100 GHz 130
5.4 DWDM-16 Systems 131
DWDM-16 ×800 GHz 132
DWDM-16 ×200 GHz 132
5.5 Conclusions 139

References **140**

5.1 State of the art

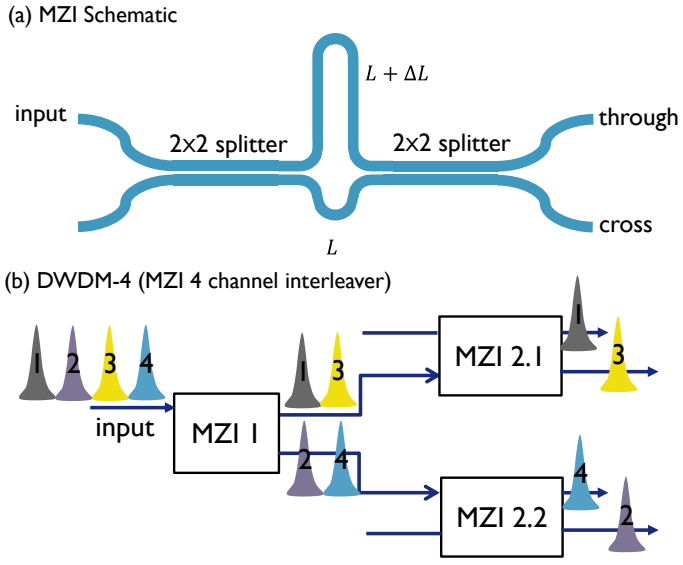

Figure 5.1: Schematic of a Mach–Zehnder interferometer (MZI) (a). Schematic of a 4 channel MZI interleaver (b).

Wavelength division multiplexing (WDM) filters are crucial in modern optical communication systems, allowing multiple signals to be transmitted over a single optical fiber using different wavelengths where each wavelength acts as an independent information channel [1]. These filters play a crucial role in increasing the bandwidth and capacity of optical networks, making them indispensable in high-speed data transmission and telecommunication applications [2, 3]. In particular, dense wavelength division multiplexing (DWDM) filters usually have a narrow wavelength spacing (a few nanometers or sub-nanometer), allowing up to hundreds of channels.

Mach–Zehnder Interferometer (MZI)-based DWDM filters (Fig. 5.1) are widely used due to their high performance, scalability, and simple design [4–10]. MZIs split an incoming light wave into two arms. A phase shift between the two arms causes interference when the light recombines. By controlling the relative phase, the interference pattern can be controlled (i.e. the free spectral range (FSR)), where

the working wavelength could be adjusted by integrated heaters (see Appendix A.2.3 and A.2.4).

Quite often wavelength-sensitive straight directional couplers (DCs) are used as the beam splitter and combiner in traditional waveguide-based MZIs for their simplicity and ease of fabrication, which often limit the operational bandwidth and cause additional insertion loss. Nonetheless, MZIs based on straight DCs often suffer from limited bandwidth and increased insertion loss, which can degrade the overall performance of WDM systems [11–13]. This is mainly due to the wavelength sensitive coupling coefficients of straight DCs, particularly in high-index contrast systems like in silicon photonics. In order to optimize the performance of MZIs and MZI-based WDM systems, the 2×2 splitters should ideally be broadband, low-loss, robust, and compact, as discussed in detail in previous chapters about broadband bent DCs and adiabatic couplers.

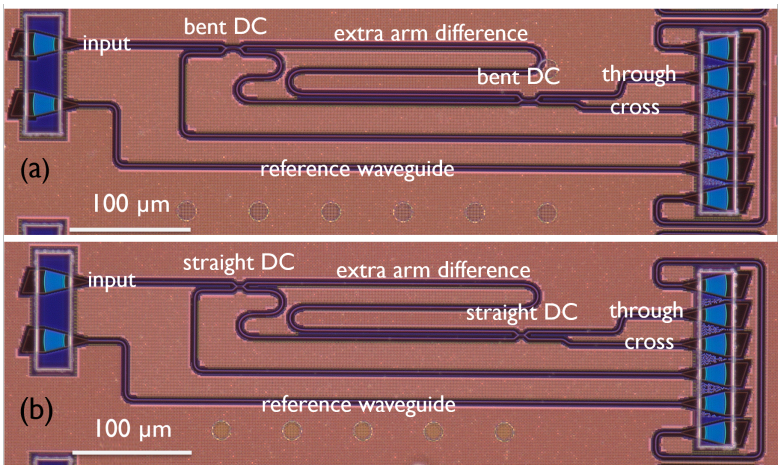

Figure 5.2: Microscope image for DWDM-2 $\times$100 GHz interleaver based on $0.5 : 0.5$ *bent DCs (d) and based on* $0.5 : 0.5$ *straight DCs (e). The bent DC has an* $R = 16\,\mu$m *and* $\theta = 9.2°$*. The straight DC has an* $L = 2\,\mu$m*. Waveguide material stacks are SOI with silicon oxide as top cladding, using imec iSiPP300 platform. All DCs are based on strip waveguides with nominal silicon thickness of* 220 nm*, waveguide width of* 450 nm*, and coupling gap of* 100 nm*.*

This chapter delves into DWDM systems, emphasizing enhancements in operational wavelength range and channel isolation, which are key factors for high-capacity optical communication networks [14, 15]. By leveraging the advantages of bent directional couplers (DCs) as robust, low-loss, broadband, and compact 2×2 splitters [16], this work demonstrates their high performance in MZI-based DWDM systems [17, 18]. The chapter begins by exploring the DWDM-2$\times$100 GHz interleaver, showcasing significant improvements in performance compared to its straight DC

counterpart while showing robust performance over the wafer. Overall, DWDM interleavers are of utmost importance as they can be used to scale up DWDM filters (i.e. in DWDM-128×100 GHz). Subsequently, transfer matrix method (TMM) calculations are employed to analyze more complex systems, including the DWDM-4×100 GHz interleaver and the DWDM-16×800 GHz filter further illustrating the scalability and efficiency of the proposed designs. Finally, the chapter presents measurement results for the fabricated DWDM-16×200 GHz system, providing insights into its performance and highlighting areas for further improvement. This chapter is partly based on results published in [3].

5.2 DWDM-2 ×100 GHz interleaver

Design and Results

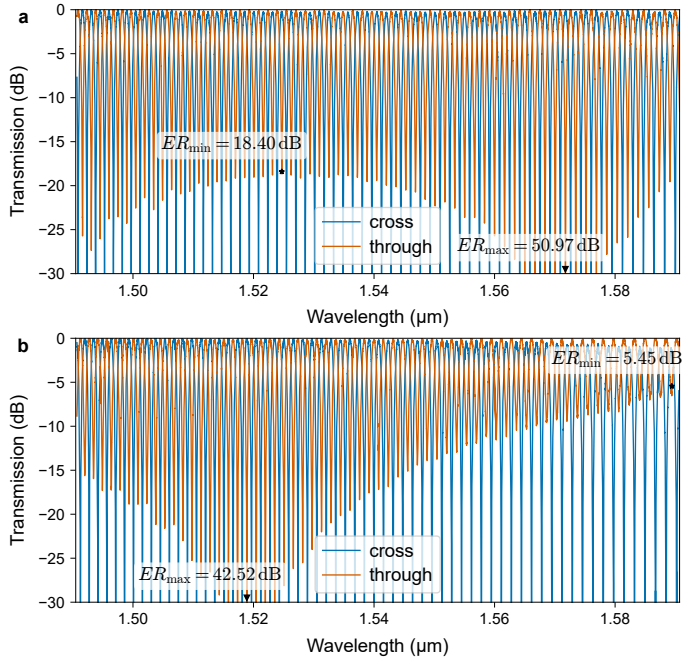

Figure 5.3: The proposed DWDM-2 ×100 GHz interleaver spectrum based on bent DCs (a), and the traditional DWDM-2 spectrum based on straight DCs (b). Minimum and maximum ER values are marked. At least 2.7× improvement in the ER wavelength operational range for the proposed interleaver is shown. The channel spacing for both DWDMs is designed to be 100 GHz.

The proposed DWDM-2×100 GHz interleaver is based on a broadband $0.5:0.5$ bent DC splitter [3], where the bent DC parameters have been optimized [16] in order to achieve broadband $0.5:0.5$ coupling over 100 nm covering the C band (Fig. 5.2(a)). The DWDM-2 ×100 GHz based on straight DCs is included for benchmarking purposes (Fig. 5.2(b)). Microscope images of the proposed DWDM-2 ×100 GHz interleaver and the straight DC based DWDM-2 counterpart are shown in Fig. 5.2(a) and Fig. 5.2(b), respectively. The fabrication is done using IMEC's advanced iSiPP300 platform allowing high waveguide quality and access to feature dimensions well below 100 nm thanks to the 193 nm immersion lithography [19].

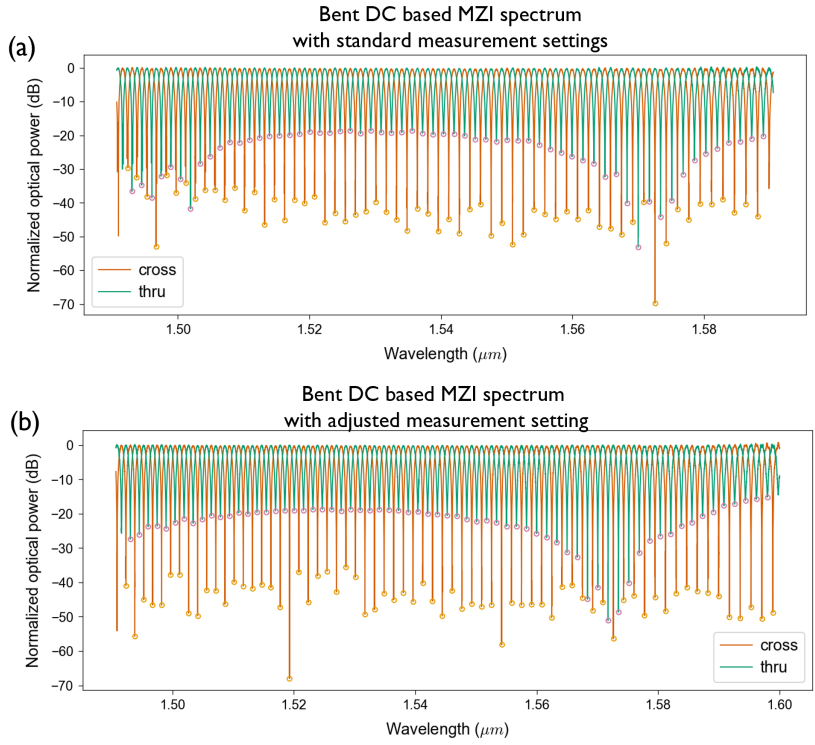

Figure 5.4: The normalized optical spectrum for the DWDM-2 ×100 GHz interleaver based on bent DCs with the 'standard' measurement setting (a) and the adjusted measurement setting (b). The 'standard' measurement setting shows a lot of nonuniformity in the dips, which is removed with the proposed measurement method. The laser wavelength spacing should be minimized to achieve accurate ER measurements with such a narrow channel spacing. The spectrum had to be measured in two subsequent steps (to ensure fine spacing and an extended wavelength range) with a low measurement power range setting (to ensure that even very small power values can be measured accurately), ultimately leading to more accurate dip values.

The proposed DWDM-2 $\times$100 GHz interleaver demonstrates a significant improvement in the operational wavelength range with high extinction ratio (ER) values (Fig. 5.3(a)) as compared to its counterpart based on straight DCs (Fig. 5.3(b)). The proposed interleaver could operate up to at least 100 nm wavelength range while maintaining an ER $\geq$ 18.4 dB. This represents at least 2.7$\times$ increase in the operational wavelength range compared to the interleaver based on straight DCs, which could only operate up to 36.7 nm with the same ER of $\geq$ 18.4 dB. Overall, achieving high ER is desirable for MZI-based WDM systems.

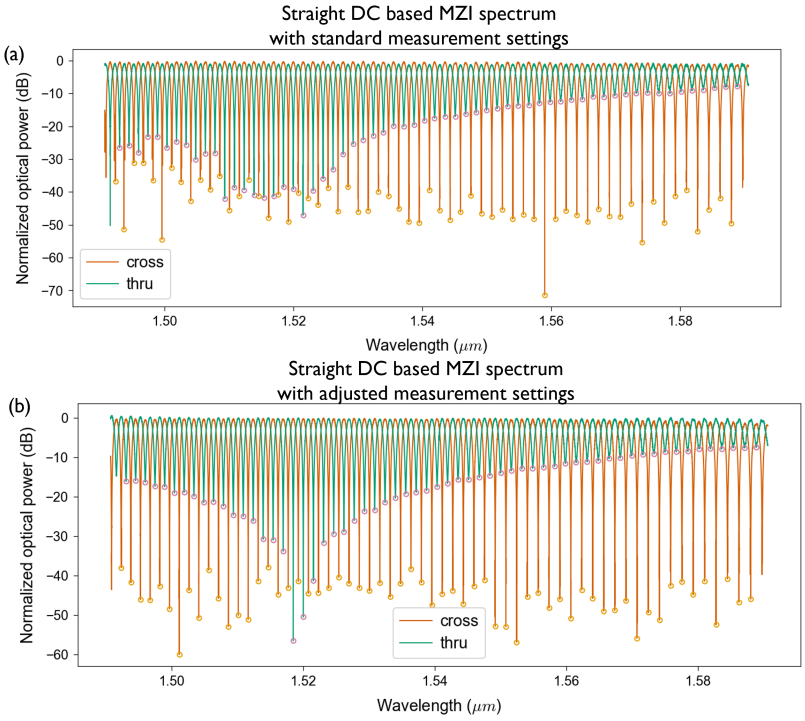

Figure 5.5: The normalized optical spectrum for the DWDM-2 $\times$100 GHz interleaver based on straight DCs with the 'standard' measurement setting (a) and the adjusted measurement setting (b).

In the presented analysis, the laser wavelength spacing was minimized in order to accurately detect the dips in the spectrum with a narrow channel spacing. In the measurement setup, there is a limitation on the number of measured wavelength values per spectrum which is approximately 20000 wavelength points, based on the measurements settings in place. Consequently, in order to measure with a fine wavelength spacing and over a large wavelength range, the spectrum was measured in two subsequent steps to ensure fine spacing and high accuracy. Furthermore, it is

paramount to use a low measurement power range setting in order to ensure accurate low power detection. This, ultimately led to accurate dip values extraction. Fig. 5.4 and Fig. 5.5 illustrate the difference between a 'standard' measurement setting and the adjusted measurement method for the bent DC based and the straight DC based interleavers, respectively. The adjusted measurements show significantly better dips uniformity and the ability to measure lower power values. The importance of using the correct measurement setting becomes even more critical when the MZI is employed to extract the 2×2 splitter coupling ratios based on the ER values. Furthermore, as explained in Appendix A.2.2, the cross port should theoretically exhibit an infinite ER, while the ER of the through port is always finite, depending on the coupling ratio of the 2×2 splitter. In practice, the cross port demonstrates finite yet high ER values, limited by the measurement precision and any losses in the system. It is noticed that the cross ER values increased to better reflect the expectation with the adjusted measurement setting.

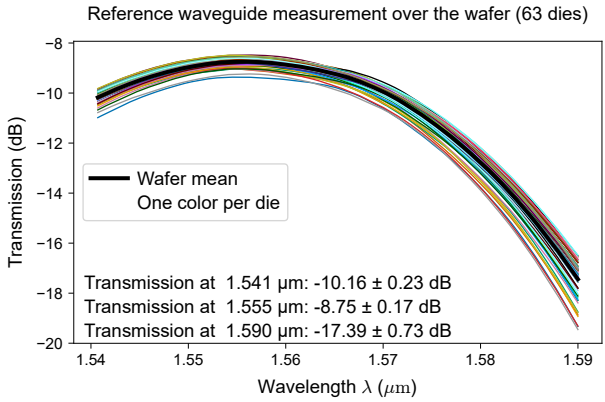

Figure 5.6: The reference waveguide transmission measurements over the wafer. Each color represents one die measurement. The line in bold black represents the average measurement over the whole wafer (63 dies)

The measured optical power values for the reference waveguide exhibit variability across the wafer, which can be attributed to several factors including measurement uncertainties (e.g., alignment precision) and fabrication-induced variations. It is worth noting that the semi-automatic optical alignment is always done at the same wavelength value. Figure 5.6 illustrates the characterization of the reference waveguide's optical power across the wafer as a function of wavelength. The standard deviation of the optical power is observed to vary with wavelength, with relatively higher values at longer wavelengths. Wafer mapping of the transmission values at $\lambda = 1.59$ μm is shown in Fig. 5.7, where the optical power ranges from -16.43 dB to -19.38 dB, with a mean value of -17.39 dB and a standard deviation of

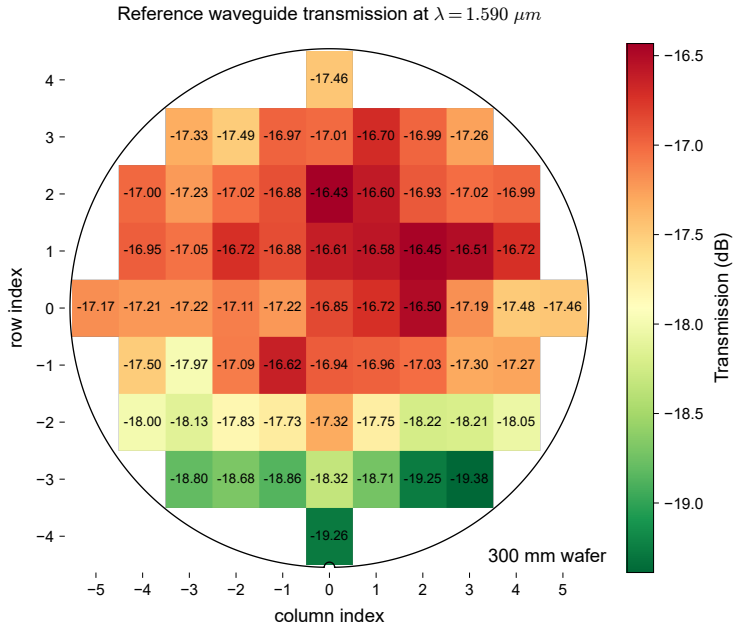

Figure 5.7: Wafer mapping of the reference waveguide transmission measurement over the wafer at λ = 1.59 μm.

0.73 dB. To eliminate interference patterns superimposed on the measured power, the Savitzky-Golay filter is applied for smoothing, as described in [20].

The performance of the DWDM-2 ×100 GHz interleaver is improved due to the use of a broadband bent DC. The $0.5 : 0.5$ bent DC demonstrates significant improvement in coupling variation over 100 nm wavelength range covering the C band (Fig. 5.8(a)), with a maximum coupling deviation as low as 0.06, compared to 0.23 for the straight DC counterpart (Fig. 5.8(b)), representing a 3.7 × improvement. It is worth mentioning that the DWDM-2 ×100 GHz measurements (Fig. 5.3(a, b)) align with the coupling measurements of the DCs (Fig. 5.8(a, b)), where the troughs in the spectra are visible around the points close to 0.5 coupling ratios. Additionally, the operational wavelength range with high ER is likely to extend beyond the measured range, but is constrained by the available laser and grating coupler bandwidth.

The bent DC is shown to have robust coupling over the wafer (Fig. 5.8 (c)), with a maximum cross-coupling shift of 0.039 with respect to the central die at $\lambda = 1.55\ \mu\mathrm{m}$ over 63 measured dies. Recently invented low loss bends are incorporated in the design, where continuous curvature and curvature derivative are guaranteed at all connections [21] enabling a low insertion loss of 0.03 ± 0.03 dB, as limited

by the measurement precision. The loss is calculated using a sinusoidal fitting for bent DCs with different coupling lengths, where the cutback method is utilized for the optical characterization [16]. Overall, this DWDM-2 interleaver achieves high ER across a broadband covering the C band without introducing further fabrication complexities or excessive loss, which has not been achieved yet in the literature to my best knowledge [3].

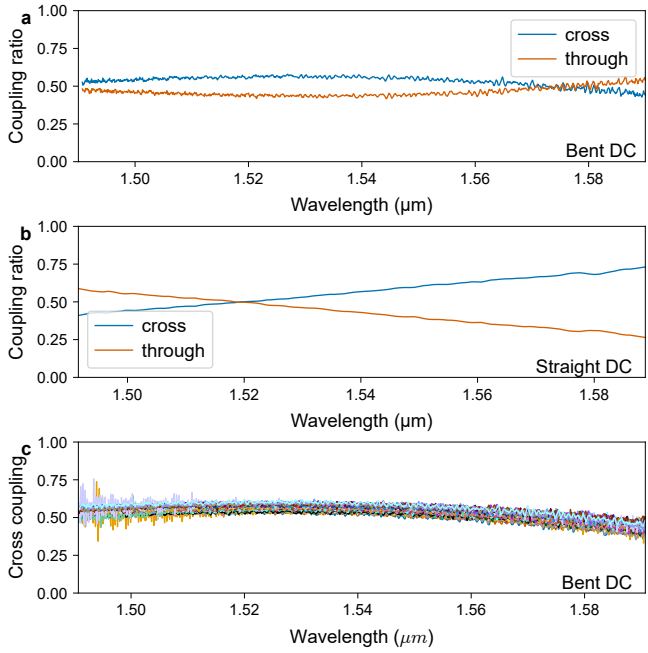

Figure 5.8: The measured coupling ratios of the bent DC (a) and straight DC (b) along with the cross coupling spectra for bent DC over 63 m*easured dies in a* 300 mm *wafer (c), where each color represents one die.* 3.7 × *less coupling variation is observed in the bent DC as compared to the straight DC. Robust performance of the bent DC is observed over the wafer.*

Wafer mapping

To validate the robustness of the proposed interleaver, wafer-scale measurements were conducted. The results demonstrate consistent and high ER values across a 300 mm wafer for the DWDM-2 ×100 GHz interleaver, with a minimum ER ranging from 14.3 dB to 18.4 dB over a 100 nm wavelength range covering the C band (Fig. 5.9(a)). These findings confirm the reliability and scalability of the design for mass production. Further, consistent ER enhancement is observed over the wafer using the proposed interleaver as compared to the traditional counterpart

with straight DCs, where the traditional counterpart minimum ER is $4.2 \sim 6.1$ dB over the same range. This confirms the proposed interleaver is robust and can be reliably used in mass production as indicated by wafer scale measurements on imec's 300 mm platform. It is worth mentioning that variations inherent to wafer-scale fabrication processes lead to minor fluctuations in the DC coupling ratios (Fig. 5.8(c)), which in turn might cause the observed variability in the ER values.

Comparison with the state of the art

We have presented a highly efficient, broadband, and robust DWDM-2 $\times$100 GHz interleaver that significantly improves the performance of MZI-based WDM systems as indicated by wafer scale measurements over 63 dies on imec's 300 mm platform. Compared to the results reported in the literature (Table 5.1), the proposed DWDM-2 $\times$100 GHz interleaver shows high ER values $\geq$18.4 dB without introducing further fabrication complexities as in [22], or compromising the excess loss as in [23].

To my best knowledge, the proposed design achieves the lowest insertion loss of 0.03 ± 0.03 dB in silicon 2×2 splitters covering the C band, while maintaining a compact length of 23 µm. Further, the proposed DWDM-2 exhibits robust ER values over the wafer, where the minimum ER values ranged between 14.3 dB and 18.4 dB over 63 measured dies. These results highlight the proposed interleaver as a key enabler for scalable and high-performance WDM systems in advanced silicon photonics applications.

Reference	Splitter structure	Splitter excess loss (dB)	Splitter length (μm)	ER (over 100 nm) (dB)
[24]	MMI	< 0.45	33.5	> 5.64
[25]	ADC	-	> 200	> 10
[23]	Rib-WG ADC	0.23	> 46.7	> 20.21
[26]	DC with phase section	< 1	31.4	> 15.03
[22]	SWG ADC	< 0.11	35	> 23.2
[27]	Rib-WG DC	0.8	> 475	> 12.52
This work	Bent DC	0.03 ± 0.03	23	> 18.4

Table 5.1: Comparison of fabricated silicon DWDM-2 interleavers covering the C band. Overall, the proposed DWDM-2 $\times$100 GHz interleaver shows high ER values $\geq$18.4 dB without introducing further fabrication complexities as in [22], or compromising the excess loss as in [23].

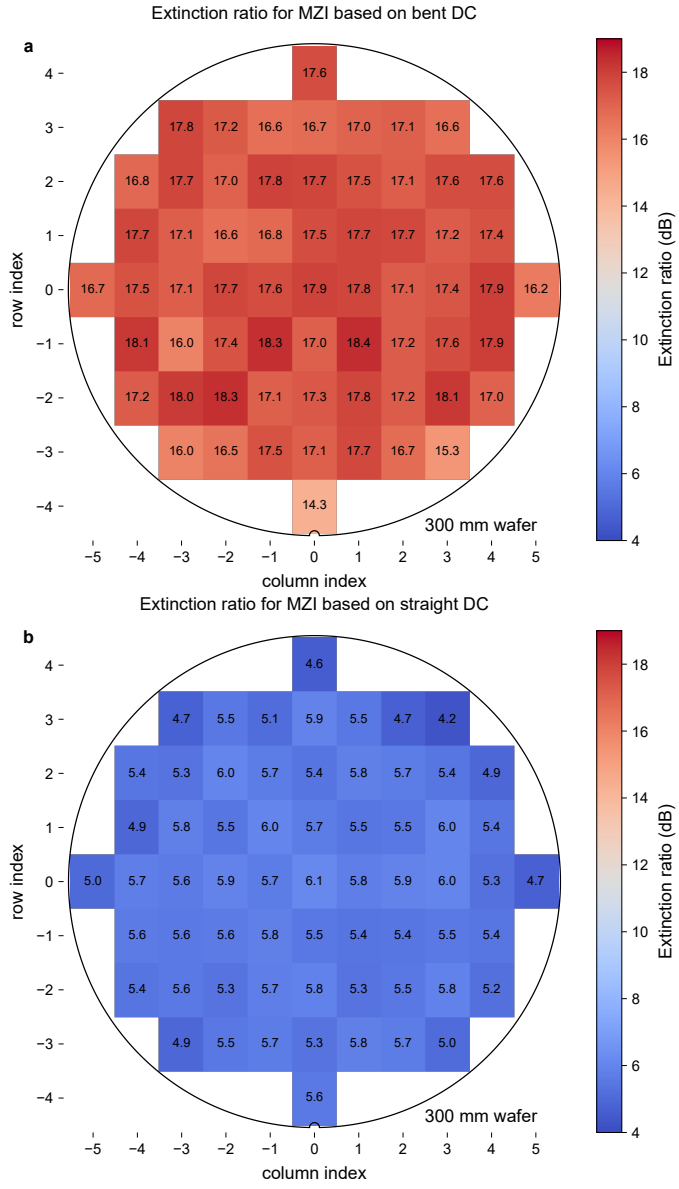

Figure 5.9: ER values wafer mapping for the DWDM-2 ×100 GHz interleaver based on bent DCs (a) and the interleaver based on straight DCs (b) over the 300 mm *wafer. Robust high ER values across the wafer is present in the interleaver based on bent DCs, showing the reliability of the design for mass production. The interleaver based on straight DCs shows significantly lower ER values across the wafer.*

5.3 DWDM-4 ×100 GHz

Having established the enhanced performance of the DWDM-2 ×100 GHz interleaver based on bent DCs, we now turn our attention to more complex DWDM architectures with higher channel counts. The scalability of DWDM systems is crucial for meeting the growing bandwidth demands of modern optical communication networks. By moving from a two-channel to a four-channel system, we can demonstrate the potential for further scaling the proposed bent DC-based approach.

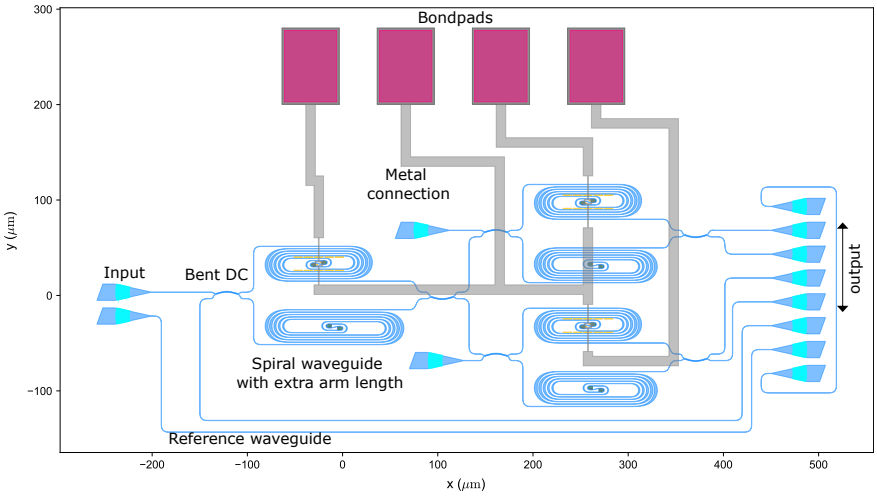

Figure 5.10: The schematic of DWDM-4 ×100 GHz filter based on cascaded MZIs, used in the transfer matrix method calculations. The MZI blocks are as illustrated in Fig. 5.2(a, b).

DWDM interleavers play a pivotal role in scaling up the channel count of WDM systems by a factor equal to the number of interleaver output ports. As illustrated in Fig. 5.1, the DWDM-4 ×100 GHz interleaver is utilized to quadruple the number of channels, enabling the realization of the DWDM-128×100 GHz system. Various DWDM-4 ×100 GHz interleavers designs have been recently taped out (Fig. 5.10) and are currently under fabrication. To evaluate the DWDM-4 ×100 GHz interleaver performance, transfer matrix method (TMM) calculations are conducted using measured data from both straight and bent DCs. In the DWDM-4 interleaver, each MZI consists of two $0.5 : 0.5$ DCs, with the additional arm length difference carefully designed to achieve the required FSR. This arm length difference is halved at each subsequent MZI stage relative to the preceding stage, as described in [28]. Integrated phase shifters are incorporated into the DWDM system to compensate for phase errors and ensure precise alignment of the working wavelength.

As shown in Fig. 5.11, the DWDM-4×100 GHz interleaver based on bent DCs

(Fig. 5.11(a)) demonstrates a substantial performance enhancement compared to its straight DC counterpart (Fig. 5.11(b)). Specifically, the worst-case channel isolation improved significantly from 4.65 dB in the straight DC-based interleaver to 16.77 dB in the bent DC-based interleaver. Additionally, the average insertion loss is reduced from 0.77 dB to 0.18 dB across the evaluated wavelength range, highlighting the improved performance of the bent DC based interleaver.

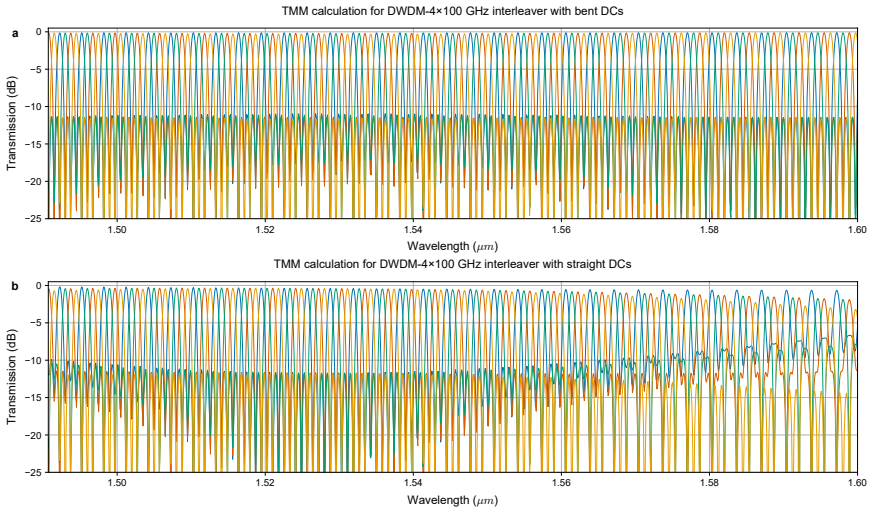

Figure 5.11: Transfer matrix method (TMM) simulation for DWDM-4× 100 GHz interleaver based on cascaded MZIs spectrum, with a channel spacing of 100 GHz, based on the measured bent DC (a) and straight DC (b). Significant improvement is observed in channels isolation and insertion loss for the WDM system based on bent DCs.

5.4 DWDM-16 Systems

Building upon the promising results observed in the DWDM-2 and DWDM-4 systems, we now expand our investigation to DWDM-16 architectures, which represent a significant increase in system complexity and channel count. The ability to efficiently manage 16 separate wavelength channels is a critical benchmark for next-generation high-capacity optical networks. In this section, we present both theoretical calculations and experimental measurements for DWDM-16 systems, providing a comprehensive analysis of their performance and challenges.

To demonstrate the effectiveness of the proposed MZI in enabling dense, scalable, and high-performance WDM systems, a more dense WDM system is considered with 16 channels based on four stages of cascaded MZIs. In this section, I will start

first with TMM calculations for a DWDM-16 ×800 GHz system based on measured bent and straight DCs data as shown in the schematic of Fig. 5.12. Subsequently, I will discuss the measurement results for a fabricated DWDM-16 ×200 GHz system.

DWDM-16 ×800 GHz

TMM calculations are performed for a DWDM-16 ×800 GHz system based on measured bent and straight DCs data as shown in the schematic of Fig. 5.12. The worst channel isolation at central wavelength improved from 5.42 dB to 17.18 dB while the average insertion loss improved from 1.02 dB to 0.30 dB in the WDM system based on bent DCs as compared to the straight DC counterpart Fig. 5.13(a, b), proving the effectiveness of the proposed MZI for scalable WDM systems.

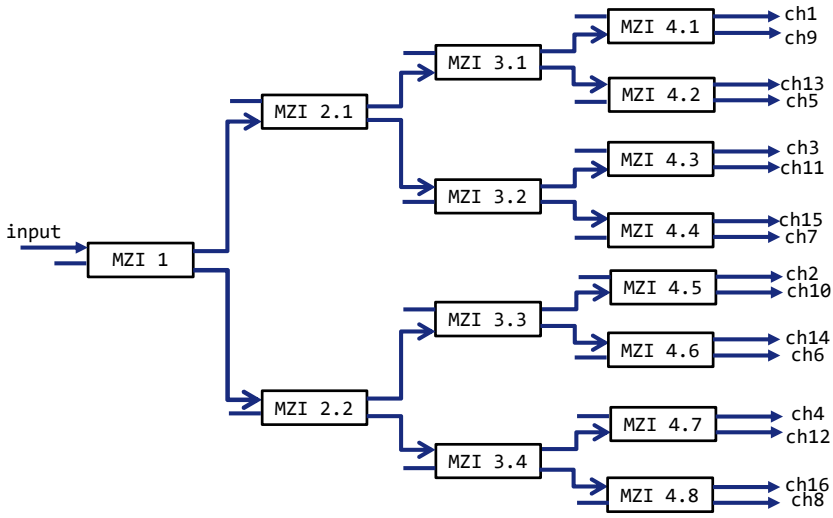

Figure 5.12: The schematic of 16 –channel *WDM filter based on cascaded MZIs, used in the transfer matrix method calculations. The MZI blocks are as illustrated in Fig. 5.2(a, b).*

DWDM-16 ×200 GHz

Overview and Design

The DWDM-16 ×200 GHz filter was fabricated using broadband bent DCs, as shown in the microscope image in Fig. 5.14. The system consists of four cascaded MZI stages to eventually demultiplex 16 channels with 200 GHz spacing. To maximize the chance of having a successful design, several DWDM-16 ×200 GHz

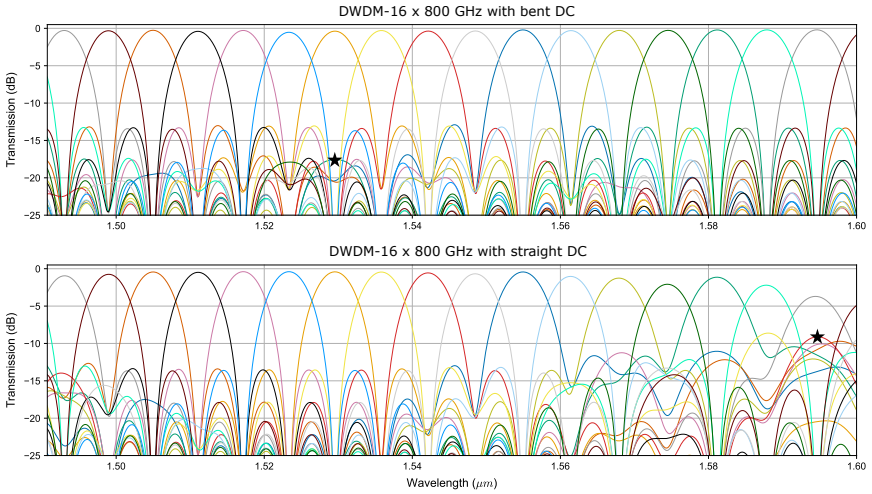

Figure 5.13: 16 −channel *cascaded MZI WDM spectrum, with a channel spacing of 800 GHz, based on the measured bent DC (a) and straight DC (b) simulated using the transfer matrix method. Significant improvement is observed in channels isolation and insertion loss for the WDM system based on bent DCs.*

filters were fabricated with different bent DCs designs, as this tapeout was done before measured results for the bent DCs were available.

The first MZI stage uses a flat-top passband design with three bent DCs of cross coupling ratios 0.5, 0.29, and 0.08 (Fig. 5.15), following the approach in [28]. The first MZI stage is critical, as its performance strongly affects subsequent stages. The remaining MZI stages use standard 0.5:0.5 bent DCs for simplicity.

Measurement and Debugging Procedure

The characterization and debugging process followed these steps:

1. **Selection of one DWDM-16 $\times$200 GHz filter:** As there are various DWDM-16 $\times$200 GHz filters with different bent DCs, the first step naturally involves choosing a DWDM-16 $\times$200 GHz filter with good bent DCs performance. The bent DCs were measured to select DWDM-16 $\times$200 GHz filter for further measurements. Fig. 5.16 shows the coupling spectra for the chosen bent DCs coupling ratios.

2. **Die Selection and Preparation:** A die showing promising bent DC performance was selected for dicing and wire bonding. The system requires

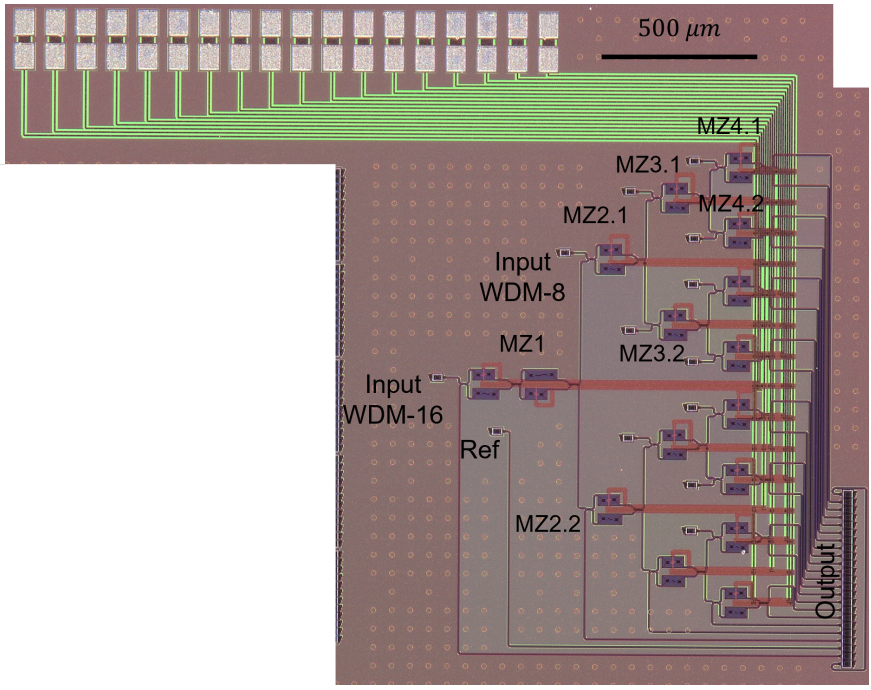

Figure 5.14: Microscope image of the fabricated DWDM-16 ×200 GHz system based on bent DCs. The system uses cascaded MZIs with integrated heaters for wavelength tuning. The layout also enables subsystem measurements of the WDM-8×400 GHz configuration.

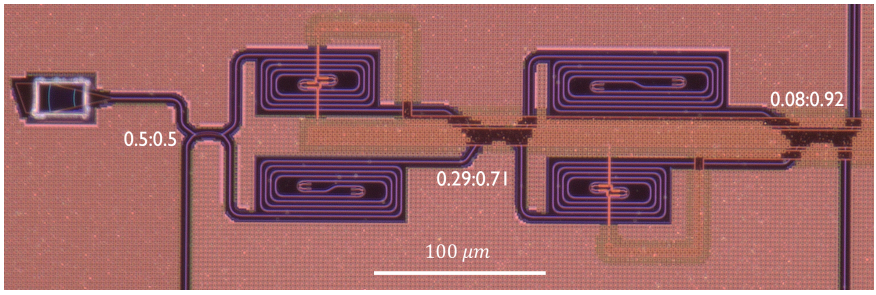

Figure 5.15: Zoomed-in image of the first MZI stage (MZ1) in the DWDM-16 ×200 GHz system, showing the implementation of three bent DCs with cross coupling ratios of 0.5, 0.29, and 0.08 to achieve flat-top passbands.

18 electric connections for integrated heaters, necessitating a multi-channel current source.

3. **Initial System Test:** The untuned response of all 16 channels was measured (Fig. 5.17), revealing significant signal distortions and the need for phase

tuning.

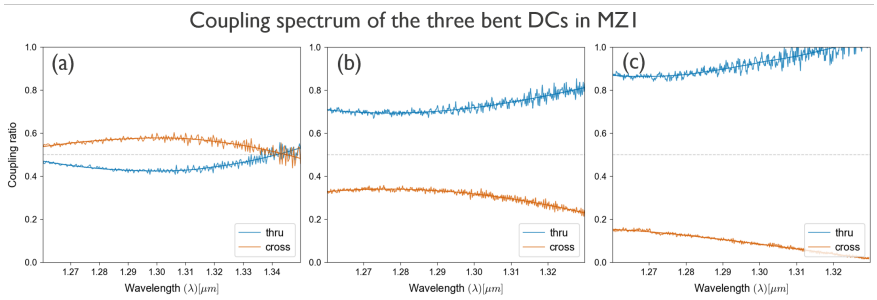

Figure 5.16: Measured coupling spectra from the selected die showing bent DCs with design goals of (a) 0.5:0.5, (b) 0.29:0.71, and (c) 0.08:0.92 coupling ratios.

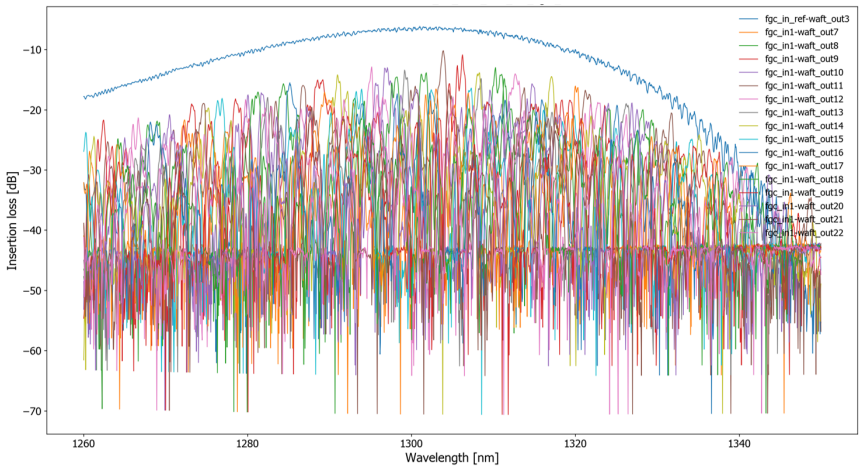

Figure 5.17: Output spectrum of the DWDM-16×200 GHz system without any phase tuning, showing significant signal distortions that require optimization.

Tuning and Observed Challenges

1. **First Stage Tuning:** Tuning began with the first MZ stage (MZ1: flat-top stage), adjusting heater currents and monitoring the summed optical power across eight channels. Despite optimization, only low ER values were achieved (Fig. 5.18), likely due to non-optimal broadband performance of the unoptimized 0.29 and 0.08 bent DCs.

2. **Subsystem Testing:** To isolate issues, the WDM-8×400 GHz subsystem (using only 0.5:0.5 bent DCs) was tested. The untuned response (Fig. 5.19) showed overall better performance than the full WDM-16, suggesting the non-optimal coupling ratios in the flat-top configuration contributed to the performance degradation of the DWDM-16 ×200 GHz filter.

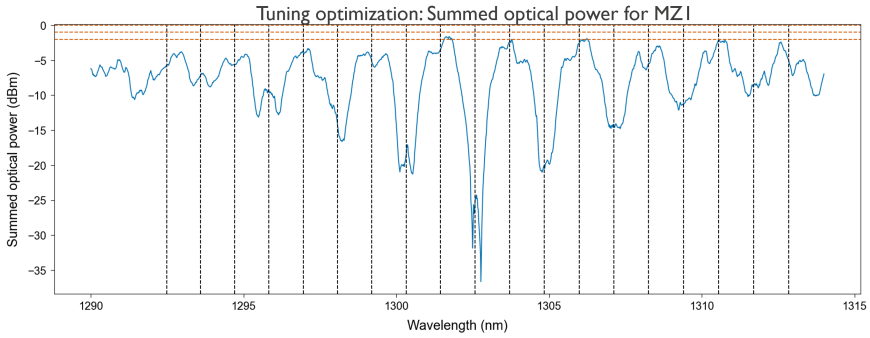

Figure 5.18: Normalized sum of eight output channels during the MZ1 tuning process, showing limited extinction ratio despite optimization efforts.

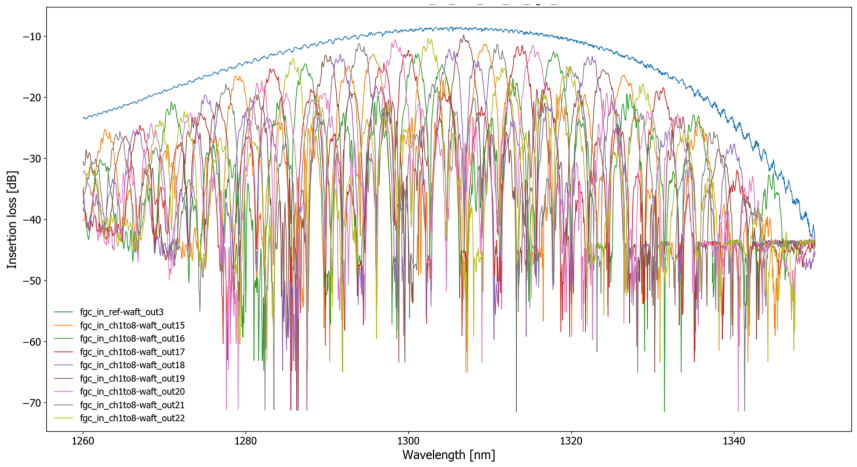

Figure 5.19: Untuned output spectrum of the WDM-8×400 GHz subsystem, showing better performance overall compared to the full WDM-16 system.

3. **Progressive Tuning:** Subsystem MZIs (for the WDM-8×400 GHz subsystem) were tuned in sequence:

    - For MZ 2.1, it is mainly responsible for wavelength grid alignment,

therefore its tuning can be skipped initially, as we are mostly interested in debugging the system at this stage.

- For MZ 3.1, a current of 0.276 mA yielded a relatively good ER performance. However, an FSR mismatch was observed, as evidenced by the asymmetric side lobes in Fig. 5.20. Upon further investigation, this mismatch was attributed to wrong placement of the bent DCs in the MZI stages. The bent DC arms have unequal optical path lengths, and when the coupler is not flipped, this asymmetry introduces a differential optical delay between the two interferometer arms, leading to the observed FSR mismatch. This design issue occurred during the very early stages of the project; all subsequent designs have incorporated the correct configuration and therefore do not exhibit this problem. This FSR mismatch can eventually cause unwanted peaks and undermine the overall system performance.
- For MZ 4.1, An undesired peak was observed near the center of the passband of an adjacent channel (Fig. 5.21). This effect arises from an FSR mismatch within the MZI stages, which becomes more pronounced as additional MZI stages are cascaded. Notably, this issue cannot be compensated for by tuning the phase shifters.
- MZ 4.2 was subsequently tuned, and the output spectra of both MZ 4.1 and MZ 4.2 are overlaid in Fig. 5.22. The results clearly show unwanted peaks that interfere with adjacent channels, significantly degrading the overall system performance.

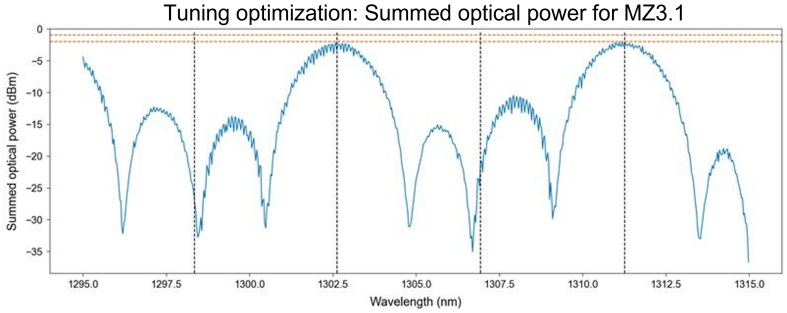

Figure 5.20: Summed, normalized measurements for two output waveguides during tuning of MZ 3.1 in the WDM-8×400 GHz subsystem.

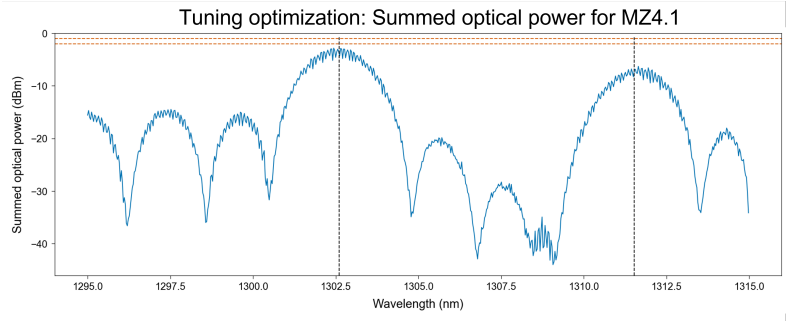

Figure 5.21: Normalized measurements for one output waveguide during tuning of MZ 4.1 in the WDM-8×400 GHz subsystem.

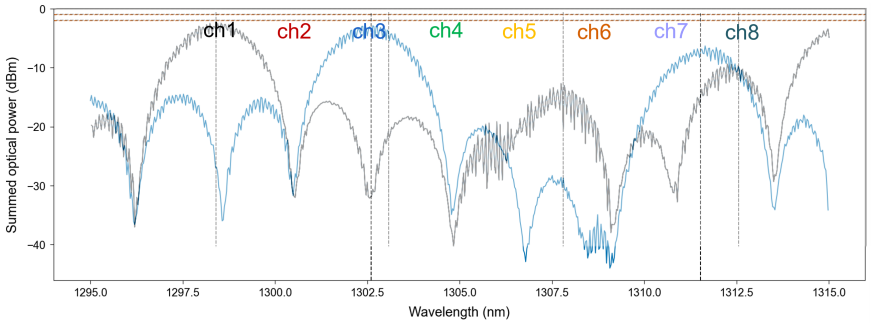

Figure 5.22: Normalized measurements for one output waveguide of both MZ 4.1 and of MZ 4.2 in the WDM-8×400 GHz subsystem. The channels centers locations are annotated in the figure.

Key Findings and Next Steps

- **Coupling Ratio Limitations:** The 0.29 and 0.08 bent DCs in the flat-top configuration did not provide optimal broadband performance, which is probably the reason for the low quality of the output signal. Future systems will use fully characterized bent DCs with optimized broadband performance for all required coupling ratios.
- **FSR mismatch:** FSR mismatch can significantly degrade WDM systems performance. In order to avoid this issue, the bent DC should be flipped between MZI stages to ensure no extra arm length difference is introduced in the DCs sections. All other WDM designs do not have this issue.

These improvements are expected to resolve the current limitations and enable high-performance DWDM-16×200 GHz operation in future iterations.

5.5 Conclusions

This chapter has demonstrated significant advancements in dense wavelength division multiplexing (DWDM) systems enabled by the use of broadband bent directional couplers (DCs). The proposed DWDM-2 $\times$100 GHz interleaver achieved a remarkable 2.7$\times$ increase in operational wavelength range compared to traditional straight DC-based systems, while maintaining a high extinction ratio (ER) of $\geq$ 18.4 dB. Wafer-scale measurements validated the robustness and scalability of the design, showcasing consistent performance across a 300 mm wafer, with minimum ER values ranging from 14.3 dB to 18.4 dB over a 100 nm wavelength range.

The chapter also presented transfer matrix method calculations for more complex DWDM systems, including DWDM-4 $\times$100 GHz and DWDM-16 $\times$800 GHz interleavers. The DWDM-4 $\times$100 GHz system in particular is of high importance as it can be used to scale up the channel count (as the case in the DWDM-128 $\times$100 GHz system). These calculations highlighted the enhanced performance of bent DC-based designs, with significant improvements in channel isolation and insertion loss. For instance, the worst-case channel isolation improved from 4.65 dB to 16.77 dB in the DWDM-4 $\times$100 GHz system, while the average insertion loss was reduced from 0.77 dB to 0.18 dB. Similarly, the DWDM-16 $\times$800 GHz system demonstrated an improvement in worst-case channel isolation from 5.42 dB to 17.18 dB and a reduction in average insertion loss from 1.02 dB to 0.30 dB.

The fabricated DWDM-16 $\times$200 GHz system, although facing initial challenges, provided valuable insights for further optimization. The challenges included non-optimal coupling ratios in the flat-top MZI configuration and ER limitations in the MZIs. Debugging steps, such as subsystem measurements revealed the importance of precise coupling ratio design and correct bent DCs placement in the MZIs.

Overall, this chapter underscores the potential of broadband bent DCs as a key enabler for scalable, high-performance DWDM systems. By addressing the limitations of traditional straight DC-based designs, the proposed solutions pave the way for next-generation optical communication networks with enhanced bandwidth, channel isolation, and robustness. These advancements are critical for meeting the growing demands of high-capacity data transmission in modern telecommunication and data center applications.

Finally, it is worth mentioning that additional DWDM systems have been taped out in a recent run and are currently under fabrication. These systems include DWDM-2, DWDM-4, and DWDM-8 configurations, aiming to further explore and enhance DWDM systems, where flat-top configurations have been explored.

References

[1] Qixiang Cheng, Meisam Bahadori, Madeleine Glick, Sébastien Rumley, and Keren Bergman. Recent advances in optical technologies for data centers: a review. *Optica*, 5(11):1354, October 2018. ISSN 2334-2536. doi: 10.1364/optica.5.001354.

[2] Qingzhong Deng, Ahmed H. El-Saeed, Alaa Elshazly, Guy Lepage, Chiara Marchese, Hakim Kobbi, Rafal Magdziak, Jeroen De Coster, Neha Singh, Marko Ersek Filipcic, Kristof Croes, Dimitrios Velenis, Maumita Chakrabarti, Peter De Heyn, Peter Verheyen, Philippe Absil, Filippo Ferraro, Yoojin Ban, and Joris Van Campenhout. 32x100 GHz WDM filter based on ultra-compact silicon rings with a high thermal tuning efficiency of 5.85 mw/pi. In *Optical Fiber Communication Conference (OFC)*, page W1A, 2024.

[3] Ahmed Bayoumi, Mehmet Oktay, Alaa Elshazly, Hakim Kobbi, Rafal Magdziak, Guy Lepage, Chiara Marchese, Javad Rahimi Vaskasi, Swetanshu Bipul, Dieter Bode, Dimitrios Velenis, Maumita Chakrabarti, Peter Verheyen, Philippe Absil, Filippo Ferraro, Yoojin Ban, Joris Van Campenhout, Wim Bogaerts, and Qingzhong Deng. Enhanced operation range of silicon MZI filters using a broadband bent directional coupler. *IEEE Photonics Technology Letters*, 37(9):500–503, May 2025. ISSN 1941-0174. doi: 10.1109/lpt.2025.3553059.

[4] Laiwen Yu, Jingshu Guo, Hengtai Xiang, Guojiang Yang, Yuqi Zhao, Yuanrong Li, and Daoxin Dai. Ultra-compact and high-performance four-channel coarse wavelength-division (de)multiplexing filters based on cascaded mach-zehnder interferometers with bezier-shape directional couplers. *Optics Express*, 32(5):7774, February 2024. ISSN 1094-4087. doi: 10.1364/oe.509936.

[5] Qiyuan Yi, Shuang Zheng, Zhiwei Yan, Guanglian Cheng, Fanglu Xu, Qiyuan Li, and Li Shen. Silicon photonic flat-top WDM (de)multiplexer based on cascaded mach-zehnder interferometers for the 2 μm wavelength band. *Optics Express*, 30(15):28232, July 2022. ISSN 1094-4087. doi: 10.1364/oe.467473.

[6] Zhizun Zhao, Zhen Li, Jiaqi Niu, Gaolu Zhang, Hongliang Chen, Xin Fu, and Lin Yang. Eight-Channel LAN WDM (De)Multiplexer Based on Cascaded Mach–Zehnder Interferometer on SOI for 400GbE. *Photonics*, 9(4):252, April 2022. ISSN 2304-6732. doi: 10.3390/photonics9040252. URL https://www.mdpi.com/2304-6732/9/4/252.

[7] Hongnan Xu, Daoxin Dai, and Yaocheng Shi. Low-crosstalk and fabrication-tolerant four-channel CWDM filter based on dispersion-engineered Mach-Zehnder interferometers. *Optics Express*, 29(13):20617–20631, June 2021.

ISSN 1094-4087. doi: 10.1364/OE.428352. URL https://opg.optica.org/oe/abstract.cfm?uri=oe-29-13-20617. Publisher: Optica Publishing Group.

[8] Tzu-Hsiang Yen and Yung-Jr Hung. Fabrication-Tolerant CWDM (de)Multiplexer Based on Cascaded Mach–Zehnder Interferometers on Silicon-on-Insulator. *Journal of Lightwave Technology*, 39(1):146–153, January 2021. ISSN 1558-2213. doi: 10.1109/JLT.2020.3026314. Conference Name: Journal of Lightwave Technology.

[9] Seok-Hwan Jeong. Broadband 1×8 channel silicon-nanowire-waveguide WDM filter based on point-symmetric mach-zehnder interferometric optical couplers in the O-band spectral regime. *OSA Continuum*, 2(12):3564, December 2019. ISSN 2578-7519. doi: 10.1364/osac.2.003564.

[10] Qingzhong Deng, Lu Liu, Rui Zhang, Xinbai Li, Jurgen Michel, and Zhiping Zhou. Athermal and flat-topped silicon mach-zehnder filters. *Optics Express*, 24(26):29577, December 2016. ISSN 1094-4087. doi: 10.1364/OE.24.029577. URL https://www.osapublishing.org/abstract.cfm?URI=oe-24-26-29577.

[11] Dajian Liu, Hongnan Xu, Ying Tan, Yaocheng Shi, and Daoxin Dai. Silicon photonic filters. *Microwave and Optical Technology Letters*, 63(9):2252–2268, 2021. ISSN 1098-2760. doi: 10/gg6sj8.

[12] Qingzhong Deng, Ahmed H. El-Saeed, Alaa Elshazly, Guy Lepage, Chiara Marchese, Hakim Kobbi, Rafal Magdziak, Jeroen De Coster, Neha Singh, Marko Ersek Filipcic, Kristof Croes, Dimitrios Velenis, Maumita Chakrabarti, Peter De Heyn, Peter Verheyen, Philippe Absil, Filippo Ferraro, Yoojin Ban, and Joris Van Campenhout. 32 ×100 GHz WDM filter based on ultra-compact silicon rings with a high thermal tuning efficiency of 5.85 mw/π. In *Optical Fiber Communication Conference (OFC) 2024*, OFC, page W1A.3. Optica Publishing Group, 2024. doi: 10.1364/ofc.2024.w1a.3.

[13] Nabarun Saha, Giuseppe Brunetti, Annarita di Toma, Mario Nicola Armenise, and Caterina Ciminelli. Silicon photonic filters: A pathway from basics to applications. *Advanced Photonics Research*, March 2024. ISSN 2699-9293. doi: 10.1002/adpr.202300343.

[14] Wei Shi, Ye Tian, and Antoine Gervais. Scaling capacity of fiber-optic transmission systems via silicon photonics. *Nanophotonics*, 9(16):4629–4663, October 2020. ISSN 2192-8606. doi: 10.1515/nanoph-2020-0309.

[15] D. Miller. Device requirements for optical interconnects to silicon chips. *Proceedings of the IEEE*, 97(7):1166–1185, July 2009. ISSN 1558-2256. doi: 10.1109/jproc.2009.2014298.

[16] Ahmed H. El-Saeed, Alaa Elshazly, Hakim Kobbi, Rafal Magdziak, Guy Lepage, Chiara Marchese, Javad Rahimi Vaskasi, Swetanshu Bipul, Dieter Bode, Marko Ersek Filipcic, Dimitrios Velenis, Maumita Chakrabarti, Peter De Heyn, Peter Verheyen, Philippe Absil, Filippo Ferraro, Yoojin Ban, Joris Van Campenhout, Wim Bogaerts, and Qingzhong Deng. Low-loss silicon directional coupler with arbitrary coupling ratios for broadband wavelength operation based on bent waveguides. *Journal of Lightwave Technology*, 42 (17):6011–6018, September 2024. ISSN 1558-2213. doi: 10.1109/jlt.2024.3 407339.

[17] George F. R. Chen, Jun Rong Ong, Thomas Y. L. Ang, Soon Thor Lim, Ching Eng Png, and Dawn T. H. Tan. Broadband Silicon-On-Insulator directional couplers using a combination of straight and curved waveguide sections. *Scientific Reports*, 7(1):7246, August 2017. ISSN 2045-2322. doi: 10.1038/s41598-017-07618-6.

[18] Laiwen Yu, Jingshu Guo, Hengtai Xiang, Chaoyue Liu, Yuqi Zhao, and Daoxin Dai. High-performance 2×2 bent directional couplers designed with an efficient semi-inverse design method. *Journal of Lightwave Technology*, 42(2):1–8, January 2024. ISSN 1558-2213. doi: 10.1109/JLT.2023.3315214.

[19] F. J. Ferraro, P. De Heyn, M. Kim, N. Rajasekaran, M. Berciano, G. Muliuk, D. Bode, G. Lepage, S. Janssen, R. Magdziak, J. De Coster, H. Kobbi, S. Lardenois, N. Golshani, L. Shiramin, C. Marchese, S. Rajmohan, S. Nadarajan, N. Singh, S. Radhakrishnan, A. Tsiara, P. Xu, A. Karagoz, D. Yudistira, M. Martire, A. Shahar, M. Chakrabarti, D. Velenis, W. Guo, A. Miller, Kristof Croes, S. Balakrishnan, P. Verheyen, Y. Ban, J. Van Campenhout, and P. P. Absil. Imec silicon photonics platforms: performance overview and roadmap. In *Next-Generation Optical Communication: Components, Sub-Systems, and Systems XII*, volume 12429, pages 22–28. SPIE, March 2023. doi: 10.1117/12.2650579.

[20] Abraham. Savitzky and M. J. E. Golay. Smoothing and Differentiation of Data by Simplified Least Squares Procedures. *Analytical Chemistry*, 36(8): 1627–1639, July 1964. ISSN 0003-2700, 1520-6882. doi: 10/dktbw4. ZSCC: 0017054.

[21] Qingzhong Deng, Ahmed H. El-Saeed, Alaa Elshazly, Guy Lepage, Chiara Marchese, Pieter Neutens, Hakim Kobbi, Rafal Magdziak, Jeroen De Coster, Javad Rahimi Vaskasi, Minkyu Kim, Yeyu Tong, Neha Singh, Marko Ersek

Filipcic, Pol Van Dorpe, Kristof Croes, Maumita Chakrabarti, Dimitrios Velenis, Peter De Heyn, Peter Verheyen, Philippe Absil, Filippo Ferraro, Yoojin Ban, and Joris Van Campenhout. Low-loss and low-power silicon ring based WDM 32×100 GHz filter enabled by a novel bend design. *Laser & Photonics Reviews*, November 2024. ISSN 1863-8899. doi: 10.1002/lpor.202401357.

[22] Han Yun, Lukas Chrostowski, and Nicolas A. F. Jaeger. Ultra-broadband 2×2 adiabatic 3 dB coupler using subwavelength-grating-assisted silicon-on-insulator strip waveguides. *Optics Letters*, 43(8):1935–1938, April 2018. ISSN 1539-4794. doi: 10/gmqffw. Publisher: Optical Society of America.

[23] Keun Il Kim, Dong Kim, Vinh Nguyen, Sangyoon Han, and Tae Seok. High-Performance and Compact Silicon Photonic 3-dB Adiabatic Coupler Based on Shortest Mode Transformer Method. *IEEE Photonics Journal*, August 2021. doi: 10.1109/JPHOT.2021.3107852.

[24] Devendra Chack and Shamsul Hassan. Design and experimental analysis of multimode interference-based optical splitter for on-chip optical interconnects. *Optical Engineering*, 59(10):105102, October 2020. ISSN 0091-3286, 1560-2303. doi: 10.1117/1.OE.59.10.105102. Publisher: SPIE.

[25] Liang Cao, Ali Elshaari, Abdelsalam Aboketaf, and Stefan Preble. Adiabatic couplers in SOI waveguides. *Conference on Lasers and Electro-Optics 2010*, page CThAA2, 2010. doi: 10.1364/CLEO.2010.CThAA2.

[26] Zeqin Lu, Han Yun, Yun Wang, Zhitian Chen, Fan Zhang, Nicolas A. F. Jaeger, and Lukas Chrostowski. Broadband silicon photonic directional coupler using asymmetric-waveguide based phase control. *Optics Express*, 23(3):3795–3808, February 2015. ISSN 1094-4087. doi: 10/gmf37j.

[27] Ramesh K. Gupta, Sujith Chandran, and Bijoy Krishna Das. Wavelength-Independent Directional Couplers for Integrated Silicon Photonics. *Journal of Lightwave Technology*, 35(22):4916–4923, November 2017.

[28] Folkert Horst, William M. J. Green, Solomon Assefa, Steven M. Shank, Yurii A. Vlasov, and Bert Jan Offrein. Cascaded mach-zehnder wavelength filters in silicon photonics for low loss and flat pass-band WDM (de-)multiplexing. *Optics express*, 21(10):11652–11658, 2013. doi: 10.1364/OE.21.011652.

6

Coarse Wavelength Division Multiplexing Systems

In the previous chapter, the design and implementation of broadband directional couplers (DCs) for dense wavelength division multiplexing (DWDM) systems were presented. These DCs were shown to significantly enhance the wavelength operation range and channel isolation, serving as critical components in the DWDM-128×100 GHz system as interleavers. In this chapter, the focus shifts to the utilization of broadband bent DCs for the realization of robust coarse wavelength division multiplexing (CWDM) systems with high channel isolation and low loss. Specifically, CWDM-2 × 3.2 THz and CWDM-4 × 3.2 THz systems are developed. The large channel spacing combined with reduced phase errors enables these CWDM filters to achieve high channel isolation without thermal tuning. The presented CWDM systems play an essential role in demonstrating the DWDM-128×100 GHz system as will be demonstrated in this chapter.

6.1 State of the art 146
6.2 Scaling WDM filters with CWDM architectures 148
FSR tolerance bounds for CWDM-2 149
6.3 CWDM-2 systems 152
CWDM-2 × 3.2 THz 152
CWDM-2 × 6.4 THz 157
Phase error improvement in CWDM-2 systems 161

6.4 CWDM-4 × 3.2 THz 166
6.5 Conclusions 169
References 171

6.1 State of the art

Wavelength Division Multiplexing (WDM) is a cornerstone technology for scaling the data capacity of optical communication systems, where each wavelength carries an independent signal [1, 2]. Over the years, various designs have been proposed on the silicon photonics platform, achieving efficient and high-channel-count WDM systems [3–7]. However, one of the primary challenges in WDM system design is wavelength drift, which can arise from fabrication variabilities or thermal effects due to the high thermo-optic coefficient of silicon [8–10].

Coarse Wavelength Division Multiplexing (CWDM) filters, with wider channel spacing (typically a few tens of nanometers), support fewer channels compared to Dense Wavelength Division Multiplexing (DWDM) systems, which have much narrower channel spacing (e.g., 0.2 nm). The wider spacing in CWDM systems reduces the complexity of optical components and improves yield, making them more cost-effective and less sensitive to fabrication tolerances [11, 12]. CWDM is commonly used in short-reach applications, such as metropolitan area networks (MANs) and access networks, where high spectral efficiency is not a primary requirement [13]. Additionally, CWDM systems relax the need for precise wavelength alignment and environmental temperature control [14].

Various silicon-based CWDM filters have been demonstrated in the literature, including systems based on Arrayed Waveguide Gratings (AWGs) [15–17], Echelle diffraction gratings [18, 19], and Mach-Zehnder Interferometers (MZIs) [4, 20, 21]. Both AWGs and Echelle gratings are known for their low crosstalk and high channel isolation, with Echelle gratings typically offering better performance for CWDM applications compared to AWGs. However, the performance of both AWGs and Echelle gratings heavily depends on fabrication tolerances, where manufacturing variabilities can significantly affect the CWDM system's reliability and spectral characteristics [22]. In contrast, MZI-based CWDM systems are widely adopted due to their simple fabrication process, low losses, and ability to achieve a flat-top passband [6]. However, the performance of such systems is highly dependent on the 2×2 splitter performance and often requires strategies to mitigate wavelength drifts caused by fabrication variabilities or thermal effects.

In this thesis, MZI-based CWDM systems are emphasized due to their fabrication simplicity, low loss, and compactness. To address the wavelength sensitivity of

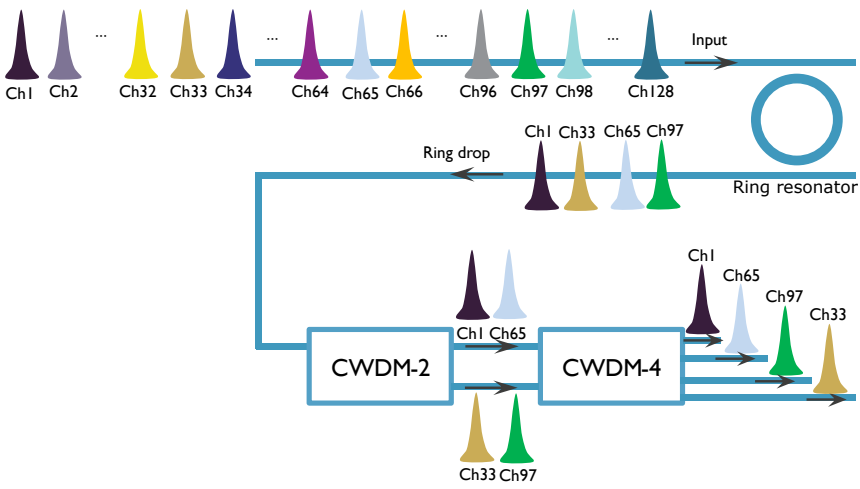

Figure 6.1: Simplified block diagram of DWDM-CWDM architecture where a drop port of a ring resonator is connected to a CWDM-2 and subsequently a CWDM-4 to eventually demultiplex 4 channels.

directional couplers (DCs) used in MZI-based CWDM filters, various broadband designs, as discussed in previous chapters, are employed. Regarding wavelength drifts, one approach involves increasing the waveguide width to reduce phase errors [6, 23], achieving up to three times less spectral shift compared to conventional designs [23]. Another approach involves the use of waveguides with different widths in the MZI arms [24]. However, limitations are encountered with this method, particularly when the waveguide widths of the two arms deviate in opposite directions, as waveguide width deviations could exhibit significant randomness [25].

The realization of CWDM filters with low insertion loss, minimal crosstalk, and high fabrication tolerance on the silicon-on-insulator (SOI) platform remains a significant challenge. In this chapter, a novel approach is proposed to mitigate phase errors and enhance the stability of CWDM systems. Compact MZI configurations with minimized common arm lengths are utilized, achieved through innovative designs such as half-ring resonators and whispering-gallery-mode (WGM) bends. These configurations are specifically designed to reduce phase errors caused by fabrication variabilities. Additionally, broadband bent DCs are employed to enhance the wavelength operation range and channel isolation. Thanks to the large channel spacing and reduced phase errors, the proposed CWDM filters can operate without thermal tuning, saving power and simplifying system design. The following sections detail the design principles, experimental validation, and wafer-scale performance of these advanced CWDM architectures.

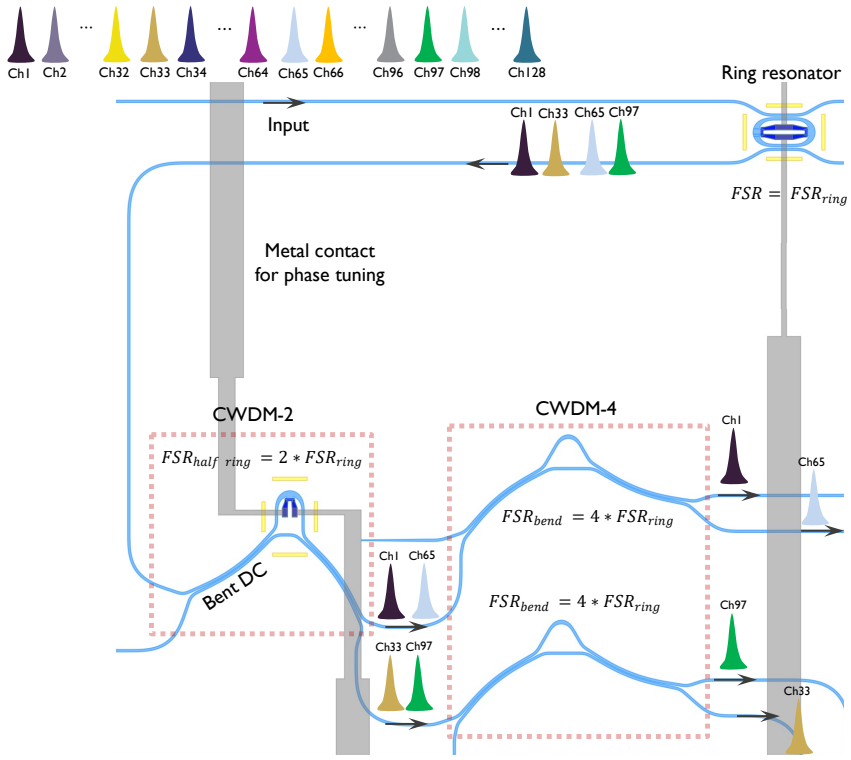

Figure 6.2: Schematic of the cascaded DWDM–CWDM architecture enabling DWDM-128 × 100 GHz. The drop port of a ring resonator with $\mathrm{FSR} = 3.2\,\mathrm{THz}$ *is connected to a CWDM-2 and subsequently a CWDM-4, enabling a fourfold increase in channel count. The CWDM filters are designed to scale the channel count by leveraging differences in arm lengths, while maintaining passive operation without thermal tuning.*

6.2 Scaling WDM filters with CWDM architectures

CWDM filters can effectively scale up the channel count in DWDM systems. For instance, in the proposed DWDM-128×100 GHz system, each ring resonator drop port is cascaded with a CWDM-4×3.2 THz filter, enabling a fourfold increase in channel count, as illustrated in the simplified block diagram in Fig. 6.1 and in the schematic in Fig. 6.2. Assuming an input of 128 channels with a channel spacing of 100 GHz, a ring resonator with a free spectral range (FSR) of $\mathrm{FSR} = 3.2\,\mathrm{THz}$ will output four distinct channels, specifically channels 1, 33, 65, and 97, at its drop port. These four channels are subsequently passed through a CWDM-2 filter.

The CWDM-2 stage employs two broadband bent DCs with an arm length difference designed to be half that of the ring resonator, ensuring the FSR is doubled. This

results in two output channels at each of the CWDM-2's through and cross ports: channels (1, 65) and (33, 97), respectively. The outputs of the CWDM-2 stage are then cascaded with a CWDM-4 system, which incorporates a whispering-gallery-mode (WGM) 120° bend. This bend is engineered to achieve double the FSR of the CWDM-2 stage. In both the CWDM-2 and CWDM-4 stages, the design minimizes common arm lengths. As will be demonstrated, large common arm lengths increase the CWDM phase error.

This configuration further scales the output by a factor of four, ultimately demultiplexing the original four channels into four separate output ports. The design maintains a hierarchical doubling of the free spectral range (FSR) at each subsequent stage. The overall FSR relationships across the stages can be expressed as:

$$\begin{aligned} \mathrm{FSR}_{\mathrm{ring}} &= 3.2\ \mathrm{THz}, \\ \mathrm{FSR}_{\mathrm{half\ ring}} &= 2 \times \mathrm{FSR}_{\mathrm{ring}} = 6.4\ \mathrm{THz}, \\ \mathrm{FSR}_{\mathrm{bend}} &= 4 \times \mathrm{FSR}_{\mathrm{ring}} = 12.8\ \mathrm{THz}. \end{aligned} \tag{6.1}$$

This overall architecture does not complicate the DWDM system design or impose additional power requirements. Thanks to the large channel spacing, the CWDM systems could operate without the need for thermal tuning. In the following sections, CWDM-2 and CWDM-4 systems are demonstrated, with a detailed discussion of their respective phase errors.

FSR tolerance bounds for CWDM-2

The following section analyzes the tolerance bounds for deviations in the FSR of the CWDM-2 in the ring-CWDM unit. The following is assumed:

- A ring resonator with FSR of $\mathrm{FSR}_{\text{ring}} = 3.2\,\mathrm{THz}$ and 10-dB bandwidth $\mathrm{BW}_{\text{ring}} = 278\,\mathrm{GHz}$.
- A CWDM-2 with an ideal FSR of $\mathrm{FSR}_{\text{cwdm2, ideal}} = 2 \times \mathrm{FSR}_{\text{ring}} = 6.4\,\mathrm{THz}$, a passband bandwidth with $ER \geq 10$ dB of $\mathrm{BW}_{\text{cwdm2}} = 1.33\,\mathrm{THz}$, and actual FSR of $\mathrm{FSR}_{\text{cwdm2}} = \mathrm{FSR}_{\text{cwdm2, ideal}} + \delta$. The parameter δ represents the FSR deviation from the ideal value that we aim to characterize.
- The ring resonator generates resonances at frequencies $f_n = f_0 + n \cdot \mathrm{FSR}_{\text{ring}}$, where f_0 denotes the reference resonance frequency and n is the integer resonance index.
- Perfect alignment at the reference resonance ($n = 0$).

- CWDM-2 passbands exhibit perfect periodicity with FSR of $\mathrm{FSR}_{\text{cwdm2}}$.

The CWDM-2 interleaver separates channels into two outputs with channel dependent positioning:

$$\text{Output} = \begin{cases} 1 \text{ (Even } n) & \text{for } n = 0, 2, \ldots \\ 2 \text{ (Odd } n) & \text{for } n = 1, 3, \ldots \end{cases}$$

The target passband centers follow the relationship:

$$\begin{aligned} \text{Base odd channel: } & f_{\text{odd}} = f_0 + \frac{\mathrm{FSR}_{\text{cwdm2}}}{2}, \\ \text{Subsequent odd channels: } & f_{\text{target}}(n) = f_{\text{odd}} + k \cdot \mathrm{FSR}_{\text{cwdm2}}, \\ \text{Base even channel: } & f_{\text{even}} = f_0, \\ \text{Subsequent even channels: } & f_{\text{target}}(n) = f_{\text{even}} + k \cdot \mathrm{FSR}_{\text{cwdm2}}, \end{aligned}$$

where k is the channel index.

The frequency error $\Delta f(n)$ represents the absolute difference between the ring resonance frequency and its target CWDM-2 passband center. The error can be characterized for each channel as follows:

1. **Ch1** ($n = 0$**, even**):

$$\begin{aligned} f_{\text{target}}(0) &= f_0 \\ \Delta f_0 &= |f_0 - f_0| = 0 \end{aligned}$$

2. **Ch33** ($n = 1$**, odd**):

$$\begin{aligned} f_{\text{target}}(1) &= f_0 + \frac{\mathrm{FSR}_{\text{cwdm2}}}{2} \\ \Delta f_1 &= \left| (f_0 + 3.2\,\mathrm{THz}) - \left(f_0 + \frac{6.4\,\mathrm{THz} + \delta}{2} \right) \right| \\ &= \left| 3.2\,\mathrm{THz} - 3.2\,\mathrm{THz} - \frac{\delta}{2} \right| = \left| \frac{\delta}{2} \right| \end{aligned}$$

3. **Ch65** ($n = 2$**, even**):

$$\begin{aligned} f_{\text{target}}(2) &= f_0 + \mathrm{FSR}_{\text{cwdm2}} \\ \Delta f_2 &= |(f_0 + 6.4\,\mathrm{THz}) - (f_0 + 6.4\,\mathrm{THz} + \delta)| \\ &= |\delta| \end{aligned}$$

4. **Ch97 ($n = 3$, odd)**:

$$\begin{aligned} f_{\text{target}}(3) &= f_{\text{target}}(1) + \text{FSR}_{\text{cwdm2}} \\ &= \left(f_0 + \frac{\text{FSR}_{\text{cwdm2}}}{2} \right) + \text{FSR}_{\text{cwdm2}} \\ &= f_0 + 1.5 \cdot \text{FSR}_{\text{cwdm2}} \\ \Delta f_3 &= |(f_0 + 9.6\,\text{THz}) - (f_0 + 1.5(6.4\,\text{THz} + \delta))| \\ &= |9.6\,\text{THz} - 9.6\,\text{THz} - 1.5\delta| = 1.5|\delta| \end{aligned}$$

For proper operation, each resonance must be fully contained within the interleaver passband:

$$\Delta f(n) + \frac{\text{BW}_{\text{ring}}}{2} \leq \frac{\text{BW}_{\text{cwdm2}}}{2}.$$

Substituting the 10-dB bandwidth values:

$$\Delta f(n) + 0.139\,\text{THz} \leq 0.665\,\text{THz}, \quad \Delta f(n) \leq 0.526\,\text{THz}.$$

Applying this constraint for each channel:

1. **Ch1** ($n = 0$): $\Delta f_0 = 0 \leq 0.526$ THz (always satisfied).
2. **Ch33** ($n = 1$):

$$\left| \frac{\delta}{2} \right| \leq 0.526\,\text{THz}, \quad |\delta| \leq 1.052\,\text{THz}.$$

3. **Ch65** ($n = 2$):

$$|\delta| \leq 0.526\,\text{THz}.$$

4. **Ch97** ($n = 3$):

$$1.5|\delta| \leq 0.526\,\text{THz}, \quad |\delta| \leq 0.351\,\text{THz}.$$

The tightest constraint comes from Ch97 ($n = 3$):

$$|\delta| \leq 0.351\,\text{THz}.$$

Thus, the valid FSR range is:

$$\begin{aligned} \text{FSR}_{\text{cwdm2}} &\in [6.4\,\text{THz} - 0.35\,\text{THz}, 6.4\,\text{THz} + 0.35\,\text{THz}] \\ &= [6.05\,\text{THz}, 6.75\,\text{THz}]. \end{aligned} \tag{6.2}$$

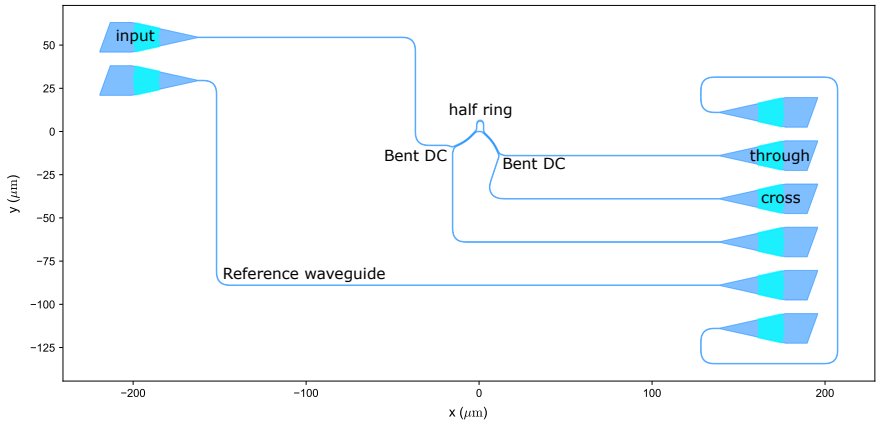

Figure 6.3: The layout of the CWDM-2 × 3.2 THz system using bent DCs. The design incorporates minimized common arm lengths to reduce phase errors.

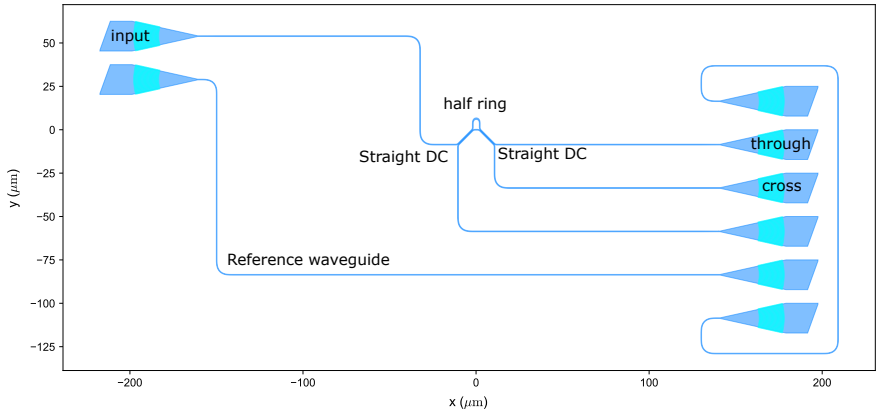

Figure 6.4: The layout of the CWDM-2 × 3.2 THz system using straight DCs. This structure serves as a reference to evaluate the performance improvements enabled by bent DCs.

6.3 CWDM-2 systems

CWDM-2 × 3.2 THz

CWDM-2 interleavers play a key role in scaling the number of channels in WDM filter architectures. By cascading the drop port of a ring resonator to a CWDM-2 filter, the number of output channels can be effectively doubled. To enable practical and simple deployment, it is preferred to eliminate the need for thermal tuning in CWDM circuits. CWDM filters typically have a large channel spacing, which

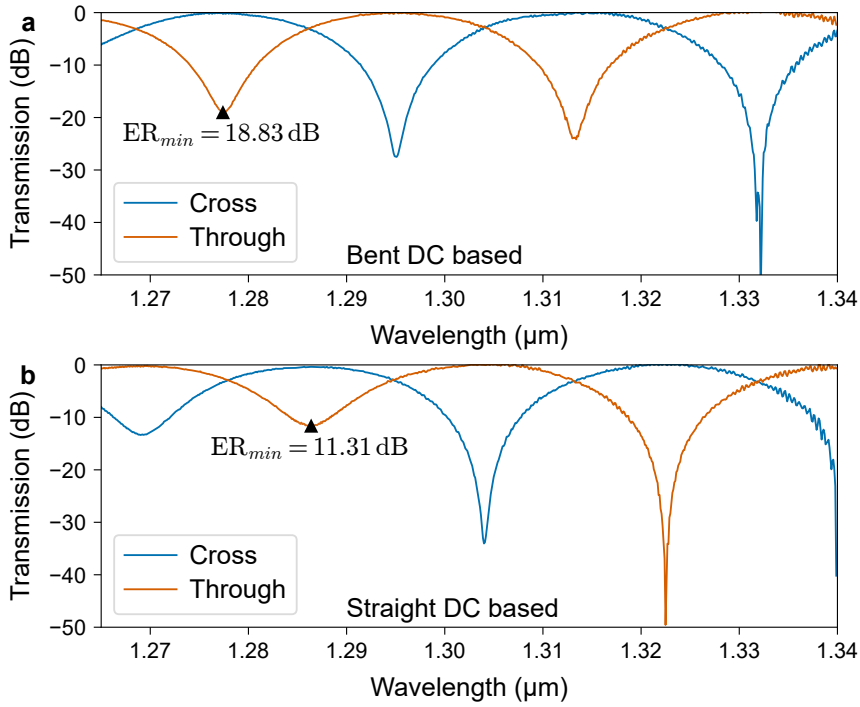

Figure 6.5: Measured spectra of the CWDM-2 × 3.2 THz for bent DCs (a) and straight DCs (b). A significant improvement in the lowest extinction ratio (ER) is observed with the use of broadband bent DCs. The bent DC design achieves a higher worst-case ER of 18.1 dB, compared to 12.8 dB for the straight DC configuration. The corresponding designs are shown in Fig. 6.3 and Fig. 6.4 for the bent and straight DCs, respectively.

relaxes the requirements for precise wavelength alignment. However, phase errors can still significantly affect the performance of CWDM systems, particularly in terms of channel isolation. Herein, the phase error is reduced by means of minimizing the common arm lengths within the CWDM design, as these significantly contribute to phase errors. First, the spectrum of the CWDM-2 systems will be presented showing the enhancement in the ER and wafer mapping for a few dies. This is followed by extracting the exact parameters to fine tune the FSR value. Finally, the phase error improvement in comparison with regular MZI designs is presented.

A CWDM-2 × 3.2 THz system was fabricated, with corresponding schematics shown in Fig. 6.3 and Fig. 6.4, representing the bent and straight DCs implementations, respectively. The CWDM-2 design is based on half of the ring as presented in Fig. 6.2, in order to ensure doubling of the FSR as discussed earlier. The trans-

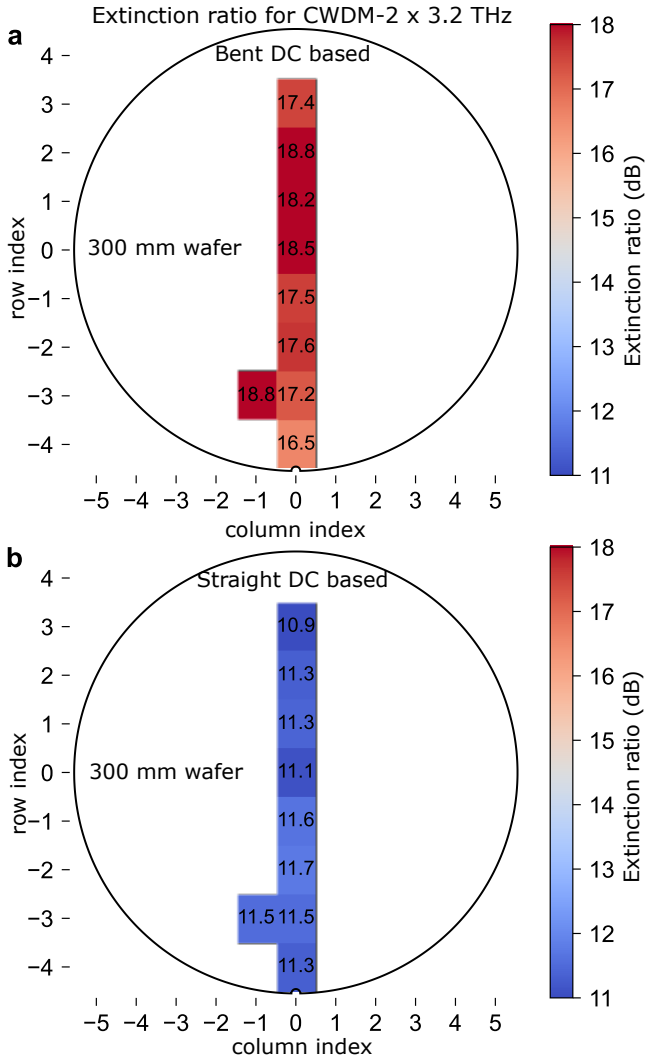

Figure 6.6: Wafer mapping of the extinction ratio (ER) for CWDM-2 × 3.2 THz for a few dies, showing the improvement in ER with the use of bent DCs compared to straight DCs. The CWDM-2 × 3.2 THz based on the bent DC demonstrates ER values ranging from 16.5 to 18.8 dB, while the straight DC shows ER values from 10.9 to 11.7 dB.

mission spectra of both designs are presented in Fig. 6.5(a) and (b), corresponding to the bent and straight DC implementations. Notably, the worst-case extinction ratio (ER) improved from 12.8 dB to 18.1 dB when utilizing the broadband bent DC configuration.

The proposed CWDM-2 architecture is robust over a 300 mm wafer. Wafer mapping

of a few dies demonstrates a consistent improvement in the ER while using the bent DC compared to the straight DC in the CWDM-2 $\times$ 3.2 THz system, as shown in Fig. 6.6. Specifically, the CWDM-2 $\times$ 3.2 THz based on the bent DC exhibited high ER values ranging from 16.5 to 18.8 dB, while the CWDM-2 based on the straight DC had lower ER values ranging from 10.9 to 11.7 dB. Overall, there is low variation in the ER values. Any variation in the ER values can generally be attributed to fabrication variabilities across the measured dies and/or any measurement uncertainties.

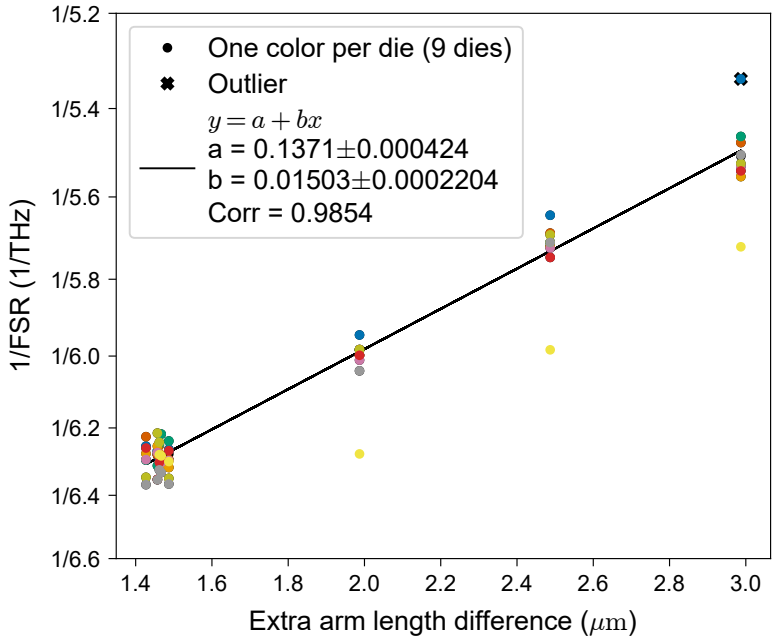

Figure 6.7: Linear fitting between the designed extra arm length difference and the inverse of the free spectral range ($1/FSR$) for the CWDM-2 structure where the arm length difference is utilizing half the ring. Extra arm length difference is added to half of the ring to fine tune the FSR. This relationship is used to determine the arm length required to achieve an FSR of 6.4 THz. The extra arm length differences are chosen for the given range only to make sure an FSR of 6.4 THz can be attained.

The CWDM-2 structure is cascaded to the drop ports of the ring resonators to double the number of output channels. For this cascaded configuration to operate correctly, the FSR of the CWDM-2 is designed to be 6.4 THz. It should be noted that the FSR of the ring resonators is quite robust with respect to the wavelength. When the central wavelength changes in the ring resonator, the FSR of the ring shifts slightly. For instance, even with significant wavelength shifts equivalent to one FSR, the ring's FSR value changes by only approximately 2% (from 3.20 THz

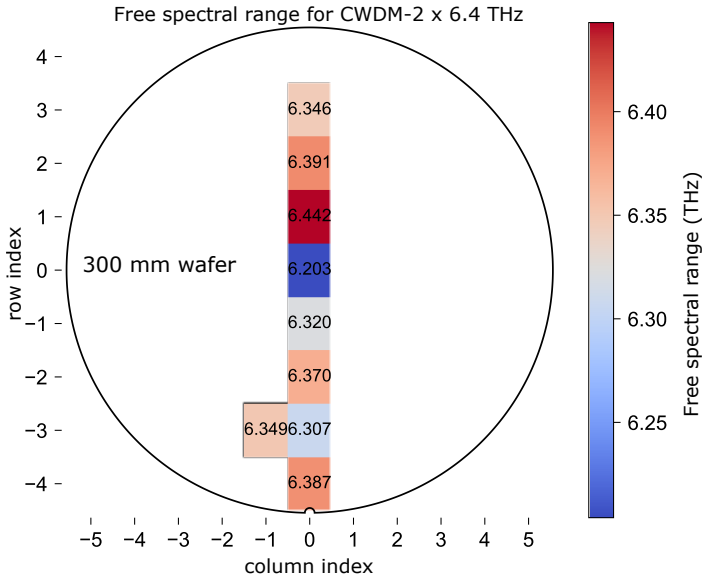

Figure 6.8: Wafer-scale mapping of the free spectral range (FSR) for the fabricated CWDM-2 structures designed for $6.4\,\mathrm{THz}$ *operation. The measured FSR values range from* $6.2\,\mathrm{THz}$ *to* $6.44\,\mathrm{THz}$*, indicating good uniformity and process control across the wafer.*

to 3.13 THz). This inherent stability ensures reliable operation of the ring-CWDM system across the entire wavelength band of interest.

The design of the CWDM-2×3.2 THz is based on half the ring resonator, where extra straight waveguide sections are added to fine-tune the FSR of the system. Different etching conditions between the ring resonator and the half ring could result in slight variations between the ring and half the ring, making FSR fine-tuning necessary. To facilitate accurate design, a linear fit is performed between the extra arm length and $1/\mathrm{FSR}$ over 9 different dies, leveraging the expected inverse proportionality. The resulting linear relationship is shown in Fig. 6.7. Based on the fitting, an arm length difference of 1.33 μm is required to achieve an FSR of $6.4\,\mathrm{THz}$. It is worth mentioning that the low correlation value of the fitting is mainly due to the small range on the x-axis ($\approx 0.5\ \mu m$).

Wafer-scale mapping of the FSR for the fabricated CWDM-2 structures targeting $6.4\,\mathrm{THz}$ operation is shown in Fig. 6.8. The measured FSR values exhibit an average of $6.35\,\mathrm{THz}$ with a standard deviation of $0.06\,\mathrm{THz}$, demonstrating good uniformity across the wafer. The FSR values range from $6.2\,\mathrm{THz}$ to $6.44\,\mathrm{THz}$. Future iterations can further enhance the accuracy of the designed FSR by leveraging the linear fitting relationship shown in Fig. 6.7.

CWDM-2 × 6.4 THz

The CWDM-2 with a channel spacing of 6.4 THz (i.e., FSR of 12.8 THz) serves as a fundamental building block for the CWDM-4×3.2 THz architecture, which is composed of two cascaded CWDM-2 stages, as illustrated in Fig. 6.2. Accurate realization of this system with the correct FSR, broadband operation, and minimal phase error is critical to ensure proper spectral alignment and minimal channel crosstalk across the full WDM grid.

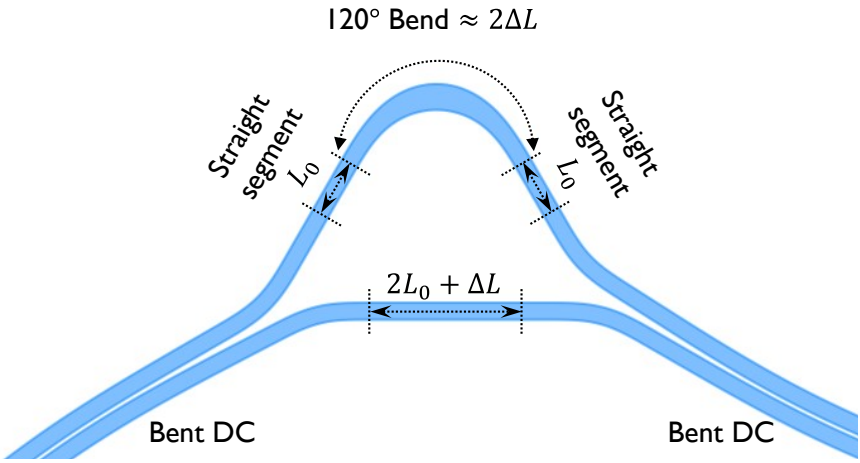

Figure 6.9: Schematic of the CWDM2 with a 120° *bend and a minimum common arm length of* L_0*. The total arm length difference in this configuration is* ΔL*. The* 120° *bend has an effective arm length of* $2\Delta L$*. Each straight waveguide section connecting the bent DCs and the* 120° *bend has a length of* L_0*. The FSR of this MZ configuration can be manipulated by adjusting* ΔL*, where* L_0 *is always chosen as the minimum required value to minimize the common arm length.*

In the CWDM-2 × 6.4 THz system, the 180° half-ring architecture is no longer feasible. Doubling the FSR of the half-ring (to achieve an FSR of 12.8 THz) would necessitate a ring bending radius of approximately $1\ \mu\mathrm{m}$, which would result in excessive insertion loss. Instead, a 120° WGM bend is employed within a configuration that minimizes the common waveguide length in the CWDM arms. In this configuration, the 120° bend (with an effective length of $2\Delta L$) is symmetrically connected to two arms of length L_0, while the third arm has a length of $2L_0 + \Delta L$. The schematic layout of this design is illustrated in Fig. 6.9. Here, the common arm length, L_0, is chosen as the geometrically required minimum value based on the desired arm length difference, ΔL, to minimize phase errors, as will be demonstrated in the following sections.

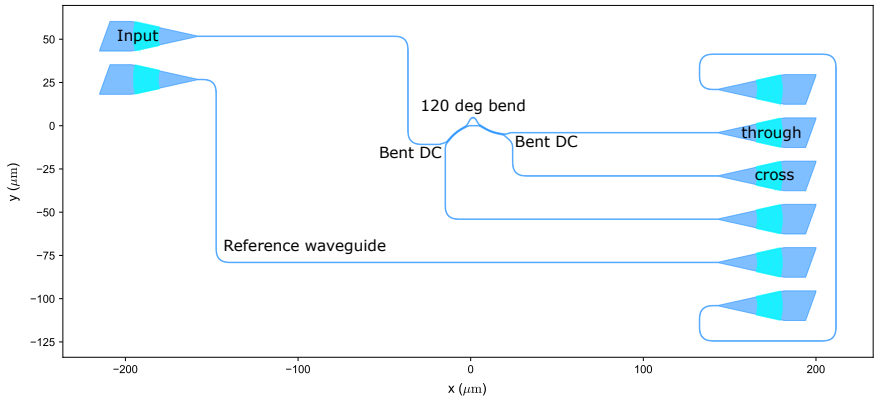

Figure 6.10: The layout of the CWDM-2 × 6.4 THz system based on 120° *bend using bent DCs. The design incorporates minimized common arm lengths to reduce phase errors.*

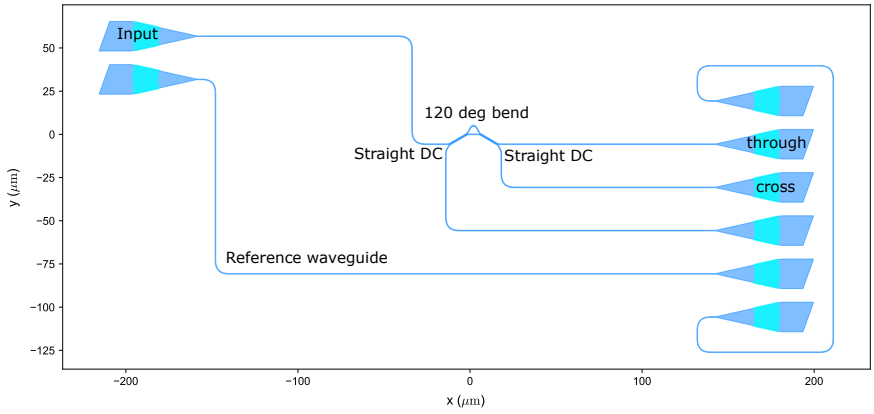

Figure 6.11: The layout of the CWDM-2 × 6.4 THz system based on 120° *bend using straight DCs. The design incorporates minimized common arm lengths to reduce phase errors.*

A CWDM-2 × 6.4 THz system was fabricated, with the corresponding schematic layouts depicted in Fig. 6.10 and Fig. 6.11. The measured transmission spectra for both implementations utilizing bent and straight DCs are presented in Fig. 6.12(a) and (b), respectively. A notable enhancement in performance is observed with the broadband bent DC design, where the worst-case ER increases from 7.82 dB to 18.32 dB.

Wafer-scale mapping across multiple dies demonstrates a consistent enhancement in the ER with the use of bent DCs, as shown in Fig. 6.13. The CWDM-2 × 6.4 THz system based on bent DCs achieved ER values ranging from 16.4 to

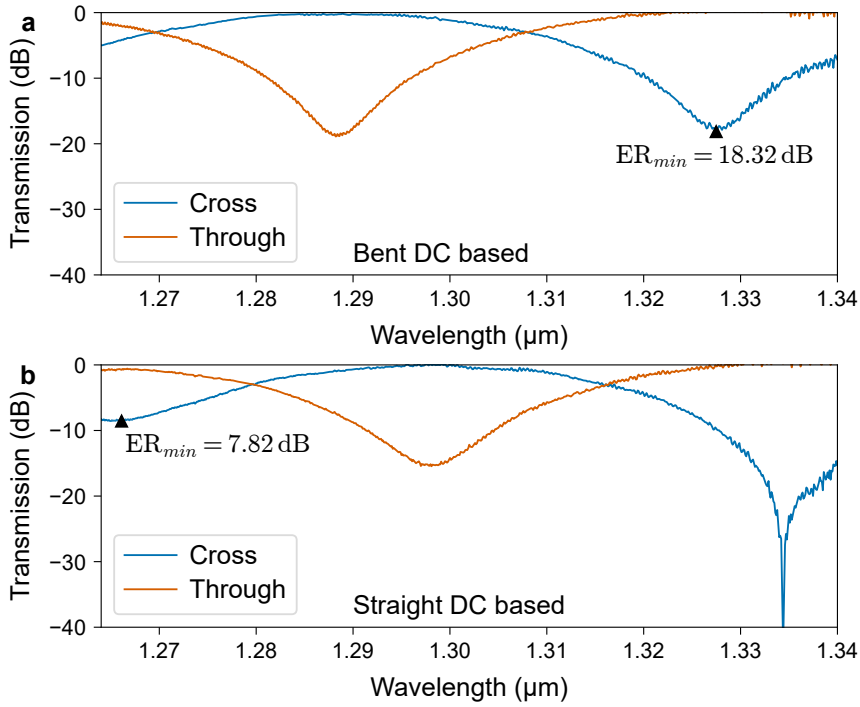

Figure 6.12: Measured spectra of the CWDM-2 × 6.4 THz for bent DCs (a) and straight DCs (b). A significant improvement in the lowest extinction ratio (ER) is observed with the use of broadband bent DCs. The bent DC design achieves a better worst-case extinction ratio of 18.3 dB, compared to 7.8 dB for the straight DC configuration. The corresponding designs are shown in Fig. 6.10 and Fig. 6.11 for the bent and straight DCs, respectively.

18.3 dB, significantly outperforming the straight DC configuration, which exhibited ER values between 6.6 and 8.1 dB.

Similarly to the half ring FSR tuning, it is also essential to control the optical path length difference to achieve the desired FSR of 12.8 THz for the 120° WGM bend. A linear fitting is done for the inverse of the FSR of the CWDM-2×6.4 THz as a function of the extra arm length difference (ΔL, as explained in Fig. 6.9), over 9 dies, as shown in Fig. 6.14, where ΔL should be set to -1.22 μm to achieve an FSR of 12.8 THz. It is worth mentioning that the fitting is done for all the points from all dies at once.

Wafer-scale mapping of the FSR for the fabricated CWDM-2 structures targeting 12.8 THz operation is shown in Fig. 6.15. The measured FSR values exhibit an average of 12.47 THz with a standard deviation of 0.52 THz. The FSR values range from 11.23 THz to 12.99 THz. Overall, the FSR of the CWDM-2 × 6.4 THz

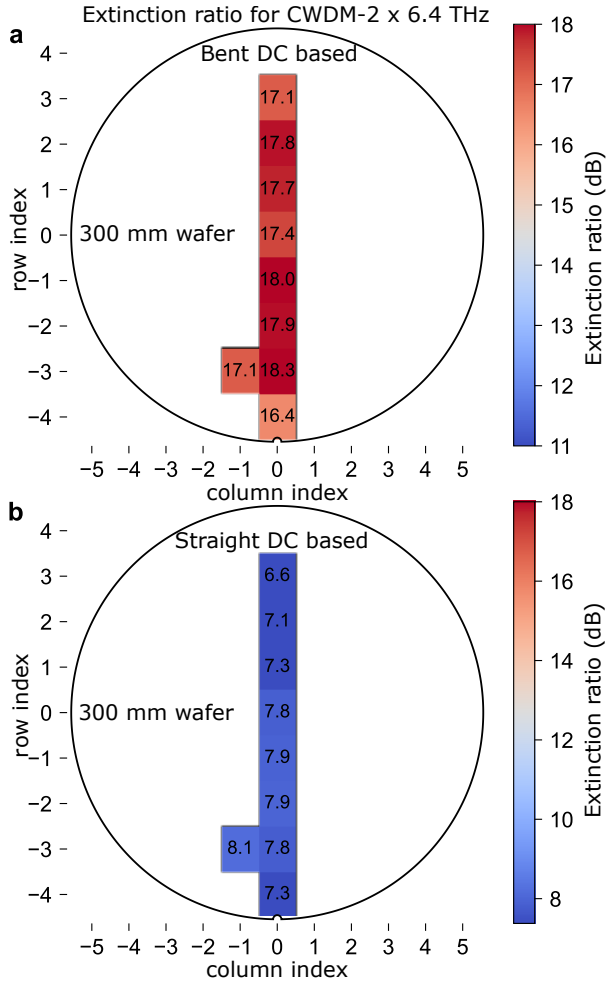

Figure 6.13: Wafer mapping of extinction ratio (ER) for multiple dies, showing the improvement in ER with the use of bent DCs compared to straight DCs. The CWDM-2×6.4 THz based on the bent DC demonstrates ER values ranging from 16.4 to 18.3 dB, while the straight DC shows ER values from 6.6 to 8.1 dB.

systems can tolerate up to ± 0.52 THz error for an allowed ER $\geq$ 10dB, with similar analysis as done in the previous section. Future iterations can enhance the accuracy of the designed FSR further by leveraging the linear fitting relationship shown in Fig. 6.14.

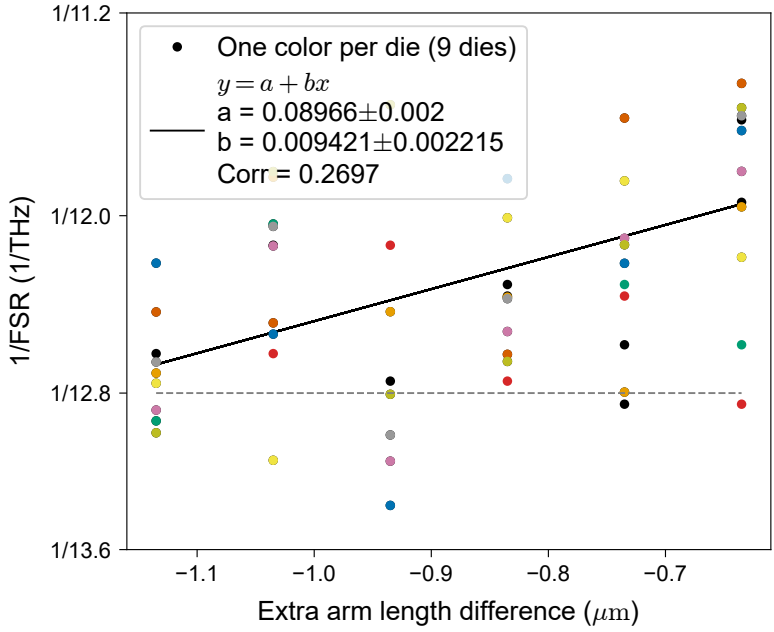

Figure 6.14: Linear fitting between the extra arm length difference and $(1/FSR)$ for the CWDM-2 structure based on 120° WGM bend. This relationship is used to determine the arm length required to achieve an FSR of 12.8 THz.

Phase error improvement in CWDM-2 systems

Minimizing power consumption in photonic integrated circuits is a critical design objective. In WDM architectures, a significant portion of power dissipation often arises from thermal phase tuning, which compensates for phase errors induced by fabrication variations. These variations include, but not limited to, discrepancies in waveguide dimensions (length and width), non-uniform gaps, and random scattering at waveguide edges. To mitigate such variations, reducing the common optical waveguide lengths in MZI configurations can help minimize phase errors. Accordingly, in the CWDM-2 $\times$3.2 THz design, the arm length difference was implemented using half of a ring resonator where the ring resonator has an FSR of 3.2 THz, and consequently the half ring has an FSR of 6.4 THz. Furthermore, for the CWDM-2 $\times$6.4 THz, a WGM bend is used in a configuration to minimize the common waveguide length. In this section, phase error is characterized in the presented CWDM-2 configurations and benchmarked with a conventional MZI configuration, and statistical data is shown over the 300 mm wafer.

To quantitatively assess the phase error in the proposed CWDM configurations

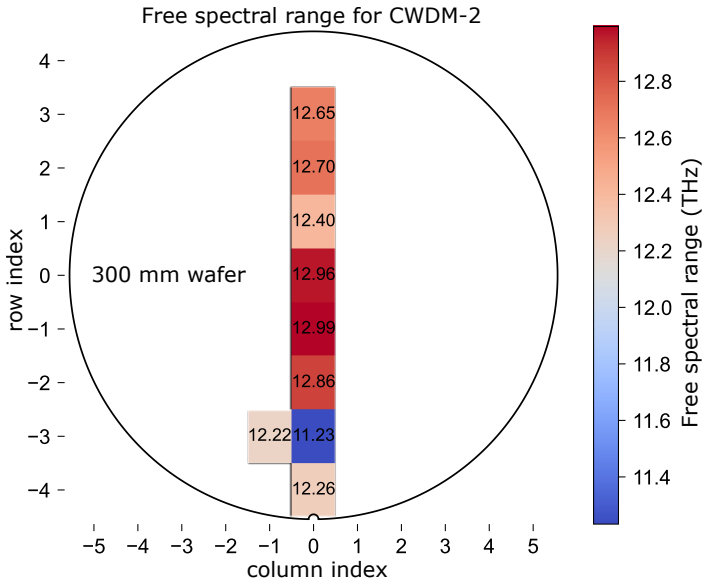

Figure 6.15: Wafer-scale mapping of the free spectral range (FSR) for the fabricated CWDM-2 structures designed for 12.8 THz *operation. The measured FSR values range from* 11.23 THz *to* 12.99 THz*, which should provide high quality filtering, indicating good uniformity and process control across the wafer.*

(half ring and 120° bend) relative to a traditional MZI with non-optimized common arm length, the MZI designs were replicated multiple times, and the corresponding phase error was extracted based on wafer-level measurements. The corresponding schematics are shown in Fig. 6.16(a), (b), and (c) for the traditional MZI, the half ring based MZI and the 120° bend MZI, respectively.

The corresponding optical spectrum of the aforementioned MZIs are shown in Fig. 6.17(a), (b), and (c) for the traditional MZI, the half ring based MZI and the 120° bend MZI, respectively. In these figures, the repeated identical devices are measured to show the phase error, where the phase error is improved with the compact configurations.

Phase errors result in shifting of the constructive interference wavelength of MZI structures. The phase errors in the three MZI configurations are quantified by evaluating variations in the constructive interference wavelength of each device relative to the mean value across identically designed structures. For each die, the spectral response is analyzed to identify all constructive interference peaks. The phase error for each device is then calculated using the relation:

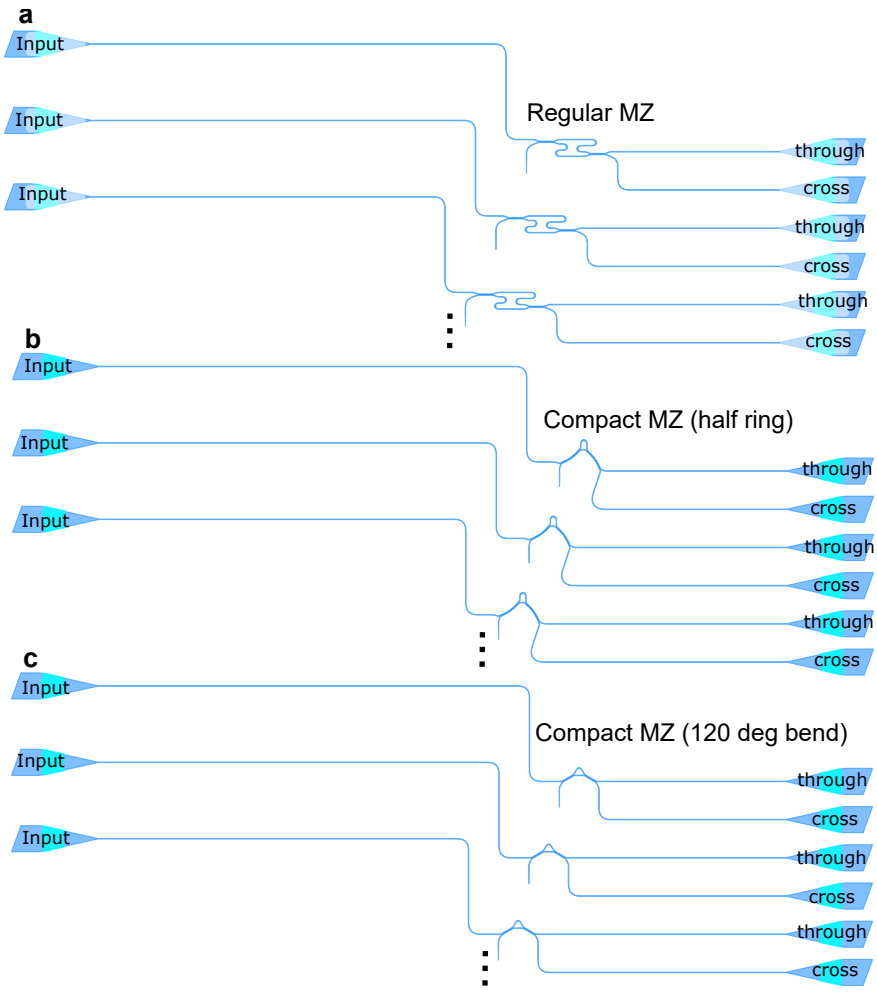

Figure 6.16: Phase error characterization layout for CWDM-2 × based on regular MZ structure (a), the half ring based MZ structure (b), and the 120° bend MZ structure (c), where the same MZ design is replicated multiple times next to each other. Only a three duplicates are shown in this figure for each test site.

$$\Delta\phi = 2\pi \cdot OL_{eff} \cdot \left(\frac{1}{\lambda_i} - \frac{1}{\bar{\lambda}}\right), \tag{6.3}$$

where OL_{eff} represents the optical path length difference between the interferometer arms, λ_i is the constructive interference wavelength of the individual device, and $\bar{\lambda}$ is the mean constructive interference wavelength across all devices. This expression quantifies the phase deviation introduced by fabrication-induced variations

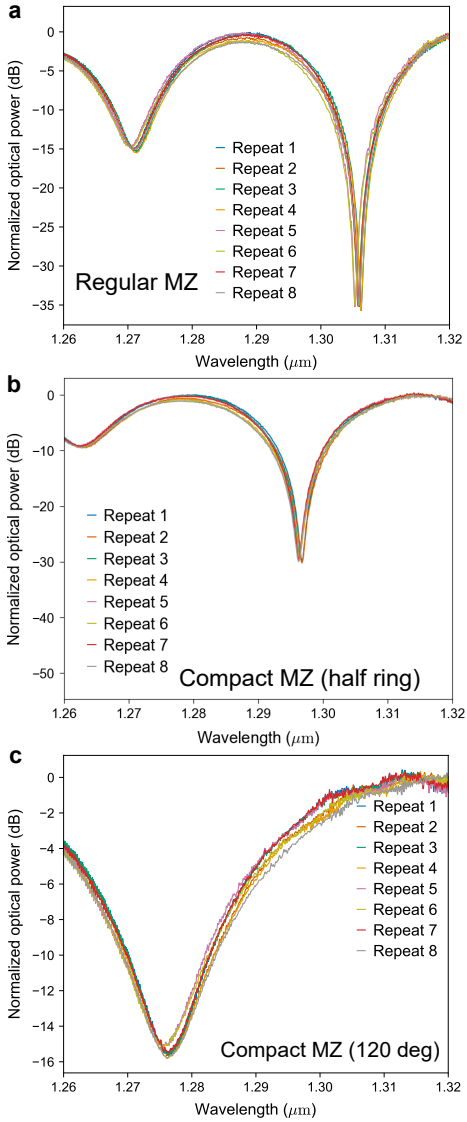

Figure 6.17: The cross power transmission spectra for identical MZI configurations: (a) traditional MZI structure, (b) half-ring based MZI structure, and (c) 120° bend MZI structure. Each panel shows 8 identical devices placed next to each other on the reticle to demonstrate phase error variations. Note the progressively reduced constructive interference wavelength shifts from (a) to (c), indicating decreasing phase errors as we move from traditional to more compact MZI configurations. The designs correspond to those shown in Fig. 6.16.

in the effective optical length. The resulting distribution of phase errors is then statistically analyzed to assess the uniformity and robustness of the MZI structures across the wafer.

The phase error distributions for both the conventional and compact MZI configurations are presented in Fig. 6.18. Measurements were conducted across 19 dies, revealing a reduction in phase error when utilizing the compact MZI design compared to the conventional structure. Specifically, the standard deviation of the phase error for the conventional MZI is $0.545\,\mathrm{rad}$, while the compact MZI based on a half-ring configuration demonstrates a significantly lower deviation of $0.152\,\mathrm{rad}$. This value is further reduced to $0.040\,\mathrm{rad}$ when employing a 120-degree whispering-gallery-mode (WGM) bend.

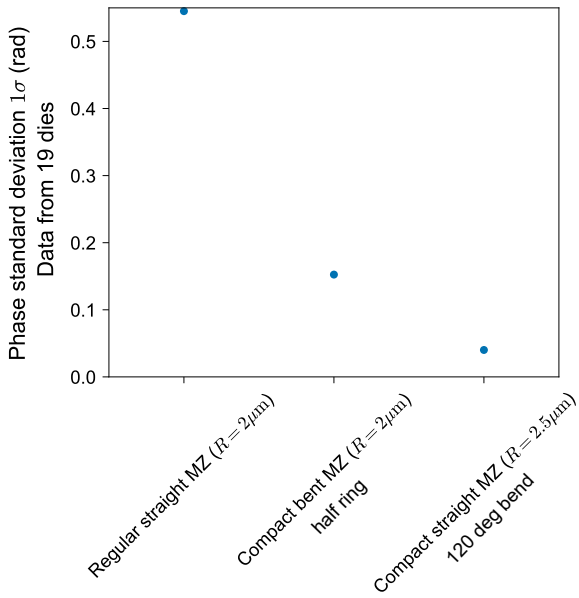

Figure 6.18: Standard deviation of phase error measured across 19 dies for various MZI configurations. The results highlight a substantial reduction in phase error for compact MZI designs, particularly those incorporating compact MZ structures including the half ring and the 120° *bend.*

Additional measurements were performed on three dies using the half-ring design. These yielded comparable standard deviations of $0.037\,\mathrm{rad}$ and $0.026\,\mathrm{rad}$ for the bent and straight DC-based compact MZI variants, respectively.

6.4 CWDM-4 × 3.2 THz

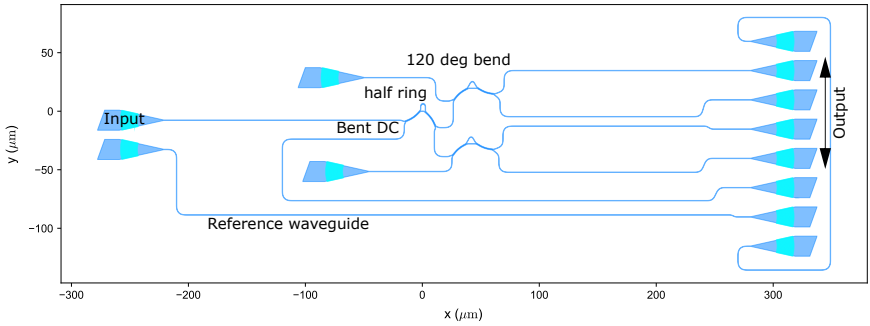

Figure 6.19: The layout of the CWDM-4 × 3.2 THz system using bent DCs. The design incorporates CWDM-2 × 3.2 THz in the first stage and CWDM-2× 6.4 THz in the second stage.

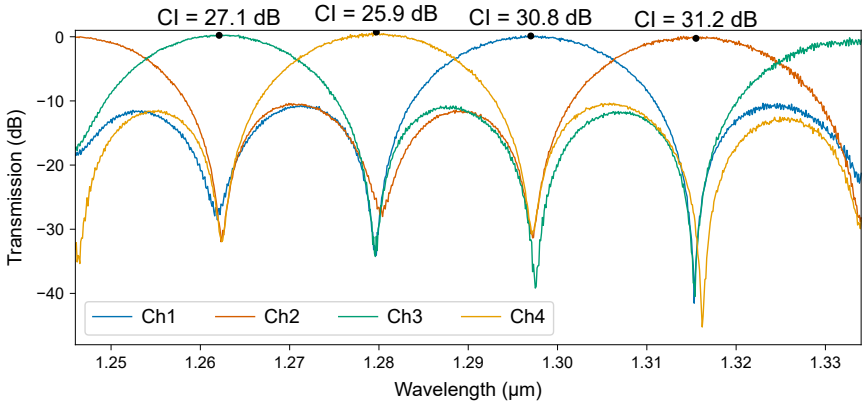

Figure 6.20: Optical spectrum for the CWDM-4 × 3.2 THz system based on broadband bent DCs. The worst channel isolation (CI) is 25.9 dB covering a bandwidth> 12.8 THz. The channel losses are minimal, where the loss is smaller than the measurement error.

The CWDM-4 × 3.2 THz system is essential in the DWDM-128×100 GHz architecture as demonstrated earlier. It offers an efficient and scalable approach to quadruple the channel count by cascading the ring drop port with a CWDM-4 × 3.2 THz demultiplexer. The CWDM-4 × 3.2 THz system is designed to operate with a channel spacing of 3.2 THz, corresponding to an FSR of 12.8 THz, and is based on the previously discussed CWDM-2 systems.

The fabricated CWDM-4 × 3.2 THz system, illustrated in Fig. 6.19, was experimentally characterized. As shown in Fig. 6.20, the system achieves a worst-case channel

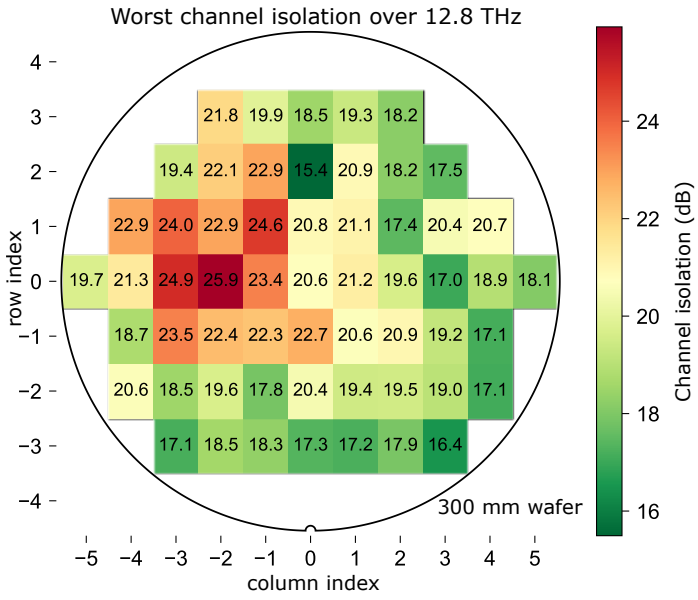

Figure 6.21: Wafer mapping of the worst channel isolation (CI) over 12.8 THz band over a 300 mm wafer for the proposed CWDM-4 × 3.2 THz system. High values of CIs are observed across the wafer showing the robustness of the proposed design.

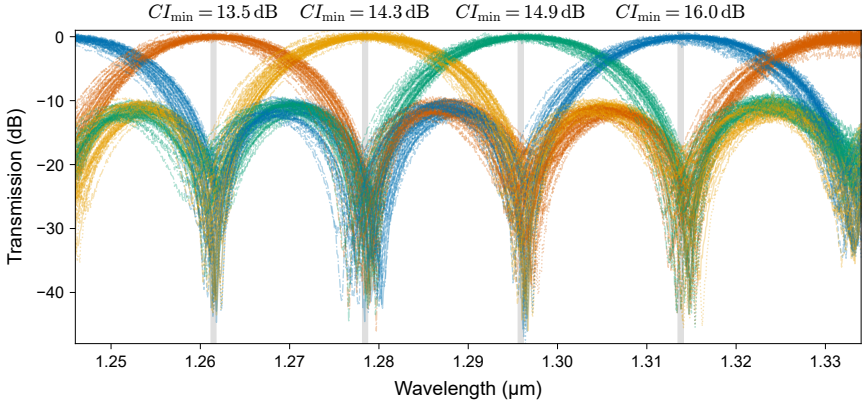

Figure 6.22: Transmission of CWDM-4 × 3.2 THz system based on bent DCs over 54 dies. Each color represents a different channel. The measurements show the robustness of the design to be used in mass manufacturing, where a channel spacing of 3.2 THz with each channel having a passband of 100 GHz showing a minimum CI of at least 13.5 dB.

isolation of 25.94 dB across the four channels, with low insertion loss value that are below the measurement accuracy threshold. The four channels cover $>$ 12.8 Thz

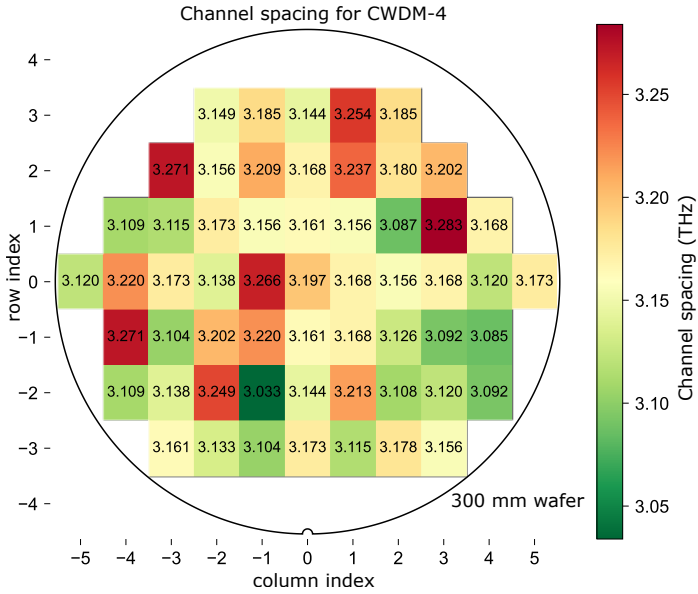

Figure 6.23: Wafer mapping for the channel spacing in THz for the proposed CWDM-4×3.2 THz system using bent DCs. The channel spacing ranges between 3.033 and 3.283 THz proving the robustness of the design over the whole wafer.

of bandwidth, thanks to the use of broadband bent DCs. It is worth mentioning that the channel isolation can be potentially further improved by using more broadband bent DC or adiabatic couplers designs, as discussed in earlier chapters.

To assess the robustness of the system, channel isolation was evaluated across a 300 mm wafer, as shown in Fig. 6.21. The worst-case channel isolation varies between 15.4 dB and 25.9 dB, underscoring the consistency and quality of the design across the wafer.

Furthermore, in order to assess the usability of the CWDM-4 $\times$ 3.2 THz system without thermal tuning, the spectral response was measured across 54 dies. The results are shown in Fig. 6.22, where the optical spectrum is presented for each channel in a separate color. The measurements indicate a high level of uniformity across the dies, with a minimum channel isolation of 13.5 dB calculated across 100 GHz band around each channel center. The spectral responses exhibit minimal variation, confirming the design's robustness for mass manufacturing without the need for thermal tuning.

It is worth noting that the large bandwidth and low phase errors of the proposed CWDM systems enhance their robustness to temperature variations. Specifically, the CWDM system can tolerate temperature variations of up to approximately 77 K,

corresponding to a 1 dB bandwidth of 9.4 nm and an allowable wavelength shift of half the bandwidth value.

Finally, the measured channel spacing across the wafer, shown in Fig. 6.23, remains robust with values ranging from 3.033 and 3.283 THz, further validating the stability of the system under process variations.

6.5 Conclusions

This chapter presented the design, implementation, and validation of robust CWDM systems for scaling WDM architectures. The proposed CWDM-2 and CWDM-4 systems achieved high channel isolation, low insertion loss, and minimized phase errors. These systems are integral to the DWDM-128$\times$100 GHz architecture, offering heater-free implementation to scale up the number of channels.

The CWDM-2 $\times$ 3.2 THz system, based on half-ring resonators, and the CWDM-2 $\times$ 6.4 THz system, utilizing 120° WGM bends were demonstrated with improved extinction ratios, and reduced phase errors. Wafer-scale measurements confirmed their uniformity and fabrication tolerance. Further, a linear fitting is presented to accurately determine the FSR of these systems based on the extra arm lengths.

The CWDM-4 $\times$ 3.2 THz system, constructed by cascading CWDM-2 stages based on broadband bent DC, scaled up the channel count by a scale of four while maintaining a high channel isolation of $\geq$ 25.9 dB across a bandwidth of ¿12.8 THz and low insertion loss. The CWDM-4 $\times$ 3.2 THz system was shown to be robust over the wafer, where the channel isolation varied between 15.4 dB and 25.9 dB, and the channel isolation had a minimum value of 13.5 dB across 100 GHz band around each channel center.

In summary, these CWDM systems address key challenges in WDM architectures, offering scalable, energy-efficient, and fabrication-tolerant solutions for next-generation optical communication systems.

References

[1] Nabarun Saha, Giuseppe Brunetti, Annarita di Toma, Mario Nicola Armenise, and Caterina Ciminelli. Silicon photonic filters: A pathway from basics to applications. *Advanced Photonics Research*, March 2024. ISSN 2699-9293. doi: 10.1002/adpr.202300343.

[2] Ahmed Bayoumi, Mehmet Oktay, Alaa Elshazly, Hakim Kobbi, Rafal Magdziak, Guy Lepage, Chiara Marchese, Javad Rahimi Vaskasi, Swetanshu Bipul, Dieter Bode, Dimitrios Velenis, Maumita Chakrabarti, Peter Verheyen, Philippe Absil, Filippo Ferraro, Yoojin Ban, Joris Van Campenhout, Wim Bogaerts, and Qingzhong Deng. Enhanced operation range of silicon MZI filters using a broadband bent directional coupler. *IEEE Photonics Technology Letters*, 37(9):500–503, May 2025. ISSN 1941-0174. doi: 10.1109/lpt.2025.3553059.

[3] Qingzhong Deng, Ahmed H. El-Saeed, Alaa Elshazly, Guy Lepage, Chiara Marchese, Pieter Neutens, Hakim Kobbi, Rafal Magdziak, Jeroen De Coster, Javad Rahimi Vaskasi, Minkyu Kim, Yeyu Tong, Neha Singh, Marko Ersek Filipcic, Pol Van Dorpe, Kristof Croes, Maumita Chakrabarti, Dimitrios Velenis, Peter De Heyn, Peter Verheyen, Philippe Absil, Filippo Ferraro, Yoojin Ban, and Joris Van Campenhout. Low-loss and low-power silicon ring based WDM 32×100 GHz filter enabled by a novel bend design. *Laser & Photonics Reviews*, November 2024. ISSN 1863-8899. doi: 10.1002/lpor.202401357.

[4] Hongnan Xu and Yaocheng Shi. Flat-Top CWDM (De)Multiplexer Based on MZI With Bent Directional Couplers. *IEEE Photonics Technology Letters*, 30 (2):169–172, January 2018. ISSN 1941-0174. doi: 10.1109/LPT.2017.2779489.

[5] Qingzhong Deng, Ahmed H. El-Saeed, Alaa Elshazly, Guy Lepage, Chiara Marchese, Hakim Kobbi, Rafal Magdziak, Jeroen De Coster, Neha Singh, Marko Ersek Filipcic, Kristof Croes, Dimitrios Velenis, Maumita Chakrabarti, Peter De Heyn, Peter Verheyen, Philippe Absil, Filippo Ferraro, Yoojin Ban, and Joris Van Campenhout. 32x100 GHz WDM filter based on ultra-compact silicon rings with a high thermal tuning efficiency of 5.85 mw/pi. In *Optical Fiber Communication Conference (OFC)*, page W1A, 2024.

[6] Folkert Horst, William M. J. Green, Solomon Assefa, Steven M. Shank, Yurii A. Vlasov, and Bert Jan Offrein. Cascaded mach-zehnder wavelength filters in silicon photonics for low loss and flat pass-band WDM

(de-)multiplexing. *Optics express*, 21(10):11652–11658, 2013. doi: 10.1364/OE.21.011652.

[7] Dajian Liu, Ming Zhang, Yaocheng Shi, and Daoxin Dai. Four-channel CWDM multiplexers using cascaded multimode waveguide gratings. *IEEE Photonics Technology Letters*, 32(4):192–195, February 2020. ISSN 1941-0174. doi: 10.1109/lpt.2020.2966073.

[8] Yikai Su, Yong Zhang, Ciyuan Qiu, Xuhan Guo, and Lu Sun. Silicon Photonic Platform for Passive Waveguide Devices: Materials, Fabrication, and Applications. *Advanced Materials Technologies*, 5(8):1901153, 2020. ISSN 2365-709X. doi: 10/gh3525. ZSCC: 0000015 _eprint: tex.ids= su_silicon_2020-1.

[9] Qingzhong Deng, Lu Liu, Rui Zhang, Xinbai Li, Jurgen Michel, and Zhiping Zhou. Athermal and flat-topped silicon mach-zehnder filters. *Optics Express*, 24(26):29577, December 2016. ISSN 1094-4087. doi: 10.1364/OE.24.029577. URL https://www.osapublishing.org/abstract.cfm?URI=oe-24-26-29577.

[10] Han Yun, Wei Shi, Yun Wang, Lukas Chrostowski, and Nicolas A. F. Jaeger. 2×2 adiabatic 3-dB coupler on silicon-on-insulator rib waveguides. pages 89150V–89150V. International Society for Optics and Photonics, 2013.

[11] Eslam El-Fiky, Mohamed Osman, Alireza Samani, Claude Gamache, Michael H. Ayliffe, Jingsi Li, Maxime Jacques, Yun Wang, Amar Kumar, and David V. Plant. First demonstration of a 400 Gb/s 4λ CWDM TOSA for datacenter optical interconnects. *Optics Express*, 26(16):19742, July 2018. ISSN 1094-4087. doi: 10.1364/oe.26.019742.

[12] Hongliang Chen, Zhen Li, Xin Fu, and Lin Yang. Fabrication-tolerant CWDM filter based on cascaded mach–zehnder interferometers with low phase error waveguide bend. *Journal of Lightwave Technology*, 43(5):2076–2083, March 2025. ISSN 1558-2213. doi: 10.1109/jlt.2024.3486065.

[13] Enrico Forestieri, Marco Secondini, Luca Poti, and Fabio Cavaliere. High-speed optical communications systems for future WDM centralized radio access networks. *Journal of Lightwave Technology*, 40(2):368–378, January 2022. ISSN 1558-2213. doi: 10.1109/jlt.2021.3131399.

[14] Dajian Liu, Hongnan Xu, Ying Tan, Yaocheng Shi, and Daoxin Dai. Silicon photonic filters. *Microwave and Optical Technology Letters*, 63(9):2252–2268, 2021. ISSN 1098-2760. doi: 10/gg6sj8.

[15] Joost Brouckaert, Wim Bogaerts, Pieter Dumon, Dries Van Thourhout, and Roel Baets. Planar concave grating demultiplexer fabricated on a nanophotonic

silicon-on-insulator platform. *Journal of Lightwave Technology*, 25(5):1269–1275, 2007. doi: 10.1109/JLT.2007.893025.

[16] Tatsuhiko Fukazawa, Fumiaki Ohno, and Toshihiko Baba. Very compact arrayed-waveguide-grating demultiplexer using Si photonic wire waveguides. *Japanese Journal of Applied Physics*, 43(5B):L673, 2004. ISSN 0021-4922. doi: 10.1143/jjap.43.l673.

[17] K. Sasaki, F. Ohno, A. Motegi, and T. Baba. Arrayed waveguide grating of 70×60 [micro sign]m2 size based on Si photonic wire waveguides. *Electronics Letters*, 41(14):801–801, 2005. doi: 10.1049/el:20051541.

[18] F. Horst, W.M.J. Green, B.J. Offrein, and Y.A. Vlasov. Silicon-on-insulator echelle grating WDM demultiplexers with two stigmatic points. *IEEE Photonics Technology Letters*, 21(23):1743–1745, December 2009. ISSN 1941-0174. doi: 10.1109/lpt.2009.2032151.

[19] Ahmed Abumazwed, Sujith Chandran, Yusheng Bian, Won Suk Lee, Jessica Zhang, Dan Deptuck, Michal Rakowski, Andy Stricker, Jae Gon Lee, and Ted Letavic. Compact echelle grating filter for monolithic silicon photonics. In *CLEO 2023*, CLEO SI, page SF1O.4. Optica Publishing Group, 2023. doi: 10.1364/cleo_si.2023.sf1o.4.

[20] Hongnan Xu, Daoxin Dai, and Yaocheng Shi. Low-crosstalk and fabrication-tolerant four-channel CWDM filter based on dispersion-engineered Mach-Zehnder interferometers. *Optics Express*, 29(13):20617–20631, June 2021. ISSN 1094-4087. doi: 10.1364/OE.428352. URL https://opg.optica.org/oe/abstract.cfm?uri=oe-29-13-20617. Publisher: Optica Publishing Group.

[21] Tzu-Hsiang Yen and Yung-Jr Hung. Fabrication-Tolerant CWDM (de)Multiplexer Based on Cascaded Mach–Zehnder Interferometers on Silicon-on-Insulator. *Journal of Lightwave Technology*, 39(1):146–153, January 2021. ISSN 1558-2213. doi: 10.1109/JLT.2020.3026314. Conference Name: Journal of Lightwave Technology.

[22] S. Pathak, P. Dumon, D. Van Thourhout, and W. Bogaerts. Comparison of AWGs and echelle gratings for wavelength division multiplexing on silicon-on-insulator. *IEEE Photonics Journal*, 6(5):1–9, October 2014. ISSN 1943-0655. doi: 10.1109/jphot.2014.2361658.

[23] Seok-Hwan Jeong and Yu Tanaka. Silicon-wire optical demultiplexers based on multistage delayed mach–zehnder interferometers for higher production yield. *Applied Optics*, 57(22):6474, July 2018. ISSN 2155-3165. doi: 10.1364/ao.57.006474.

[24] Sarvagya Dwivedi, Herbert D'heer, and Wim Bogaerts. Maximizing fabrication and thermal tolerances of all-silicon FIR wavelength filters. *IEEE Photonics Technology Letters*, 27(8):871–874, April 2015. ISSN 1941-0174. doi: 10.1109/lpt.2015.2398464.

[25] Seok-Hwan Jeong, Tsuyoshi Horikawa, and Takahiro Nakamura. Phase behaviors for silicon-wire multistage delayed interferometric WDM filters across a whole 300-mm silicon-on-insulator wafer. *Journal of the Optical Society of America B*, 37(6):1847, May 2020. ISSN 1520-8540. doi: 10.1364/josab.385978.

7

Conclusions

7.1 Summary of Key Contributions

This PhD thesis addresses several challenges in wavelength division multiplexing (WDM) systems, with a primary focus on Mach-Zehnder Interferometer (MZI) based WDM architectures due to their ease of integration, high performance, low loss, and relatively compact footprint. Broadband optical splitters (and couplers) are critical components in various WDM architectures, particularly in MZI-based systems. These splitters are used multiple times throughout the WDM circuit, making their optimization crucial, as any performance limitations (e.g., loss, wavelength dependence, large footprint) can scale up significantly.

Two types of broadband splitters are demonstrated in this thesis: broadband bent directional couplers (DCs) and adiabatic couplers. Broadband bent DCs have been experimentally validated with high-performance specifications, including low coupling variation, low insertion loss, compact footprint, and support for arbitrary coupling ratios. Adiabatic couplers, on the other hand, have numerically demonstrated even lower coupling variation over a wider wavelength range, with an ultra-compact footprint (the smallest reported taper length to my best knowledge) and low loss based on a novel design approach. These adiabatic couplers have been included in two tapeouts and are currently under fabrication.

Building on the broadband bent DCs, several WDM architectures have been demonstrated, including dense WDM (DWDM) interleavers, coarse WDM (CWDM) filters, and a high-density DWDM system with 128 channels at 100 GHz spacing, which is currently under fabrication. The DWDM interleavers have been experimentally shown to achieve extended operational bandwidth while maintaining high channel isolation and low insertion loss. Furthermore, CWDM filters with reduced phase error compared to traditional MZI structures have been demonstrated. These CWDM filters exhibit high channel isolation, low loss, and a wide operational wavelength range. Their robustness has been validated across the wafer, with the CWDM-4 system demonstrating high performance even within a 100 GHz range around each channel's central wavelength. This robustness highlights their ability to operate without thermal tuning.

Quantitatively, the key contributions of this thesis can be summarized as follows:

1. **Broadband Bent Directional Couplers:** Developed and experimentally validated bent DCs that achieve a record-low coupling variation of 0.051 over an 80 nm wavelength range (7.67$\times$ improvement over straight DCs) with the lowest reported insertion loss (0.006 $\pm$ 0.004 dB) among all silicon 2$\times$2 splitters, limited by measurement precision. Formulated a comprehensive analytical model based on coupled-mode theory that explains the enhanced broadband behavior and enables systematic design of arbitrary coupling ratios.

2. **Ultra-Compact Adiabatic Couplers:** Introduced a minmax optimization strategy for adiabatic couplers that achieves minimal coupling variation (0.02 over 120 nm wavelength range) while reducing taper length to just 1.44 μm, orders of magnitude shorter than conventional designs that typically extend to hundreds of micrometers.

3. **High-Performance DWDM Systems:** Demonstrated DWDM interleavers with extended operational bandwidth (2.7$\times$ increase to 100 nm) while maintaining high extinction ratios ($\geq$ 18.4 dB). Showed transfer matrix calculations of more complex DWDM systems highlighting improved performance of bent DC-based designs, with significant enhancements in channel isolation and insertion loss.

4. **CWDM Systems with Reduced Phase Errors:** Successfully implemented CWDM systems (CWDM-2$\times$3.2 THz, CWDM-2$\times$6.4 THz, and CWDM-4$\times$3.2 THz) that operate without thermal tuning by incorporating MZI structures with reduced phase errors, including half-ring configurations and 120° whispering-gallery-mode bends. These systems achieved extinction ratio improvements from 6.6-8.1 dB to 16.4-18.3 dB.

5. **DWDM-128×100 GHz system:** Designed a high-density DWDM system with 128 channels at 100 GHz spacing, integrating the developed broadband bent DCs, DWDM-4 interleavers, and CWDM-4 filters in a hierarchical architecture. The system has been taped out and is currently under fabrication.

7.2 Perspectives

The contributions in this thesis represent a significant leap forward in silicon photonics and optical communications, enabling higher-capacity optical networks with enhanced signal integrity to meet the growing bandwidth demands of data centers and long-haul communications. The energy-efficient architectures, with minimized phase errors, substantially reduce the need for thermal tuning, providing sustainable solutions that lower operational costs. Moreover, the robust, fabrication-tolerant designs validated across 300 mm wafers underscore their maturity and readiness for industrial deployment in next-generation optical systems.

Building on this thesis, future research could explore athermal design approaches to mitigate temperature sensitivity in silicon photonic WDM filters. Scaling to higher channel counts, such as 256 or 512 channels with narrower spacing (e.g., 50 GHz), could push spectral efficiency while aiming for a high channel isolation. Aligning WDM filters with Multi-Source Agreement (MSA) grids would ensure compatibility with industry standards, facilitating seamless integration with existing optical communication infrastructure. Implementing the proposed adiabatic couplers in WDM designs and investigating higher-order broadband corrections, such as bent couplers with varying cross section along the bend, could further enhance device performance and operational bandwidth. Furthermore, it could be worthwhile to explore the optimization of the ring resonators with the introduction of broadband coupling in the bus-ring coupling sections.

A Appendix

A.1 Coupled Mode Theory

Coupled Mode Theory (CMT) provides a robust analytical framework for modeling the interaction of optical modes in waveguide structures. It offers a mathematically elegant approach to analyze mode coupling phenomena in integrated photonics, enabling precise predictions of coupling strength, power transfer dynamics, and phase-matching conditions. CMT is particularly indispensable for the design and optimization of directional couplers (DCs) and other photonic devices where mode interactions play a pivotal role.

The core principle of CMT is that when optical waveguides are brought into close proximity, their electromagnetic field distributions overlap, facilitating energy transfer between guided modes. This interaction is governed by a set of coupled differential equations that describe the evolution of mode amplitudes along the propagation direction. Solving these equations yields critical parameters such as coupling length, maximum coupling efficiency, and the conditions for phase matching.

To build a comprehensive understanding of coupled waveguides, as in the case of a DC, we will begin with simple scenarios and progressively increase the complexity until we reach the full analysis of directional couplers.

It is worth noting that the CMT analysis is largely based on [1].

Unperturbed Waveguide Modes

In the absence of perturbations and losses, the electric and magnetic fields of a guided mode at angular frequency ω in a single waveguide can be expressed in the form:

$$\mathbf{E}_\nu(\mathbf{r}) = \mathcal{E}_\nu(x,y)\exp(\mathrm{i}\beta_\nu z), \tag{A.1}$$

$$\mathbf{H}_\nu(\mathbf{r}) = \mathcal{H}_\nu(x,y)\exp(\mathrm{i}\beta_\nu z), \tag{A.2}$$

where ν denotes the mode index, $\mathcal{E}_\nu(x,y)$ and $\mathcal{H}_\nu(x,y)$ represent the transverse electric and magnetic field profiles respectively, and β_ν is the propagation constant of the ν-th mode. These field distributions satisfy Maxwell's equations for the unperturbed waveguide geometry.

A waveguide supports a finite number of guided modes and an infinite number of radiation modes, collectively forming a complete orthogonal basis set. Guided modes are confined within the waveguide core, carrying power along the propagation direction with minimal attenuation. Radiation modes, conversely, are not confined and represent fields that propagate away from the waveguide, resulting in power loss [2].

Under normal conditions, the modes of an individual waveguide are mutually orthogonal, meaning there is no energy exchange between different modes as they propagate. This orthogonality can be expressed mathematically as:

$$\int_{-\infty}^{\infty}\int_{-\infty}^{\infty}(\mathcal{E}_\nu \times \mathcal{H}_\mu^* - \mathcal{E}_\mu^* \times \mathcal{H}_\nu)\cdot\hat{\mathbf{z}}\,\mathrm{d}x\,\mathrm{d}y = N_\nu\delta_{\nu\mu}, \tag{A.3}$$

where $\delta_{\nu\mu}$ is the Kronecker delta function (equal to 1 when $\nu = \mu$ and 0 otherwise), and N_ν is a normalization factor.

The total electromagnetic field within an unperturbed waveguide can be represented as a linear superposition of all supported modes:

$$\mathbf{E}(\mathbf{r}) = \sum_\nu A_\nu\hat{\mathcal{E}}_\nu(x,y)\exp(\mathrm{i}\beta_\nu z), \tag{A.4}$$

$$\mathbf{H}(\mathbf{r}) = \sum_{\nu} A_\nu \hat{\mathcal{H}}_\nu(x, y) \exp(\mathrm{i}\beta_\nu z), \tag{A.5}$$

where $\mathbf{E}(\mathbf{r})$ and $\mathbf{H}(\mathbf{r})$ represent the total electric and magnetic fields respectively. The summation includes all supported modes: both guided and radiation modes. Here, A_ν denotes the amplitude coefficient of the ν-th mode, while $\hat{\mathcal{E}}_\nu(x, y)$ and $\hat{\mathcal{H}}_\nu(x, y)$ are the normalized electric and magnetic field distributions of that mode.

Importantly, in an unperturbed waveguide, the amplitudes A_ν remain constant along the propagation direction (independent of z), reflecting the fact that modes propagate without coupling in the absence of perturbations.

Perturbation and Mode Coupling

When a spatial perturbation is introduced into a waveguide system, such as an adjacent waveguide or a localized change in refractive index, the orthogonality of the original waveguide modes is broken. This perturbation enables energy exchange between modes that would otherwise propagate independently.

The perturbation can be represented as a modification to the permittivity distribution $\epsilon(\mathbf{r})$ of the original waveguide:

$$\epsilon_{\text{perturbed}}(\mathbf{r}) = \epsilon_{\text{unperturbed}}(\mathbf{r}) + \Delta\epsilon(\mathbf{r}), \tag{A.6}$$

where $\Delta\epsilon(\mathbf{r})$ is the spatial perturbation in permittivity.

As a result of this coupling, the mode amplitudes become functions of the propagation coordinate z, i.e., $A_\nu \to A_\nu(z)$ in order to mathematically capture the fact that there exists now power transfer between modes as they propagate in z. The total electromagnetic fields in the perturbed system are therefore expressed as:

$$\mathbf{E}(\mathbf{r}) = \sum_{\nu} A_\nu(z) \hat{\mathcal{E}}_\nu(x, y) \exp\left(\mathrm{i}\beta_\nu z\right), \tag{A.7}$$

$$\mathbf{H}(\mathbf{r}) = \sum_{\nu} A_\nu(z) \hat{\mathcal{H}}_\nu(x, y) \exp\left(\mathrm{i}\beta_\nu z\right). \tag{A.8}$$

It is important to note that in CMT, we continue to use the unperturbed waveguide modes as our basis set, but we now allow their amplitudes to vary with z. This is a key approximation that makes the theory tractable while maintaining sufficient

accuracy for most practical applications. The validity of this approximation improves when the perturbation is relatively weak, allowing the original mode profiles to remain largely unchanged [2].

Our goal is to derive a set of differential equations governing the evolution of these z-dependent amplitudes $A_\nu(z)$. These coupled-mode equations provide the mathematical framework for analyzing how energy transfers between modes as they propagate through the perturbed region.

Single Waveguide Coupling

To derive the coupled mode equations for a perturbed waveguide, we begin with Maxwell's equations. When a perturbation is present, it can be represented as a change in the polarization field $\Delta\mathbf{P}(\mathbf{r})$. The modified Maxwell's equations then take the form:

$$\nabla \times \mathbf{E} = -\frac{\partial \mathbf{B}}{\partial t} = \mathrm{i}\omega\mu_0\mathbf{H}, \tag{A.9}$$

$$\nabla \times \mathbf{H} = \frac{\partial \mathbf{D}}{\partial t} + \frac{\partial \Delta\mathbf{P}}{\partial t} = -\mathrm{i}\omega\epsilon\mathbf{E} - \mathrm{i}\omega\Delta\mathbf{P}. \tag{A.10}$$

Equations (A.9) and (A.10) together form our starting point, with the perturbation represented by the additional term $-\mathrm{i}\omega\Delta\mathbf{P}$ in the second equation.

We now employ the Lorentz reciprocity theorem, which relates two sets of electromagnetic fields that satisfy Maxwell's equations in the same region but with potentially different sources. For any two such field sets, denoted by subscripts 1 and 2, the following relationship holds for time-harmonic fields:

$$\nabla \cdot (\mathbf{E}_1 \times \mathbf{H}_2^* - \mathbf{E}_2^* \times \mathbf{H}_1) = -\mathrm{i}\omega \left(\mathbf{E}_1 \cdot \Delta\mathbf{P}_2^* - \mathbf{E}_2^* \cdot \Delta\mathbf{P}_1\right). \tag{A.11}$$

For our analysis, let $\mathbf{E}_1$ and $\mathbf{H}_1$ represent the fields in the perturbed system, while $\mathbf{E}_2$ and $\mathbf{H}_2$ represent the fields of an unperturbed mode. Since the unperturbed mode has no perturbation polarization, $\Delta\mathbf{P}_2 = 0$, and we can simplify Eq. (A.11) to:

$$\nabla \cdot (\mathbf{E}_1 \times \mathbf{H}_2^* - \mathbf{E}_2^* \times \mathbf{H}_1) = \mathrm{i}\omega \left(\mathbf{E}_2^* \cdot \Delta\mathbf{P}_1\right), \tag{A.12}$$

The left side of Eq. (A.12) involves the divergence of a vector field. In a waveguide geometry where we're primarily interested in the variation along the propagation

direction z, we integrate both sides of this equation over the transverse (x,y) plane and apply the divergence definition to the left side:

$$\int_{-\infty}^{\infty}\int_{-\infty}^{\infty} \nabla \cdot (\mathbf{E}_1 \times \mathbf{H}_2^* - \mathbf{E}_2^* \times \mathbf{H}_1)\, \mathrm{d}x\, \mathrm{d}y = \frac{\mathrm{d}}{\mathrm{d}z}\int_{-\infty}^{\infty}\int_{-\infty}^{\infty} (\mathbf{E}_1 \times \mathbf{H}_2^* - \mathbf{E}_2^* \times \mathbf{H}_1) \cdot \hat{\mathbf{z}}\, \mathrm{d}x\, \mathrm{d}y, \quad \text{(A.13)}$$

$$\frac{\mathrm{d}}{\mathrm{d}z}\int_{-\infty}^{\infty}\int_{-\infty}^{\infty} (\mathbf{E}_1 \times \mathbf{H}_2^* - \mathbf{E}_2^* \times \mathbf{H}_1) \cdot \hat{\mathbf{z}}\, \mathrm{d}x\, \mathrm{d}y = \mathrm{i}\omega \int_{-\infty}^{\infty}\int_{-\infty}^{\infty} \mathbf{E}_2^* \cdot \Delta\mathbf{P}_1\, \mathrm{d}x\, \mathrm{d}y, \quad \text{(A.14)}$$

We now substitute the field expansions from Eqs. (A.7) and (A.8) for the perturbed fields $\mathbf{E}_1$ and $\mathbf{H}_1$, and an unperturbed mode from Eqs. (A.1) and (A.2) for $\mathbf{E}_2$ and $\mathbf{H}_2$ into Eq. (A.14). Using the mode index μ for this unperturbed mode, we obtain:

$$\sum_{\nu} \frac{\mathrm{d}}{\mathrm{d}z} A_\nu(z) \mathrm{e}^{\mathrm{i}(\beta_\nu - \beta_\mu)z} \int_{-\infty}^{\infty}\int_{-\infty}^{\infty} \left(\hat{\mathcal{E}}_\nu \times \hat{\mathcal{H}}_\mu^* - \hat{\mathcal{E}}_\mu^* \times \hat{\mathcal{H}}_\nu\right) \cdot \hat{\mathbf{z}}\, \mathrm{d}x\, \mathrm{d}y = \mathrm{i}\omega \mathrm{e}^{-\mathrm{i}\beta_\mu z} \int_{-\infty}^{\infty}\int_{-\infty}^{\infty} \hat{\mathcal{E}}_\mu^* \cdot \Delta\mathbf{P}_1\, \mathrm{d}x\, \mathrm{d}y. \quad \text{(A.15)}$$

The integral in the left-hand side of Eq. (A.15) represents the inner product between the ν-th and μ-th modes. For orthogonal modes, this integral evaluates to zero when $\nu \neq \mu$ and to a non-zero constant when $\nu = \mu$. Using the orthonormality relationship:

$$\int_{-\infty}^{\infty}\int_{-\infty}^{\infty} \left(\hat{\mathcal{E}}_\nu \times \hat{\mathcal{H}}_\mu^* - \hat{\mathcal{E}}_\mu^* \times \hat{\mathcal{H}}_\nu\right) \cdot \hat{\mathbf{z}}\, \mathrm{d}x\, \mathrm{d}y = \delta_{\nu\mu}, \quad \text{(A.16)}$$

The left-hand side of Eq. (A.15) simplifies, leaving only the term where $\nu = \mu$:

$$\frac{\mathrm{d}A_\mu}{\mathrm{d}z} = \mathrm{i}\omega \mathrm{e}^{-\mathrm{i}\beta_\mu z} \int_{-\infty}^{\infty}\int_{-\infty}^{\infty} \hat{\mathcal{E}}_\mu^* \cdot \Delta\mathbf{P}_1\, \mathrm{d}x\, \mathrm{d}y. \quad \text{(A.17)}$$

Note that for backward-propagating modes ($\beta_\mu < 0$), the sign of the left-hand side changes resulting in:

$$\pm\frac{\mathrm{d}A_\mu}{\mathrm{d}z} = \mathrm{i}\omega \mathrm{e}^{-\mathrm{i}\beta_\mu z} \int_{-\infty}^{\infty}\int_{-\infty}^{\infty} \hat{\mathcal{E}}_\mu^* \cdot \Delta\mathbf{P}_1 \,\mathrm{d}x\,\mathrm{d}y, \tag{A.18}$$

where the plus sign applies to forward-propagating modes ($\beta_\mu > 0$) and the minus sign to backward-propagating modes ($\beta_\mu < 0$).

For many practical cases, the perturbation polarization can be represented in terms of a change in permittivity:

$$\Delta\mathbf{P}_1 = \Delta\epsilon\mathbf{E}_1 = \Delta\epsilon \sum_\nu A_\nu(z)\hat{\mathcal{E}}_\nu(x,y)\exp(\mathrm{i}\beta_\nu z), \tag{A.19}$$

where $\Delta\epsilon$ represents the spatial variation in permittivity due to the perturbation. Substituting this expression into Eq. (A.18), and for simplicity considering only forward-propagating modes, we obtain:

$$\frac{\mathrm{d}A_\mu}{\mathrm{d}z} = \mathrm{i}\omega \mathrm{e}^{-\mathrm{i}\beta_\mu z} \int_{-\infty}^{\infty}\int_{-\infty}^{\infty} \hat{\mathcal{E}}_\mu^* \cdot \Delta\epsilon \sum_\nu A_\nu(z)\hat{\mathcal{E}}_\nu(x,y)\exp(\mathrm{i}\beta_\nu z)\,\mathrm{d}x\,\mathrm{d}y. \tag{A.20}$$

By rearranging the terms in Eq. (A.20), we can move the summation outside the integral:

$$\frac{\mathrm{d}A_\mu}{\mathrm{d}z} = \sum_\nu \mathrm{i}\omega A_\nu(z)\mathrm{e}^{\mathrm{i}(\beta_\nu-\beta_\mu)z} \int_{-\infty}^{\infty}\int_{-\infty}^{\infty} \Delta\epsilon\hat{\mathcal{E}}_\mu^* \cdot \hat{\mathcal{E}}_\nu \,\mathrm{d}x\,\mathrm{d}y. \tag{A.21}$$

The integral in Eq. (A.21) quantifies the coupling strength between modes μ and ν due to the perturbation $\Delta\epsilon$. This motivates the definition of the coupling coefficient $\kappa_{\mu\nu}$:

$$\kappa_{\mu\nu} = \omega \int_{-\infty}^{\infty}\int_{-\infty}^{\infty} \Delta\epsilon\hat{\mathcal{E}}_\mu^* \cdot \hat{\mathcal{E}}_\nu \,\mathrm{d}x\,\mathrm{d}y. \tag{A.22}$$

It is worth mentioning that based on Eq. (A.22), $\kappa_{\mu\nu} = \kappa_{\nu\mu}^*$ in a lossless waveguide.

With this definition, the coupled mode equation takes a more elegant form:

$$\frac{\mathrm{d}A_\mu}{\mathrm{d}z} = \sum_\nu \mathrm{i}\kappa_{\mu\nu}A_\nu(z)\mathrm{e}^{\mathrm{i}(\beta_\nu-\beta_\mu)z}. \tag{A.23}$$

More generally, accounting for both forward and backward propagating modes:

$$\pm\frac{\mathrm{d}A_\mu}{\mathrm{d}z} = \sum_\nu \mathrm{i}\kappa_{\mu\nu}A_\nu(z)\mathrm{e}^{\mathrm{i}(\beta_\nu-\beta_\mu)z}, \tag{A.24}$$

The coupling coefficient $\kappa_{\mu\nu}$ has several important physical interpretations:

1. **Overlap Integral:** The magnitude of $\kappa_{\mu\nu}$ depends on the spatial overlap between the electric field profiles of modes μ and ν, weighted by the perturbation $\Delta\epsilon$, as per Eq. (A.22). Stronger overlap leads to stronger coupling.
2. **Phase-Matching Term:** The exponential factor $\mathrm{e}^{\mathrm{i}(\beta_\nu-\beta_\mu)z}$ in Eq. (A.23) represents a phase-matching condition. Efficient coupling occurs when $\beta_\nu \approx \beta_\mu$, as the exponential term oscillates slowly, allowing cumulative energy transfer over long distances.
3. **Perturbation Strength:** The magnitude of $\kappa_{\mu\nu}$ scales with the perturbation strength $\Delta\epsilon$. In the limit of vanishing perturbation, the coupling coefficients approach zero, and the modes propagate independently.

Equation (A.23) forms the foundation of CMT. It describes how the amplitude of each mode evolves due to coupling with all other modes in the system. The summation extends over all modes that might couple with mode μ, although in practice, only a few modes with similar propagation constants contribute significantly to the coupling.

Multiple Waveguide Coupling

The analysis of optical structures with multiple waveguides presents additional complexity compared to single waveguide systems. Two fundamentally different approaches can be employed to analyze such a system:

1. **Rigorous Electromagnetic Approach:** Solve Maxwell's equations for the entire multi-waveguide structure as a unified system. This yields exact eigenmodes (often called supermodes) of the composite structure, accounting for all interactions between waveguides inherently. While mathematically precise, this approach becomes computationally intensive for complex geometries and provides less intuitive insight into the physics of coupling.
2. **CMT Approach:** Solve for the modes of each individual isolated waveguide separately, then apply perturbation theory to account for the coupling between adjacent waveguides. This approach is more computationally efficient

and provides clearer physical insight into mode coupling phenomena and particularly interesting for DCs. However, it is approximate and assumes that the presence of neighboring waveguides constitutes a relatively weak perturbation to each waveguide.

In the CMT approach, we first solve for the normal modes of each individual waveguide in isolation. We then treat the presence of other waveguides as perturbations to each waveguide. From the perspective of any single waveguide, the perturbation in permittivity ($\Delta\epsilon$) arises from the presence of adjacent waveguides.

When applying the coupled mode formalism derived earlier, a critical distinction arises in multiple waveguide systems: the modes of different waveguides are not automatically orthogonal to each other, even in the absence of a perturbation. This non-orthogonality leads to more complex coupling dynamics.

In a multi-waveguide system, the coupling coefficients derived in Eq. (A.22) need modification to account for the non-orthogonality between modes of different waveguides. The modified coupling coefficient $\kappa_{\nu\mu}$ is expressed as:

$$\kappa_{\nu\mu} = c_{\nu\nu} \left[\mathbf{c}^{-1} \cdot \tilde{\kappa}\right]_{\nu\mu}, \tag{A.25}$$

where the index pairs (ν, μ) now refer to specific modes in specific waveguides. Here, $\mathbf{c}$ is the mode overlap matrix and $\tilde{\kappa}$ is the matrix of uncorrected coupling coefficients computed from the overlap integrals.

For forward-propagating modes, $c_{\nu\nu} = +1$, and the elements of matrices $\mathbf{c}$ and $\tilde{\kappa}$ are given by:

$$c_{\nu\mu} = \int_{-\infty}^{\infty}\int_{-\infty}^{\infty} \left(\hat{\mathcal{E}}_\nu^* \times \hat{\mathcal{H}}_\mu - \hat{\mathcal{E}}_\mu \times \hat{\mathcal{H}}_\nu^*\right) \cdot \hat{\mathbf{z}}\, \mathrm{d}x\, \mathrm{d}y = c_{\mu\nu}^*, \tag{A.26}$$

$$\tilde{\kappa}_{\nu\mu} = \omega \int_{-\infty}^{\infty}\int_{-\infty}^{\infty} \hat{\mathcal{E}}_\nu^* \cdot \Delta\epsilon_\mu \cdot \hat{\mathcal{E}}_\mu\, \mathrm{d}x\, \mathrm{d}y, \tag{A.27}$$

where $\Delta\epsilon_\mu$ is the permittivity perturbation from the perspective of the mode μ.

The overlap coefficient $c_{\nu\mu}$ quantifies the overlap between the fields of modes ν and μ from potentially different waveguides. Several important properties of these coefficients should be noted:

1. **Normalization:** The fields used in Eq. (A.26) are normalized such that $|c_{\nu\mu|} \leq 1$ for all mode pairs.

2. **Self-overlap:** For a properly normalized mode, $c_{\nu\nu} = \pm 1$, with the positive sign for forward-propagating modes and the negative sign for backward-propagating modes.
3. **Non-orthogonality:** Unlike modes within a single waveguide, modes of different waveguides are not necessarily orthogonal, meaning $c_{\nu\mu} \neq 0$ for $\nu \neq \mu$. The degree of non-orthogonality depends on the spatial separation and the degree of modal confinement.
4. **Phase-matched coupling:** Symmetric and efficient coupling occurs primarily when the two interacting modes have nearly identical propagation constants ($\beta_\nu \approx \beta_\mu$).
5. **Identical waveguides:** For geometrically identical waveguides, symmetric coupling occurs between corresponding modes (e.g., the fundamental mode of one waveguide couples most strongly to the fundamental mode of the other).

Using the reciprocity theorem, an important relationship exists between the coupling coefficients and propagation constants:

$$\tilde{\kappa}_{\nu\mu} - \tilde{\kappa}^*_{\mu\nu} = \frac{c_{\nu\mu} + c^*_{\mu\nu}}{2}(\beta_\nu - \beta_\mu) = c_{\nu\mu}(\beta_\nu - \beta_\mu), \tag{A.28}$$

where we've used the property that $c_{\nu\mu} = c^*_{\mu\nu}$, as per Eq. (A.26), which follows from the Hermitian symmetry of the overlap integral between electromagnetic field modes. This Hermitian property ensures that the mathematical formulation preserves power conservation in the physical system.

This relationship has several important implications:

1. Symmetric coupling ($\kappa_{\nu\mu} = \kappa^*_{\mu\nu}$) occurs only when $\beta_\nu = \beta_\mu$ (phase matching) or when $c_{\nu\mu} = c^*_{\mu\nu} = 0$ (no coupling). This is because normal modes in different waveguides are not necessarily orthogonal.
2. **Orthogonal Modes:** For single waveguide systems where modes are orthogonal, $c_{\nu\mu} = c^*_{\mu\nu} = 0$ for $\nu \neq \mu$, and Eq. (A.28) is automatically satisfied. This confirms that orthogonal modes within the same waveguide do not exchange energy in the absence of perturbations.
3. **Propagation-Coupling Relationship:** There exists an inherent relationship between coupling coefficients and propagation constants in multi-waveguide systems. This means that modifications to the waveguide geometry that affect propagation constants will also affect coupling coefficients, a crucial consideration in device design.

Two-Mode Coupling

Many practical integrated photonic devices, such as DCs, can be analyzed as two-mode coupling systems. In these systems, the interaction is predominantly between two specific modes, for example, the fundamental modes of two adjacent waveguides. The general CMT framework simplifies considerably in this case, allowing for analytical solutions that provide valuable design insights.

For a two-mode system with amplitudes A and B (representing, for instance, the amplitude of the fundamental mode in each of two coupled waveguides), the general coupled mode equation (Eq. (A.24)) reduces to:

$$\frac{\mathrm{d}A}{\mathrm{d}z} = \mathrm{i}\kappa_{aa}A + \mathrm{i}\kappa_{ab}B\mathrm{e}^{\mathrm{i}(\beta_b-\beta_a)z}, \tag{A.29}$$

$$\frac{\mathrm{d}B}{\mathrm{d}z} = \mathrm{i}\kappa_{bb}B + \mathrm{i}\kappa_{ba}A\mathrm{e}^{\mathrm{i}(\beta_a-\beta_b)z}. \tag{A.30}$$

Here, we assume forward-propagating modes for simplicity. The coefficients κ_{aa} and κ_{bb} represent self-coupling terms, while κ_{ab} and κ_{ba} represent cross-coupling between the two modes.

Using Eq. (A.25), these coupling coefficients can be expressed in terms of the overlap coefficients and uncorrected coupling coefficients:

$$\begin{aligned}
\kappa_{aa} &= \frac{\tilde{\kappa}_{aa} - c_{ab}\tilde{\kappa}_{ba}/c_{bb}}{1 - c_{ab}c_{ba}/(c_{aa}c_{bb})}, \\
\kappa_{ab} &= \frac{\tilde{\kappa}_{ab} - c_{ab}\tilde{\kappa}_{bb}/c_{bb}}{1 - c_{ab}c_{ba}/(c_{aa}c_{bb})}, \\
\kappa_{ba} &= \frac{\tilde{\kappa}_{ba} - c_{ba}\tilde{\kappa}_{aa}/c_{aa}}{1 - c_{ab}c_{ba}/(c_{aa}c_{bb})}, \\
\kappa_{bb} &= \frac{\tilde{\kappa}_{bb} - c_{ba}\tilde{\kappa}_{ab}/c_{aa}}{1 - c_{ab}c_{ba}/(c_{aa}c_{bb})}.
\end{aligned} \tag{A.31}$$

The self-coupling terms κ_{aa} and κ_{bb} arise from the fact that the presence of neighboring waveguides modifies the effective index profile experienced by each mode. Physically, these terms represent a perturbation-induced shift in the propagation constants.

To simplify the analysis, we can eliminate these self-coupling terms by defining modified mode amplitudes:

$$A(z) = \tilde{A}(z) \exp\left[\mathrm{i}\int_0^z \kappa_{aa}(z')\,\mathrm{d}z'\right], \tag{A.32}$$

$$B(z) = \tilde{B}(z) \exp\left[\mathrm{i}\int_0^z \kappa_{bb}(z')\,\mathrm{d}z'\right]. \tag{A.33}$$

Substituting these definitions into Eqs. (A.29) and (A.30) yields a simplified set of coupled equations:

$$\frac{\mathrm{d}\tilde{A}}{\mathrm{d}z} = \mathrm{i}\kappa_{ab}\tilde{B}\mathrm{e}^{\mathrm{i}2\delta z}, \tag{A.34}$$

$$\frac{\mathrm{d}\tilde{B}}{\mathrm{d}z} = \mathrm{i}\kappa_{ba}\tilde{A}\mathrm{e}^{-\mathrm{i}2\delta z}, \tag{A.35}$$

where the phase mismatch parameter δ is defined as:

$$2\delta = (\beta_b + \kappa_{bb}) - (\beta_a + \kappa_{aa})\,. \tag{A.36}$$

This parameter δ represents the effective phase mismatch between the two coupled modes, incorporating both the intrinsic propagation constant difference and the perturbation-induced shifts.

Several important observations can be made regarding two-mode coupling systems:

1. **Coupling Coefficient Dependence:** The coupling coefficients κ_{ab} and κ_{ba} are generally independent of z for uniform waveguide structures. However, if the waveguide geometry or the perturbation $\Delta\epsilon$ varies along z (as in tapered couplers or grating-assisted couplers), κ becomes a function of z. In such cases, analytical solutions to Eqs. (A.34) and (A.35) may not be possible, and numerical methods are required.

2. **Effective Propagation Constants:** The self-coupling terms modify the effective propagation constants of the modes. The adjusted propagation constants become $\beta_a' = \beta_a + \kappa_{aa}$ and $\beta_b' = \beta_b + \kappa_{bb}$.

3. **Phase Matching:** Efficient power transfer between modes requires near-phase-matching conditions, i.e., $\delta \approx 0$. The phase mismatch δ determines the efficiency of coupling, with maximum power transfer occurring only when $\delta = 0$. As $|\delta|$ increases, the maximum fraction of power that can be transferred decreases according to the relationship $P_{\text{max}}/P_{\text{in}} = \kappa^2/(\kappa^2 + \delta^2)$, where κ represents the coupling strength.

4. **Coupling Strength:** The magnitude of the coupling coefficients $|\kappa_{ab}|$ and $|\kappa_{ba}|$ determines the rate of power transfer between modes. These values depend on the waveguide geometry, separation distance, and refractive index contrast.

The simplified coupled mode equations (Eqs. (A.34) and (A.35)) form the foundation for analyzing DCs and other two-mode coupling devices in integrated photonics. Their analytical or numerical solutions provide critical design parameters such as coupling length and power transfer efficiency.

Co-directional Coupling

Optical coupling in waveguide systems can occur in two fundamental configurations: co-directional coupling, where both coupled modes propagate in the same direction, and contra-directional coupling, where the modes propagate in opposite directions. DCs, which are ubiquitous in integrated photonics, operate on the principle of co-directional coupling. We will focus on this configuration, which is most relevant for this thesis.

In co-directional coupling, both modes propagate in the forward direction with positive propagation constants ($\beta_a > 0$ and $\beta_b > 0$). The simplified coupled mode equations developed in the previous section become:

$$\frac{\mathrm{d}\tilde{A}}{\mathrm{d}z} = \mathrm{i}\kappa_{ab}\tilde{B}\mathrm{e}^{\mathrm{i}2\delta z}, \tag{A.37}$$

$$\frac{\mathrm{d}\tilde{B}}{\mathrm{d}z} = \mathrm{i}\kappa_{ba}\tilde{A}\mathrm{e}^{-\mathrm{i}2\delta z}, \tag{A.38}$$

where the phase mismatch parameter δ is defined as:

$$\delta = \frac{\beta_b' - \beta_a'}{2} = \frac{(\beta_b + \kappa_{bb}) - (\beta_a + \kappa_{aa})}{2}. \tag{A.39}$$

The coupled differential equations (Eqs. (A.37) and (A.38)) can be solved analytically as an initial-value problem. Given the amplitudes $\tilde{A}(z_0)$ and $\tilde{B}(z_0)$ at some position $z = z_0$, the solution at any other position z can be expressed in a concise matrix form:

$$\begin{bmatrix}\tilde{A}(z)\\ \tilde{B}(z)\end{bmatrix} = \mathbf{T}(z; z_0)\begin{bmatrix}\tilde{A}(z_0)\\ \tilde{B}(z_0)\end{bmatrix}, \tag{A.40}$$

where $\mathbf{T}(z; z_0)$ is a transfer matrix that describes the evolution of the mode amplitudes from z_0 to z. This matrix is given by:

$$\mathbf{T}(z; z_0) = \begin{bmatrix} T_{11} & T_{12} \\ T_{21} & T_{22} \end{bmatrix}, \tag{A.41}$$

with the individual elements defined as [1]:

$$T_{11} = \frac{\beta_\mathrm{c} \cos[\beta_\mathrm{c}(z - z_0)] - \mathrm{i}\delta \sin[\beta_\mathrm{c}(z - z_0)]}{\beta_\mathrm{c}} \mathrm{e}^{\mathrm{i}\delta(z - z_0)}, \tag{A.42}$$

$$T_{12} = \frac{\mathrm{i}\kappa_{ab}}{\beta_\mathrm{c}} \sin[\beta_\mathrm{c}(z - z_0)] \mathrm{e}^{\mathrm{i}\delta(z + z_0)}, \tag{A.43}$$

$$T_{21} = \frac{\mathrm{i}\kappa_{ba}}{\beta_\mathrm{c}} \sin[\beta_\mathrm{c}(z - z_0)] \mathrm{e}^{-\mathrm{i}\delta(z + z_0)}, \tag{A.44}$$

$$T_{22} = \frac{\beta_\mathrm{c} \cos[\beta_\mathrm{c}(z - z_0)] + \mathrm{i}\delta \sin[\beta_\mathrm{c}(z - z_0)]}{\beta_\mathrm{c}} \mathrm{e}^{-\mathrm{i}\delta(z - z_0)}. \tag{A.45}$$

Here, β_c is the effective coupling coefficient, defined as:

$$\beta_\mathrm{c} = \sqrt{\kappa_{ab}\kappa_{ba} + \delta^2}. \tag{A.46}$$

This parameter β_c determines the rate of power oscillation between the coupled modes. It incorporates both the direct coupling strength ($\kappa_{ab}\kappa_{ba}$) and the phase mismatch effect (δ^2).

To illustrate how the CMT describes the power transfer between waveguides, we consider a practical example where light is initially launched only into mode a at the input ($z = 0$). The initial conditions are thus $\tilde{A}(0) \neq 0$ and $\tilde{B}(0) = 0$.

By applying the aforementioned boundary conditions to the transfer matrix formalism in Eq. (A.40) and setting $z_0 = 0$ in Eqs. (A.42)–(A.45), we obtain the explicit solutions for the mode amplitudes:

$$\tilde{A}(z) = \tilde{A}(0) \left(\cos \beta_\mathrm{c} z - \frac{\mathrm{i}\delta}{\beta_\mathrm{c}} \sin \beta_\mathrm{c} z \right) e^{\mathrm{i}\delta z}, \tag{A.47}$$

$$\tilde{B}(z) = \tilde{A}(0) \left(\frac{\mathrm{i}\kappa_{ba}}{\beta_\mathrm{c}} \sin \beta_\mathrm{c} z \right) e^{-\mathrm{i}\delta z}. \tag{A.48}$$

The power distribution between the two modes as a function of propagation distance can be derived from these amplitude expressions. Using the relation $P \propto |A|^2$, we obtain:

$$\frac{P_a(z)}{P_a(0)} = \frac{|A(z)|^2}{|A(0)|^2} = \frac{|\tilde{A}(z)|^2}{|\tilde{A}(0)|^2} = \frac{\kappa_{ab}\kappa_{ba}}{\beta_c^2}\cos^2\beta_c z + \frac{\delta^2}{\beta_c^2}, \tag{A.49}$$

$$\frac{P_b(z)}{P_a(0)} = \frac{|B(z)|^2}{|A(0)|^2} = \frac{|\tilde{B}(z)|^2}{|\tilde{A}(0)|^2} = \frac{|\kappa_{ba}|^2}{\beta_c^2}\sin^2\beta_c z. \tag{A.50}$$

These equations reveal the oscillatory nature of power exchange between the coupled modes. Notably, when $\delta = 0$ (perfect phase matching), complete power transfer occurs periodically, while for $\delta \neq 0$, only a fraction of power can be transferred between the modes.

Building on the power evolution equations derived above, we can determine a parameter of central importance in DC design: the coupling length l_c. This represents the propagation distance required for complete power transfer from one waveguide to another under phase-matched conditions.

Using Eq. (A.50), we can quantify the coupling efficiency η for a waveguide of length l as the ratio of power transferred to the second waveguide to the input power in the first waveguide:

$$\eta = \frac{P_b(l)}{P_a(0)} = \frac{|\kappa_{ba}|^2}{\beta_c^2}\sin^2\beta_c l. \tag{A.51}$$

Thus, power is exchanged periodically between the two modes as the light propagates along the waveguides. The coupling length l_c is defined as the propagation distance at which maximum power transfer occurs:

$$l_c = \frac{\pi}{2\beta_c}. \tag{A.52}$$

This corresponds to the distance required for $\sin^2\beta_c l = 1$ in Eq. (A.51). Complete power transfer (100% coupling efficiency) occurs only under perfect phase-matching conditions ($\delta = 0$). When phase mismatch exists, the maximum power transfer is reduced.

Furthermore, Eq. (A.51) reveals the characteristic sinusoidal behavior of DCs. The coefficient $|\kappa_{ba}|^2/\beta_c^2$ quantifies the coupler's asymmetry (equal to unity for symmetric structures), while β_c determines the coupling strength. In practical implementations, an additional phase term ϕ can be included to account for contributions from input and output bend sections.

Supermode Formulation

While the coupled-mode theory previously developed provides valuable insights into the interactions between waveguide modes, an alternative and complementary approach is to examine DCs through the framework of supermodes. This approach transforms our understanding from interacting individual waveguide modes to a system of composite eigenmodes of the entire structure.

We begin by expressing the total electromagnetic field in terms of the previously derived solutions. The variation of field amplitudes in the two coupled waveguides as a function of propagation distance is given by Eqs. (A.47) and (A.48) for initial conditions $\tilde{A}(0) \neq 0$ and $\tilde{B}(0) = 0$. To obtain the complete field profile, we need to construct the total electromagnetic field by substituting the solutions for $\tilde{A}(z)$ and $\tilde{B}(z)$ into the original mode expansion. For a constant perturbation where $\Delta\epsilon$ is not a function of z, all coupling coefficients κ_{aa}, κ_{bb}, κ_{ab}, and κ_{ba} are constants independent of z. We can express the original mode amplitudes in terms of the transformed amplitudes as:

$$A(z) = \tilde{A}(z)e^{i\kappa_{aa}z}, \tag{A.53}$$

$$B(z) = \tilde{B}(z)e^{i\kappa_{bb}z}. \tag{A.54}$$

Substituting these expressions along with Eqs. (A.47) and (A.48) into the mode expansion from Eq. (A.7), the total electric field becomes:

$$\mathbf{E}(\mathbf{r}) = \tilde{A}(0)\left[\hat{\mathcal{E}}_a\Big(\cos\beta_c z - \frac{\mathrm{i}\delta}{\beta_c}\sin\beta_c z\Big)e^{\mathrm{i}(\beta_a+\kappa_{aa}+\delta)z} + \hat{\mathcal{E}}_b\frac{\mathrm{i}\kappa_{ba}}{\beta_c}\sin\beta_c z e^{\mathrm{i}(\beta_b+\kappa_{bb}-\delta)z}\right] \tag{A.55}$$

This expression can be mathematically reformulated by factoring out common terms and rearranging:

$$\mathbf{E}(\mathbf{r}) = \tilde{A}(0)\Bigg[\frac{(\beta_c - \delta)\hat{\mathcal{E}}_a + \kappa_{ba}\hat{\mathcal{E}}_b}{2\beta_c} e^{i(\bar{\beta}+\beta_c)z} + \frac{(\beta_c + \delta)\hat{\mathcal{E}}_a - \kappa_{ba}\hat{\mathcal{E}}_b}{2\beta_c} e^{i(\bar{\beta}-\beta_c)z}\Bigg] \tag{A.56}$$

where

$$\bar{\beta} = \frac{(\beta_a + \kappa_{aa}) + (\beta_b + \kappa_{bb})}{2} \tag{A.57}$$

represents the average propagation constant. This form reveals that the field can be expressed as a superposition of two independent modes:

$$\mathbf{E}(\mathbf{r}) = \tilde{A}(0)\Big[\mathcal{E}_1(x,y)e^{i\beta_1 z} + \mathcal{E}_2(x,y)e^{i\beta_2 z}\Big], \tag{A.58}$$

with the following definitions:

$$\mathcal{E}_1 = \frac{(\beta_c - \delta)\hat{\mathcal{E}}_a + \kappa_{ba}\hat{\mathcal{E}}_b}{2\beta_c}, \tag{A.59}$$

$$\mathcal{E}_2 = \frac{(\beta_c + \delta)\hat{\mathcal{E}}_a - \kappa_{ba}\hat{\mathcal{E}}_b}{2\beta_c}, \tag{A.60}$$

$$\beta_1 = \bar{\beta} + \beta_c, \quad \beta_2 = \bar{\beta} - \beta_c. \tag{A.61}$$

These field patterns $\mathcal{E}_1(x,y)$ and $\mathcal{E}_2(x,y)$ with propagation constants β_1 and β_2 are the true eigenmodes of the composite two-waveguide structure, known as supermodes. It's important to note that the expressions in Eqs. (A.59) and (A.60) are not normalized.

The characteristics of supermodes depend critically on the interplay between phase mismatch (δ) and coupling strength ($\kappa_{ab}\kappa_{ba}$). We can analyze this through several limiting cases:

Weak Coupling Regime ($\delta^2 \gg \kappa_{ab}\kappa_{ba}$): When the waveguides are significantly mismatched ($\delta > 0$), we find $\beta_c \approx \delta$. Consequently, $\beta_1 \approx \beta_b + \kappa_{bb}$ and $\beta_2 \approx \beta_a + \kappa_{aa}$. In this limit, Eqs. (A.59) and (A.60) simplify to:

$$\mathcal{E}_1 \to \frac{\kappa_{ba}}{2\delta}\hat{\mathcal{E}}_b \approx 0, \quad \mathcal{E}_2 \to \hat{\mathcal{E}}_a - \frac{\kappa_{ba}}{2\delta}\hat{\mathcal{E}}_b \approx \hat{\mathcal{E}}_a. \tag{A.62}$$

Physically, this means the supermodes essentially revert to the isolated waveguide modes. The total field becomes:

$$\mathbf{E}(\mathbf{r}) \approx \tilde{A}(0)\mathcal{E}_2 e^{i\beta_2 z} \approx \tilde{A}(0)\hat{\mathcal{E}}_a e^{i\beta_a z}, \tag{A.63}$$

indicating that with large phase mismatch, the waveguides are effectively decoupled. For $\delta < 0$, the same principle applies with indices interchanged.

Symmetric Coupler Case: For identical waveguides, $\beta_a = \beta_b$, $\kappa_{aa} = \kappa_{bb}$, $\kappa_{ab} = \kappa_{ba}^* \equiv \kappa$ (real and positive), and $\delta = 0$. The supermodes simplify to:

$$\mathcal{E}_1 = \frac{\hat{\mathcal{E}}_a + \hat{\mathcal{E}}_b}{2} \equiv \mathcal{E}_{\text{even}}, \tag{A.64}$$

$$\mathcal{E}_2 = \frac{\hat{\mathcal{E}}_a - \hat{\mathcal{E}}_b}{2} \equiv \mathcal{E}_{\text{odd}}, \tag{A.65}$$

with propagation constants:

$$\beta_1 = \bar{\beta} + \kappa \equiv \beta_{\text{even}}, \tag{A.66}$$

$$\beta_2 = \bar{\beta} - \kappa \equiv \beta_{\text{odd}}. \tag{A.67}$$

In this case, the coupling length reduces to:

$$l_c^{\text{PM}} = \frac{\pi}{\beta_{\text{even}} - \beta_{\text{odd}}} = \frac{\pi}{2\kappa}, \tag{A.68}$$

and complete power transfer occurs because of perfect phase matching. The even supermode exhibits a symmetric field distribution, while the odd supermode shows an antisymmetric pattern. For a coupler with fixed structural parameters, reducing the spacing between waveguides increases coupling strength and therefore decreases the coupling length.

Phase Retardation in DCs

A fundamental characteristic of symmetric DCs is the fixed phase relationship between the output ports. Specifically, when light is launched into one waveguide of a symmetric DC, there is always a $\pi/2$ (90°) phase difference between the

optical fields in the two waveguides at the output. This intrinsic phase relationship is of critical importance for many photonic applications, including optical interferometers.

To demonstrate this phase relationship, we start with the coupled mode equations for a symmetric DC. In a symmetric coupler, the waveguides are identical, meaning $\beta_a = \beta_b$, $\kappa_{aa} = \kappa_{bb}$, and the coupling coefficients are real with $\kappa_{ab} = \kappa_{ba} = \kappa$. Under these conditions, the phase mismatch parameter $\delta = 0$ from Eq. (A.36).

The coupled mode equations (Eqs. (A.37) and (A.38)) simplify to:

$$\frac{\mathrm{d}\tilde{A}}{\mathrm{d}z} = \mathrm{i}\kappa\tilde{B}, \tag{A.69}$$

$$\frac{\mathrm{d}\tilde{B}}{\mathrm{d}z} = \mathrm{i}\kappa\tilde{A}. \tag{A.70}$$

For the initial condition where light is launched only into waveguide a, we have $\tilde{A}(0) = A_0$ and $\tilde{B}(0) = 0$. Solving these differential equations yields:

$$\tilde{A}(z) = A_0 \cos(\kappa z), \tag{A.71}$$

$$\tilde{B}(z) = A_0 i \sin(\kappa z). \tag{A.72}$$

The key observation here is the presence of the imaginary unit i in the expression for $\tilde{B}(z)$. This imaginary factor represents a $\pi/2$ phase shift relative to $\tilde{A}(z)$. When power transfers from waveguide a to waveguide b, it acquires this additional phase.

Specifically, at the coupling length $z = l_c = \pi/(2\kappa)$ (where maximum power transfer occurs):

$$\tilde{A}(l_c) = A_0 \cos\left(\frac{\pi}{2}\right) = 0, \tag{A.73}$$

$$\tilde{B}(l_c) = A_0 i \sin\left(\frac{\pi}{2}\right) = A_0 i. \tag{A.74}$$

Thus, all power has transferred to waveguide b, and the field in waveguide b has a phase of $\pi/2$ relative to the input field in waveguide a.

The $\pi/2$ phase relationship can also be understood through the supermode formulation. Recall from Eqs. (A.65) that in a symmetric coupler, the supermodes are:

$$\mathcal{E}_{\text{even}} = \frac{\hat{\mathcal{E}}_a + \hat{\mathcal{E}}_b}{2}, \tag{A.75}$$

$$\mathcal{E}_{\text{odd}} = \frac{\hat{\mathcal{E}}_a - \hat{\mathcal{E}}_b}{2}. \tag{A.76}$$

When light is launched into waveguide a only, both supermodes are excited with equal amplitudes. As the light propagates, the supermodes accumulate different phases due to their different propagation constants:

$$\beta_{\text{even}} = \beta + \kappa, \tag{A.77}$$

$$\beta_{\text{odd}} = \beta - \kappa, \tag{A.78}$$

where $\beta = \beta_a = \beta_b$ is the propagation constant of the isolated waveguides. The total field at any point z can be expressed as:

$$\mathbf{E}(x, y, z) = \frac{A_0}{2}[\mathcal{E}_{\text{even}} e^{i\beta_{\text{even}} z} + \mathcal{E}_{\text{odd}} e^{i\beta_{\text{odd}} z}]. \tag{A.79}$$

Substituting the supermode field patterns and expanding:

$$\begin{aligned}
\mathbf{E}(x, y, z) &= \frac{A_0}{2}\left[\frac{\hat{\mathcal{E}}_a + \hat{\mathcal{E}}_b}{2} e^{i(\beta+\kappa)z} + \frac{\hat{\mathcal{E}}_a - \hat{\mathcal{E}}_b}{2} e^{i(\beta-\kappa)z}\right] \\
&= \frac{A_0}{4}\left[(\hat{\mathcal{E}}_a + \hat{\mathcal{E}}_b)e^{i(\beta+\kappa)z} + (\hat{\mathcal{E}}_a - \hat{\mathcal{E}}_b)e^{i(\beta-\kappa)z}\right] \\
&= \frac{A_0}{4} e^{i\beta z}\left[(\hat{\mathcal{E}}_a + \hat{\mathcal{E}}_b)e^{i\kappa z} + (\hat{\mathcal{E}}_a - \hat{\mathcal{E}}_b)e^{-i\kappa z}\right] \\
&= \frac{A_0}{2} e^{i\beta z}\left[\hat{\mathcal{E}}_a \cos(\kappa z) + \hat{\mathcal{E}}_b i \sin(\kappa z)\right].
\end{aligned} \tag{A.80}$$

This final form reveals that the amplitude in waveguide b has an additional factor of i compared to the amplitude in waveguide a, which represents the $\pi/2$ phase difference.

It's important to note that this fixed $\pi/2$ phase relationship holds only for symmetric DCs. In asymmetric couplers (including bent DCs), where the waveguides have different propagation constants ($\beta_a \neq \beta_b$), the phase relationship becomes more complex and depends on the degree of asymmetry through the phase mismatch parameter δ.

A.2 Mach-Zehnder Interferometer Analysis

Mach-Zehnder Interferometers (MZIs) are fundamental building blocks in integrated photonics, serving crucial roles in optical filters, switches, modulators, and sensing applications. This section presents a comprehensive analysis of MZIs using the transfer matrix method (TMM), which offers an elegant and efficient approach to modeling their behavior.

Transfer Matrix Analysis of Mach-Zehnder Interferometer

The transfer matrix method (TMM) provides a powerful analytical framework for modeling complex optical devices. For a Mach-Zehnder Interferometer, the TMM approach systematically accounts for all optical interactions within the device structure.

A standard MZI consists of two DCs separated by a phase-shifting section. The structure follows the sequence: DC – Phase Section – DC. Under the assumption of no intrinsic loss, the overall transfer matrix $\mathbf{S}$ is constructed by cascading the matrices of individual components:

$$\mathbf{S} = \mathbf{DC}_2 \cdot \mathbf{\Phi} \cdot \mathbf{DC}_1, \tag{A.81}$$

where $\mathbf{DC}_1$, $\mathbf{DC}_2$ represent the coupler matrices, and $\mathbf{\Phi}$ is the phase section matrix.

For a symmetric DC, the transfer matrix can be expressed as:

$$\mathbf{DC} = \begin{pmatrix} t & \mathrm{i}r \\ \mathrm{i}r & t \end{pmatrix}, \quad t = \sqrt{T}, \quad r = \sqrt{R}, \quad T + R \leq 1, \tag{A.82}$$

where t and r are the field transmission and coupling coefficients, respectively, and T and R are their corresponding power coefficients. The imaginary unit i in the off-diagonal elements represents the $\pi/2$ phase shift that naturally occurs in the cross coupled port in DCs, as established in the preceding section on CMT.

The phase shifting matrix, which characterizes the differential phase accumulation between the two arms, is given by:

$$\mathbf{\Phi} = \begin{pmatrix} e^{\mathrm{i}\phi_1} & 0 \\ 0 & e^{\mathrm{i}\phi_2} \end{pmatrix}, \tag{A.83}$$

where ϕ_1 and ϕ_2 represent the phase shifts in the upper and lower arms of the MZI, respectively.

Multiplying these matrices in sequence, we obtain the total transfer matrix $\mathbf{S}$ of the MZI:

$$\mathbf{S} = \begin{pmatrix} t & \mathrm{i}r \\ \mathrm{i}r & t \end{pmatrix} \begin{pmatrix} e^{\mathrm{i}\phi_1} & 0 \\ 0 & e^{\mathrm{i}\phi_2} \end{pmatrix} \begin{pmatrix} t & \mathrm{i}r \\ \mathrm{i}r & t \end{pmatrix}. \tag{A.84}$$

Performing the matrix multiplication and simplifying yields:

$$\mathbf{S} = \begin{pmatrix} t^2 e^{\mathrm{i}\phi_1} - r^2 e^{\mathrm{i}\phi_2} & \mathrm{i}rt(e^{\mathrm{i}\phi_1} + e^{\mathrm{i}\phi_2}) \\ \mathrm{i}rt(e^{\mathrm{i}\phi_1} + e^{\mathrm{i}\phi_2}) & t^2 e^{\mathrm{i}\phi_2} - r^2 e^{\mathrm{i}\phi_1} \end{pmatrix}. \tag{A.85}$$

To determine the optical power at each output port, we compute the magnitude squared of the matrix elements of $\mathbf{S}$. Defining $\Delta\phi = \phi_2 - \phi_1$ as the differential phase shift between the two arms, and assuming t and r are real values, we obtain:

$$|\mathbf{S}|^2 = \begin{pmatrix} t^4 + r^4 - 2t^2 r^2 \cos(\Delta\phi) & 4t^2 r^2 \cos^2(\Delta\phi/2) \\ 4t^2 r^2 \cos^2(\Delta\phi/2) & t^4 + r^4 - 2t^2 r^2 \cos(\Delta\phi) \end{pmatrix}. \tag{A.86}$$

The phase difference $\Delta\phi$ is a function of wavelength and can be expressed as:

$$\Delta\phi = \frac{2\pi}{\lambda} n_{\text{eff}}(\lambda) \Delta L + \Delta\phi_{\text{ext}}, \tag{A.87}$$

where:

- λ is the wavelength of light,
- ΔL is the physical path length difference between the arms,
- $n_{\text{eff}}(\lambda)$ is the effective refractive index of the waveguide mode, which can be determined via eigenmode simulations,
- $\Delta\phi_{\text{ext}}$ represents externally applied phase difference (e.g., through thermo-optic or electro-optic effects).

Power Transmission at Output Ports

The power transmission at the output ports of the Mach-Zehnder Interferometer can be derived directly from the transfer matrix elements. For light injected into the first input port, the transmission to the output ports is given by:

$$P_{\text{through}} = |S_{11}|^2 = t^4 + r^4 - 2t^2r^2\cos(\Delta\phi), \tag{A.88}$$

$$P_{\text{cross}} = |S_{21}|^2 = 4t^2r^2\cos^2\left(\frac{\Delta\phi}{2}\right), \tag{A.89}$$

where t and r are the field transmission and coupling coefficients of the DCs, respectively, with their corresponding power coefficients defined as:

$$T = |t|^2, \quad R = |r|^2, \quad T + R = 1 \text{ (for lossless couplers).} \tag{A.90}$$

Substituting these definitions into Eqs. (A.88) and (A.89):

$$P_{\text{through}} = T^2 + R^2 - 2TR\cos(\Delta\phi), \tag{A.91}$$

$$P_{\text{cross}} = 4TR\cos^2\left(\frac{\Delta\phi}{2}\right). \tag{A.92}$$

For a perfectly balanced MZI with 3 dB couplers ($T = R = 0.5$), these equations simplify to:

$$P_{\text{through}} = \sin^2\left(\frac{\Delta\phi}{2}\right), \tag{A.93}$$

$$P_{\text{cross}} = \cos^2\left(\frac{\Delta\phi}{2}\right). \tag{A.94}$$

These expressions reveal the complementary sinusoidal response of the two output ports, with power conservation ensuring that $P_{\text{through}} + P_{\text{cross}} = 1$ for a lossless device.

Extinction Ratio

The extinction ratio (ER) is a critical performance metric for optical devices in communication systems, defined as the ratio of maximum power (P_{max}) to minimum power (P_{min}) at an output port:

$$\text{ER} = \frac{P_{\text{max}}}{P_{\text{min}}}. \tag{A.95}$$

Using the transmission equations derived earlier, we can determine the extinction ratios for both the through and cross ports of an MZI.

For the through port, the maximum power occurs at $\Delta\phi = \pi$ and equals $(T + R)^2$, while the minimum power occurs at $\Delta\phi = 0$ and equals $(T - R)^2$. Thus, the extinction ratio is:

$$\text{ER}_{\text{through}} = \frac{(T + R)^2}{(T - R)^2}. \tag{A.96}$$

For the cross port, the maximum power occurs at $\Delta\phi = 0$ and equals $4TR$, while the minimum power occurs at $\Delta\phi = \pi$ and ideally equals zero:

$$\text{ER}_{\text{cross}} = \frac{4TR}{0} \to \infty \quad \text{(ideal case)}. \tag{A.97}$$

The extinction ratio is commonly expressed in decibels:

$$\text{ER}_{\text{through}}\ (\text{dB}) = 10 \cdot \log_{10}\left(\frac{(T + R)^2}{(T - R)^2}\right). \tag{A.98}$$

This analysis reveals a fundamental asymmetry between the two output ports of an MZI:

1. The through port exhibits a finite extinction ratio, which is maximized when $T = R = 0.5$ (perfect 3 dB couplers).
2. The cross port theoretically offers infinite extinction in an ideal MZI. However, in practice, fabrication imperfections, measurement precision, coupler imbalance, and optical losses result in a finite (usually large) value

The extinction ratio directly impacts the signal-to-noise ratio (SNR) and overall system performance in optical communication systems. Higher extinction ratios improve signal quality, reduce crosstalk between channels, and are particularly important for high-capacity wavelength-division multiplexing (WDM) systems.

Figure A.1 illustrates the extinction ratio of the through port of an MZI as a function of the DC's power coupling coefficient $\kappa^2 = R$ (assuming identical, lossless couplers at both ends of the MZI). The plot demonstrates that the ER reaches its theoretical maximum value (infinity) when $\kappa^2 = 0.5$, corresponding to perfect 3 dB couplers. Moreover, the ER remains greater than 14 dB for coupling coefficients between 0.4 and 0.6, indicating a reasonable window. This analysis highlights the

critical importance of designing broadband DCs with coupling coefficients close to 0.5 across the operating wavelength range to achieve high-performance MZI devices.

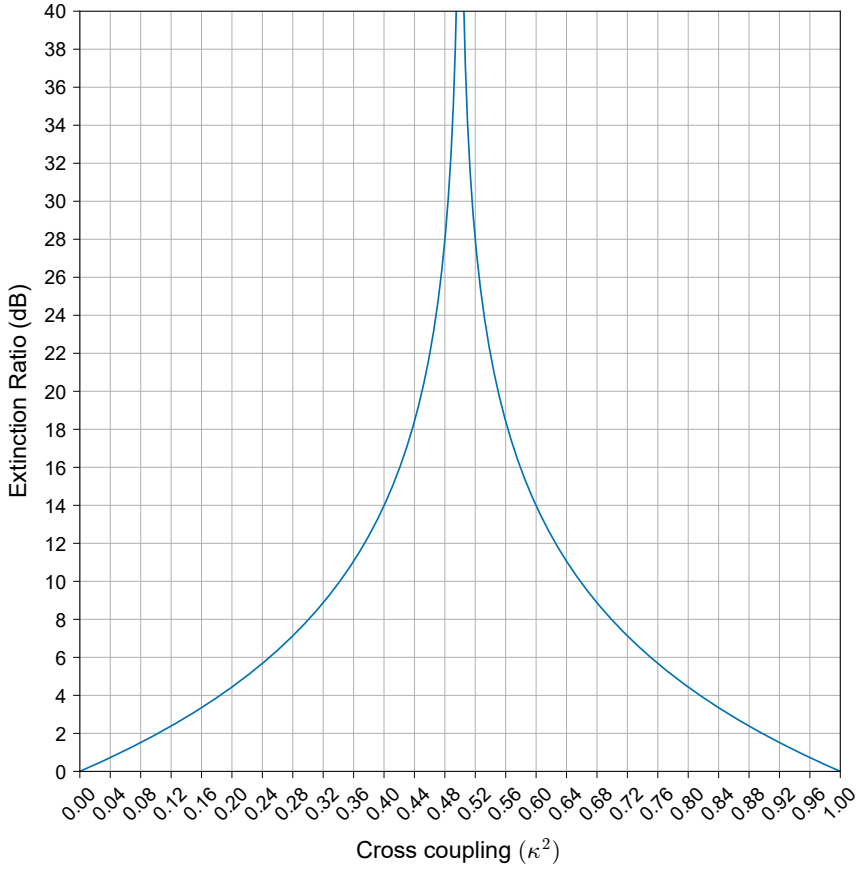

Figure A.1: Extinction Ratio (ER) of the through port of a Mach-Zehnder Interferometer as a function of the DC's power coupling coefficient κ^2. The ER approaches infinity at $\kappa^2 = 0.5$ (perfect 3 dB coupling), and remains above 14 dB for κ^2 values in the range 0.4–0.6. This demonstrates the sensitivity of MZI performance to coupler balance and defines practical fabrication tolerance limits for high-extinction devices.

Working Wavelength and Free Spectral Range (FSR)

In Mach-Zehnder Interferometers, the spectral response is characterized by periodic maxima and minima in transmission, determined by the wavelength-dependent interference between the two arms. Understanding these spectral characteristics is

essential for designing MZI-based wavelength filters and sensors.

Derivation of Constructive Interference Condition

The relative phase difference between the two arms of an MZI is given by:

$$\Delta\phi(\lambda) = \frac{2\pi n_{\text{eff}}(\lambda)\Delta L}{\lambda}, \tag{A.99}$$

where λ is the wavelength, $n_{\text{eff}}(\lambda)$ is the wavelength-dependent effective refractive index of the guided mode, and ΔL is the physical path length difference between the arms.

Constructive interference at the cross port (or destructive interference at the through port) occurs when the phase difference is an integer multiple of 2π, leading to the consecutive interference condition:

$$\frac{n_{\text{eff}}(\lambda_m)\Delta L}{\lambda_m} = m, \quad m \in \mathbb{Z}, \tag{A.100}$$

where λ_m is the m-th order constructive interference wavelength.

Free Spectral Range Calculation

The Free Spectral Range (FSR) is defined as the wavelength spacing between two adjacent peaks (or troughs) in the transmission spectrum of the MZI. :

$$\text{FSR} = \lambda_{m+1} - \lambda_m = \Delta\lambda. \tag{A.101}$$

Using the constructive interference condition (Eq. (A.100)) for adjacent orders m and $m + 1$:

$$\frac{n_{\text{eff}}(\lambda_m)\Delta L}{\lambda_m} = m, \tag{A.102}$$

$$\frac{n_{\text{eff}}(\lambda_{m+1})\Delta L}{\lambda_{m+1}} = m + 1. \tag{A.103}$$

Subtracting these equations, we obtain:

$$\Delta L \left(\frac{n_{\text{eff}}(\lambda_{m+1})}{\lambda_{m+1}} - \frac{n_{\text{eff}}(\lambda_m)}{\lambda_m} \right) = 1. \tag{A.104}$$

To solve for $\Delta\lambda$, we expand the function $f(\lambda_{m+1}) = \frac{n_{\text{eff}}(\lambda_{m+1})}{\lambda_{m+1}}$ around $\lambda = \lambda_m$ using a first-order Taylor series approximation:

$$\frac{n_{\text{eff}}(\lambda_{m+1})}{\lambda_{m+1}} \approx \frac{n_{\text{eff}}(\lambda_m)}{\lambda_m} + \frac{\mathrm{d}}{\mathrm{d}\lambda} \left(\frac{n_{\text{eff}}(\lambda)}{\lambda} \right) \Big|_{\lambda_m} \cdot \Delta\lambda. \tag{A.105}$$

Substituting this approximation into Eq. (A.104) and solving for $\Delta\lambda$:

$$\Delta\lambda = \frac{1}{\Delta L \, \frac{\mathrm{d}}{\mathrm{d}\lambda} \left(\frac{n_{\text{eff}}(\lambda)}{\lambda} \right) \Big|_{\lambda_m}}. \tag{A.106}$$

Applying the product rule to evaluate the derivative:

$$\frac{\mathrm{d}}{\mathrm{d}\lambda} \left(\frac{n_{\text{eff}}(\lambda)}{\lambda} \right) = \frac{1}{\lambda} \frac{\mathrm{d}n_{\text{eff}}}{\mathrm{d}\lambda} - \frac{n_{\text{eff}}}{\lambda^2}. \tag{A.107}$$

Substituting Eq. (A.107) into Eq. (A.106), we obtain the general expression for the FSR:

$$\Delta\lambda = \frac{1}{\Delta L \left(\frac{1}{\lambda} \frac{\mathrm{d}n_{\text{eff}}}{\mathrm{d}\lambda} - \frac{n_{\text{eff}}}{\lambda^2} \right)}. \tag{A.108}$$

FSR in Terms of Group Index

The expression for FSR can be simplified by introducing the group index n_g, which accounts for material and waveguide dispersion:

$$n_g = n_{\text{eff}} - \lambda \frac{\mathrm{d}n_{\text{eff}}}{\mathrm{d}\lambda}. \tag{A.109}$$

Rearranging Eq. (A.109):

$$\frac{\mathrm{d}n_{\text{eff}}}{\mathrm{d}\lambda} = \frac{n_{\text{eff}} - n_g}{\lambda}. \tag{A.110}$$

Substituting Eq. (A.110) into Eq. (A.107):

$$\frac{\mathrm{d}}{\mathrm{d}\lambda}\left(\frac{n_{\text{eff}}(\lambda)}{\lambda}\right) = \frac{1}{\lambda}\cdot\frac{n_{\text{eff}}-n_g}{\lambda} - \frac{n_{\text{eff}}}{\lambda^2}$$
$$= \frac{n_{\text{eff}}-n_g-n_{\text{eff}}}{\lambda^2} = -\frac{n_g}{\lambda^2}. \tag{A.111}$$

Finally, substituting Eq. (A.111) into Eq. (A.108), we obtain the elegant expression for the FSR:

$$\text{FSR} = \Delta\lambda \approx \frac{\lambda^2}{n_g \Delta L}. \tag{A.112}$$

This result reveals that the FSR is:

- Inversely proportional to both the path length difference ΔL and the group index n_g
- Quadratically dependent on the operating wavelength λ

The approximation in Eq. (A.112) is valid when $\Delta\lambda \ll \lambda$ and n_g varies slowly over the wavelength range of interest. This expression is fundamental for designing MZI-based wavelength filters with specific channel spacing requirements.

Thermal Tuning of MZI Filters

Dynamic control of the spectral response is an essential requirement for many photonic applications. Thermal tuning offers an effective method for post-fabrication adjustment and real-time control of MZI filter characteristics, exploiting the thermo-optic effect in silicon photonic waveguides.

Thermo-Optic Effect in Silicon Waveguides

Thermal tuning of MZI filters is typically implemented by placing a metallic heater element above one arm of the interferometer. When current flows through this resistive element, the resulting Joule heating induces a local temperature increase in the silicon waveguide underneath. Silicon exhibits a strong positive thermo-optic coefficient:

$$\frac{\mathrm{d}n_{\text{Si}}}{\mathrm{d}T} \approx 1.8 \times 10^{-4}\,\text{K}^{-1}. \tag{A.113}$$

This coefficient translates to the effective index of the guided mode with a similar magnitude:

$$\frac{\mathrm{d}n_{\text{eff}}}{\mathrm{d}T} \approx 1.8 \times 10^{-4}\,\mathrm{K}^{-1}, \tag{A.114}$$

with small variations depending on the specific waveguide geometry and wavelength.

Temperature-Dependent Effective Index

For moderate temperature changes, the effective index varies linearly with temperature:

$$n_{\text{eff}}(T) = n_{\text{eff}}(T_0) + \frac{\mathrm{d}n_{\text{eff}}}{\mathrm{d}T} \cdot (T - T_0), \tag{A.115}$$

where $n_{\text{eff}}(T_0)$ is the effective index at the reference temperature T_0, and $(T - T_0) = \Delta T$ is the temperature change.

Wavelength Tuning Mechanism

When a heater is activated on one arm of an MZI, the phase difference between the arms is modified according to:

$$\Delta\phi_{\text{thermal}} = \frac{2\pi}{\lambda} \cdot \frac{\mathrm{d}n_{\text{eff}}}{\mathrm{d}T} \cdot \Delta T \cdot L_{\text{heater}}, \tag{A.116}$$

where L_{heater} is the length of the heated waveguide section. This thermally-induced phase shift effectively tunes the spectral response of the MZI.

Working Wavelength Tuning

The constructive interference condition for an MZI requires that the phase difference between arms be an integer multiple of 2π:

$$\frac{2\pi}{\lambda_m} n_{\text{eff}}(\lambda_m, T)\Delta L = 2\pi m, \quad m \in \mathbb{Z}. \tag{A.117}$$

Solving for the resonant wavelength as a function of temperature:

$$\lambda_m(T) = \frac{n_{\text{eff}}(T)\Delta L}{m} = \frac{\left(n_{\text{eff}}(T_0) + \frac{\mathrm{d}n_{\text{eff}}}{\mathrm{d}T} \cdot \Delta T\right)\Delta L}{m}. \tag{A.118}$$

Differentiating Eq. (A.118) with respect to temperature yields the wavelength tuning efficiency:

$$\frac{\mathrm{d}\lambda_m}{\mathrm{d}T} = \frac{\Delta L}{m} \cdot \frac{\mathrm{d}n_{\text{eff}}}{\mathrm{d}T} = \frac{\lambda_m}{n_{\text{eff}}} \cdot \frac{\mathrm{d}n_{\text{eff}}}{\mathrm{d}T}. \tag{A.119}$$

These characteristics make thermal tuning an essential capability for reconfigurable photonic circuits, particularly in applications requiring dynamic wavelength selection, phase error compensation, or wavelength stabilization in dense wavelength-division multiplexing systems.

Doubling MZI Channels: Impact on Crosstalk and Insertion Loss

Cascading MZIs offers a scalable approach to increase channel count in wavelength filtering applications. However, this scaling introduces several performance challenges that require careful consideration. While channel count increases, system complexity grows considerably, particularly regarding phase tuning requirements to maintain proper wavelength alignment across all stages of the cascade.

The transfer matrix method was employed to quantitatively analyze performance degradation when scaling from four to eight channels. Figure A.2 presents the calculated transmission spectra for both configurations, clearly illustrating the performance trade-offs.

The analysis reveals two significant performance impacts when doubling the channel count:

1. **Crosstalk degradation:** The worst-case (cumulative) crosstalk worsened from -15.89 dB in the four-channel system to -14.68 dB in the eight-channel configuration. This degradation results from the cumulative effect of increased channel count, where each additional channel contributes to spectral overlap at adjacent wavelengths.

2. **Insertion loss increase:** The average insertion loss increased from 0.18 dB (four channels) to 0.26 dB (eight channels). This increase occurs because optical signals must propagate through additional cascade stages, accumulating losses.

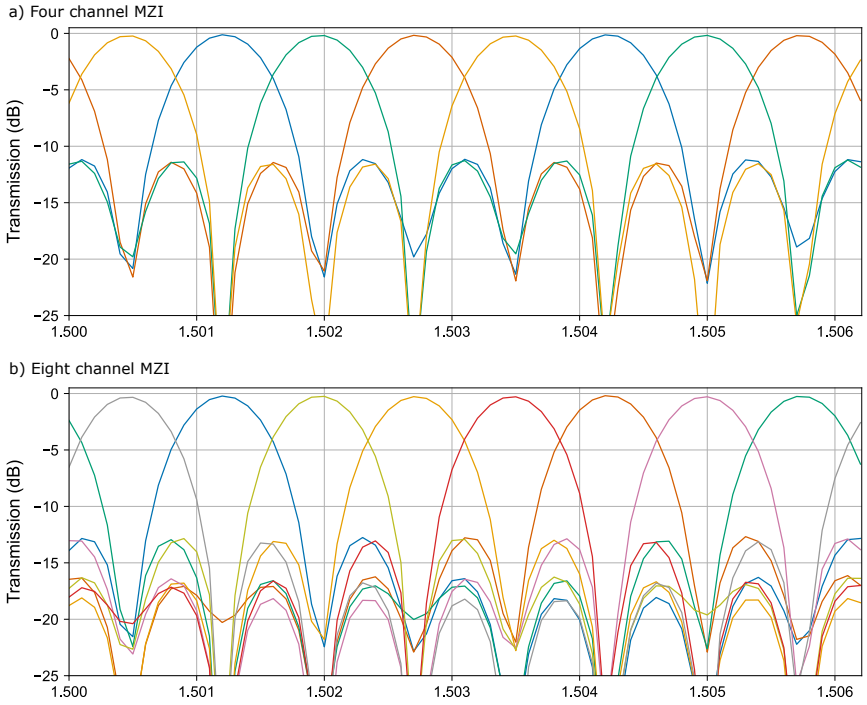

Figure A.2: Transfer matrix method calculation for the transmission spectra comparison between cascaded MZI interleavers based on bent DCs: (a) four-channel configuration and (b) eight-channel configuration, showing wavelength-dependent response characteristics. In each graph, one color is given per output waveguide. The channel spacing is fixed as 100 GHz for both configurations.

These results highlight two critical design requirements for scalable MZI-based wavelength division multiplexing systems:

- The need to minimize excess loss in individual DCs to prevent cumulative loss escalation in cascaded architectures
- The importance of achieving broadband DCs with consistently high extinction ratios across the entire operating wavelength range to maintain channel isolation as channel count increases

A.3 Uncertainty Analysis for Directional Coupler Coupling Ratio Extraction

This section presents a rigorous mathematical analysis of measurement uncertainties [3] for three distinct methods used to determine the DC coupling ratios (κ^2). The uncertainty quantification is crucial for identifying the most appropriate measurement technique. For the derivations that follow, we make the following assumptions:

- A relative power measurement uncertainty δ exists in all optical power measurements.
- Waveguides are considered lossless for analytical simplicity.
- Measurement errors are statistically independent.

The analysis employs two fundamental mathematical approaches for uncertainty propagation:

- **Propagation of uncertainty**: For a function $f(x_1, x_2, \ldots, x_n)$ of multiple variables with uncertainties σ_{x_i}, the combined uncertainty is given by:

$$\sigma_f^2 = \sum_{i=1}^{n} \left(\frac{\partial f}{\partial x_i} \sigma_{x_i} \right)^2$$

- **Linear regression uncertainty**: For parameters derived from linear regression, the uncertainty in the slope m is related to the variance in the dependent variable σ_y^2 and the sum of squares S_{xx} by:

$$\sigma_m = \frac{\sigma_y}{\sqrt{S_{xx}}}$$

Direct Method

Measurement Principle

This method represents the most straightforward approach for determining coupling ratios. The direct method determines the power coupling ratio κ^2 by directly measuring the cross-port power P_{cross} relative to a reference waveguide power P_{ref}:

$$\kappa^2 = \frac{P_{\text{cross}}}{P_{\text{ref}}} \tag{A.120}$$

Here, P_{cross} is the optical power at the cross port of the DC, and P_{ref} is the optical power through a reference waveguide with identical input/output coupling conditions.

Uncertainty Derivation

The derivation of uncertainty for the direct method is based on propagation of uncertainty for a ratio of two measured quantities:

1. For any ratio of two independent measurements $Q = A/B$, the uncertainty follows from the general formula for propagation of uncertainty for a quotient [3]:

$$\sigma_Q = Q\sqrt{\left(\frac{\sigma_A}{A}\right)^2 + \left(\frac{\sigma_B}{B}\right)^2} \tag{A.121}$$

2. Applying this to the power ratio $\kappa^2 = P_{\text{cross}}/P_{\text{ref}}$ with relative uncertainty $\sigma_P/P = \delta$:

$$\sigma_{\kappa^2} = \kappa^2\sqrt{\delta^2 + \delta^2} = \kappa^2\delta\sqrt{2} \tag{A.122}$$

Therefore, the uncertainty in the cross coupling coefficient when using the direct method is:

$$\sigma_{\kappa^2} = \sqrt{2}\delta\kappa^2 \tag{A.123}$$

Ring Based Method

Measurement Principle

This method uses the extinction ratio (ER) at the drop port of a symmetric add-drop ring resonator with a negligible loss to determine the cross coupling coefficient κ^2 of the DC. For such a configuration, the drop port ER can is given by [4, 5]:

$$ER = \frac{T_{\max}}{T_{\min}} \tag{A.124}$$

$$ER = \frac{(2-\kappa^2)^2}{\kappa^4} \tag{A.125}$$

Here, $T_{\max}$ and $T_{\min}$ represent the maximum and minimum transmission values observed in the ring resonator drop port spectral response, respectively.

Solving for κ^2:

$$\kappa^2 = \frac{2}{\sqrt{ER}+1} \tag{A.126}$$

Uncertainty Derivation

The uncertainty analysis for κ^2 for the ring resonator method follows these steps:

1. We first determine the uncertainty in the extinction ratio ER from the standard formula for the error propagation in a quotient [3]:

$$\sigma_{ER} = ER\sqrt{\left(\frac{\sigma_{T_{\max}}}{T_{\max}}\right)^2 + \left(\frac{\sigma_{T_{\min}}}{T_{\min}}\right)^2} \tag{A.127}$$

$$= ER\sqrt{\delta^2+\delta^2} = ER\delta\sqrt{2} \tag{A.128}$$

2. For mathematical convenience, we introduce the substitution $u = \sqrt{ER}$ and rewrite κ^2 as:

$$\kappa^2 = \frac{2}{u+1} \tag{A.129}$$

3. We compute the derivative $\partial\kappa^2/\partial u$:

$$\frac{\partial\kappa^2}{\partial u} = -\frac{2}{(u+1)^2} \tag{A.130}$$

4. The uncertainty in u is derived from σ_{ER}:

$$\sigma_u = \left|\frac{\partial u}{\partial ER}\right|\sigma_{ER} = \frac{1}{2\sqrt{ER}}\cdot ER\delta\sqrt{2} = \frac{\sqrt{ER}\delta\sqrt{2}}{2} = \frac{u\delta}{\sqrt{2}} \tag{A.131}$$

5. The uncertainty in κ^2 is then:

$$\sigma_{\kappa^2} = \left|\frac{\partial\kappa^2}{\partial u}\right|\sigma_u = \frac{2}{(u+1)^2}\cdot\frac{u\delta}{\sqrt{2}} = \frac{\sqrt{2}u\delta}{(u+1)^2} \tag{A.132}$$

6. Substitute $u = \sqrt{ER}$ and express in terms of κ^2 using $u = \frac{2}{\kappa^2} - 1$ and $\kappa^2 = \frac{2}{u+1}$:

$$\sigma_{\kappa^2} = \frac{\sqrt{2}\delta\left(\frac{2}{\kappa^2}-1\right)\kappa^4}{4} = \frac{\sqrt{2}}{4}\delta\kappa^2(2-\kappa^2) \tag{A.133}$$

Therefore, the uncertainty in κ^2 when using the ring resonator based method:

$$\sigma_{\kappa^2} = \frac{\sqrt{2}}{4}\delta\kappa^2(2-\kappa^2) \tag{A.134}$$

Cutback Method

Measurement Principle

The cutback method represents a statistical approach to determining coupling ratios by measuring the output power from multiple identical cascaded DCs. This technique leverages statistical averaging to reduce measurement uncertainty.

For a cascade of N identical DCs, the output power follows:

$$P_N = P_0(\kappa^2)^N \tag{A.135}$$

Where P_0 is a constant and κ^2 is the cross coupling coefficient of each individual DC. Taking the natural logarithm of both sides yields a linear relationship:

$$\ln P_N = \ln P_0 + N \cdot \underbrace{\ln(\kappa^2)}_{m} \tag{A.136}$$

This transformation allows us to determine κ^2 by performing a linear regression, where the slope $m = \ln(\kappa^2)$ directly relates to the cross coupling coefficient.

Uncertainty Derivation

The uncertainty analysis for the cutback method proceeds as follows:

1. We first use the uncertainty in the logarithmic power values [3] to quantify the uncertainty in lnP_N:

$$\sigma_{\ln P_N} = \left|\frac{\partial \ln P_N}{\partial P_N}\right| \sigma_{P_N} = \frac{1}{P_N} \cdot (\delta P_N) = \delta \tag{A.137}$$

2. For a linear regression analysis with k cascaded structures, we define:

$$x_i = i \quad \text{(number of cascades, } i = 1, 2, \ldots, k) \tag{A.138}$$

$$y_i = \ln P_i \quad \text{(logarithm of measured power)} \tag{A.139}$$

$$m = \ln(\kappa^2) \quad \text{(regression slope)} \tag{A.140}$$

3. The uncertainty in the slope of a linear regression is given by the standard formula:

$$\sigma_m = \frac{\sigma_y}{\sqrt{S_{xx}}} \tag{A.141}$$

where $\sigma_y = \delta$ and S_{xx} denotes the sum of squares of the deviations of the independent variable x from its mean:

$$S_{xx} = \sum_{i=1}^{k} (x_i - \bar{x})^2$$

Substituting the expression for $\bar{x}$, the sum of squares becomes:

$$S_{xx} = \sum_{i=1}^{k} \left(i - \frac{k+1}{2} \right)^2 \tag{A.142}$$

Using a known identity for arithmetic series, we obtain the closed-form expression:

$$S_{xx} = \frac{k(k^2-1)}{12} \tag{A.143}$$

4. The uncertainty in the regression slope is:

$$\sigma_m = \frac{\sigma_y}{\sqrt{S_{xx}}} = \frac{\delta}{\sqrt{\frac{k(k^2-1)}{12}}} = \delta \sqrt{\frac{12}{k(k^2-1)}} \tag{A.144}$$

5. Finally, we determine the uncertainty in κ^2 by applying the propagation of uncertainty formula:

$$\kappa^2 = e^m \tag{A.145}$$

$$\frac{d\kappa^2}{dm} = e^m = \kappa^2 \tag{A.146}$$

$$\sigma_{\kappa^2} = \left| \frac{d\kappa^2}{dm} \right| \sigma_m = \kappa^2 \cdot \delta \sqrt{\frac{12}{k(k^2-1)}} \tag{A.147}$$

The uncertainty in the coupling ratio when using the cutback method with k cascaded structures is:

$$\sigma_{\kappa^2} = \kappa^2 \cdot \delta \cdot \sqrt{\frac{12}{k(k^2-1)}} \tag{A.148}$$

This expression demonstrates that the uncertainty decreases proportionally to $k^{-3/2}$ as the number of cascaded structures increases, making this method increasingly precise with larger cascade numbers.

Comparison and Conclusions

Uncertainty Formulas Summary

The derived uncertainty expressions for the three methods are summarized as follows:

$$\textbf{Direct Method:} \quad \sigma_{\kappa^2} = \kappa^2\sqrt{2}\delta \tag{A.149}$$

$$\textbf{Ring-based Method:} \quad \sigma_{\kappa^2} = \frac{\sqrt{2}}{4}\delta\kappa^2(2-\kappa^2) \tag{A.150}$$

$$\textbf{Cutback method:} \quad \sigma_{\kappa^2} = \kappa^2\delta\sqrt{\frac{12}{k(k^2-1)}} \tag{A.151}$$

Comparative Analysis ($\delta = 0.01$, 5 cascades ($k = 5$))

To illustrate the practical implications of these uncertainty formulas, we calculate the expected uncertainty for each method across different coupling regimes, assuming a measurement uncertainty of $\delta = 0.01$ (1%) and $k = 5$ cascaded structures for the cutback method, as shown in Fig. A.3 and the following table:

κ^2	Direct Method	Ring Based Method	Cutback Method
0.1	1.41×10^{-3}	6.72×10^{-4}	3.16×10^{-4}
0.5	7.07×10^{-3}	2.65×10^{-3}	1.58×10^{-3}
0.9	1.27×10^{-2}	3.5×10^{-3}	2.85×10^{-3}

These numerical results demonstrates that the cutback method with $k = 5$ has the least uncertainties amongst the three methods and is therefore considered a highly reliable method.

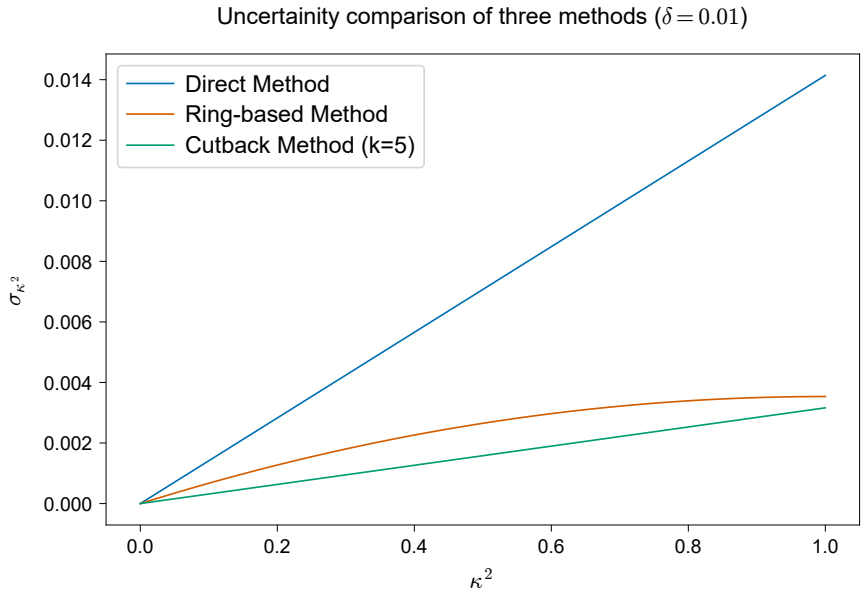

Figure A.3: Uncertainty comparison of the direct method, ring-based method, and the cutback method for extracting κ^2 in a directional coupler. The cutback method with 5 cascades exhibit the least uncertainty among all three methods.

References

[1] Jia ming Liu. *Photonic Devices*. Cambridge University Press, April 2005. ISBN 9780521551953. doi: 10.1017/cbo9780511614255.

[2] Amnon Yariv. Coupled-Mode Theory for Guided-Wave Optics. *IEEE Journal of Quantum Electronics*, 9(9):919–933, 1973. ISSN 1558-1713. doi: 10.1109/JQE.1973.1077767. tex.ids= yariv_coupled-mode_1973-1 conferenceName: IEEE Journal of Quantum Electronics.

[3] John R. Taylor. *An Introduction to Error Analysis: The Study of Uncertainties in Physical Measurements*. University Science Books, Sausalito, CA, 2nd edition, 1997. ISBN 978-0935702750.

[4] W. Bogaerts, P. De Heyn, T. Van Vaerenbergh, K. De Vos, S. Kumar Selvaraja, T. Claes, P. Dumon, P. Bienstman, D. Van Thourhout, and R. Baets. Silicon microring resonators. *Laser & Photonics Reviews*, 6(1):47–73, 2012. ISSN 1863-8899. doi: 10/cr3dtz. ZSCC: 0001902 _eprint:.

[5] Ramón José Pérez Menéndez. *Fiber-Optic Ring Resonator Interferometer*. IntechOpen, August 2019. ISBN 9781838802974. doi: 10.5772/intechopen.80569.